

UNIVERSITA' DEGLI STUDI DI TRIESTE

Dipartimento di Fisica



XXIV CICLO DEL DOTTORATO DI RICERCA IN FISICA

STUDY OF STRUCTURE FORMATION AND EVOLUTION  
IN NON-STANDARD COSMOLOGICAL MODELS

DOTTORANDA

COORDINATORE DEL COLLEGIO DEI DOCENTI

Barbara Sartoris

Chiar.mo Prof. Paolo Camerini

Università degli Studi di Trieste

Firma:\_\_\_\_\_

Firma:\_\_\_\_\_

SUPERVISORE

Chiar.mo Prof. Stefano Borgani

Università degli Studi di Trieste

Firma:\_\_\_\_\_

CO-SUPERVISORE

Dr. Piero Rosati

European Southern Observatory

Firma:\_\_\_\_\_



# Contents

<b>Preface</b>	<b>13</b>
<b>1 Clusters as cosmological probes</b>	<b>19</b>
1.1 Cosmological Framework . . . . .	20
1.2 Cosmic Structure Formation . . . . .	26
1.2.1 The Top-hat Spherical Collapse . . . . .	28
1.3 Statistical properties . . . . .	30
1.4 Matter Power spectrum . . . . .	31
1.5 The mass function . . . . .	35
1.5.1 The Press & Schechter approach . . . . .	35
1.5.2 Numerical calibration of the mass function . . . . .	38
1.5.3 Mass function as a cosmological tool . . . . .	41
1.6 Cluster Bias . . . . .	44
1.7 Cluster power spectrum and RSDs . . . . .	47
1.8 Non-standard cosmological models . . . . .	49
1.8.1 Dark Energy models . . . . .	51
1.8.2 Modified gravity models . . . . .	53
1.9 Primordial Non-Gaussianity . . . . .	55
1.9.1 Mass function . . . . .	57
1.9.2 Bias . . . . .	58
1.10 Cosmological constraints from clusters . . . . .	60
<b>2 Surveys of Galaxy Clusters</b>	<b>67</b>
2.1 Cluster surveys in the optical/near-IR band . . . . .	68
2.1.1 Identification of clusters . . . . .	68
2.1.2 Mass estimation . . . . .	70
2.2 Clusters X-ray Properties and Surveys . . . . .	76
2.2.1 The physics and the structure of the ICM . . . . .	77
2.2.2 Identification of clusters . . . . .	79

2.2.3	Mass estimation: Cluster Scaling Relation . . . . .	82
2.2.4	Phenomenological scaling relations . . . . .	84
2.3	Clusters Microwave properties and surveys . . . . .	84
2.3.1	SZ-Mass scaling relation . . . . .	88
<b>3</b>	<b>Forecasting cosmological constraints</b>	<b>91</b>
3.1	Forecasts on DE models . . . . .	92
3.1.1	DE models. . . . .	93
3.2	Forecast on Non-Gaussian primordial density fluctuations .	95
3.3	The analysis method . . . . .	96
3.3.1	Number counts . . . . .	96
3.3.2	Power spectrum . . . . .	98
3.3.3	Reference values for the cosmological parameters . .	100
3.3.4	Planck CMB experiment . . . . .	101
3.4	Characteristics of the WFXT surveys . . . . .	102
3.4.1	Surveys mass thresholds. . . . .	103
3.4.2	Mass parameters . . . . .	105
3.5	Characteristics of the EUCLID surveys . . . . .	110
3.6	Results . . . . .	112
3.6.1	Cosmological constraints . . . . .	116
3.6.2	Constraints on non-Gaussianity . . . . .	134
3.7	Conclusions . . . . .	143
<b>4</b>	<b>Current constraints from X-ray clusters</b>	<b>149</b>
4.1	The ROSAT Deep Cluster Survey . . . . .	150
4.1.1	The sample selection . . . . .	150
4.1.2	Mass measurements . . . . .	155
4.2	The analysis method . . . . .	161
4.2.1	Survey Volume . . . . .	164
4.3	Results . . . . .	166
4.3.1	High redshift cluster mass function . . . . .	168
4.3.2	Constraints on $\sigma_8$ and $\Omega_m$ . . . . .	169
4.3.3	Constraints on Dark Energy parameters . . . . .	170
4.4	High redshift massive cluster test . . . . .	171
4.5	Conclusions . . . . .	176
<b>A</b>	<b>Fisher Matrix technique</b>	<b>187</b>

# List of Figures

1.1	Hubble diagram . . . . .	21
1.2	Universe component evolution with redshift . . . . .	25
1.3	Growth factor for different set of cosmological parameters .	28
1.4	Matter power spectra for different DM scenarios and $\Omega_m$ . .	33
1.5	Transfer function for different values of $\Omega_b$ . . . . .	36
1.6	Ratio between different mass function prescription . . . . .	40
1.7	Mass function for different set of cosmological parameters .	43
1.8	Discovery probability as a function of cluster mass . . . . .	45
1.9	Halo bias as a function of mass . . . . .	48
1.10	RSDs effect . . . . .	50
1.11	Ratio between non-Gaussian and Gaussian mass functions .	59
1.12	Ratio between non-Gaussian and Gaussian bias . . . . .	61
1.13	Cosmological constraints from Vikhlinin et al. 2009 . . . . .	64
1.14	Cosmological constraints from Mantz et al. 2010 . . . . .	65
1.15	Cosmological constraints from Rozo et al. 2010 . . . . .	66
2.1	Red sequence of cluster Abell 1682 . . . . .	69
2.2	$L_{op} - M_{500}$ relation in the $i$ SDSS band . . . . .	72
2.3	Sky coverage as a function of X-ray flux . . . . .	80
2.4	L-M scaling relation . . . . .	85
2.5	L-Y scaling relation . . . . .	86
2.6	Selection function in X-ray and SZ surveys . . . . .	88
2.7	$Y_{SZ}$ -mass scaling relation . . . . .	90
3.1	Effective flux limits for WFXT . . . . .	105
3.2	WFXT surveys mass thresholds. . . . .	106
3.3	WFXT cumulative redshift distributions for $\Lambda$ CDM . . . . .	107
3.4	WFXT cumulative redshift distributions for EDE model . . .	108
3.5	Selection function for the Euclid survey . . . . .	113
3.6	Cumulative number of clusters for the Euclid survey . . . .	113

3.7	RDCS logN-logS . . . . .	114
3.8	Redshift distribution from RDCS and prediction from $\Lambda$ CDM	115
3.9	Constraints on $(\Omega_m, \sigma_8)$ and $(w_0, w_a)$ parameters from WFXT	119
3.10	Mass-parameters analysis: constraints on $(\Omega_m, \sigma_8)$ and $(w_0, w_a)$	120
3.11	Contribution analysis: constraints $(\Omega_m, \sigma_8)$ and on $(w_0, w_a)$	124
3.12	Shape analysis: constraints on $(\Omega_m, \sigma_8)$ . . . . .	127
3.13	RSDs analysis: constraints on $(w_0, w_a)$ . . . . .	129
3.14	Constraints on EDE EoS . . . . .	130
3.15	Figures-of-Merit for the $(w_0, w_a)$ parameters . . . . .	133
3.16	Constraints on $(w_0, w_a)$ from Euclid . . . . .	135
3.17	Constraints on $(w_0, \Omega_{DE})$ current and future surveys . . . . .	136
3.18	Constraints on $(f_{NL}, \sigma_8)$ from NC and PS separately . . . . .	137
3.19	Constraints on $(f_{NL}, \sigma_8)$ . . . . .	139
3.20	Effective volume . . . . .	141
3.21	Mass parameters analysis: constraints on $(f_{NL}, \sigma_8)$ . . . . .	142
3.22	$f_{NL}$ dependence on mass parameters . . . . .	144
4.1	RDCS sky coverage . . . . .	152
4.2	Areas and flux limits of RDCS surveys . . . . .	153
4.3	XMM COSMOS and RDCS cumulative cluster number density	155
4.4	RDCS redshift distribution . . . . .	156
4.5	RDCS cluster images (1) . . . . .	157
4.6	RDCS cluster images (2) . . . . .	158
4.7	Mass reconstruction of RDCS-J1252-2927 cluster . . . . .	162
4.8	Cluster mass functions for our low- and high-z samples . . . . .	171
4.9	Constraints on $(\Omega_m, \sigma_8)$ from 400d and zRDCS-1 samples . . . . .	172
4.10	Constraints on $(\Omega_{DE}, \sigma_8)$ from 400d and zRDCS-1 samples . . . . .	173
4.11	Number of clusters as a function of $\sigma_8$ and $f_{NL}$ . . . . .	177
4.12	Cluster finding probability . . . . .	178

# List of Tables

3.1	Characteristics of the WFXT surveys . . . . .	105
3.2	Figure of Merit and r.m.s. uncertainty on $(w_0, w_a)$ . . . . .	118
3.3	Prior on mass parameters and FoM . . . . .	122
3.4	FoM of structure formation timing . . . . .	138
4.1	Characteristics of the zRDCS-1 sample . . . . .	159
4.2	Mass and luminosity parameters from RDCS sample . . . . .	167



# Acronyms

**ACT** Atacama Cosmology Telescope

**AGN** Active Galactic Nucleus

**BAOs** Baryonic Acoustic Oscillations

**CDM** Cold Dark Matter

**CMB** Cosmic Microwave Background

**DE** Dark Energy

**DGP** Dvali, Gabadadze, and Porrati braneworld model

**DM** Dark Matter

**EFE** Einstein field equations

**EoS** Equation of State

**ESSENCE** Equation of State: Supernovae Trace Cosmic Expansion

**FM** Fisher Matrix

**FoV** Field of View

**FRW** Friedman-Robertson-Walker metric

**GR** General Theory of Relativity

**HDM** Hot Dark Matter

**HEW** Half Energy Width

**HST** Hubble Space Telescope

**ICM** Intracluster Medium

**ISM** Intrastellar Medium

$\Lambda$ CDM Lambda Cold Dark Matter

**LSS** Large Scale Structure

**MCMC** Montecarlo Markov-Chain

**ML** Maximum Likelihood

**RSDs** Redshift Space Distortions

**RDCS-3** ROSAT Deep Cluster Survey,  $f_x = 3 \times 10^{-14} \text{ erg s}^{-1} \text{ cm}^{-2}$ , [0.5-2]keV

**PS** Press & Schechter 1974

**PSF** Point Spread Function

**RASS** ROSAT All Sky Survey

**SB** Surface Brightness

**SC** Spherical Collapse

**SDSS** Sloan Digital Sky Survey

**SNLS** Supernova Legacy Survey

**SN Ia** type Ia Supernovae

**SO** Spherical Overdensity

**SPT** South Pole Telescope

**ST** Sheth & Tormen 1999

**SMT** Sheth Mo Tormen 2001

**SZ** Sunyaev-Zel'dovich

**UDM** Unified Dark Matter model

**VLT** Very Large Telescope

**XDCP** XDSP survey

**WFXT** Wide Field X-ray Telescope

**WL** Weak Gravitational Lensing



# Preface

This Ph.D. Thesis is devoted to the derivation of cosmological constraints by using clusters of galaxies as probes.

Clusters of galaxies provide potentially powerful means to measure the growth of cosmic structures, as well as excellent astrophysical laboratories. As such they have played an important role in establishing the current cosmological paradigm.

The number density of nearby galaxy clusters provides constraints on the amplitude of the power spectrum while its evolution is directly related to the growth rate of density perturbations and thus to the amount of Dark Energy (DE) and Dark Matter (DM) at a given redshift. Additionally, distribution of clusters (i.e., correlation function and power spectrum) provides direct information on the shape and amplitude of the power spectrum of density perturbations and the evolution of clustering properties is again sensitive to the growth rate of such perturbations. A crucial aspect concerning the possibility of using clusters as cosmological tools regards the measurement of their mass and how this mass can be related to observational quantities (i.e., X-ray temperature, Sunyaev-Zel'dovic signal, velocity dispersion of member galaxies, strong and weak lensing effects).

In order to be able to constrain cosmological parameters, we need to determine the evolution of the space density of clusters, and this requires counting the number of clusters of a given mass per unit volume at different redshifts. In this respect having an efficient method to find clusters over a wide redshift range, and an observable estimator of the cluster mass is not enough. A robust method to compute the selection function i.e. the survey volume within which clusters are found, is also essential.

The cosmological constraints obtained from clusters so far have been mostly derived from X-ray observations and, more specifically, from relatively small ROSAT-based samples, containing  $\sim 100$  clusters at  $z < 1$ . Future large galaxy cluster surveys, like the one to be carried out with

the forthcoming eROSITA<sup>1</sup>, satellite will increase by orders of magnitude the statistics of detected clusters out to  $z \sim 1$ , while future high-sensitivity wide-area telescopes, such as the approved optical/near-IR EUCLID<sup>2</sup> telescope or the proposed Wide Field X-ray Telescope (WFXT<sup>3</sup>), will have the capability of measuring mass proxies for such clusters out to  $z \sim 1.5$ . In view of future large surveys to be carried out with the next generation of telescopes, it is crucial to quantify the constraining power of such surveys and understand the possible limiting factor in their cosmological exploitation.

This Thesis is divided into five Chapters. Chapter 1 presents a concise review about the general framework of  $\Lambda$ CDM cosmological model and the main aspects of hierarchical cosmic structure formation. We will focus on the cosmological tests provided by galaxy clusters that have been used in the rest of this Thesis. We present the statistical properties of the perturbation density fields, describing how the cluster distribution changes according to the underlying Dark Matter scenario, and how this distribution can be used as a geometrical test on the Universe evolution. We describe the sensitivity of the cluster mass function to cosmological parameters, and we highlight the differences and the limits of the most commonly used calibration of the mass function as obtained from N-body simulation. Then, we summarize the main classes of non-standard cosmological models, and we briefly describe the primordial non-Gaussian density fluctuation scenario. Finally, the current constraints on cosmological parameters as obtained from cluster analysis, are summarized.

In Chapter 2, the observational methodology used to build samples of galaxy clusters in the optical/near-IR, in the X-ray and in the Microwave bands is reviewed. We highlight the principal advantages and the disadvantages of clusters observation in each of these three bands. We summarize how clusters are detected and identified, and how we can determine the selection function of a specific survey. Finally, we discuss the principal methods to estimate masses of galaxy clusters.

The original work of my Ph.D. project can be divided in two main parts which constitute the remaining two Chapters.

In Chapter 3, we present results on forecasts for different parametrizations of the DE equation of state from WFXT surveys. This analysis is

---

<sup>1</sup><http://www.mpe.mpg.de/heg/www/Projects/erosita/index.php>

<sup>2</sup><http://sci.esa.int/science-e/www/area/index.cfm?fareaid=102>

<sup>3</sup><http://www.wfxt.eu/>

based on computing the Fisher-Matrix for number counts and large-scale power spectrum of clusters. The Appendix A, is dedicated to the definition of the Fisher Matrix to the we explanation of its statistical properties. Based on the so-called self-calibration approach, and including prior knowledge of cosmological parameters to be provided by CMB observations with the Planck satellite in our analysis, in Chapter 3, we derive constraints on nine cosmological parameters and four parameters, which define the relation between cluster mass and X-ray flux. This study on DE models is performed with the main purpose of dissecting the cosmological information provided by geometrical and growth tests, which are both included in the analysis of number counts and clustering of galaxy clusters. We compare cosmological constraints obtained by assuming different levels of prior knowledge of the parameters which define the relation between cluster mass and X-ray observables. This comparison demonstrates the fundamental importance of having a well calibrated observable-mass relation and, most importantly, its redshift evolution. These results will be published in Sartoris et al. (2012, MNRAS).

With the Fisher Matrix methodology developed in this work, we also provide forecasts for constraints on the DE for the cluster survey to be carried out with the optical near-infrared EUCLID satellite, which has been recently approved by the European Space Agency (ESA). This analysis has been used for the definition of the scientific case of this mission, and have been included in the EUCLID mission definition study (Laureijs et al., 2011).

We extend the above analysis by also computing forecasts for constraints on deviations from Gaussian distribution of primordial density perturbations expected from the WFXT experiment. Because of the scale dependence of large-scale bias induced by local-shape non-Gaussianity, we find that the power spectrum provides strong constraints on the non-Gaussianity parameter,  $f_{\text{NL}}$ , which complement the stringent constraints on the power spectrum normalization,  $\sigma_8$ , from the number counts. These results have been published in Sartoris et al. 2010, MNRAS, 407, 2339.

In Chapter 4, we present the results derived from the analysis of nine clusters at redshift  $z \geq 0.8$  that belong to the ROSAT Deep Cluster Survey (RDCS).

Despite the steady increase of the number of detected clusters at high redshift, the RDCS survey until recently was the deepest ROSAT survey available. It includes a sample of 107 clusters out to  $z = 1.3$ , all confirmed by optical and spectroscopic observations. Nine of these clusters are at

redshift  $z \geq 0.8$ , and for most of them, deep follow-up observations provided by *Chandra* and Hubble Telescope images have been collected in the last years, as well as spectroscopic campaigns with the VLT and Keck telescopes. Thanks to these deep observations all these high- $z$  RDCS clusters but two have mass measurements from X-ray temperature and for five of them weak lensing masses are also available.

After developing a fitting algorithm based on the Montecarlo Markov-Chain (MCMC) and the maximum likelihood criterion, and by using the available mass measurements for RDCS clusters, we present the mass function for redshift  $0.8 \leq z < 1.3$  for the concordant  $\Lambda$ CDM cosmology. With the same MCMC tool, using current lower redshift results as a prior, we study the increment of the constraining power of clusters on the cosmological parameters, contributed by such high redshift clusters. This analysis demonstrate the key relevance of high redshift clusters to extend the redshift range over which the evolution of perturbation growth is studied. We check the consistency between the prediction at  $z > 0.8$  of the  $\Lambda$ CDM model based on cluster observation at lower redshift, and the number density of clusters observed in the high- $z$  RDCS sample. In our analysis we take into account the errors in the calibration of the observable-mass scaling relations. Moreover, we consider uncertainties in the computation of the survey volume originated from a X-ray flux limited (i.e. not mass limited) sample. The results of this analysis will be published in Sartoris et al. (2012, in preparation).

During the last decade, a significant improvement in the detection and study of massive clusters up to  $z \sim 1$  and beyond has been done, thanks to *Chandra* and XMM observatories and thanks to observations of the Sunyaev-Zel'dovic effect carried out by the Planck Satellite<sup>4</sup>, and by dedicated ground-based millimeter telescopes (South Pole Telescope<sup>5</sup>, Atacama Cosmology Telescope<sup>6</sup>). Because the cluster mass function is particularly sensitive to the cosmological parameters at high masses and high redshift, using the same procedure defined in the RDCS analysis, we calculate the likelihood of finding a cluster with a given mass and redshift within its survey volume according to the mass function in order to test any cosmological model. In order to use this test one needs a precise measure of the cluster mass and a full accounting of the effects of errors in the calibration of the mass-observable scaling relations, as well

---

<sup>4</sup><http://www.rssd.esa.int/index.php?project=Planck>

<sup>5</sup><http://pole.uchicago.edu/>

<sup>6</sup><http://physics.princeton.edu/act/>

as a complete understanding of the survey volume within the cluster has been found.

In the last Chapter, we summarize the results obtained in this Thesis. We empathize which are the challenge for clusters to be used as powerful probes in the era of precision cosmology, focusing on the importance of having a well calibrated theoretical mass function on a wide range of masses, and for non-standard cosmological models. From an observation point of view, future experiments will increase the number of detected clusters up to a few thousand or even more. In order to provide robust cosmological constraints, we stress the importance of having deep high-sensitive observations for a large subsample of the detected clusters to study the evolutionary trends in a number of independent physical parameters including the cluster mass, the gas density and temperature, the underlying galactic mass, and star formation rates. The combination of studies carried out with cluster sample in different bands will further help in reducing the impact of the systematic errors on the final constraints.



# Chapter 1

## Clusters of galaxies as cosmological probes

Clusters of galaxies are a particularly rich source of information about the underlying cosmological model, making possible a number of critical tests. These objects allow us to constrain the value of the parameters that describe cosmological models and to distinguish among different models that predict different evolution or structure formation history of the Universe. The number density and the distribution of galaxy clusters are highly sensitive to specific cosmological scenarios and directly trace the process of structure formation in the Universe.

In this Chapter the general framework of standard  $\Lambda$ CDM cosmological model will be reviewed. Then, the main aspects of hierarchical structure formation scenarios will be introduced focusing on the cosmological tests provided by galaxy clusters that have been used in the rest of this Thesis. Furthermore, we will briefly describe the main classes of non-standard cosmological models, and the primordial non-Gaussian density fluctuation scenario. The last Section of this Chapter summarizes the current constraints on cosmological parameters as obtained from cluster analysis. A more complete treatment of cosmological models and structure formation scenarios can be found in classical textbooks as Dodelson (2003); Coles & Lucchin (2002); Peacock (1999); Peebles (1993); Weinberg (1972).

## 1.1 Cosmological Framework

In 1998, two teams (Riess et al., 1998; Perlmutter et al., 1999) independently presented evidence that the Universe undergoes a phase of accelerating expansion. By studying type Ia Supernovae (SN Ia) data in the redshift regime  $0.2 < z < 0.8$ , they showed that the luminosity distances of observed SN Ia tend to be larger than those predicted in a flat matter dominated Universe. These observations point to a new Dark Energy (DE) density or negative pressure in the vacuum perceived by gravitational interactions. The simplest way to describe these results, in the context of the current cosmological theories was the introduction of a small positive value for the cosmological constant  $\Lambda$  in Einstein equations of General Relativity.

Over the past decade, subsequent observations confirmed that the Universe entered the epoch of cosmic acceleration after the matter - dominated era. These observations included more detailed studies of Supernovae; for instance, two large ground-based surveys, the SNLS (Supernova Legacy Survey) (Astier et al., 2006) and the ESSENCE (Equation of State: Supernovae Trace Cosmic Expansion) survey (Miknaitis et al., 2007), measured light curves for several hundred SNe Ia over the redshift range  $z \sim 0.3 - 0.9$ . Moreover, independent evidences of accelerating expansion were provided by clusters of galaxies (e.g. Allen et al., 2004, 2008), large-scale structure (LSS) (e.g. Eisenstein et al., 2005) and the cosmic microwave background radiation (CMB) (e.g. Komatsu et al., 2011).

After the accelerated expansion of the Universe has been confirmed, the Lambda Cold Dark Matter scenario ( $\Lambda$ CDM, Perlmutter et al., 1999) has been adopted as the concordance standard model. According to this model, the Universe is composed of radiation, baryons, a non collisional, non baryonic matter, called Dark Matter (DM), and a form of energy density with negative pressure, called dark energy (DE).

The standard model is based, among the others, on the validity of the following arguments:

1. The *Copernican Principle*: on scale larger than 100 – 200 Mpc the Universe can be considered as homogeneous and isotropic. According to this assumption, the space-time metric is the *Friedman-Robertson-Walker* (FRW) one:

$$ds^2 = c^2 dt^2 - a^2(t) \left[ \frac{dr^2}{1 - k r^2} + r^2 (d\theta^2 + \sin^2\theta d\phi^2) \right] \quad (1.1)$$

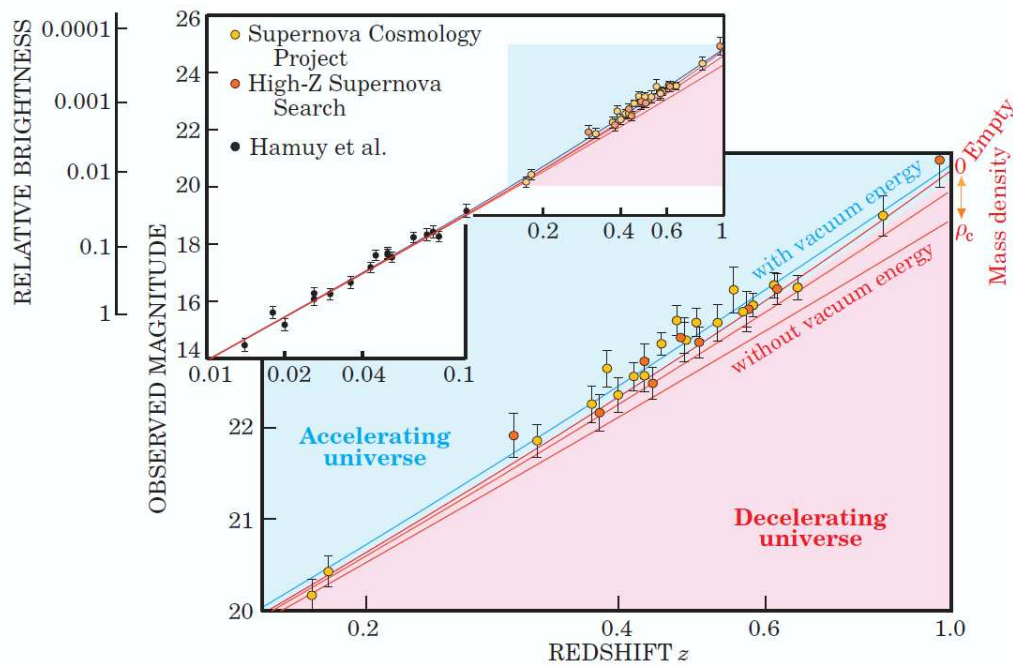


Figure 1.1: Observed magnitude versus redshift is plotted for SNe Ia measured by the Supernova Cosmology Project (Perlmutter et al., 1999), the High-z Supernova Team (Riess et al., 1998) and (in the inset) by Hamuy et al. (1995) for nearby SNIa. The four curves show from top to bottom four cosmological models:  $\Omega_m = 0.3, \Omega_{DE} = 0.7$ ;  $\Omega_m = 0, \Omega_{DE} = 0$ ;  $\Omega_m = 0.3, \Omega_{DE} = 0$ ;  $\Omega_m = 1, \Omega_{DE} = 0$ . Figure from Perlmutter (2003).

where  $r, \theta, \phi$  are the comoving spatial coordinates,  $t$  is time, and the expansion is described by the cosmic scale factor,  $a(t)$  (by convention,  $a = 1 \equiv a_0$  today). The quantity  $k$  is the curvature of 3-dimensional space:  $k = 0$  corresponds to a spatially flat geometry,  $k > 0$  to the positive curvature (3-sphere), and  $k < 0$  to the negative curvature. In the  $\Lambda$ CDM model, the geometry of the Universe is Euclidean.

2. The *Standard Model of particle physics* that describes the properties of the subatomic particles and how the dynamic of such particles is mediated by the electromagnetic, weak, and strong nuclear interactions.
3. The *General Theory of Relativity* (GR) which describes the gravitational attraction between masses as a result of space-time being curved by matter and energy. This relation between the geometry of a 4-dimensional space-time manifold with its material and energy content is described by a set of ten equations, the Einstein field equations (EFE):

$$G_{\alpha\beta} = R_{\alpha\beta} - \frac{1}{2} R g_{\alpha\beta} = \frac{8\pi G}{c^4} T_{\alpha\beta} + \Lambda g_{\alpha\beta} \quad (1.2)$$

In this equation  $\alpha, \beta = 0, 1, 2, 3$ ,  $G_{\alpha\beta}$  is the Einstein tensor,  $R_{\alpha\beta}$  is the Ricci tensor,  $R$  is the Ricci scalar,  $g_{\alpha\beta}$  is the metric tensor, and  $\Lambda$  is the cosmological constant, proposed by Einstein to achieve a stationary Universe.  $T_{\alpha\beta}$  is the energy-momentum tensor, and describes the matter content of the Universe. For a perfect fluid,  $T_{\alpha\beta}$  can be expressed as:

$$T_{\alpha\beta} = (\rho + p) u_\alpha u_\beta + p g_{\alpha\beta} \quad (1.3)$$

where  $u_\alpha$  and  $u_\beta$  are the fluid four-velocity,  $\rho$  and  $p$  are respectively the energy density and the pressure in the rest frame of the fluid.

4. The *Inflation model* which is the theorized accelerated expansion of the early Universe driven by a negative-pressure vacuum energy density right after the Big Bang, that amplified quantum fluctuations of the inflation field to produce the seed fluctuations that will evolve according to the standard formation scenario. Moreover, as a consequence of the expansion, all of the observable Universe originated in a small causally connected region.

By including the FRW metric (Eq. 1.1) in the GR equation (Eq. 1.2), we obtain the *Friedman equations* that describe the expansion of the space in homogeneous and isotropic models of the Universe within the context of general relativity. From the 00 component and from the trace of Einstein field equations respectively, the following equations are derived:

$$\dot{a}^2 = \frac{8\pi G}{3} \rho a^2 + \frac{1}{3} c^2 \Lambda a^2 + k c^2, \quad (1.4)$$

$$\ddot{a}^2 = -\frac{4\pi G}{3} \left( \rho + \frac{3p}{c^2} \right) a + \frac{1}{3} c^2 \Lambda a. \quad (1.5)$$

Here, dots represent the time derivatives of the scale factor  $a(t)$ ,  $\rho$  is the density,  $p$  is the pressure,  $\Lambda$  is the Einstein's cosmological constant, and  $k$  is the space time curvature constant ( $k = 0$  in  $\Lambda$ CDM model). Assuming the equation of state of a perfect fluid,  $p = w \rho c^2$ , the density of each of the major energy components changes with the expansion as  $\rho_i(a) \propto a^{-3(1+w)}$ . Here  $w = 0$  for the matter (DM and baryonic) component,  $\rho_m$ ,  $w = 1/3$  for the radiation component,  $\rho_r$ , and  $w < -1/3$  for the Dark Energy,  $\rho_{DE}$ .

The ratio of the expansion velocity and the scale factor defines the Hubble parameter  $H(a)$ , i.e. the fractional increase of the Universe per unit time:

$$H(a) \equiv \frac{\dot{a}}{a}. \quad (1.6)$$

All energy densities can be transformed into dimensionless parameters by stating them in units of the critical energy density  $\rho_{cr}$ . The latter quantity is defined as the total energy density that results from Eq. 1.4 in a flat global geometry of the Universe, with  $\Lambda = 0$ . At  $z = 0$  the value of  $\rho_{cr}$  is:

$$\rho_{cr} = \frac{3H_0^2}{8\pi G} = 1.879 \times 10^{-29} \text{ h}^2 \text{ M}_\odot \text{ Mpc}^{-3} \quad (1.7)$$

Here, the value of the Hubble constant at  $z = 0$ ,  $H_0$  is parametrized as  $H_0 = h \times 100 \text{ km s}^{-1} \text{ Mpc}^{-1}$ , where  $h$  is a constant. Thus, the dimensionless energy components as measured today are:

$$\Omega_m \equiv \frac{\rho_m}{\rho_{cr}}; \quad \Omega_{DE} \equiv \frac{\rho_{DE}}{\rho_{cr}} = \frac{\Lambda c^2}{3H_0^2}; \quad \Omega_r \equiv \frac{\rho_r}{\rho_{cr}}; \quad (1.8)$$

and the parameter that describe the curvature of the Universe is defined as:

$$\Omega_k \equiv 1 - \Omega_m - \Omega_{DE} - \Omega_r. \quad (1.9)$$

If we define the redshift as  $z = 1/a - 1$ , by combining Eqs. 1.4, 1.6 and 1.8, the Hubble expansion history equation is obtained:

$$\begin{aligned} H^2(z) &= H_0^2 E^2(z) \\ &= H_0^2 [\Omega_m (1+z)^3 + \Omega_{DE} (1+z)^3 \exp \left\{ 3 \int_0^{z'} \frac{w(z')}{1+z'} dz' \right\} \\ &\quad + \Omega_r (1+z)^4 + \Omega_k (1+z)^{-2}]. \end{aligned} \quad (1.10)$$

According to the  $\Lambda$ CDM prescription, the DE equation of state (EoS) parameters  $w$  is equal to  $-1$ . However, a plethora of models, characterized by different DE EoS that evolve with evolution, have been proposed (see Section 1.8). The commonly used parametrization of the DE EoS is:

$$w_{DE}(a) = w_0 + w_a (1 - a) = w_0 + w_a \left( \frac{z}{1+z} \right), \quad (1.11)$$

has been originally proposed by Linder (2003), and has been adopted in the Dark Energy Task Force reports (DETF; Albrecht et al., 2006) to assess the constraining power of different cosmological experiments.

Evolution of energy densities with redshift,  $\Omega_i$ , are:

$$\Omega_i(z) = \Omega_i(z=0) (1+z)^{3(1+w)} [H(z)/H_0]^{-2}. \quad (1.12)$$

In Figure 1.2 it is shown the dependence of  $\Omega_m(z)$ ,  $\Omega_{DE}(z)$  and  $\Omega_r(z)$  on the redshift for different set of values of present-day cosmological parameters. Because these densities scale differently in time, two important redshifts can be defined. The first is the transition from a radiation-dominated Universe to a matter-dominated one, this transition occurs at the so called *equivalence redshift*:

$$z_{eq} = 2.38 \times 10^4 \Omega_{m,0} h^2 \quad (1.13)$$

The second transition occurs when the Dark Energy term starts to dominate expansion history of the Universe. In Figure 1.2 it is shown how much the redshift of this transition change for different values of  $\Omega_m$ ,  $\Omega_{DE}$  and of the Dark Energy equation of state parameter ( $w_{DE}$ ). The redshift of the transition between matter and DE dominated Universe lie in a range that can be well explored by galaxy clusters, moreover the values of  $\Omega_{DE}$ ,  $\Omega_m$ , and  $w_{DE}$  parameters influences the structure formation history and thus the properties of the cluster population as we will see in the next Section.

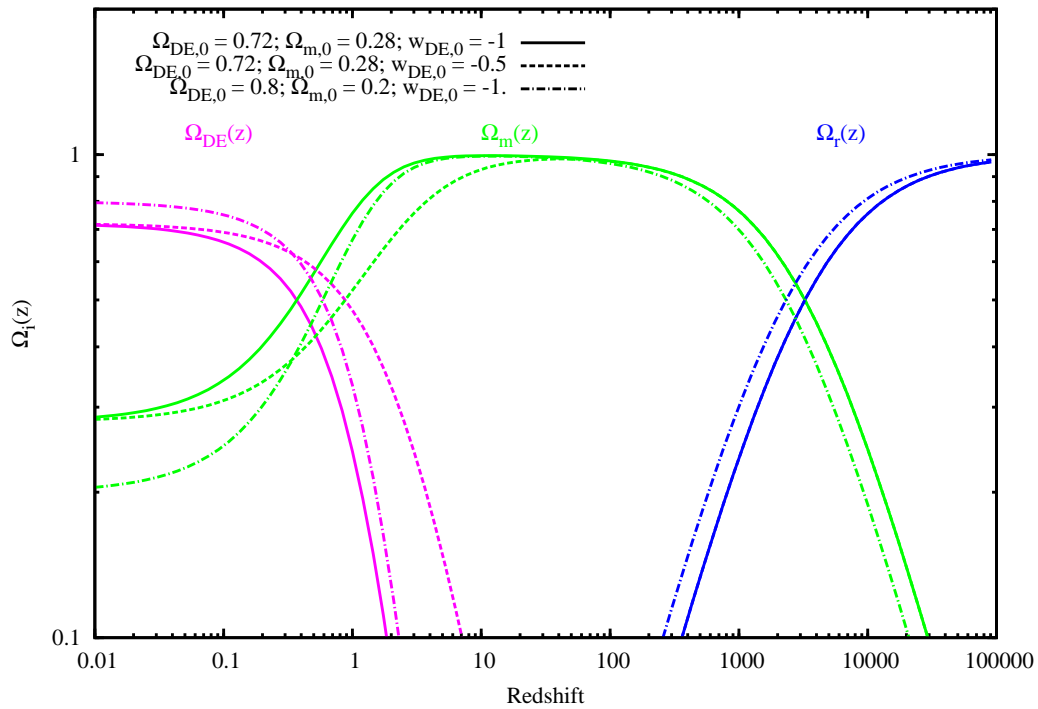


Figure 1.2: Different types of curves represent the dependence of  $\Omega_m(z)$  (green curves),  $\Omega_{DE}(z)$  (magenta curves) and  $\Omega_r(z)$  (blue curves) on redshift for various sets of present-day cosmological parameters:  $\Omega_{DE,0} = 0.72; \Omega_{m,0} = 0.28; w_{DE,0} = -1$  (solid curves)  $\Omega_{DE,0} = 0.72; \Omega_{m,0} = 0.28; w_{DE,0} = -0.5$  (dotted curves)  $\Omega_{DE,0} = 0.8; \Omega_{m,0} = 0.2; w_{DE,0} = -1$  (dot-dashed curves). Adapted from Voit (2005).

## 1.2 Cosmic Structure Formation

In the previous Section, we derived the equations that describe the evolution of the Universe and of its components in the context of the standard  $\Lambda$ CDM model. In this Section we will review the basic concepts of linear cosmological perturbation theory and the structure formation scenarios (for a comprehensive treatment of the subject see Dodelson, 2003).

According to the standard prescription, we assume the gravitational instability model proposed by Jeans in the early 1900s. Jeans demonstrated that an overdense region, if its pressure is negligible compared to the gravitational strength, accretes material from its surroundings until the overdensity is strong enough to separate from the background expansion. Then, it becomes unstable and finally collapses into a gravitational bound system. If the perturbations are small ( $\delta X \ll X$ ), they can be studied in the linear regime.

If we model the Universe as a multicomponent fluid, we can consider each fluid described by the density  $\rho_i$ , the pressure  $p_i$  and the velocity  $v^\alpha$  in a gravitational potential  $\Phi$ , adopting the space coordinates  $r_\alpha$ . Such fluid evolves according to the standard equations for a self gravitating medium. The continuity equation:

$$\frac{\partial \rho}{\partial t} + \partial_\alpha (\rho v^\alpha) = 0 \quad (1.14)$$

which describes the mass conservation. The Euler equation

$$\frac{\partial v_\alpha}{\partial t} + v^\beta \partial_\beta v_\alpha + \frac{1}{\rho} \partial_\alpha p + \partial_\alpha \Phi = 0 \quad (1.15)$$

which gives the momentum conservation, and the Poisson equation

$$\partial^2 \Phi = 4\pi G \rho \quad (1.16)$$

which specifies the Newtonian nature of the gravitational force. In the above equation  $\partial^2 = \partial^\alpha \partial_\alpha$  is the associated Laplacian operator. This system of equations is valid inside the Hubble radius<sup>1</sup> for non-relativistic components.

---

<sup>1</sup>The Hubble radius is the proper distance that corresponds to the speed of the light  $c$ :  $R_H(z) = c/H(z)$ . This radius represents the region within it is possible to exchange information.

We assume a barotropic fluid where  $p = p(\rho)$  and we consider small perturbations on the background solution:

$$\rho = \rho_0 + \rho_1; \quad p = p_0 + p_1; \quad v^\alpha = v_0^\alpha + v_1^\alpha; \quad \Phi = \Phi_0 + \Phi_1 \quad (1.17)$$

where  $\rho_1$ ,  $p_1$ ,  $v_1^\alpha$ ,  $\Phi_1$  are the perturbation at first order with spatial and temporal dependence. Because it is advantageous to employ dimensionless variables for first order quantities, we define the density contrast

$$\delta \equiv \frac{\rho(\mathbf{x}) - \bar{\rho}}{\bar{\rho}} \quad (1.18)$$

where  $x$  is the comoving coordinate ( $r_\alpha = ax_\alpha$ ),  $\rho(\mathbf{x})$  is the matter density field, which is a continuous function of the position vector  $\mathbf{x}$ ,  $\bar{\rho}$  ( $\bar{\rho} \equiv \rho_0$ ) is its average density computed over a sufficiently large (representative) volume of the Universe. By including Eq. 1.17 in the fluid Eqs. 1.14, 1.15 and 1.16, in a comoving coordinate frame, the linear evolution equation of the density contrast is:

$$\ddot{\delta} + 2H\dot{\delta} = \delta \left[ 4\pi G\bar{\rho} - \frac{c_s^2 k^2}{a^2} \right] \quad (1.19)$$

where dots represent the derivatives with respect to the time. This equation has the form of a damped wave equation where the term with the Hubble expansion  $H$  (Eq. 1.10) acts as a friction force (called *Hubble drag*) and always suppress the growth of  $\delta$ . The right hand side of Eq. 1.17 describes the conflict between pressure support and gravity. Here  $c_s$  is the speed of sound,  $k$  is the curvature and  $a$  is the scale factor.

The solution of the above equation can be cast in the form:

$$\delta(x, t) = \delta_+(x, t_i)D_+(t) + \delta_-(x, t_i)D_-(t) \quad (1.20)$$

where  $D_+$  and  $D_-$  describes the growing and decaying modes of the density perturbation, respectively. For a collisionless fluid in a Universe with  $\Omega_m < 1$  and  $\Omega_{DE} = 1 - \Omega_m$  like the  $\Lambda$ CDM one, the expression for the growing mode of perturbations is given by:

$$D_+(z) = \frac{5}{2}\Omega_m E(z) \int_z^\infty \frac{1+z'}{E^3(z')} dz \quad (1.21)$$

where  $E(z) = H(z)/H_0$  (Eq. 1.10). In Figure 1.3 we show the sensitivity of factor  $D \equiv D_+$  to the cosmological parameters  $\Omega_m$ ,  $\Omega_{DE}$ , and

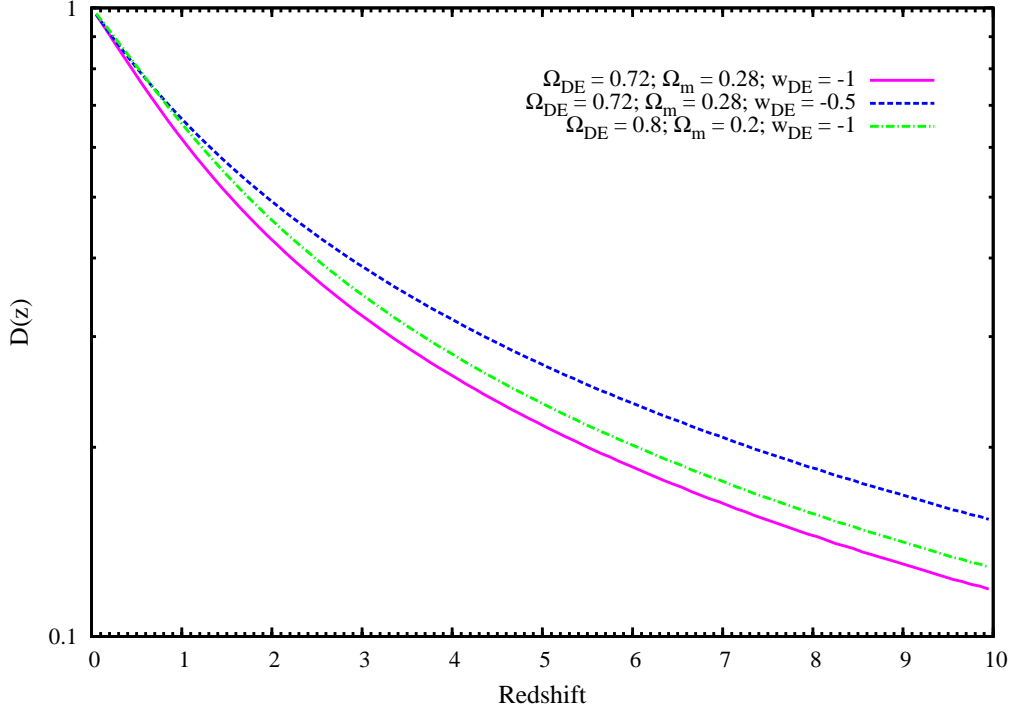


Figure 1.3: Different curves represent the growth factor  $D(z)$  (Eq. 1.21) normalized at 1 for  $z = 0$  for three different set of cosmological parameters:  $\Omega_{DE,0} = 0.72; \Omega_{m,0} = 0.28; w_{DE,0} = -1$  (solid magenta curve)  $\Omega_{DE,0} = 0.72; \Omega_{m,0} = 0.28; w_{DE,0} = -0.5$  (dotted blue curve)  $\Omega_{DE,0} = 0.8; \Omega_{m,0} = 0.2; w_{DE,0} = -1$  (dot-dashed green curve).

$w_{DE}$ . Any observational quantity that sample the evolution with redshift of density perturbations corresponds to a sensitive probe of cosmological parameters. Being conceptually different to those provided by the geometrical tests based on luminosity and angular-size distances, such test can provide important complementary information on the underling cosmological model.

### 1.2.1 The Top-hat Spherical Collapse

The spherical top-hat model is the only case for which the collapse of an overdense region can be treated analytically. We consider a spherical region with radius  $R$  and an overdensity  $\delta$  (Eq. 1.18) embedded in a background field with constant mean density  $\bar{\rho}$ . This approach is based of the validity of the Birkhoff's theorem, which states that a closed sphere

within a homogeneous Universe evolves independent of its surroundings, i.e. as if no external forces are exerted on the sphere. This implies that any overdense region of the Universe can be conceived as a homogeneous mini-Universe with the evolution driven by the local density parameters of the region under consideration. We stress that the spherical collapse model do not consider external tidal forces and is based only on the gravitational physics. According to Birkhoff's theorem, the evolution of this region can be considered independent of the background field and can be described by the Newtonian approximation of the first Friedmann equation (Eq. 1.4), i.e. with vanishing pressure and zero cosmological constant term.

In analogy to a closed Universe, this finite region will expand up to a maximum radius  $R_{max}$  at turn-around time  $t_{turn}$ . After reaching the maximum expansion, the perturbation evolves by detaching from the general Hubble expansion and then re-collapses in a time-symmetric fashion at time  $t_{col} = 2t_{turn}$ . Actually, the overdense region will not collapse to a point but stabilize in a bound dynamic equilibrium state at radius  $R_{vir} = R_{max}/2$  once the Virial equilibrium condition ( $2E_{kin} + E_{pot} = 0$ ) is satisfied supported by the velocity dispersion of DM particles.

In the case of an Einstein-de Sitter cosmology ( $\Omega_m = 1$ ), at collapse time  $t_{col} \equiv t_{vir}$ , the overdensity increased to its final equilibrium value of:

$$\Delta_{vir} \sim 178. \quad (1.22)$$

This value explains why an average overdensity of 200 times the critical density  $\rho_{cr}(z)$  (Eq. 1.7) is usually considered as typical for a DM halo which has reached the condition of virial equilibrium.

In comparison, the linear extrapolation of the density contrast according to Eq. 1.21 at  $t_{vir}$  yields

$$\delta_c \equiv \delta_+(t_{vir}) \simeq 1.69, \quad (1.23)$$

emphasizing the onset of the non-linear regime and the break-down of the linear approximation during object collapse. The linear extrapolated density contrast at  $t_{vir}$  characterized the mass function of virialized halos. It gives the overdensity that a perturbation in the initial density field must have to end up in a virialized structure (see Section 1.5).

### 1.3 Statistical properties of the perturbation density field

According to the definition of  $\delta(\mathbf{x}, z)$  (Eq. 1.18), the spatial average at a given redshift requires  $\langle \delta(\mathbf{x}, z) \rangle = 0$ .

The next momentum of the matter density probability distribution, the variance, is:

$$\langle \delta(\mathbf{x}_1, z) \delta(\mathbf{x}_2, z) \rangle = \xi(\mathbf{x}_1, \mathbf{x}_2, z) = \xi(|\mathbf{x}_1 - \mathbf{x}_2|, z) = \xi(r, z) \quad (1.24)$$

where we have defined the density *auto-correlation function* as the excess probability of finding masses at separation  $r$ :

$$d\mathcal{P} = \bar{\rho}^2 [1 + \xi(r)] dV_1 dV_2 \quad (1.25)$$

The function  $\xi$  depends only on the distance between the coordinates  $\mathbf{x}_1$  and  $\mathbf{x}_2$ , because we have assumed the Universe to be statistical isotropic. If the initial density field is described with a Gaussian distribution, as derived from a class of standard inflation models, the mean and the variance alone completely describe the matter density distribution; in Section 1.9 we will discuss what happens to the structure evolution history if we relax this assumption of initial Gaussian fluctuations.

The density distribution of matter can be defined also in the Fourier space, where it can be described by the superposition of planes waves, which evolve independent one of each other during linear evolution. The Fourier Transform of  $\delta$  (Eq. 1.18) is

$$\tilde{\delta}(\mathbf{k}, z) = \int d^3x e^{i\mathbf{k}\cdot\mathbf{x}} \delta(\mathbf{x}, z) \quad (1.26)$$

When we can calculate the variance of  $\tilde{\delta}(\mathbf{k}, z)$ , we obtain:

$$\sigma^2(z) = \langle \tilde{\delta}(\mathbf{k}, z) \tilde{\delta}^*(\mathbf{k}', z) \rangle = \frac{1}{2\pi^2} \int_0^\infty P(k, z) k^2 dk \quad (1.27)$$

where  $P(k, z)$  is the *power spectrum* of density fluctuations as a function of redshift. Similar to  $\xi(r, z)$ , which is only a function of the modulus of the distance vector,  $P(k, z)$  depends only on the absolute value of the wave-number,  $k = |\mathbf{k}|$ .

We want to study a class of observable structures of mass  $M$  which arise from the collapse of initial perturbations of size  $R$ , thus it is useful to introduce the smoothed density field:

$$\delta_R(\mathbf{k}, z) = \delta_M(\mathbf{k}, z) = \int \delta(\mathbf{k}', z) W_R(|\mathbf{k} - \mathbf{k}'|) d\mathbf{k}' \quad (1.28)$$

where  $W_R$  is the *window function* which weights the contribution from different spatial points to the density distribution. By convolving  $\delta(\mathbf{k}, z)$  with  $W_R$ , we smooth out all the fluctuations at scale below  $R$ . Therefore, the variance of the fluctuation field at scale  $R$  is defined as:

$$\sigma_R^2(z) = \langle \delta_R^2 \rangle = \sigma_M^2 = \frac{1}{2\pi^2} \int dk k^2 P(k, z) W_R^2(k). \quad (1.29)$$

The shape of the window function that it is used in this Thesis is the top-hat one:

$$\tilde{W}_R(k) = \frac{3 [\sin(kR) - kR \cos(kR)]}{(kR)^3} \quad (1.30)$$

for which the relation between mass scale and smoothing scale is  $M = \frac{4\pi}{3} R^3 \bar{\rho}$ .

## 1.4 Matter Power spectrum as a cosmological test

In the previous Section we introduced the power spectrum  $P(k)$ . In this Section we will describe it as the main tool for the statistical description of the large-scale structure and we will focus on his dependence on the underling cosmological model.

The overall shape and features of the power spectrum can be theoretically derived, however the normalization of the power spectrum has to be determined with observations. The normalization of the power spectrum is parametrized through the quantity  $\sigma_8$ , which is defined as the variance (Eq. 1.29) computed for a top-hat window having comoving radius  $R = 8 h^{-1} \text{Mpc} \equiv R_8$ . The choice of  $R_8$  was motivated by results of early galaxy surveys (Davis & Peebles, 1983) finding  $\delta_{gal}(R_8) \simeq \delta N_{gal} / N_{gal} \simeq \delta M / M \simeq 1$ , i.e. the variance of galaxy number density in spatial bins of radius  $R_8$  is about unity. A top-hat sphere with such radius contains a mass  $M \sim 5 \times 10^{14} M_\odot$ , which is the typical mass of a moderately rich galaxy cluster. Hence,  $\sigma_8$  determines the height of density peaks and consequently the object abundance. Moreover, the mass variance of order unity on the  $R_8$  scale marks the transition region from the linear regime with  $\delta \lesssim 1$ , to the non-linear regime at  $R \ll 8 h^{-1} \text{Mpc}$ .

The power spectrum is usually described by a power law  $P(k) \propto k^{n_s}$ . Thus, the second important parameter related to the power spectrum is the index  $n_s$  of the initial power spectrum. This index is observationally

confirmed (Spergel et al., 2007) to be very close to the scale-free Harrison-Zel'dovich spectrum of primaeval adiabatic fluctuation (i.e.  $n_s = 1$ ), which is predicted by inflationary models.

Under the linear evolution assumption in the cosmic structure formation model, each mode  $\delta(\mathbf{k}, t)$  evolves independently and hence the evolution density is a linear function of the initial conditions. If the initial conditions were Gaussian, then so are the evolved quantities, but with a different power spectrum. The growing-mode solution is expected to dominate after sufficient evolution, hence the power spectrum at a given redshift is described by:

$$P(k, z) = T^2(k) D^2(z) P_{in}(k) \quad (1.31)$$

where  $D(z)$  is the linear growth mode of perturbations (Eq. 1.21), and  $P_{in}(k)$  is the initial power spectrum described by  $P(k) = A k^{n_s}$ . The amplitude  $A$  of the power spectrum at  $z = 0$  is directly linked to  $\sigma_8$ . The quantity  $T(k)$  is the transfer function (Eisenstein & Hu, 1998).

Different DM scenarios imprint the shape of the power spectrum in very different ways. There are two major non-baryonic structure formation scenarios, the Hot Dark Matter (HDM) and the Cold Dark Matter (CDM) one, and each of them predicts a different cut-off on the power spectrum shape.

According to the standard model, the matter component in the Universe is dominated by CDM. Such particles decouple when they are in a non-relativistic regime ( $z_{nr} \ll z_{eq}$ ), thus the maximum damping scale is too small ( $\ll 1Mpc$ ) to be of any cosmological relevance. Perturbations between horizon crossing and equipartition experience a weak growth, thus the density contrast increases as we move to smaller scale and the power spectrum has more small-scale power.

In the HDM scenario, is present an additional suppression in the power spectrum shape that derives on the free streaming length: this depends on the thermodynamic state of particles during the decoupling. Thus, all the perturbations, on a scale equal to the distance that a particle could reach from the decoupling till now, were erased. This has the effect of a sharp cut-off in the power spectrum (see left panel of Figure 1.4) and prevents the formation of the structures that we observe in the Universe. The HDM nowadays is no longer considered a viable model for the DM, however a small admixture of HDM could be present in the total amount of DM (e.g. Saito et al., 2011).

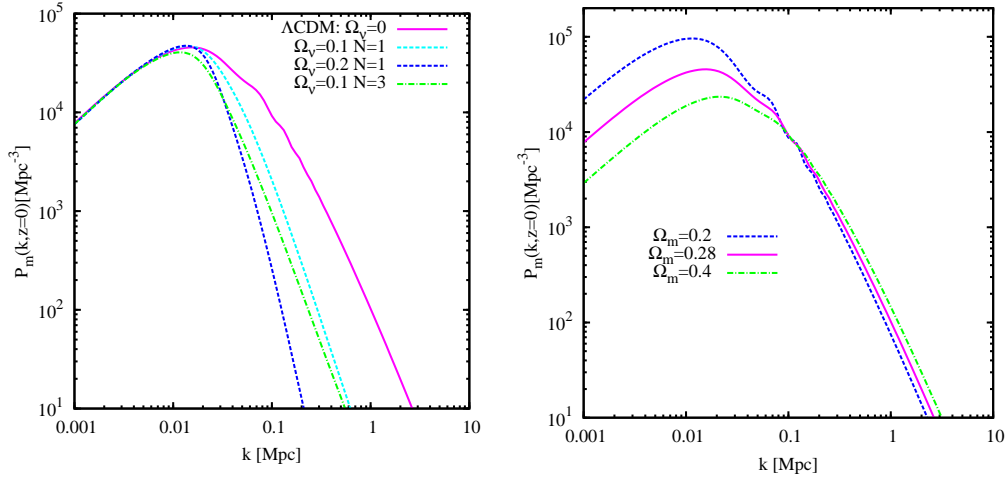


Figure 1.4: *Left panel:* Matter power spectra for Cold+Hot DM model. Dotted cyan and blue curves represent the power spectra for different amounts of the hot component,  $\Omega_\nu = 0.1$  and  $\Omega_\nu = 0.2$  respectively, provided by one massive neutrino species  $\Omega_\nu = 0.1$ . The dot-dashed green curve represents the power spectrum with  $\Omega_\nu = 0.1$  provided by three massive neutrino species. Moreover a pure CDM model is shown for comparison (magenta solid curve). *Right panel:* Matter power spectra for CDM model with  $\Omega_m = 0.2$  (dotted blue curve),  $\Omega_m = 0.4$  (dot-dashed cyan curve), and  $\Omega_m = 0.28$  (magenta curve). The latter corresponds to the fiducial value of the  $\Lambda\text{CDM}$  model (Komatsu et al., 2011). In both panels all the unspecified cosmological parameters are set to the reference value of the  $\Lambda\text{CDM}$  model according to Komatsu et al. (2011). These plots are based on the prescriptions for the transfer functions provided by Eisenstein & Hu (1998) for the CDM models and by Eisenstein & Hu (1999) for the models with massive neutrinos.

The transfer function, introduced in Eq. 1.31, contains scale-imprinting evolutionary effects that alter the original linear form of the initial power spectrum. The first imprinted scale is  $k_{eq}$ , the wavevector corresponding to the comoving scale of the Hubble radius at the epoch of transition from a radiation-dominated Universe to a matter dominated one ( $z_{eq}$ , Eq. 1.13). This scale directly influences the present-day power spectrum shape. In the radiation epoch perturbations inside the horizon in the collisionless component experience a stagnation effect, called *Meszaros effect*, because the expansion rate in the radiation-dominated era is shorter than the dynamical time-scale of the perturbations. Since perturbations on small scales ( $k > k_{eq}$ ) are suppressed in amplitude, the structure growth can only proceed on scales larger than the equivalence one ( $k < k_{eq}$ ), beyond the causal influence of the radiation pressure. Once a perturbation mode crosses the Hubble radius, further growth is suppressed and its amplitude almost freezes at the value it had at horizon crossing. As shown in Figure 1.5, the Meszaros effect causes a break in the shape of the transfer function. The transfer function is unity for  $k \ll k_{eq}$ , while  $T(k) \propto k^{-2}$  for  $k \gg k_{eq}$ . Since  $k_{eq}$  is defined as

$$k_{eq} \equiv (2 \Omega_m H_0^2 z_{eq})^{1/2} \quad (1.32)$$

in the CDM paradigm, if the amount of DM is higher also the equivalence redshift is higher and, thus, the perturbations are suppressed by the Meszaros effect earlier because they enter the horizon when it is smaller. Hence the pick of matter power spectrum shifts at higher  $k$  (Borgani et al., 1997) for higher  $\Omega_m$  as it is shown in the right panel of Figure (1.4).

On small scale, and high wave-number, the transfer function shape is affected by the dissipative effects due to the interaction between baryon and photons in the pre-recombination era (we assume  $z_{rec} < z_{eq}$ ). Adiabatic perturbations in the photon-baryon plasma suffer from collisional damping when  $z \sim z_{eq}$  because, as they approach decoupling time, the photon mean free path increases and photons can diffuse from overdense to underdense regions smoothing out any inhomogeneities in the plasma. This effect is called *Silk damping* (Silk, 1976) and the corresponding wave-number is fitted by the approximation:

$$k_{Silk} \simeq 1.6 \left( \Omega_b h^2 \right)^{0.52} \left( \Omega_m h^2 \right)^{0.73} \left[ 1 + \left( 10.4 \Omega_m h^2 \right)^{-0.95} \right] \text{Mpc}^{-1} \quad (1.33)$$

In Figure 1.5 it is shown how the presence of baryons damps the shape of the transfer function.

Another effect that is imprinted in the transfer function are the Baryonic Acoustic Oscillations (BAOs). This feature appears below the sound horizon scale, as a consequence the matter power spectrum exhibits a series of declining peaks. Baryons fall in the DM potential well and undergo both the attraction of DM gravity and their own pressure that act in the opposite direction. Such behaviour can be described with a harmonic oscillator, and makes the BAOs appear in matter power spectrum.

The presence of BAOs provides the same kind of information as the oscillations present in the CMB photon power spectrum, but we observe this information at a lower redshift. The position of the wiggles is related to the amount of DM and baryons: as  $\Omega_m h^2$  increases, first peaks are shifted to higher  $k$  and, moreover, the valleys and peaks become slightly narrower. The amplitude of the wiggles is also related to the amount of matter mainly because the oscillations grow stronger by increasing the baryon fraction.

## 1.5 The mass function

The mass function,  $n(M, z)$ , is defined as the number density of virialized halos with mass in the range  $[M, M + dM]$ , found at redshift  $z$  in a comoving volume element.

**Mass definition.** The cluster mass function inevitably depends on how one defines cluster mass. The mass

$$M_{\Delta_c} \propto \rho_c(z) \Delta_c R_{\Delta_c}^3 \quad (1.34)$$

is the amount of matter contained in a spherical region of a virialized halo of radius  $R_{\Delta_c}$  (see Section 1.3) where the cluster overdensity is  $\Delta_c$  times the critical density  $\rho_{cr}(z)$ . The quantity  $\rho_{cr}(z) = \rho_{cr,0} E^2(z)$ , where  $\rho_{cr,0}$  is to the critical density at redshift  $z = 0$  (Eq. 1.7).

### 1.5.1 The Press & Schechter approach

By combining spherical top-hat collapse model with the growth function for linear perturbations (Eq. 1.21), the cluster mass function can be expressed in terms of the mass threshold of mass variance  $\sigma_M^2$  and critical overdensity for spherical collapse  $\delta_c$ . In this approach, it is assumed that all density perturbations continue to grow according to the linear growth

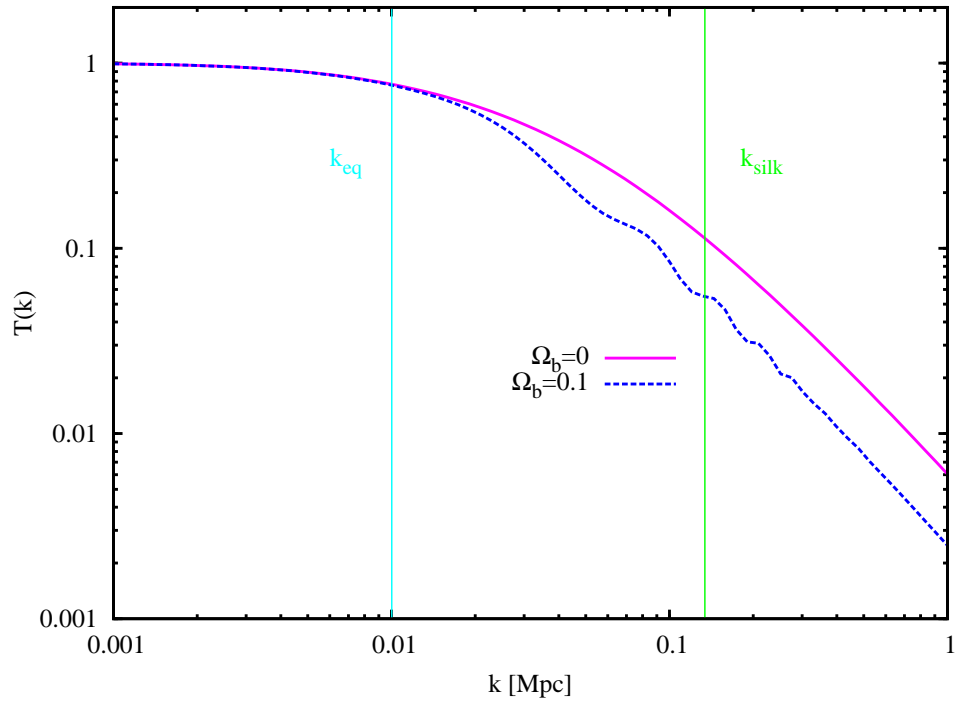


Figure 1.5: Transfer function by Eisenstein & Hu (1998) for a model with no baryons (magenta solid curve) and for a model with a high amount of baryons ( $\Omega_b = 0.1$ ) (blue dotted curve). For  $\Omega_m = 0.28$  and  $h = 0.7$ , the characteristic wave-number at the equivalence redshift,  $k_{\text{eq}}$  (Eq. 1.32), and the Silk damping scale  $k_{\text{silk}}$  (Eq. 1.33) in the case of  $\Omega_b = 0.1$  are also shown.

rate  $D(z)$ , even when their amplitudes become non-linear. When perturbations are treated in this way, their variance on mass scale  $M$  as a function of redshift can be expressed by Eq. 1.29. Moreover, it is assumed that perturbations collapse and virialize when their density contrast exceeds the critical threshold  $\delta_c$ .

According to the Press-Schechter (PS, Press & Schechter, 1974) approach, under the assumption of Gaussian perturbations, the probability for the linearly evolved smoothed field  $\delta_M$ , with mass in the range  $[M, M + dM]$ , to exceed at redshift  $z$  the critical density contrast  $\delta_c$  is

$$\begin{aligned} dp_{>\delta_c}(M, z) &= \frac{dM}{\sqrt{2\pi}\sigma_M(z)} \int_{\delta_c}^{\infty} \exp\left(-\frac{\delta_M^2}{2\sigma_M(z)^2}\right) d\delta_M \quad (1.35) \\ &= \frac{1}{2} \operatorname{erfc}\left(\frac{\delta_c}{\sqrt{2}\sigma_M(z)}\right), \end{aligned}$$

where  $\operatorname{erfc}(x)$  is the complement error function.

Eq. 1.35 implies that the shape of the mass function depends only on  $\sigma(M, z)$  and remains invariant with respect to the characteristic collapsing mass scale  $M_*(z)$  at which  $\sigma(M_*, z) = \delta_c$ . In principle, if we take the limit of arbitrarily small mass and if we consider the whole mass range, we should recover the entire mass content of the Universe and the integral of the probability should be  $\int_0^{\infty} dp_{>\delta_c} = 1$ . However, in this derivation, a point with  $\delta_M < \delta_c$ , for a given filtering mass scale  $M$  has zero probability to reach  $\delta_{M'} > \delta_c$  for some larger filtering scale  $M' > M$ . This means that the PS approach neglects the possibility for that point to end up in a collapsed halo of larger mass and for this reason  $\int_0^{\infty} dp_{>\delta_c} = 1/2$ . Bond et al. (1991) provided a derivation of the mass function, correctly accounts for the missing factor 2, at least for the particular choice of a sharp- $k$  filter (i.e., a top-hat window function in Fourier space).

Since Eq. 1.35 provides the fraction of volume in objects of a given mass, the number density of such objects will be obtained after dividing it by the volume,  $V_M = M/\bar{\rho}$ , occupied by each object and the expression for the PS mass function reads

$$\begin{aligned} \frac{dn(M, z)}{dM} &= \frac{2}{V_M} \frac{\partial p_{>\delta_c}(M, z)}{\partial M} \\ &= \sqrt{\frac{2}{\pi}} \frac{\bar{\rho}}{M^2 \sigma_M(z)} \left| \frac{d \ln \sigma_M(z)}{d \ln M} \right| \exp\left(-\frac{\delta_c^2}{2\sigma_M(z)^2}\right). \quad (1.36) \end{aligned}$$

## 1.5.2 Numerical calibration of the mass function

Sheth & Tormen (1999) generalized the expression for the PS mass function and calibrated the free parameters using numerical simulations. Later Sheth et al. (2001) refined this calculation, incorporating a moving barrier for the collapse criterion of halos in which the critical density varies with the peak height, as motivated by the more physically realistic ellipsoidal collapse model. The functional form usually adopted to describe halo abundance in simulations is:

$$\frac{dn}{dM} = f(\sigma_M) \frac{\bar{\rho}}{M} \frac{d \ln \sigma_M^{-1}}{dM}. \quad (1.37)$$

In the extended PS theory, the overdensity at a location in a linear density field follows a random walk with decreasing smoothing scale. The function  $f(\sigma_M)$  is the  $\sigma_M$ -weighted distribution of first crossings of these random walks across a barrier separating collapsed objects from uncollapsed regions (e.g. where the random-walking overdensity first crosses  $\delta_c$ ). The Sheth & Tormen (1999) expression for  $f(\sigma_M)$  is:

$$f(\sigma_M, z) = \sqrt{\frac{2a}{\pi}} C \left[ 1 + \left( \frac{\sigma_M^2}{a \delta_c^2} \right)^q \right] \frac{\delta_c}{\sigma_M} \exp \left( -\frac{a \delta_c^2}{2 \sigma_M^2} \right). \quad (1.38)$$

The best-fitting values of the parameters are  $a = 0.707$ ,  $q = 0.3$ , with  $C = 0.3222$  obtained from the normalization requirement  $\int_0^\infty f(\sigma_M) d\nu = 1$  (note that the PS expression is recovered for  $a = 1$ ,  $q = 0$  and  $C = 1/2$ ). The values of these parameters have been found by comparing Eq. 1.38 with results from N-body simulations, in which the mass of the clusters was estimated with a spherical overdensity (SO) algorithm, by computing the mass within the radius encompassing a mean overdensity equal to the virial one  $\Delta_{m,vir}$ .

Looking for a universal form of the mass function, universal in the sense that the same functional form and parameters can be used for different cosmologies and redshift, Jenkins et al. (2001) proposed the following expression for the mass function

$$f(\sigma_M, z) = A \exp(-|\ln \sigma_M^{-1} + B|^C), \quad (1.39)$$

which has been obtained as the best fit to the results of a combination of different simulations. In  $\Lambda$ CDM cosmology and for halos identified with the SO algorithm,  $A = 0.316$ ,  $B = 0.67$  and  $C = 3.82$ . The accuracy of

Eq. 1.39 in reproducing results of numerical experiments has been also discussed in Evrard et al. (2002) and White et al. (2002). These papers also stressed the role of different algorithms used to identify clusters and to estimate their mass in simulations, and discussed the universality of this expression for generic values of cosmological parameters.

**Tinker et al. (2008) mass function calibration.** In more recent studies the attention were focused on the redshift evolution of the mass function (Reed et al., 2003, 2007; Lukić et al., 2007; Cohn & White, 2008) or the impact of gas physics associated with halo baryons (Stanek et al., 2009).

In particular Tinker et al. provided in 2008 a new calibration for the cluster mass function that reads:

$$f(\sigma) = A \left[ \left( \frac{\sigma}{b} \right)^{-a} + 1 \right] e^{-c/\sigma^2} \quad (1.40)$$

where the parameter  $A$  sets the overall amplitude of the mass function,  $a$  and  $b$  set the slope and amplitude of the low-mass power law, respectively. Finally,  $c$  determines the cut-off scale where the abundance of halos exponentially decreases. This study was the first that opens the density threshold degree of freedom; their fitting parameters are published as functions of  $\Delta_m$  (see Table 2 in Tinker et al. (2008)).

The simulations by Tinker et al. (2008) achieve a fit with 5% statistical precision in halo number at  $z = 0$  for a  $\Lambda$ CDM cosmology. In order to maintain such a precision for redshifts up to 2.5 and  $200 \leq \Delta_m \leq 3200$ , it is required the introduction of mild redshift and  $\Delta_m$  dependence into the fitting parameters of Eq. 1.40 .

$$A(z) = A_0 (1+z)^{-0.14} \quad (1.41)$$

$$a(z) = a_0 (1+z)^{-0.06} \quad (1.42)$$

$$b(z) = b_0 (1+z)^{-\alpha} \quad (1.43)$$

$$\log \alpha(\Delta_m) = - \left[ \frac{0.75}{\log(\Delta_m/75)} \right]^{1.2} \quad (1.44)$$

In this respect, Tinker et al. (2008) state that the mass function cannot be represented by a universal function at this level of accuracy. In particular, as  $\Delta_m$  increases the halo masses become systematically smaller. Thus, from  $\Delta_m = 200$  to 3200, the mass scale of the exponential cut-off reduces substantially. The shape of the mass function is also altered due to two effects. First, the fractional change in mass when converting between

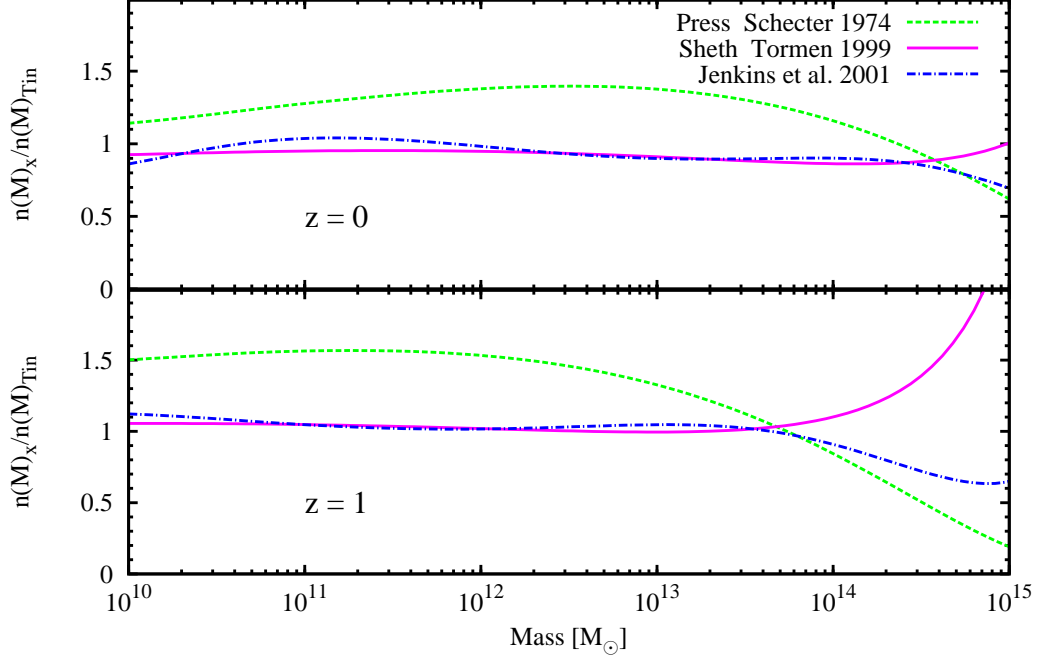


Figure 1.6: Ratio between mass functions from Press & Schechter (1974) (green dotted curve), Sheth & Tormen (1999) (magenta solid curve), and Jenkins et al. (2001) (blue dot-dashed curve) and the mass function provided by Tinker et al. (2008) ( $n(M)_{Tin}$ ) as a function of mass for two different redshift values,  $z = 0$  in the upper panel and  $z = 1$  in the lower panel.

values of  $\Delta_m$  is not a constant; it depends on halo mass. Since halo concentrations are higher for smaller halos, the fractional change is higher at lower masses, thus the mass function becomes steeper. Second, a number of low-mass objects within  $R_{200}$  of a larger halo are considered as distinct halos when halos are identified with  $\Delta_m = 3200$ . At high masses, the number of such halos decreases exponentially with mass, and therefore the contribution of such exposed halos becomes small.

Moreover, in the analysis conducted by Tinker et al. (2008), the range of cosmologies probed is narrow given the volume of parameter space, but it is wider than the allowed range for  $\Lambda$ CDM cosmologies given recent results from CMB in combination with other large-scale measures (Komatsu et al., 2009). Thus, large variations in  $\Omega_m$  at  $z=0$  (i.e.,  $\Omega_m = 0.1$  or 1), can not to be fit by  $z=0$  mass function within 5% accuracy.

An important motivation for the precision determination of the mass

function is the existence of several ongoing and upcoming surveys that aim to detect clusters via their optical, X-ray, and Sunyaev-Zel'dovich (SZ) effect signatures (Laureijs et al., 2011; Rosati et al., 2011; Predehl et al., 2007; Williamson & the SPT Team, 2011; Marriage & the ACT Team, 2011; Planck Collaboration, 2011). The number of detected clusters from the individual surveys will range from thousands to tens of thousands. To maximally extract cosmological information from these cluster surveys, the mass function must be specified to better than a few percent accuracy for a range of cosmologies. The current theoretical uncertainty in the determination of the mass function can lead to a considerable degradation in the constraints on cosmological parameters.

In Figure 1.6 we show a comparison between the more commonly used mass function at redshifts  $z = 0$  and  $z = 1$ . With respect to the Tinker et al. (2008) prescription, the PS one overestimates the number of objects with low masses and underestimate those with higher redshift. The mass functions provided by Jenkins et al. (2001) and Sheth & Tormen (1999) show a higher level of agreement with the Tinker et al. (2008) one. However, Jenkins et al.'s result is 10% – 15% below Tinker et al.'s result and the Sheth & Tormen (1999) function is similarly offset for masses below  $4 \times 10^{14} M_{\odot}$  at  $z = 0$ . At redshift  $z = 1$ , on the contrary, both the Sheth & Tormen (1999) and the Jenkins et al. (2001) predictions are slightly higher than the Tinker et al. (2008) one for masses lower than  $5 \times 10^{13} M_{\odot}$ . For high masses and especially increasing the redshift different mass function prescription can predict a very different number of objects.

The next step in the theoretical calibration of the mass function for precision cosmology should cover a wide range of masses, should include careful examination of subtle dependencies of mass function on cosmological parameters (especially on the DE EoS), effects of neutrinos with non-zero mass, effects of non-Gaussianity (Grossi et al., 2007; Dalal et al., 2008). Moreover we need to understand the effects of baryonic physics on the mass distribution of halos and consequently on the mass function, which can be quite significant (Cui et al., 2011; Stanek et al., 2009; Rudd et al., 2008).

### 1.5.3 Mass function as a cosmological tool

The exponential sensitivity to mass and redshift is evident in all the expressions for the cluster mass function that we have shown in this Section

(Eqs. 1.38,1.39,1.40). Thanks to this dependence, the mass function is a powerful probe of cosmological models. All the cosmological parameters that we have mentioned throughout this Chapter ( $\Omega_m$ ,  $\Omega_{DE}$ ,  $w(z)$ ,  $\Omega_k$ ,  $\sigma_8$ ,  $h$ ,  $n_s$ ) enter in the mass function through  $\sigma_M$  (Eq. 1.29), which depends on the power spectrum (Eq. 1.31) and on the linear perturbation growth factor (Eq. 1.21).

The abundance of massive clusters exponentially depends on the amplitude of mass fluctuations at the physical scale  $R$ , because if the amplitude of mass fluctuations is high structures form rapidly at early times, while for lower amplitude structures form more slowly. Therefore, the normalization of the power spectrum,  $\sigma_8$  has a strong impact on structure formation and evolution as we show in Figure 1.7.

The evolution with redshift of the mass function entirely depends on the growth factor 1.21. This is a well defined function of  $\Omega_m$ ,  $\Omega_{DE}$ , and  $w$  according to which perturbation growth stalls when  $\Omega_m \ll 1$ . This effect is strong for high mass clusters because these objects are the latest to be formed in the hierarchical CDM scenario (Eke et al., 1996). The value of  $\Omega_{DE}$  and  $w$  parameters modify the redshift at which  $\Omega_m$  departs significantly from unity (Figure 1.7).

**Most massive clusters test** Recently, the discovery of high redshift, massive clusters such as XMMU J2235.3-2557 at  $z \sim 1.4$  (Mullis et al., 2005; Rosati et al., 2009) and SPT-CL J0546- 5345 at  $z \sim 1.1$ . (Brodwin et al., 2010) have led to reports of possible tension with the Gaussian  $\Lambda$ CDM model (e.g. Jee et al., 2009; Holz & Perlmutter, 2010). Because the cluster mass function is particularly sensitive to the cosmological parameters at high masses and redshifts, as we show in Figure 1.7, it is worth to calculate the probability of finding a cluster with a given mass and redshift within its survey volume in order to test a specific cosmological model.

Despite the fact that such test involves only one or a few very massive clusters detected in a survey rather than the complete sample, a robust assessment of the likelihood requires a detailed understanding of the selection function as well as a full accounting for the effects of scatter in the observable-mass scaling relations (see Section 2.2). Due to the steepness of the high mass tail of the cluster mass function, errors in mass measurements at the tens of per cent level, for example (as might be expected for weak lensing measurements of an individual cluster), can modify the probability of such a cluster to be observed by up to an or-

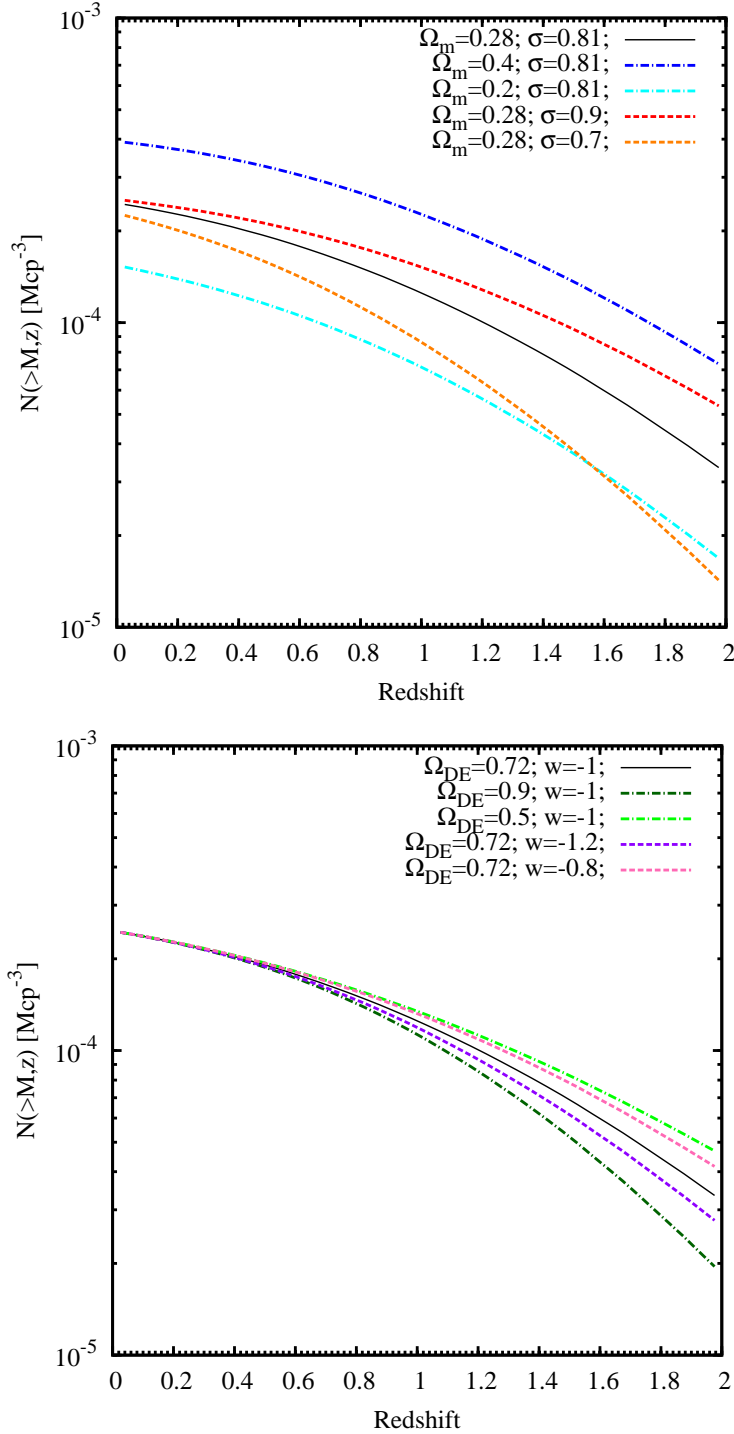


Figure 1.7: The sensitivity of evolution of  $N(> M, z)$  for  $M > 5 \times 10^{14} M_{\odot}$  at different cosmological parameters. The black solid line in both the panel corresponds to the fiducial value of the  $\Lambda$ CDM model (Komatsu et al., 2011) where  $\Omega_m = 0.28$ ,  $\sigma_8 = 0.81$ ,  $\Omega_{DE} = 0.72, w = -1$ . *Left panel:*  $N(> M, z)$  for  $\Omega_m = 0.4$  (dotted blue curve) and  $\Omega_m = 0.2$  (dotted cyan curve), for  $\sigma_8 = 0.9$  (dot-dashed red curve) and for  $\sigma_8 = 0.7$  (dot-dashed orange curve). *Right panel:*  $N(> M, z)$  for  $\Omega_{DE} = 0.5$  (dot-dashed green curve) and  $\Omega_{DE} = 0.9$  (dot-dashed dark green curve), for  $w = -0.8$  (dotted pink curve) and for  $w = -1.2$  (dotted violet curve).

der of magnitude (see Figure 1.8). Moreover, it is necessary to investigate the high mass end of mass function. As we stressed in Section 1.5.2 the existing limited-volume simulations do not constrain the number density of extremely massive clusters accurately, and the commonly used fitting functions are simply extrapolated results in this regime. Another potentially important contribution from numerical simulation is the predicted mass function specific for a given survey, which takes into account the various aspects of selection limits and projection effects. The projection effect is always a concern in the cosmological interpretation of extremely massive clusters. Certainly, a superposition of two moderately massive clusters or a long filament viewed along the line of sight can be identified with an extreme object. Mortonson et al. (2011) presented a fitting formulae, which provides the “exclusion mass” as a function of redshift for given sample and parameter variance confidence limits. Even a single cluster equal to or above the exclusion mass would rule out  $\Lambda$ CDM model. For instance, Jee et al. (2011) compared their sample of 27 clusters at  $z > 0.8$  to the exclusion curves of Mortonson et al. (2011) and claimed that the discoveries of 4 clusters, whose masses have been estimated from weak lensing analysis, within their parent survey are very rare events. In particular: XLSS J0223-0436 at  $z \simeq 1.22$  with mass  $M_{200} = 7.4_{-1.8}^{+2.25}$  has a discovery probability of 1%, RDCS J1252-2927 at  $z \simeq 1.24$  with mass  $M_{200} = 6.8_{-1.0}^{+1.2}$  has a discovery probability of 0.2%, XMMU J2235-2557 at  $z \simeq 1.39$  with mass  $M_{200} = 7.3_{-1.4}^{+1.7}$  has a discovery probability of 1.3%, CL J1226+3332 at  $z \simeq 0.89$  with mass  $M_{200} = 13.7_{-2.0}^{+2.4}$  has a discovery probability of 0.6%.

## 1.6 Cluster Bias

Fluctuations in the number density of clusters on large scales are observed to be more pronounced than the fluctuations of the underlying matter density (e.g. Bahcall & Soneira, 1983; Klypin & Kopylov, 1983). This means that, the fractional deviation of  $dn(M)/dM$  from its mean value, within a given volume of the Universe, is observed to be larger than  $\delta\rho/\rho$  in that same volume. The ratio,  $b(M)$ , between the perturbation in the number density of clusters of mass  $M$  and the perturbation amplitude of the matter density is called the bias parameter of dark mat-

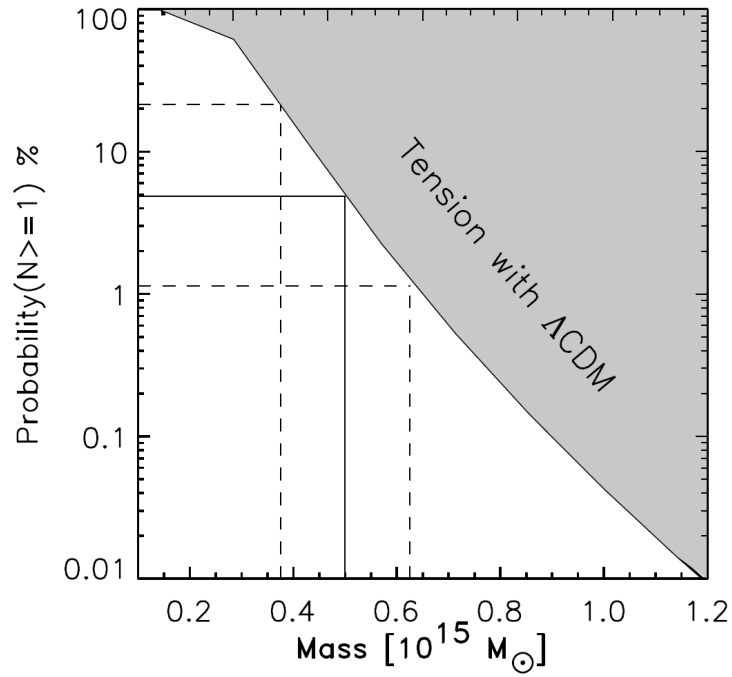


Figure 1.8: Probability to find at least one cluster in a  $50 \text{ deg}^2$  X-ray survey area with  $f_{lim}[0.5 - 2 \text{ keV}] = 1 \times 10^{-14} \text{ erg s}^{-1} \text{ cm}^{-2}$  at  $z \geq 1.58$  as a function of the virial mass computed from the  $\Lambda\text{CDM}$  mass function for WMAP-7 parameter values Komatsu et al. (2011).

ter haloes, and can be define as:

$$b^2(M) = \frac{P_h}{P_{\text{lin}}}, \quad (1.45)$$

that is the ratio of the halo power spectrum to the linear matter power spectrum.

According to the predictions based on the Spherical Collapse (SC) model for the formation of dark matter halos from Gaussian perturbations, and using the peak-background split approximation, Cole & Kaiser (1989) and Mo & White (1996) derived a bias relation of the form

$$b(\nu) = 1 + \frac{\nu^2 - 1}{\delta_c}, \quad (1.46)$$

where  $\nu = \delta_c/\sigma_M$ . However, failing the Press-Schechter mass function (Eq. 1.36) to reproduce the dark matter halo mass function found in simulations, the bias function (Eq. 1.46) also does not compare well to simulations (see, e.g. Jing, 1998, 1999; Sheth & Tormen, 1999). In particular the SC model overpredicts the bias in the range  $1 \lesssim \nu \lesssim 3$ , while underpredicting slightly the bias for the lowest mass halos in subsequent simulations by Tinker et al. (2010) (see Fig. 1.9). Using the peak-background splitting and the ST mass function, Sheth et al. (2001) (SMT) derived an improved expression for the bias

$$b(\nu) = 1 + \frac{1}{\sqrt{a}\delta_c} \left[ \frac{\sqrt{a}(a\nu^2) + \sqrt{ab}(a\nu^2)^{1-c}}{(a\nu^2)^c + b(1-c)(1-c/2)} \right], \quad (1.47)$$

where  $a = 0.707$ ,  $b = 0.5$ , and  $c = 0.6$  describe the shape of the moving barrier. It is shown (Tinker et al., 2010), the SMT bias equation underpredicts the clustering of high-peak halos while overpredicting the asymptotic bias of low-mass objects, being the SMT bias too high at low  $\nu$  and too low at high  $\nu$ . The bias function introduced by Tinker et al. (2010) has a similar but more flexible form than the SMT one:

$$b(\nu) = 1 - A \frac{\nu^a}{\nu^a + \delta_c^a} + B\nu^b + C\nu^c. \quad (1.48)$$

This equation scales as a power law of  $\nu$  at the highest masses, flattens out at low masses, and asymptotes to  $b = 1$  at  $\nu = 0$ , and provides  $a > 0$ .

The best-fit parameters of Eq. 1.48 scale smoothly with  $\Delta$ , allowing to obtain fitting functions for these parameters as a function of  $\log \Delta_m$  in a range of  $200 \leq \Delta_m \leq 3200$ . As  $\Delta_m$  increases, bias increases at all mass scales. At high masses, as  $\Delta_m$  increases, a fixed set of halos will have lower masses, but the same clustering properties, essentially shifting them along the  $\nu$ -axis. At low masses, the amplitude of the bias curve also monotonically increases with  $\Delta_m$ , owing to the substructures within high-mass halos that become distinct objects as  $R_{\Delta_m}$  decreases. Being these new low-mass halos in the vicinity of high-mass objects, they have significant clustering. The spherical collapse model is defined by a threshold for collapse that is independent of halo mass. However, peaks in the linear density field become increasingly elliptical and prolate at low- $\nu$ , delaying collapse. Therefore, in this mass regime, the barrier in the ellipsoidal collapse model is significantly higher than the constant  $\delta_c$  assumed in spherical collapse calculations. As a result, collapsed low-mass halos reside in higher density environments, making them less abundant and more biased. At high  $\nu$ , the ellipsoidal collapse barrier asymptotes to the spherical  $\delta_c$  value, and these two models should, thus, converge at high  $\nu$ . However, the numerically calibrated barrier used in the SMT fit asymptotes to a value lower than the spherical collapse  $\delta_c$  in order to produce the abundance of high-mass halos (Robertson et al., 2009). Consequently, the clustering of high- $\nu$  halos in the SMT model is lower than the spherical collapse prediction.

## 1.7 Cluster power spectrum and redshift space distortions

We do not actually measure the cluster power spectrum in real space, instead we obtain the radial position of an object through redshift measurements, by convolving the real distance with additional redshifts due to peculiar velocities. Because of these peculiar velocities the redshift-space power spectrum is distorted with respect to the power spectrum in the real space. This effect is called Redshift Space Distortions (RSDs).

Two important effects occur in redshift space.

The first important distortion is the *Fingers of God* effect where long thin filaments in redshift space point directly back at observer. Assuming we are not privileged observers, the Fingers of God effect must be non-

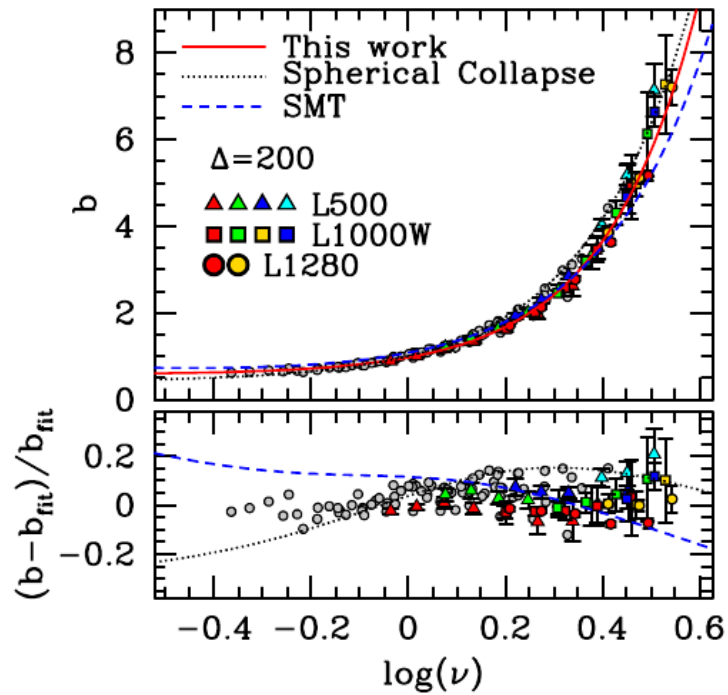


Figure 1.9: *Upper Panel:* Halo bias as a function of  $\nu$  for  $\Delta_m = 200$ , as predicted by SC (Eq. 1.46), SMT (Eq. 1.47), and Tinker et al. (2010) (Eq. 1.48). Each point type indicates a different simulation. The different colours, from left to right, go in order of increasing redshift from  $z = 0$  to  $z = 2.5$  (see Tinker et al. (2010) for details). *Lower Panel:* Fractional differences of the N-body results with the the fitting function shown in the upper panel. Figure from Tinker et al. (2010).

physical. This effect is attributed to random velocity dispersions. Galaxy clusters random peculiar velocities deviate a galaxy's velocity from pure Hubble flow, stretching out a cluster in redshift space. Since this affects only redshift and not position on the sky, the stretching occurs only radially (see Fig. 1.10).

The other important redshift distortion is called *Kaiser Effect*. This describes the peculiar velocities of objects bound to a central mass as they undergo infall. In this case the peculiar velocities are coherent, not random, towards the central mass (see Fig. 1.10).

On small transverse scales, random dispersion velocities cause the Fingers of God effect. On large scales, the Kaiser Effect causes a "flattening" of the correlation function, due to the subtle infall motion of galaxies. In particular the redshift space power spectrum gains an angular dependence through the linear Kaiser factor (Kaiser, 1987) with respect to the isotropic, real space mass power spectrum  $P(k)$ :

$$P(k, \mu) = (b + f \mu^2)^2 P(k) \quad (1.49)$$

where  $\mu$  is the cosine of the angle that  $\mathbf{k}$  makes with the line of sight and  $f$  is the dimensionless growth rate given by:

$$f = \frac{d \ln D}{d \ln a} \quad (1.50)$$

where  $a$  is the scale factor, and  $D(a)$  is the growth factor (Eq. 1.21).

## 1.8 Non-standard cosmological models

In the previous Sections, the evolution of the Universe and the structure formation history have been briefly exposed assuming the  $\Lambda$ CDM scenario. As it has already been mentioned, this model predicts that the  $\sim 75\%$  of the energy density of the Universe exists in a unknown form with large negative pressure called dark energy. This DE is expressed as a cosmological constant,  $\Lambda$ , whose equation of state is  $w_{DE} = -1$ . The  $\Lambda$ CDM cosmological model is a well defined, simple and predictive model, which is consistent with the majority of current cosmological observations (e.g. Lazkoz & Majerotto, 2007; Kowalski et al., 2008). Despite of these successes, there are observational results, e.g. on the central density profiles of DM halos and number of halo satellites, which have been claimed to be in tension with  $\Lambda$ CDM predictions. However, as of today

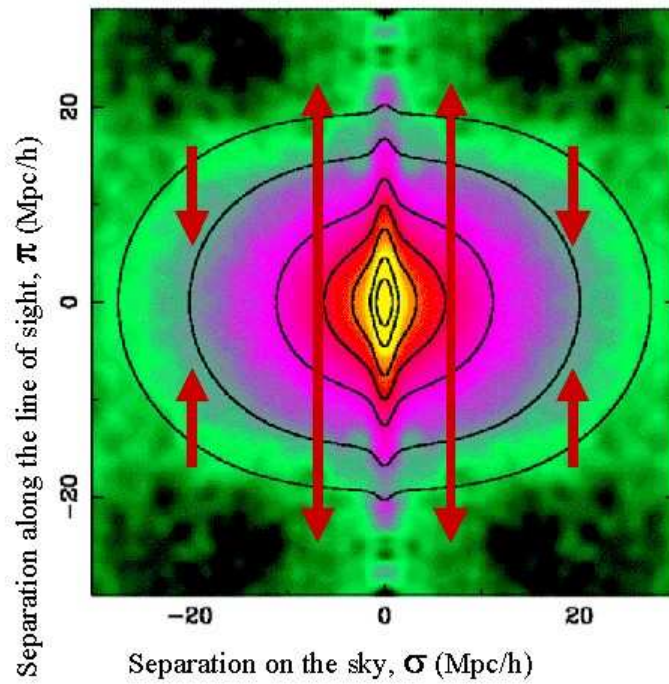


Figure 1.10: Pictorial view of Redshift Space Distortions of a spherical object in redshift space, as obtained by combining the Finger of God and the Kaiser effect. Figure from 2dF Galaxy Redshift Survey Team (2001).

it is not clear whether this tension has to do with intrinsic limitations of the CDM paradigm or just reflects the still limited understanding of the impact of baryon physics on the evolution of DM halos.

As regard the DE, its physical origin remains a deep mystery. If vacuum energy is the origin of the cosmological constant, it suffers from a serious problem because Quantum Field Theories predict a Planck-scale vacuum energy that corresponds to a value for the cosmological constant density of  $\rho_\Lambda \sim 2 \times 10^{110} \text{erg/cm}^3$ . This value is about 120 orders of magnitude larger than the observed one  $\rho_\Lambda^{(obs)} \sim 10^{10} \text{erg/cm}^3$ . This issue is usually called the *cosmological constant problem* (Weinberg, 1989).

In this Section, we will focus on the model proposed in order to overcome the Dark Energy problems. A plethora of models have been proposed that release one or more of the assumptions of the standard  $\Lambda\text{CDM}$  model, and propose alternative explanations for the physical origin of the cosmic acceleration expansion and the nature of the DE. We can divide these models in three main classes. A group of models in which the energy-momentum tensor  $T_{\alpha\beta}$  on the right hand side of the Einstein equation (Eq. 1.2) contains an exotic matter source with a negative pressure (e.g. Tsujikawa, 2010). Another possibility is that General Relativity breaks down on cosmological scales and must be replaced with a more complete theory of gravity; this would imply to change the left hand side of the Einstein equation (Eq. 1.2) (e.g. Tsujikawa, 2010; Silvestri & Trodden, 2009). A third possibility is to drop the assumption that the Universe is spatially homogeneous on large scales, but such solutions do not yet seem compelling (e.g. Tsujikawa, 2010).

### 1.8.1 Dark Energy models

Current data do not provide strong constraints on time evolution of DE EoS parameter. thus evolving models of DE remain an alternative candidates to the  $\Lambda\text{CDM}$  one. The main classes of the so called DE models are briefly introduced in the following.

**Quintessence models.** The introduction of a new degree of freedom, a canonical scalar field  $\phi$ , makes vacuum energy effectively dynamical (Caldwell et al., 1998; Zlatev et al., 1999). A given quintessence potential  $V(\phi)$  determines the expansion history by changing the DE EoS parameter. This evolves with time deviating from -1 to  $w_{DE} = w_\phi > -1$ . This

changes the Friedman equations (Eqs.1.4, 1.5) at late time, when the field energy density needs to dominate to be responsible for DE. Consequently the evolution of the Universe changes according to Equation 1.10 (see Figure 1.2), and also the structure growth history changes as we showed in Figure 1.3.

**k-essence** models realize the cosmic acceleration by a non-canonical field kinetic energy (Armendariz-Picon et al., 2000). Models with multiple attractor solutions, such that the field scales with EoS parameter  $w_{DE} = 1/3$  during the radiation era, and runs off to a de Sitter-like solution after the onset of matter domination, have been proposed as possible solutions of the coincidence problem (Armendariz-Picon et al., 2000), i.e. that DM and DE densities, differing by orders of magnitude since ever, approach one another at today's eve. However, there is another aspect of k-essence that must be considered: some of the k-essence models predict that the sound speed for the propagation of high-frequency perturbations is different from the unity, the value that the sound speed has in a canonical scalar field. The k-essence models that predict  $v_s^2 < 0$  are eliminated because they are unstable to the growth of fluctuations. Density fluctuations in models with  $0 < v_s^2 \ll 1$  can leave a strong imprint on the CMB and large-scale structure.

Fluctuations in the DE component, dependent upon the DE density EoS parameter, and sound speed can leave an imprint on large-scale structure and the CMB, by changing the predicted mass function number cluster prediction. Affecting the amount of  $\Omega_{DE}$  as a function of time, Quintessence and k-essence models indirectly change the matter power spectrum and the bias relative to galaxy clusters.

**Coupled DE** models investigate the possibility that DE may have some relation with DM, since the energy density of DE is of the same order as DMone in the present Universe. However, the quintessence scalar field non trivially couple to the CDM component, and the presence of this non trivial coupling between the quintessence scalar field and the DM component modifies the cosmological background evolutions. The evolution of CDM energy density  $\rho_{CDM}(z)$  depends explicitly on the quintessence field  $\phi$ . Due to the modify evolution of CDM energy density, the interaction between dark sectors could shift the matter-radiation equality scale factor  $a$ , and affect the locations and amplitudes of acoustic peaks

of CMB temperature anisotropies and, consequently, the turnover scales of LSS matter power spectrum. In addition, the interaction will also affect the late Integrated Sachs-Wolfe effect at large scales which is produced by the CMB photons passing through the time-evolving gravitational potential well, when DE or curvature becomes important, at later times (Brookfield et al., 2008).

**The Generalized Chaplygin gas** model allows the description of DE and DM as a single fluid. However, it needs to be set very close to the  $\Lambda$ CDM prescription to explain the observed matter power spectrum. There is a class of viable unified models of DE and DM that uses a purely k-essence field (Unified Dark Matter, UDM). This field during the structure formation behaves like the DM, while, at the present time, such field contributes to the total energy density of the Universe acting like a cosmological constant  $\Lambda$ . Those UDM models are able to reproduce the same Hubble expansion as in the  $\Lambda$ CDM model (Bertacca et al., 2007), because in such models the sound speed could be small enough to let the cosmological structures grow and reproduce the LSS we see today (Bertacca et al., 2008). An effect of the presence of a non-negligible speed of sound of the UDM scalar field is that the radius at which the perturbation collapse (i.e. the Jeans length) gains an effective time-dependence. The increase of the the sound speed, from the zero value of the  $\Lambda$ CDM model, inhibits structure formation earlier in time, thus we observe less power on small scales and, as a consequence, the matter power spectrum acquires a oscillatory features.

### 1.8.2 Modified gravity models

A different approach holds that cosmic acceleration is a manifestation of new gravitational physics, rather than a new energy momentum component.

The simplest family of modified gravity models is obtained by replacing the Ricci scalar  $R$  in the usual Hilbert-Einstein action, for some non-linear viable functions  $f(R)$  that satisfy both cosmological and local gravity constraints. The  $f(R)$  gravity (Sotiriou & Faraoni, 2010) is equivalent to a scalar-tensor theory, where  $f_R = df/dR$  is the additional scalar degree of freedom. Such field has a mass and propagates on scales smaller than the associated Compton wavelength. Well within

the Compton wavelength, the scalar mediates an enhancement of gravitational forces, which strongly effects the growth of structure in the Universe. Such enhancements is quantified by the mass of the field or equivalently by the value of the field in the background,  $f_{R0}$ . In the non-linear regime, for field values larger than  $|f_{R0}| \sim 10^{-5}$ , cosmological simulations have shown that the abundance of rare massive halos are enhanced (Schmidt et al., 2009), and the growth factor acquire a dependence on the scale (Pogosian & Silvestri, 2008). Counts of galaxy clusters therefore provide the opportunity to improve cosmological constraints on  $f(R)$  models ultimately by 4-5 orders of magnitude. Moreover the bias in  $f(R)$  scenario decreases with increasing  $|f_{R0}|$  since halos of a fixed mass become less rare and thus less highly biased (Schmidt et al., 2009).

Another class of modified gravity models is the braneworld one. According to these models a four-dimensional Universe is restricted to a brane inside a higher-dimensional space, called the bulk. A particular braneworld model has been proposed by Dvali, Gabadadze, and Porrati (DGP, Dvali et al., 2000). According to the DGP model, the bulk is a infinitely large extra dimension with a Minkowski space-time metric. Newton gravity can be recovered by adding a 4D Einstein-Hilbert action sourced by the brane curvature to the 5D action. The standard 4D gravity is recovered for small distances, whereas the effect from the 5D gravity manifests itself for large distances. The DGP model admits two Hubble parameter solutions of modified Friedmann equations: one of them presents a self-accelerating behaviour at late-times without any cosmological constant term, hence it is known as the “self-accelerating” branch. The other solution is called the “normal” branch.

Presenting the standard DGP a strong tension between Type Ia Supernova (SNIa) data and CMB distance indicators, a phenomenological extension of the DGP model has been recently proposed, the so called extended DGP model (eDGP). In this extension, the DGP cross-over length  $r_c$ , that determines the scale at which higher-dimensional gravitational effects become important, is tuned by a new additional parameter  $\alpha$ , and a cosmological-constant term is explicitly present as a non-vanishing tension on the brane. In Camera et al. (2011) a sample of cosmological observables has been selected including  $H(z)$  data, Type Ia Supernovae (SNIa) and Gamma Ray Bursts (GRBs) as standard candles, BAOs from galaxies survey and priors from CMB observation. By studying both branches of the eDGP model and the  $\Lambda$ CDM model, they found that the eDGP models can fit current data at least as well as the standard  $\Lambda$ CDM

model.

## 1.9 Primordial non-Gaussian density fluctuations

The question of how the primordial fluctuations of density field have been generated is generally answered with the inflation model (see Section 1.1)

Many different models of inflation have been proposed over the years (Guth, 1981; Linde, 1983), differing mainly in the number and the properties of the scalar field(s) driving the accelerated expansion. A class of these models predicts a scale-free power spectrum of the primordial density fluctuations, with a spectral index very close to the Harrison-Zel'dovich value of unity (see Section 1.4), and moreover it predicts that the primordial density fluctuation has a Gaussian distribution. Other models of inflation predict, instead, a spectral index that depends on the scale (running index). In this Thesis, we studied the class of models that predicts primordial density fluctuations that follow a distribution different from the Gaussian one (e.g. Bartolo et al., 2004; LoVerde et al., 2008; Giannantonio & Porciani, 2010). non-Gaussian perturbations are expected to leave their imprint on the pattern of structure growth at least in two different ways. First, we expect that a positively skewed distribution provides an enhanced probability of finding large overdensities. This translates into an enhanced probability of forming large collapsed structures at high redshift, thereby it changes the timing of structure formation, the shape and the evolution of the mass function of dark matter haloes (Matarrese et al., 2000; Grossi et al., 2007; Matarrese & Verde, 2008). Therefore in order to use clusters to detect deviations from the Gaussian scenario of structures formation, we need the non-Gaussian prescription for the halo mass function and bias (see following Sections).

Moreover, non-Gaussianity affects the large-scale clustering of haloes in such a way that the linear biasing parameter acquires a scale dependence. This modifies, in a detectable way, the power spectrum of the distribution of any tracer of cosmic structures at small wave-numbers and offers a unique way of testing the nature of primordial fluctuations (Dalal et al., 2008; Matarrese & Verde, 2008; Giannantonio & Porciani, 2010).

A commonly used way to parametrize primordial non-Gaussianity consists in writing the Bardeen's gauge invariant potential  $\Phi$  as the sum of a linear Gaussian term and a non-linear second-order term that encap-

ulates the deviation from Gaussianity (Salopek & Bond, 1990; Komatsu & Spergel, 2001),

$$\Phi = \Phi_G + f_{\text{NL}} * \left( \Phi_G^2 - \langle \Phi_G^2 \rangle \right) \quad (1.51)$$

where the dimensionless parameter  $f_{\text{NL}}$ , which weights the quadratic correction to the Gaussian random field  $\Phi_G$ , depends on scale and configuration. The symbol  $*$  denotes standard convolution, and it reduces to simple multiplication when  $f_{\text{NL}}$  is constant. Bardeen's potential  $\Phi$ , on scales smaller than the Hubble radius, is equal to  $-\Psi$ , the usual Newtonian gravitational potential.

We stress that there is some ambiguity in the normalization of Eq. 1.51. According to the LSS convention,  $\Phi$  is linearly extrapolated at  $z = 0$ . In the CMB convention, instead,  $\Phi$  is primordial, thus  $f_{\text{NL}} = g(+\infty)f_{\text{NL}}^{\text{CMB}}/g(0) \simeq 1.3f_{\text{NL}}^{\text{CMB}}$ , where  $g(z)$  is the linear growth suppression factor for cosmological models different from the Einstein de Sitter one. The function  $g(z)$  is defined as  $g(z) = g(0)D_+(z)(1+z)$ , where  $D_+(z)$  is the linear growth factor (Eq. 1.21). In this Thesis, we will use the LSS convention.

If the distribution of primordial density (and potential) perturbations is not Gaussian, it cannot be fully described by a power spectrum expressed as  $P_\phi = Bk^n$ , higher order moments are needed, such as the bispectrum  $B_\phi(\mathbf{k}_1, \mathbf{k}_2, \mathbf{k}_3)$ . In particular, different models of inflation predict different shapes of the bispectrum.

In this Thesis, we will study one particular shape, called *local shape* (LoVerde et al., 2008). According to this shape, the magnitude of the bispectrum is maximum when one of the three momenta  $(\mathbf{k}_1, \mathbf{k}_2, \mathbf{k}_3)$  has a much smaller magnitude than the other two ("squeezed" configuration). In such models,  $f_{\text{NL}}$  is a dimensionless constant and the bispectrum can be written as (Creminelli et al., 2007)

$$B_\Phi(\mathbf{k}_1, \mathbf{k}_2, \mathbf{k}_3) = 2f_{\text{NL}}B^2 \left[ k_1^{n_s-4}k_2^{n_s-4} + k_1^{n_s-4}k_3^{n_s-4} + k_2^{n_s-4}k_3^{n_s-4} \right]. \quad (1.52)$$

Inflationary models exist that produce different shapes for the primordial bispectrum, e.g. the *equilateral shape* (e.g. Crociani et al., 2009), or the *enfolding shape* (Holman & Tolley, 2008; Meerburg et al., 2009; Verde & Matarrese, 2009). However, the local shape is the one giving the largest effects especially on bias (Taruya et al., 2008; Fedeli et al., 2009).

### 1.9.1 Mass function

Generalizations to non-Gaussian models of the standard Press & Schechter (1974) mass function have been presented in Matarrese et al. (2000) and LoVerde et al. (2008). Both approaches assume that deviations from Gaussianity are small. In particular, Matarrese et al. (2000) use the saddle point approximation to compute the probability distribution of threshold crossing, and then truncate the resulting expression to the skewness. LoVerde et al. (2008) instead approximate the probability density function for the smoothed DM density field by using the Edgeworth expansion and then perform the integral of the probability distribution for threshold crossing exactly on the first few terms of the expansion itself. The two approaches give quite similar results, and both have been shown to give reasonable agreement with full numerical simulations of structure formation (Grossi et al., 2009). The generalization of the PS mass function in the Non - Gaussian scenario is

$$\begin{aligned}
n_{NG} = & -\sqrt{\frac{2}{\pi}} \frac{\bar{\rho}(z)}{M} \exp\left[-\frac{\delta_c^2(z)}{2\sigma_M^2}\right] \left[\frac{d \ln \sigma_M}{dM} \left[\frac{\delta_c^2(z)}{2\sigma_M^2}\right.\right. \\
& + \left.\left.\frac{S_3 \sigma_M}{6} \left(\frac{\delta_c^4(z)}{\sigma_M^4} - 2\frac{\delta_c^2(z)}{\sigma_M^2} - 1\right)\right]\right] \\
& + \left.\frac{1}{6} \frac{dS_3}{dM} \sigma_M \left(\frac{\delta_c^2(z)}{\sigma_M^2} - 1\right)\right] \quad (1.53)
\end{aligned}$$

where  $S_3(M)$  is the normalized skewness,  $S_3(M) = -f_{NL,0} \mu_3(M) / \sigma_M^4$ . The  $f_{NL,0}$  parameter represents the non-linear parameter evaluated at the scale  $k_{CMB} = 0.086 \text{ h Mpc}^{-1}$  roughly corresponding to the largest multipole used by Komatsu et al. (2009) to estimate non-Gaussianity in the WMAP data,  $l=700$ . In the local case  $f_{NL,0} = f_{NL}$ . The third-order moment is

$$\mu_3(M) = \int \mathcal{M}_R(k_1) \mathcal{M}_R(k_2) \mathcal{M}_R(k_3) \times B_\Phi(\mathbf{k}_1, \mathbf{k}_2, \mathbf{k}_3) \frac{d\mathbf{k}_1 d\mathbf{k}_2 d\mathbf{k}_3}{(2\pi)^9} \quad (1.54)$$

The function  $\mathcal{M}_R(k)$  relates the Fourier transform of density fluctuations smoothed on some scale  $R$  to the relative peculiar potential, and is defined as

$$\mathcal{M}_R(k) = \frac{2}{3} \frac{T(k) k^2}{H_0^2 \Omega_{m,0}} W_R(k). \quad (1.55)$$

where  $T(k)$  is the matter transfer function and  $W_R(k)$  is the top-hat window function (Eq. 1.30).

Under the assumption that the non-Gaussian correction to the mass function is independent of the approach that is taken to evaluate the mass function itself, the structure abundance in a cosmology with non-Gaussian initial conditions can be computed in compliance to a generic prescription according to

$$n(M, z) = n^{(G)}(M, z) \frac{n_{NG}(M, z)}{n_{PS}(M, z)}. \quad (1.56)$$

where  $n_{PS}(M, z)$  is the mass function computed according to the PS formula (Eq. 1.36). Here,  $n^{(G)}(M, z)$  is the one computed as specified by the preferred prescription, both of them evaluated within the Gaussian assumption.

In Figure 1.11, we show the ratio of the non-Gaussian and Gaussian mass function. As we increment the level of Non -Gaussianity, we predict more massive clusters at higher redshift.

## 1.9.2 Bias

Primordial density fluctuations with non-Gaussian probability distribution cause a scale-dependent modification to the linear bias for given mass and redshift (Dalal et al., 2008; Matarrese & Verde, 2008).

For values of  $f_{NL}$  consistent with observations, we can keep terms up to the three-point correlation function  $\zeta^{(3)}$ , obtaining that the correction to the halo correlation function,  $\Delta\tilde{\zeta}_h$ , due to a nonzero three-point function, is given by

$$\begin{aligned} \Delta\tilde{\zeta}_h &= \frac{\nu^3}{2\sigma_R^3} \left[ \tilde{\zeta}_R^{(3)}(\mathbf{x}_1, \mathbf{x}_2, \mathbf{x}_2) + \tilde{\zeta}_R^{(3)}(\mathbf{x}_1, \mathbf{x}_1, \mathbf{x}_2) \right] \\ &= \frac{\nu^3}{\sigma_R^3} \tilde{\zeta}_R^{(3)}(\mathbf{x}_1, \mathbf{x}_1, \mathbf{x}_2) \end{aligned} \quad (1.57)$$

where  $\nu = \delta_c / \sigma_R$ .

We can write the expression for the non-Gaussian contribution to the halo power spectrum as:

$$\Delta P_h(k) = b_{0,L}^2 4 f_{NL} \delta_c P_{\Phi\delta}(k) \mathcal{F}_R(k) P_\Phi(k_1) \times \int_{-1}^1 d\mu \mathcal{M}_R(\sqrt{\alpha}) \left[ \frac{P_\Phi(\sqrt{\alpha})}{P_\Phi(k)} + 2 \right]. \quad (1.58)$$

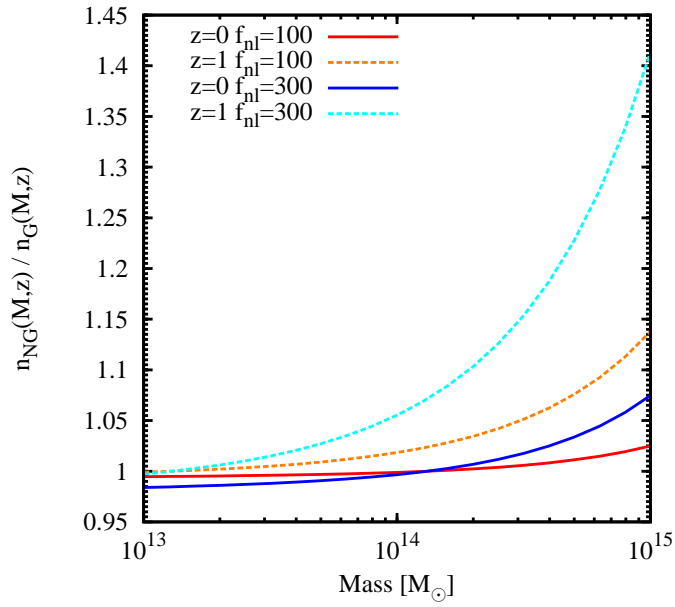


Figure 1.11: Ratio between Non - Gaussian and Gaussian mass functions for two different values of non-Gaussian parameter,  $f_{NL} = 100$  and  $f_{NL} = 300$ , at two different redshifts  $z = 0$  and  $z = 1$ .

where  $b_{0,L} \equiv \delta_c/\sigma_R^2$ , corresponding to the Lagrangian linear bias that halos would have in the Gaussian case. Moreover, in the above equation,  $P_{\phi\delta}(k) \equiv \mathcal{M}_R(k)P_\phi(k)$  and

$$\mathcal{F}_R(k) = \frac{1}{8\pi^2\sigma_R^2} \int dk_1 k_1^2 \mathcal{M}_R(k_1) \quad (1.59)$$

The expression for the halo power-spectrum can be rewritten in a more convenient form, where we make the redshift dependence explicit:

$$P_h(k, z) = \frac{\delta_c^2 P_{\delta\delta}(k, z)}{\sigma_R^4} \left[ 1 + 4 f_{\text{NL}} \delta_c(z) \frac{P_{\delta\Phi}(k) \mathcal{F}_R(k)}{P_{\delta\delta}(k)} \right] \quad (1.60)$$

with  $P_{\delta\delta}(k, z) = D^2(z)P_{\delta\delta}(k) = D^2(z)\mathcal{M}_R^2(k)P_\phi(k)$ . By defining the Lagrangian bias,  $b_L$ , of the halos from the equation  $b_L^2 = P_h(k, z)/P_{\delta\delta}(k, z)$  and by using  $b_E = 1 + b_L$ . We obtain the expression for the non-Gaussian halo bias

$$b_{\text{NG}} = 1 + \frac{\delta_c(z)}{\sigma_R^2} \left[ 1 + 2f_{\text{NL}} \frac{\delta_c(z)}{D(z)} \frac{\mathcal{F}_R(k)}{\mathcal{M}_R(k)} \right] \quad (1.61)$$

Thus  $b_{\text{NG}} \simeq b_G(1 + \Delta b/b_G)$  where  $b_h$  denotes the halo bias for the Gaussian case and is always  $> 1$ . In Figure 1.12, we show the ratio between the halo bias predicted by the non-Gaussian and Gaussian prescription. The effect of non-Gaussianity grows with mass and is higher as redshift increases. Moreover, as we show in the right panel of Figure 1.12, the bias acquires a dependence from the scale. Thus, bias becomes higher as wavenumber increases.

## 1.10 Constraints on cosmological parameters from galaxy clusters

In this final Section, we will summarize the constraints obtained on cosmological parameters in the last decade from cluster analysis.

First attempts to use evolution of the cluster mass function as a cosmological probe were limited by small sample sizes and either poor proxies for the cluster mass (e.g., the total X-ray flux). Despite such limitations, constraints on  $\Omega_m \sim 0.35 \pm 0.13$  were derived (e.g., Borgani et al., 2001; Henry, 2004). Moreover, observational results from the past several years yield for the power spectrum normalization typical uncertainties at the  $\Delta\sigma_8 \approx 0.05 - 0.10$  level despite a spread in central values that range

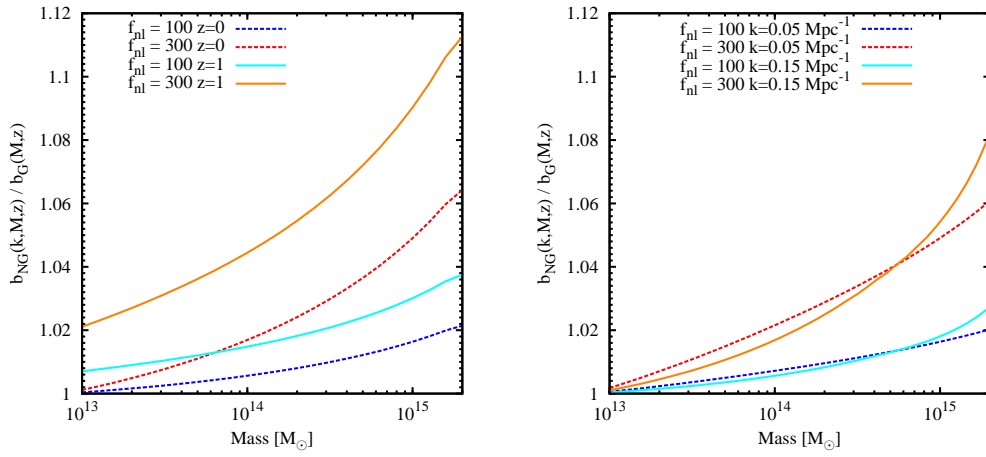


Figure 1.12: Ratio between non-Gaussian and Gaussian halo bias for two different values of Non - Gaussian parameter,  $f_{NL} = 100$  and  $f_{NL} = 300$ . *Left panel:* dotted curves represent bias ratio at redshift  $z = 0$  and solid curves represent bias ratio at redshift  $z = 1$ . *Right panel* dotted curves represent bias ratio at wave-number  $k = 0.05 Mpc^{-1}$  and solid curves represent bias ratio at wave-number  $k = 0.15 Mpc^{-1}$ .

from  $\sigma_8 \approx 0.65$  to  $\sigma_8 \approx 1.0$  (Viana & Liddle, 1996, 1999; Henry & Arnaud, 1991; Henry, 2000; Pierpaoli et al., 2001; Borgani et al., 2001; Seljak, 2002; Viana et al., 2002; Schuecker et al., 2003; Allen et al., 2003; Bahcall et al., 2003; Bahcall & Bode, 2003; Voevodkin & Vikhlinin, 2004; Rozo et al., 2007; Gladders et al., 2007; Rines et al., 2007). As for DE EoS constraints, Mantz et al. (2008) determine  $w = -1.4 \pm 0.55$  with a larger sample of distant clusters (MACS survey, see Ebeling et al., 1998), using the X-ray luminosity as a mass proxy.

More recently, Burenin et al. (2007) derives a large sample of galaxy clusters extending to  $z \sim 0.9$  from X-ray ROSAT-PSPC pointed data covering  $400 \text{ deg}^2$  (the 400d sample). Distant clusters from the 400d sample were then observed with *Chandra*, providing high-quality X-ray data and accurate mass proxies. *Chandra* observations are also available for a complete sample of low- $z$  clusters originally derived from the ROSAT All-Sky Survey. Such data have significantly improved our knowledge of the outer cluster regions and provided a much more reliable calibration of the  $M_{tot}$  vs. proxy relations than what was possible before. On the theoretical side, results from numerical simulations improved the understanding of measurement biases in the X-ray data analysis (Nagai et al., 2007; Rasia et al., 2006) and have been used to suggest new, X-ray mass proxies (Kravtsov et al., 2006). Moreover, the cluster mass functions fitting formulas provided by Tinker et al. (2008) are formally accurate to better than 5% for the cosmologies close to the concordance  $\Lambda$ CDM cosmology. Vikhlinin et al. (2009a) confirm these theoretical results by estimating the cluster mass functions from the low and high- $z$  400d cluster sample. These data show a significant evolution in the cluster comoving number density at a fixed mass threshold, by a factor of  $\approx 5$  at  $M_{500,c} = 2.5 \times 10^{14} h^{-1} M_{\odot}$  between  $z = 0$  and 0.5. Moreover Vikhlinin et al. (2009b) presented constraints on the cosmological parameters from Vikhlinin et al. (2009a) samples. The matter density has been measured as  $\Omega_m = 0.30 \pm 0.05$  in a flat  $\Lambda$ CDM model and  $0.34 \pm 0.08$  in a general cosmology. Evolution of the mass functions constrains  $\Omega_{\Lambda} = 0.83 \pm 0.15$  in non-flat  $\Lambda$ CDM cosmology, or the dark energy equation of state parameter,  $w_0 = -1.14 \pm 0.21$ , in a spatially flat Universe. By including, the information provided by Vikhlinin et al. (2009a) cluster data significantly improves the equation of state constraints obtained from combination of multiple cosmological datasets. By combining cluster data with the 5-year WMAP (Dunkley et al., 2009), recent supernovae measurements, and detection of baryonic acoustic oscillations in the SDSS (Eisenstein et al., 2005), with

their own data sets Vikhlinin et al. (2009b) obtained  $w_0 = -0.991 \pm 0.045$  (stat)  $\pm 0.040$  (sys). (Figure 1.13).

Mantz et al. (2010a) presented cosmological constraints obtained from an X-ray flux-limited sample of 238 massive galaxy clusters spanning the redshift range  $z < 0.5$ , with follow-up *Chandra* and ROSAT X-ray observations of 94 of these clusters. This analysis produces simultaneous constraints on cosmology and the cluster scaling relations using a rigorous and fully self-consistent statistical method. The constraints on spatially flat, cosmological constant models are  $\Omega_m = 0.23 \pm 0.04$  and  $\sigma_8 = 0.82 \pm 0.05$ . Introducing a constant dark energy equation of state,  $w$ , as a free parameter, they found  $w = -1.0 \pm 0.2$ , in agreement independent findings based on cluster gas mass fractions, CMB anisotropies, type Ia supernovae, baryon acoustic oscillations, galaxy redshift surveys, cosmic shear, X-ray selected galaxy clusters (Henry et al., 2009; Vikhlinin et al., 2009b) and optically selected clusters (Rozo et al., 2010) (Figure 1.14).

As for the optical band, Rozo et al. (2010) derived cosmological constraints from the SDSS maxBCG cluster sample (Koester et al., 2007b) and the statistical weak lensing mass measurement from Johnston et al. (2007). Rozo et al. (2010) performed a joint analysis of the abundance and weak lensing mass estimates of the maxBCG clusters detected using SDSS imaging data. By using a prior on the scatter in the mass-richness relation derived from the consistency between the weak lensing and X-ray mass estimates of the clusters, their cosmological constraints can be summarized as  $\sigma_8(\Omega_m/0.25)^{0.41} = 0.832 \pm 0.033$ . With a joint maxBCG and WMAP5 analysis Rozo et al. (2010) reported  $\sigma_8 = 0.807 \pm 0.020$  and  $\Omega_m = 0.265 \pm 0.016$  (Figure 1.15).

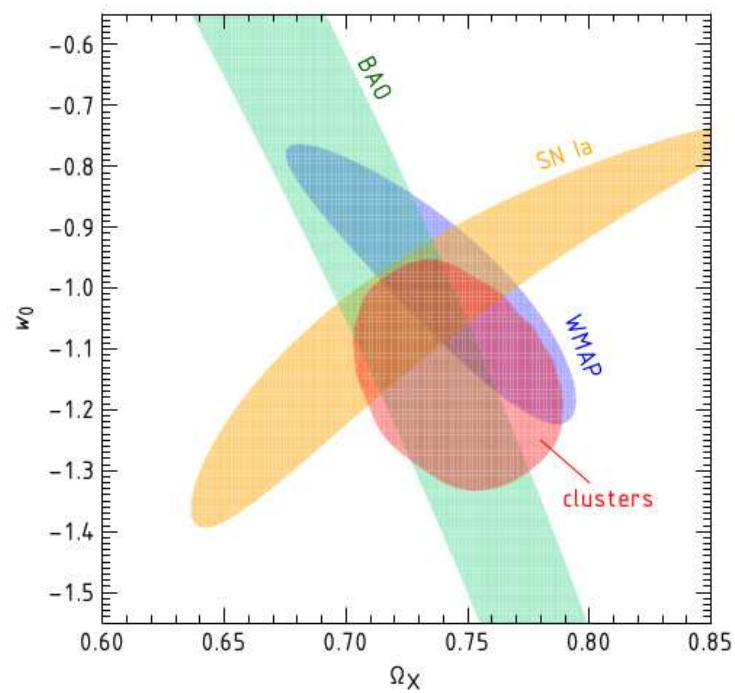


Figure 1.13: Constraints at 68 % CL on the  $(w_0, \Omega_{DE})$  parameters for flat  $\Lambda$ CDM cosmology from the Vikhlinin et al. (2009a) sample, WMAP-5 , SNIa and BAO. See Vikhlinin et al. (2009b) for details.

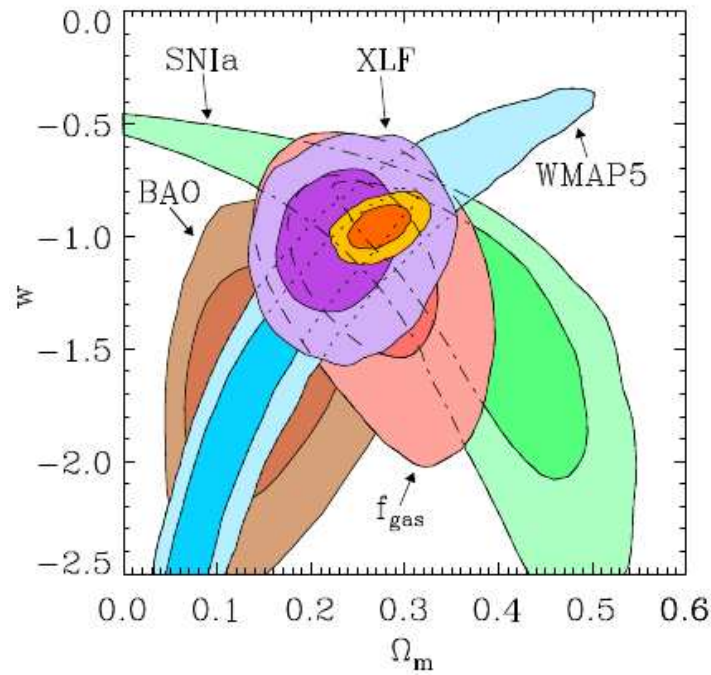


Figure 1.14: Constraints at 68.3 and 95.4 % CL on  $(\Omega_m, w_0)$  for  $\Lambda$ CDM model. Constraints from the XLF (Mantz et al., 2010a), cluster  $f_{gas}$  data Allen et al. (2008), WMAP-5 (Dunkley et al., 2009), SNIa data (Kowalski et al., 2008), and BAO observations (Percival et al., 2007). Results from combining these 5 data sets are also shown in gold. Figure from (Mantz et al., 2010a).

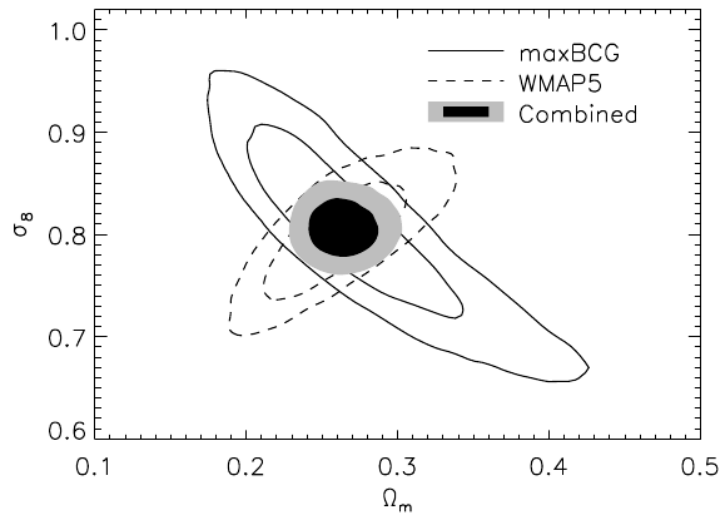


Figure 1.15: Constraints at 68 and 95 % CL on the  $(\sigma_8, \Omega_m)$  parameters from maxBCG (solid) and WMAP-5 (dashed) (Dunkley et al., 2009) for flat  $\Lambda$ CDM cosmology. Combined results are shown with filled ellipses. Figure from Rozo et al. (2010).

## Chapter 2

# Surveys of Galaxy Clusters

Galaxy clusters represent the place where astrophysics and cosmology meet each other. As we showed in Chapter 1, according to the hierarchical growth structure model, clusters are the largest and most recent objects that have undergone gravitational relaxation and entered into virial equilibrium. They represent the end result of the collapse of density fluctuations involving comoving scales of about 10 Mpc. On scales larger than this, gravitational dynamics drive the formation of structures, and gas-dynamical effects play a minor role. However, on scales smaller than 10 Mpc, the complex astrophysical processes related to galaxy formation and evolution, significantly change the evolution of cosmic baryons and, therefore, the observational properties of the structures. For these reasons, in order for clusters to be used as cosmological tools, one needs to understand in detail the astrophysical processes which determine their observational properties.

In this Chapter the methodology used to construct samples of galaxy clusters in the optical/near-IR, in the X-ray and in the Microwave bands will be reviewed. We will summarize for each of these bands the three essential tools required to build a cluster sample and to use it for cosmological applications: an efficient method to identify clusters over a wide redshift range; a method to define the selection function or equivalently the survey volume within which clusters are found; and, finally, an observable estimator or “proxy” of the cluster mass.

## 2.1 Cluster surveys in the optical/near-IR band

### 2.1.1 Identification of clusters

Optical identification of galaxy clusters has been going on since the end of the eighteenth century with Charles Messier (1784) and William Herschel (1785). Finally, in 1989, Abell et al. provided the first extensive, statistically complete sample of galaxy clusters. Based on purely visual inspection, clusters were identified as enhancements in the galaxy surface density and were characterized by their *richness* and estimated distance. The richness of a cluster is a measure of the number of galaxies associated with that cluster. In order to include a cluster in a catalogue, it is necessary to specify the threshold in the surface number density enhancement and the linear or angular scale of such enhancement. Because clustering exists on a very wide range of angular and intensity scales (Peebles, 1980), it is not possible to define unambiguously what a rich cluster is.

Another problem of optical surveys is the presence of background and foreground galaxies. For this reason, it is not possible to state with absolute confidence if a galaxy belongs to a given cluster. In fact, projection effects in galaxy distribution represent the main issue in optical survey. Filamentary structures along the line of sight can mimic a moderately rich cluster when projected onto the plane of the sky. In addition, the background galaxy distribution, against which two dimensional over-densities are selected, is far from uniform. The colours of the cluster members place them on a narrow and distinctive locus, known as the *red sequence*, in a plot of galaxy colour versus magnitude (e.g. Gladders & Yee, 2000). The red-sequence represents the reddest galaxies of a set of galaxies at the same redshift, and is easily detectable in the colour-magnitude diagram since early-type galaxies dominate the bright end of luminosity function in clusters. Therefore, selecting galaxies around the red-sequence, it is possible to exclude most of background and foreground galaxies, which are redder and bluer respectively. In Figure 2.1), we show, as an example, the colour-magnitude diagram in the  $2 h^{-1}\text{Mpc}$  surrounding fields of Abell 1682. For this cluster at  $z = 0.23$ , the cluster members (small plus signs) place on the red sequence and thus they can be clearly distinguished from the galaxies of the field (dots).

Detecting clusters through surface number over-density in the galaxy distribution, without any other information does not guarantee that such systems are gravitationally bound. In this respect, it is crucial to obtain

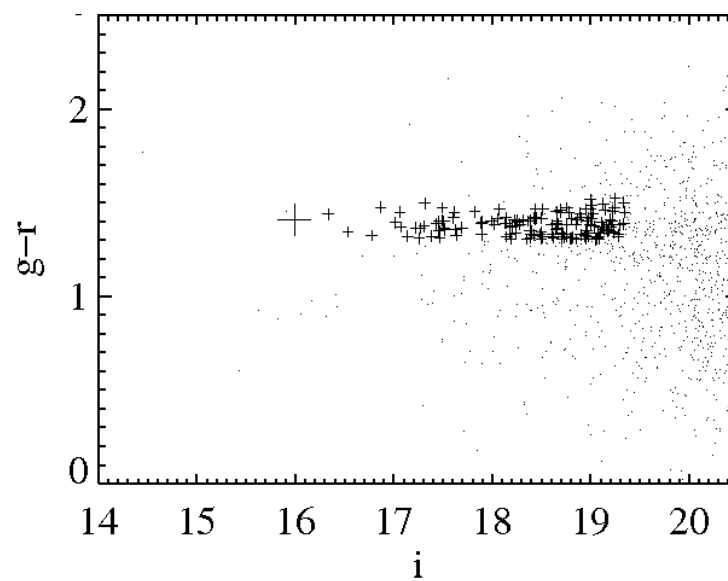


Figure 2.1: BCGs and cluster members in the fields of cluster Abell 1682. The colour-magnitude diagram in the  $2h^{-1}\text{Mpc}$  surrounding fields of Abell 1682 ( $z = 0.23$ ). The large plus sign is the BCG, dots are field galaxies within  $2h^{-1}\text{Mpc}$ , and small plus signs are cluster members. Figure from Koester et al. (2007b).

the radial velocities,  $v_r$ , of the cluster galaxies from their redshifts. Under the assumption of a cluster to be relaxed, the distribution of velocities of member galaxies is expected to be Gaussian. Consequently galaxies with velocities falling well outside the best-fitting Gaussian are unlikely to be cluster members. On the other hand, when the velocity distribution of the potential cluster galaxies is far from Gaussian, probably the galaxies surface over-density is a superposition of unbounded structures. Fitting the velocity distribution to the candidates galaxies yields the one-dimensional velocity dispersion  $\sigma_v$  for the cluster. The accuracy of  $\sigma_v$  depends critically on the number of the measured galaxies velocities and on the method used to identify and eliminate spurious cluster members.

Because of the ambiguities in the definition of a cluster and in the background subtraction process that can produce spurious low-richness clusters during searches for clusters in galaxy catalogues, and because of the loose relation between galaxy counts and the overall optical luminosities of clusters, the definition of a selection function that ensures a statistically complete and pure catalogue of galaxy clusters in the optical band is difficult.

A significant step forward in exploring clusters in the local Universe has been made with the wave-band photometry provided by the Sloan Digital Sky Survey (SDSS, York et al., 2000), by increasing the number of observed passbands. To cover a range of redshifts as large as possible, multi-colour photometry is needed to track the intrinsic 4000 Angstrom break feature of old stellar populations as it reddens. The five band photometry of the SDSS has allowed such selection. The *maxBCG* catalogue (Koester et al., 2007a) of 13,823 clusters with optical richness  $N_{gal} = 10$  was produced using  $g$  and  $r$  colours and spans the redshift range  $0.1 < z < 0.3$ . Cosmological constraints from this sample are provided by Rozo et al. (2010). Recently, larger SDSS clusters samples have been provided by Wen et al. (2009); Hao et al. (2010). These catalogues contain between 40,000 and 69,000 clusters reading redshift  $z \approx 0.6$ , and cover roughly 8000 deg<sup>2</sup>.

### 2.1.2 Mass estimation

A primary challenge to cosmological analysis using optically based catalogues is the definition of robust cluster mass proxies that have minimal and well understood scatter across the full mass and redshift ranges of interest.

### Richness-mass scaling relation

All variations of the Abell criteria classify clusters according to the definitions of richness, which generally has a loose relation with the cluster mass. However any cosmological application, requires that the observable, on which the cluster selection is based, is a reliable and robust proxy of the cluster mass.

Under the assumption that light traces mass in the universe, the total optical luminosity of a cluster is an indicator of a cluster mass. The luminosity distribution function of cluster galaxies is nearly the same for all clusters. Thus the high luminosity tip of this distribution normalizes the overall galaxy luminosity function for the cluster, yielding estimates of the cluster total optical luminosity and consequently its mass (Cohn et al., 2007; Rozo et al., 2011).

The increasing quality of photometric data for the cluster galaxy population and the ever improving capability of removing fore/background galaxies thanks to larger spectroscopic galaxy samples have allowed to demonstrate that  $L_{\text{op}}$  can be used to estimate the cluster mass. In particular in Figure 2.2, we show the results obtained by Popesso et al. (2005) by analysing SDSS data for a set of clusters which have been identified in the RASS in the  $i$  band. They estimated cluster mass from the velocity dispersions as estimated from the SDSS spectroscopic data. The optical luminosity tightly correlates with the cluster mass, with a slope of  $1.5 \pm 0.05$  and with an intrinsic scatter of 40%, smaller than the scatter obtained for the  $L_X$ -M correlation.

These results stress that cluster samples with precisely measured optical luminosities can be employed to constrain cosmological parameters. However, it is useful to point out that sample selection function can be extracted from an optically selected sample only in an indirect way, while X-ray luminosity traces cluster mass provides a criterion to precisely determine the sample selection function at the same time.

### Galaxy Velocities

Under the assumption of virial equilibrium, which applies to steady, gravitationally bound systems, the mass of a spherical, isolated cluster can be estimated by knowing position and redshift for a high enough number of member galaxies:

$$M = \frac{\pi}{2} \frac{3 \sigma_v^2 R_{vir}}{G}. \quad (2.1)$$

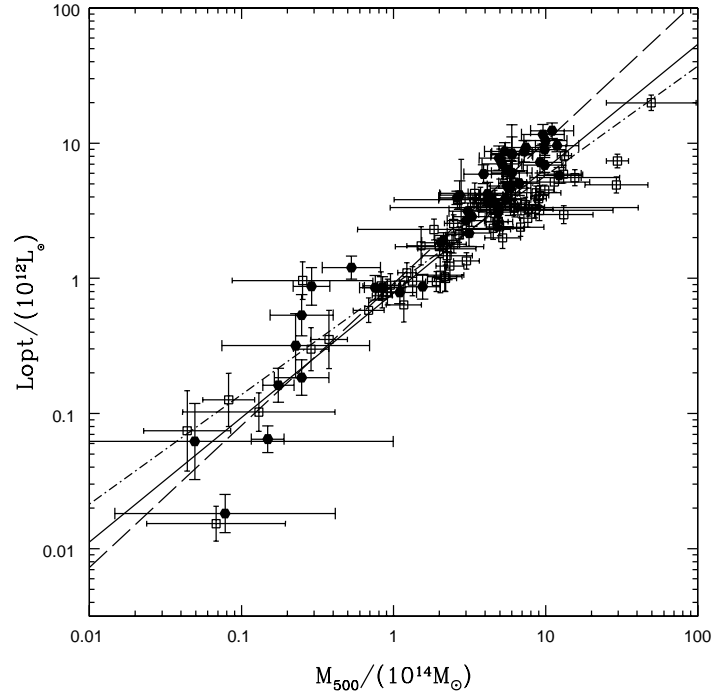


Figure 2.2:  $L_{\text{op}} - M_{500}$  relation in the  $i$  SDSS band. Empty squares indicate clusters with mass estimated from the velocity dispersions analysis as estimate from the SDSS spectroscopic data. The filled points indicate systems with mass estimated from the  $M - T_X$  relation. The dot-dashed line is the best fit line obtained for the O sample. The dashed line is the best fit line for the X sample and the solid line is the result obtained from the E sample. O refers to the sample with masses estimated from the dynamical analysis performed with the optical spectroscopic data. X refers to the sample with masses estimated from the  $M - T_X$  relation. E refers to the enlarged sample, which comprises all the clusters in the RASS-SDSS galaxy cluster catalogue with known mass. Figure from Popesso et al. (2005).

In this equation  $\sigma_v$  is the line-of-sight velocity dispersion and  $R_{vir}$  is the virialization radius, which depends on the positions and the number of the cluster galaxy members.

Tests of the accuracy of mass estimates based on the galaxy velocity method have been performed by using hydrodynamical simulations of galaxy clusters. The results (Frenk et al., 1996; Biviano et al., 2006) showed that galaxies identified in the simulations tracers the underlying dynamics with no systematic bias in the estimate of cluster masses, but with a large scatter between true and recovered masses, mostly induced by projection effects.

This method has been extensively applied to measure masses for statistical samples of both nearby (e.g. Rines et al., 2003; Biviano & Girardi, 2003; Girardi & Mezzetti, 2001) and distant (e.g. Girardi et al., 2005; Borgani et al., 1999) clusters.

### Gravitational Lensing

In contrast to X-ray and optical dynamical methods, gravitational lensing offers a way to directly study the mass distribution in the Universe on different scales, regardless of its baryon content, mass-to-light ratio and dynamical state (e.g. Bartelmann, 2010; Peacock & Schneider, 2006), because it only depends on the gravitational potential well of the lens.

Gravitational lensing is predicted by the theory of General Relativity. Instead of light from a source travelling in a straight line (in three dimensions), it is bent by the presence of a massive body, whose gravitational potential well distorts the space time.

The space-time curvature is ruled by the effective refraction index  $n \equiv 1 - 2\phi/c^2$ , where  $\phi$  is the gravitational potential due to the mass distribution of the lens. This index determines the deflection angle of the light passing throughout the gravitational lens. This leads to the distortion of the images of background sources stretched tangentially to the gradient of the gravitational potential, and to the formation of multiple images and giant luminous arcs (Schneider, 2006). Observations of these features allow to reconstruct the distribution of the mass responsible for the deflection.

In particular, *strong gravitational lensing* is a gravitational lensing effect that is strong enough to produce multiple images, arcs, or even Einstein rings. An Einstein ring is a special case of gravitational lensing, caused by the exact alignment of the source, the lens and the observer. This results

in a symmetry around the lens, causing a ring-like structure. The size of an Einstein ring is given by the Einstein radius:

$$\theta_E = \sqrt{\frac{4GM}{c^2} \frac{D_{ls}}{D_l D_s}},$$

where  $G$  is the gravitational constant,  $M$  is the mass of the lens,  $c$  is the speed of light,  $D_l$  is the angular diameter distance to the lens,  $D_s$  is the angular diameter distance to the source, and  $D_{ls}$  is the angular diameter distance between the lens and the source. Generally, the strong lensing effect requires the projected lens mass density to be greater than the critical density  $\Sigma_{cr}$ . For point-like background sources, strong lensing causes multiple images; for extended background emissions, there can be arcs or rings. Strong lensing enables precise measurements of the projected masses through regions enclosed by gravitational arcs.

Because lensing is sensitive to the cluster's mass within a given projected radius  $r_\perp$ , when the deflection angle is small compared to a background galaxy's angular distance from the cluster centre, *weak lensing* shifts each point in the galaxy's image to a slightly larger angular distance from the cluster's centre, thereby distorting the image by stretching it tangentially to  $r_\perp$ .

While triaxiality of clusters is expected to introduce scatter in individual (de-projected) mass measurements at the level of tens of per cent (Corless & King, 2007; Meneghetti et al., 2010), the measurement of the shear distortion of an entire field of background galaxies, under the assumption that any intrinsic deviations of galaxy images from circular symmetry are uncorrelated for statistical samples and using suitable mass estimators, working over optimized radial ranges and with good knowledge of the redshift distribution of the background population, are expected to provide almost unbiased results on the mean mass (Rasia et al., 2012; Becker & Kravtsov, 2011).

In general, the observable quantity for weak lensing is not the gravitational shear  $\gamma$  but the complex reduced shear,

$$g(\boldsymbol{\theta}) = \frac{\gamma(\boldsymbol{\theta})}{1 - \kappa(\boldsymbol{\theta})}, \quad (2.2)$$

where  $\boldsymbol{\theta}$  indicate the observed position, the *convergence*  $\kappa$  is expressed as:

$$\kappa(\boldsymbol{\theta}) = \Sigma(\boldsymbol{\theta}) / \Sigma_{crit} \quad (2.3)$$

, namely, the projected mass density  $\Sigma(\theta)$  in units of the critical surface mass density for gravitational lensing, defined as

$$\Sigma_{\text{crit}} = \frac{c^2}{4\pi G D_l} \langle \beta \rangle^{-1}, \quad \beta(z_s) \equiv \max \left[ 0, \frac{D_{ls}(z_s)}{D_s(z_s)} \right], \quad (2.4)$$

where  $z_s$  is the redshift of the source,  $D_s$ ,  $D_l$ , and  $D_{ls}$  are the proper angular diameter distances from the observer to the source, from the observer to the deflecting lens, and from the lens to the source, respectively, and  $\langle \beta \rangle$  is the mean distance ratio averaged over the population of source galaxies in the cluster field. A lens with projected mass density larger than  $\Sigma_{\text{crit}}$  in its core can produce strong lensing effects, such as multiple images; instead, a lens with  $\Sigma \ll \Sigma_{\text{crit}}$  produces only weak lensing effects.

Accurate measurements of the shapes (ellipticities) of background galaxies lead to the estimate of the lens (reduced) shear  $g$ . The major uncertainty in these shear maps comes by the density of background galaxies (Lombardi & Bertin, 1998). The reduced shear on a single galaxy depends on the galaxy redshift. However, even without knowing the individual redshifts of all the background galaxies, we can perform a weak lensing analysis, assuming the redshift distribution of these background galaxies (Lombardi et al., 2005). According to Eq. 2.2, once that we have calculated the reduced shear, we can directly inverted it into the convergence  $\kappa$  (Eq. 2.3). However, this quantity is defined up to an arbitrary additive constant, i.e. the convergence can only be determined up to the transformation  $\kappa = \kappa\lambda + (1 - \lambda)$ . This issues is known as the mass-sheet degeneracy. In the weak lensing regime, this degeneracy can be avoided measuring the magnification that is defined as the ratio of the image area to the source area, and that can be written as a function of the shear  $\gamma$  and the convergence  $\kappa$  as well as  $g$ :

$$\mu = \frac{1}{[(1 - \kappa)^2 - \gamma^2]}. \quad (2.5)$$

There are two popular ways of deriving the lensing mass from tangential shear: aperture-mass densitometry (Fahlman et al., 1994) and parametrized model fitting (Umetsu et al., 2011). Aperture-mass densitometry is useful when one attempts to estimate the total projected mass within some aperture radius without requiring an assumption on the behaviour of the cluster mass profile. However, this approach is not practical for data sets, which provides areas smaller than the virial radii of the clusters. The

second method determines the parameters of analytic halo models from the observed tangential shear. Several studies, most notably those based on panoramic deep imaging typically with the SUPRIMEcam on the SUBARU telescope, show that the tangential shear profiles are well fitted by parametric models such as the NFW profile (Eq. 2.7) (e.g. Jee et al., 2005; Hoekstra, 2007). This parametric method has the advantage to circumvent the inherent mass-sheet degeneracy of weak lensing measurements. On the other hand, the model independent aperture-mass method removes the mass sheet degeneracy by setting to zero the shear signal in the cluster outskirts, clearly this is appropriate only when wide and deep imaging data are available to trace the shear at large radii (i.e. well beyond the virial radius).

The main systematic problem in weak-lensing mass measurements comes from the lensing done by excess mass outside the virial radius but along the line of sight through the cluster. Simulations of large-scale structure formation suggest that superposition of other mass concentrations limit the accuracy of weak-lensing masses, at least for clusters defined to be within spherical volumes. Projected mass fluctuations along the line of sight to a distant cluster can be on the order of  $\sim 10^{14} M_{\odot}$  (Metzler et al., 2001; Hoekstra, 2001). Therefore, unless one resorts to stacking analyses, the application of the weak lensing method to low mass clusters remains difficult.

In Chapter 4, we will present constraints derived from high- $z$  RDCS sample, in combination with the Vikhlinin et al. (2009a) sample. The mass of five clusters out of nine belonging to the high- $z$  RDCS sample has been calculated with weak lensing analysis by Jee et al. (2011).

## 2.2 Clusters X-ray Properties and Surveys

In order to determine the methodology used to build an X-ray galaxy cluster sample, we will briefly outline the main characteristics of X-ray emission. Despite the name, the galaxies are not the dominant component of galaxy clusters. They can be defined, instead, as Dark Matter halos, whose gravitational potential wells are filled by the so called the Intracluster Medium (ICM), and by the bound cluster galaxy populations. Approximately 80 – 85 % of a cluster is constituted by the Dark Matter, whose presence is inferred from gravitational effects on visible matter.

The ICM is a plasma at a temperature of  $k_B T \simeq 2 - 10$  keV (corre-

sponding to  $T \simeq (20 - 100) \times 10^6$  K) and consists, mainly, of ionized hydrogen and helium. The ICM constitutes most of the baryonic material in clusters and provides approximately 15% of the total cluster mass. Only the 2 – 5 % of the total mass of a cluster is provided by cool baryons in stars and galaxies.

Clusters can be considered as “closed boxes” that retain all their gaseous matter, thanks to their deep gravitational potential well. Such potential well compresses the associated baryonic gas and heats it to X-ray emitting temperatures. The gas temperature inferred from a cluster X-ray spectrum therefore indicates the depth of a cluster potential well, and the emission-line strength in that spectrum indicates the abundance of elements like iron, oxygen, and silicon in the ICM.

### 2.2.1 The physics and the structure of the ICM

Felten et al. (1966) first suggested that the X-ray emission from clusters is due to hot diffuse gas, the ICM, that is in thermal and dynamical equilibrium with the galaxies and the Dark Matter within the gravitational potential well.

Since the gas shares the same dynamics of the member galaxies, the typical atomic velocity is similar to the velocity of the galaxies in the cluster. Thus, the gas, composed mainly of hydrogen, has a temperature of  $T \simeq 10^7$  K or  $k_B T \geq 1$  keV) and the dominant X-ray emission mechanism is thermal bremsstrahlung (free-free radiation). The bremsstrahlung emissivity for a plasma at temperature  $T$ , i.e. the energy per unit time, frequency  $\nu$  and volume  $V$ , is:

$$\epsilon_{\nu}^{ff} \equiv \frac{dL}{dV d\nu} \simeq 6.8 \times 10^{-38} Z_i^2 n_e n_i g^{ff}(\nu, T) \frac{e^{-\frac{h_p \nu}{k_B T}}}{\sqrt{T}} \text{ erg s}^{-1} \text{ cm}^{-3} \text{ Hz}^{-1}, \quad (2.6)$$

where  $n_e$  and  $n_i$  are the number densities of electrons and ions respectively,  $Z_i$  is the ion charge, and  $g^{ff}(\nu, T) \propto \ln(9k_b T / (4h_p \nu))$  is the frequency-dependent Gaunt factor.

Emission lines of heavy elements are another important feature of the X-ray spectra of clusters of galaxies. For clusters with temperature greater than 3 keV the contribution to the luminosity is not relevant, since at these temperatures most of the atoms are completely ionized. Instead, line emission and recombination radiation are more important for low

temperature clusters, in particular below 2 keV (e.g. Raymond & Smith, 1977).

The most important X-ray line feature for massive clusters is the K-shell line complex of hydrogen-like iron FeXXVI around 6.7 keV, with slightly shifted energies for other ionization states. At lower temperatures, additional important line features originate from the Fe L line complex at  $\sim 1$  keV and ions of O, Mg, Si, S, Ar, Ca, and Ne.

The angle-averaged global spatial structure of the ICM can be described by the *King model* for a self-gravitating, isothermal sphere (King, 1966). If an additional scaling of the ICM density profile with respect to the underlying Dark Matter profile of the form  $\rho_{gas} \propto \rho_{DM}$  is allowed, then the three dimensional  $\beta$ -model for the radial ICM profile  $\rho_{gas}(r)$  is obtained (Cavaliere & Fusco-Femiano, 1976)

$$\rho_{gas}(r) = \frac{\rho_{gas,0}}{\left[1 + \left(\frac{r}{r_c}\right)^2\right]^{3\beta/2}}, \quad (2.7)$$

where the core radius  $r_c$  determines the characteristic extent scale of the source. The  $\beta$  parameter represents the ratio of their kinetic energy of galaxies and the thermal energy of the gas,

$$\beta \equiv \frac{\mu m_p \sigma_r^2}{k_B T}. \quad (2.8)$$

where  $\sigma_r$  denotes the radial velocity dispersion,  $m_p$  the proton mass, and  $\mu$  the mean molecular weight of the gas ( $\mu \simeq 0.6$  for a primordial gas composition). If  $\beta$  parameter deviates from unity, then the galaxies, as dynamic tracers of the Dark Matter potential, exhibit a different velocity dispersion with respect to the ICM gas, according to  $\sigma_{gal}^2 = \beta \sigma_{gas}^2$ .

By relating the gas density profile  $\rho_{gas}(r)$  to the X-ray emissivity and by projecting the distribution on the plane of the sky, the observed two dimensional X-ray surface brightness profile  $S(r)$  of the  $\beta$ -model is obtained. The resulting radially symmetric profile

$$S(\Theta) = \frac{S_0}{\left[1 + \left(\frac{r}{r_c}\right)^2\right]^{3\beta - \frac{1}{2}}} \quad (2.9)$$

contains the fit parameters  $r_c$  for the angular core radius size, the central surface brightness  $S_0$ , and the  $\beta$  value. The  $\beta$ -model is now known not to

give a precise description of the gas distribution, more accurate models have been used for example by Vikhlinin et al. (2006)

### 2.2.2 Identification of clusters and definition of the selection function

Because diffuse emission from a hot ICM is the direct manifestation of the existence of a potential well within which the gas is in dynamical equilibrium with the cool baryonic matter (galaxies) and the dark matter, the X-ray selection of clusters has the advantage of revealing physically-bound systems.

By integrating the emissivity over the energy range of the X-ray emission and over the gas distribution, we obtain typical values for the luminosity of the order of  $L_X \sim 10^{43} - 10^{45} \text{ erg s}^{-1}$ . Therefore, another advantage of X-ray selection of clusters is that given such powerful luminosities, clusters can be identified as extended sources out to large cosmological distances. Moreover, being the bremsstrahlung emissivity proportional to the square of the gas density ( $\epsilon_v^{ff} \propto n_e n_i \approx n_e^2$ ), and given the relatively low surface density of X-ray sources, a cluster in the X-ray band is observed as a peaked, high contrast signature of the central cluster regions.

On the other hand, the concentration of the X-ray emission could represent a problem for objects with faint flux and a proper detection algorithm should be used to distinguish clusters from point sources. An algorithm developed specifically to source detection and characterization in cluster surveys is based on wavelet techniques. This detection algorithm was designed to examine a broad range of cluster parameters (X-ray flux, surface brightness, morphology) and to deal with source confusion especially at faint flux levels. Moreover, a proper characterization of the telescope properties is crucial in order to detect sources and to distinguish point sources (mostly AGN and star-forming galaxies) from extended sources (galaxy clusters and groups).

Once we have identified clusters, in order to use them for cosmological applications, we need to evaluate the selection function of the survey. In order to define such selection function, we need to compute the specific sky coverage  $A(f(L, z))$ . This is defined as the *effective area* covered by the survey as a function of flux (see Figure 2.3). Because the exposure time, the background and the PSF<sup>1</sup> are not uniform across the field of view of

---

<sup>1</sup>The Point Spread Function describes the response of an imaging system to a point

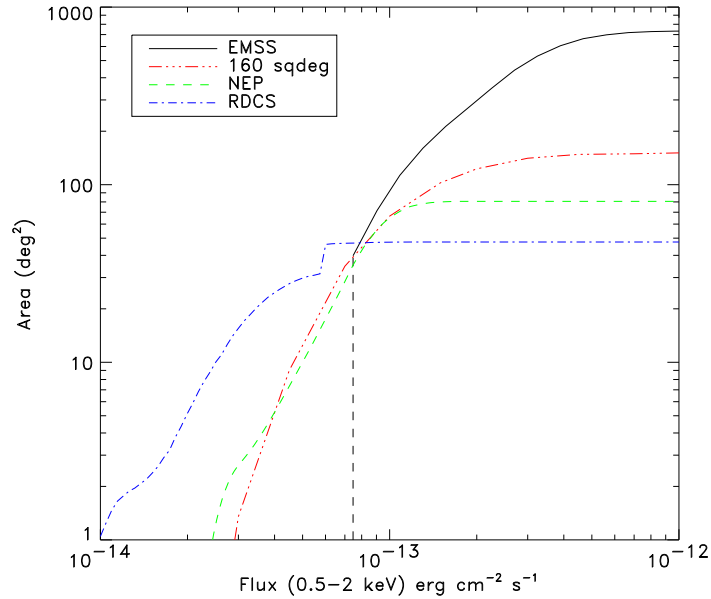


Figure 2.3: Sky coverage as a function of X-ray flux of several serendipitous surveys: the Einstein Observatory Extended Medium Sensitivity Survey (EMSS, solid black curve), the North Ecliptic Pole survey (NEP, dashed green curve), the ROSAT Deep Cluster Survey (RDCS, dot-dashed blue curve), and the 160 deg<sup>2</sup> survey (dot-dashed red curve). Figure from Rosati et al. (2002).

X-ray telescopes, effects such as reflectivity and vignetting cause the geometric area of a telescope to be reduced to a smaller effective area. The PSF degrades at increasing off-axis angles and, as a result, the sensitivity to source detection varies significantly across the survey area so that only bright sources can be detected over the entire solid angle of the survey, whereas at faint fluxes the effective area decreases. The background is contributed by two main components: a part is due to the internal or instrumental background and another part is due to unresolved astrophysical X-ray sources like cosmic X-ray background and Galactic X-ray background.

---

object or point source. In more general terms the observed image of each source is the result of the convolution between the PSF and the original image of the source. For extended sources the larger is the real image, the larger is the observed one with respect to the PSF. So an effective separation between point sources and extended sources must rely on a precise determination and characterization of the PSF as a function of the energy and the off-axis angle.

In order to be sure that the sample is complete, in all flux-limited samples of extended sources (e.g. optical galaxy surveys), one has to check that the sample does not become surface brightness (SB) limited at very faint fluxes. As the source flux decreases, clusters with smaller mean SB have a higher chance of being missed because their signal-to-noise ratio is likely to drop below the detection threshold. SB dimming at high redshifts ( $SB \propto (1+z)^{-4}$ ) can thus create a serious source of incompleteness at the faintest flux levels. This depends critically on the steepness of the SB profile of distant X-ray clusters and its evolution.

Once that the selection function is defined, it is possible to compute the maximum search volume,  $V_{max}$ , within which a cluster of a given luminosity is found in that survey:

$$V_{max} = \int_0^{z_{max}} A[f(L, z)] \left( \frac{d_L(z)}{1+z} \right)^2 \frac{c dz}{H(z)}. \quad (2.10)$$

In this equation  $A(f)$  is the survey sky coverage, and  $d_L(z)$  is the luminosity distance<sup>2</sup>,  $H(z)$  (Eq. 1.10) is the Hubble constant at  $z$ , and  $z_{max}$  is the maximum redshift out to which the flux of an object of luminosity  $L$  lies above the flux limit.

To date, there are no X-ray surveys which are not based on previous ROSAT observations and eventual optical follow-up to derive redshift and thus luminosities. The most recent constraints on cosmological parameters from clusters, are based on the *Chandra* follow-up of 400 deg<sup>2</sup> ROSAT serendipitous survey and of the All-Sky Survey (Vikhlinin et al., 2009a,b; Mantz et al., 2010a). Moreover X-ray surveys of clusters have been build from the compilation of serendipitous medium and deep-exposure extragalactic pointings from *Chandra* and *XMM-Newton* telescope (Boschin, 2002; Barkhouse et al., 2006; Pierre et al., 2011; Fassbender et al., 2011).

### X-ray redshift

Although all the advantages of X-ray selection of the galaxy clusters and the ability to define flux-limited sample, the main disadvantages of X-ray

---

<sup>2</sup>The luminosity distance,  $d_L$ , is defined by the relation between the flux  $f$  and the luminosity  $L$ :  $d_L \equiv \sqrt{L/(4\pi f)}$ . It turns out that this is related to the angular diameter distance  $d_A$  by  $d_L = (1+z)^2 d_A$  (Weinberg, 1972). This relation follows from the fact that the surface brightness of a receding object is reduced by a factor  $(1+z)^{-4}$ , and the angular area goes down as  $d_A^{-2}$ .

surveys is that it is still not possible to measure cluster redshifts from X-ray observations in a survey without recurring to time consuming follow-up. The detection of the Fe line could in principle provide a way to measure such redshifts in X-ray band. A few redshifts have been measured using X-ray spectral analysis (e.g. Lamer et al., 2008), and first studies confirm the agreements between X-ray and optical redshift (Bignamini, 2010). However this approach has never been used systematically in cluster surveys. The main reason is that most of the existing X-ray cluster surveys are based on source samples selected by ROSAT (e.g. Voges et al., 1999; Rosati et al., 1998), whose energy range is 0.1 – 2.4 keV, hence does not cover the hard band where the Fe lines lie (Yu et al., 2011). A systematic study of the methods and the limits in measuring X-ray based redshifts from archival *Chandra* observations of clusters at  $0.15 < z < 1.4$  has shown the power of this methodology (Yu et al., 2011). To date, most ROSAT clusters have been confirmed through optical imaging and spectroscopic observations. To make a landmark progress in this area a X-ray survey mission combining a large collecting area and good angular resolution over  $\sim 1 \text{deg}^2$  would be needed (Rosati et al., 2011). In particular, in Chapter 3, we will explain the case of the Wide Field X-ray Telescope, for which we have derived forecast for constraints on cosmological parameters.

### 2.2.3 Mass estimation: Cluster Scaling Relation

Assuming spherical symmetry, the condition of hydrostatic equilibrium connects the local gas pressure  $p$  to its density  $\rho_{gas}$  according to

$$\frac{dp}{dr} = -\frac{GM(< r)\rho_{gas}(r)}{r^2}. \quad (2.11)$$

By inserting the equation of state for a perfect gas,  $p = \rho_{gas} k_B T / \mu m_p$ , one can express  $M(< r)$ , the total gravitating mass within  $r$ , as

$$M(< r) = -\frac{k_B T r}{G \mu m_p} \left( \frac{d \log \rho_{gas}}{d \log r} + \frac{d \log T}{d \log r} \right). \quad (2.12)$$

The simplest model that explains the physics of the ICM is based on the assumption that gravity only determines the thermodynamical properties of the hot diffuse gas. Since gravity does not have a preferred scale, we expect clusters of different sizes to be the scaled version of each other

as long as gravity only determines the ICM evolution. This is the reason why the ICM model based on the effect of gravity only is said to be self-similar.

More specifically, the self-similar model for the ICM is based on the following assumptions:

- The internal structure of clusters of different mass is similar.
- All clusters identified at a given redshift have the same characteristic density that scales with the critical density of the Universe as:

$$\langle \rho \rangle = \frac{GM_{\Delta_c}}{R_{\Delta_c}^3} = \frac{4\pi}{3} \rho_c(z) \delta. \quad (2.13)$$

- The ICM evolves in the gravitational potential of the dark matter; the gas mass fraction is thus constant,  $f_{gas} = M_{gas} / M_{\Delta_c}$ .
- The ICM is in approximate hydrostatic equilibrium, allowing application of the virial theorem. This assumption imply that power-law relations exist between a X-ray observable,  $X$ , and the mass  $M$  at redshift  $z$ , such that  $X \propto A(z)M^\alpha$ . In this scenario the gas mass and total mass scale as  $M_{gas} \propto M_{\Delta_c} \propto T^{3/2}E^{-1}(z)$ . With the further assumption of bremsstrahlung emission, the X-ray luminosity scales as  $L_X \propto E(z)T^2$ .

In 2006, Kravtsov et al. proposed a new X-ray mass estimator: the quantity  $Y_X$  defined as

$$Y_X = T_X \times M_{gas}. \quad (2.14)$$

$Y_X$  approximates the total thermal energy of the ICM within  $R_{\Delta_c}$ , and also the integrated low-frequency Sunyaev-Zeldovich flux (Sunyaev & Zeldovich, 1972). The total thermal energy,  $Y_X$ , was found in simulations to be a very good indicator of the total cluster mass. In the simplest self-similar model  $Y_X$  scales with the cluster mass as

$$M_{\Delta_c} \propto Y_X^{3/5} E^{-2/5}(z) \quad (2.15)$$

Deviations with respect to the relations that have been derived in this Section witness the presence of more complex physical processes, beyond gravitational dynamics only, which affect the thermodynamical properties of the diffuse baryons and, therefore, the relation between observables and cluster masses.

Hydrodynamic simulations show that the expected scaling is valid. Moreover, the relation shows a smaller scatter in  $M_{\Delta_c}$  for fixed  $Y_x$  than, e.g., the  $M_{\Delta_c} - T_X$  relation. The primary reason is that the total thermal energy of the ICM is not strongly disturbed by cluster mergers. The  $M_{\Delta_c} - Y_X$  relation also appears to be not very sensitive to the effects of gas cooling, star formation, and energy feedback (Stanek et al., 2010; Fabjan et al., 2011). Gas cooling tends to remove from the ICM the lowest-entropy gas, increasing the average temperature of the remaining gas and thus affecting  $T_X$  and  $M_{gas}$  in opposite ways.

### 2.2.4 Phenomenological scaling relations

A number of observational determinations now exist, pointing toward a relation  $L_X \propto T^\alpha$ , with  $\alpha \simeq 2.5 - 3$  (Maughan et al., 2006), possibly flattening towards the self-similar scaling only for the very hot systems with  $T > 10$  keV. The scatter around the best-fitting relation, generally non negligible, is significantly reduced after excising the contribution to the luminosity from the cluster cooling regions (Maughan, 2007).

As for the  $L_X - M_\Delta$  relation, observation probed that exist a well defined relation between X-ray luminosity and mass (Figure 2.4), although with some scatter, thus confirming that  $L_X$  can be used as a proxy of the cluster mass. However, the slope of the relation is found to be steeper than the self-similar scaling, thus consistent with the observed  $L_X - T$  relation.

As for the  $Y_X - M_\Delta$  relation, Maughan (2007) found that it follow very closely the expected self-similar scaling also for unrelaxed clusters, since  $Y_X$  is so insensitive to the cluster dynamical state (Figure 2.5).

## 2.3 Clusters Microwave properties and surveys

The hot gas in galaxy clusters can be detected not only in the X-ray band but also in the microwave, through its effects on the CMB. The CMB spectrum is nearly a perfect black body spectrum with a temperature of about 2.7 K (Mather et al., 1990). Soon after the discovery of this background radiation, Weymann (1966) computed how the Compton scattering would distort its spectrum, shifting some of the microwave photons to higher energies as they passed through hot intergalactic gas. Then Sunyaev & Zeldovich (1970) predicted that ICM electrons would produce the distortions into the CMB spectrum. This phenomenon is

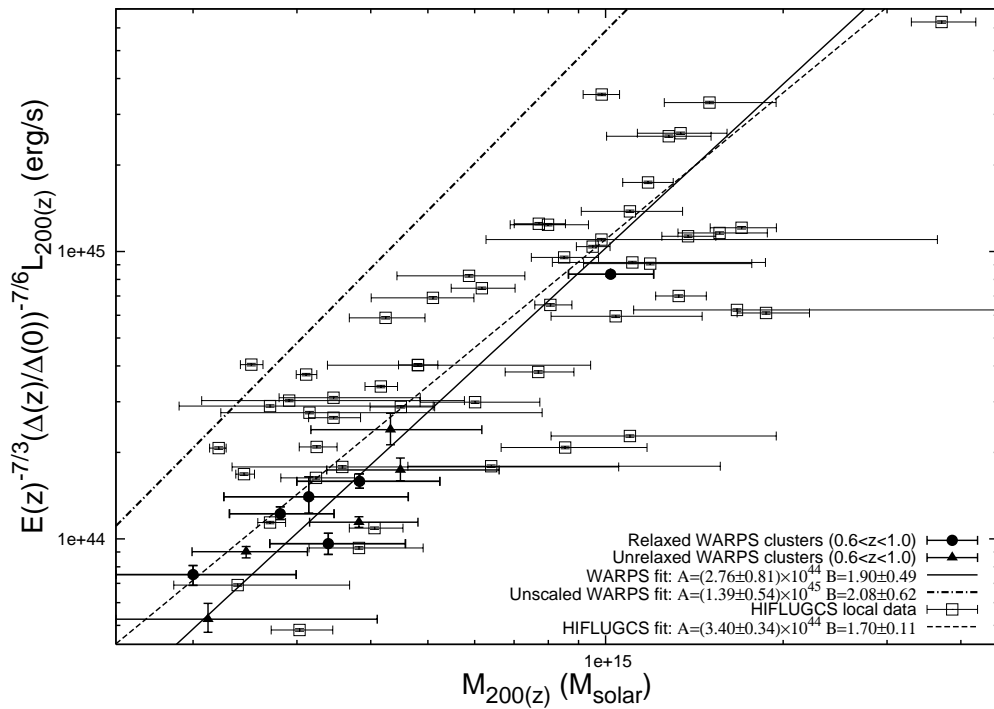


Figure 2.4:  $L_X - M_{200}$  relation for the low- $z$  HIFLUGCS clusters and the high- $z$  WARPS systems. Masses were measured within  $R_{200}$  assuming isothermality and luminosities within the same radius were scaled by the evolution predicted by the self-similar model. The dot-dashed line is the best fit to the unscaled high-redshift clusters and can be used to judge the significance of the self-similar scaling. Figure from Maughan et al. (2006)

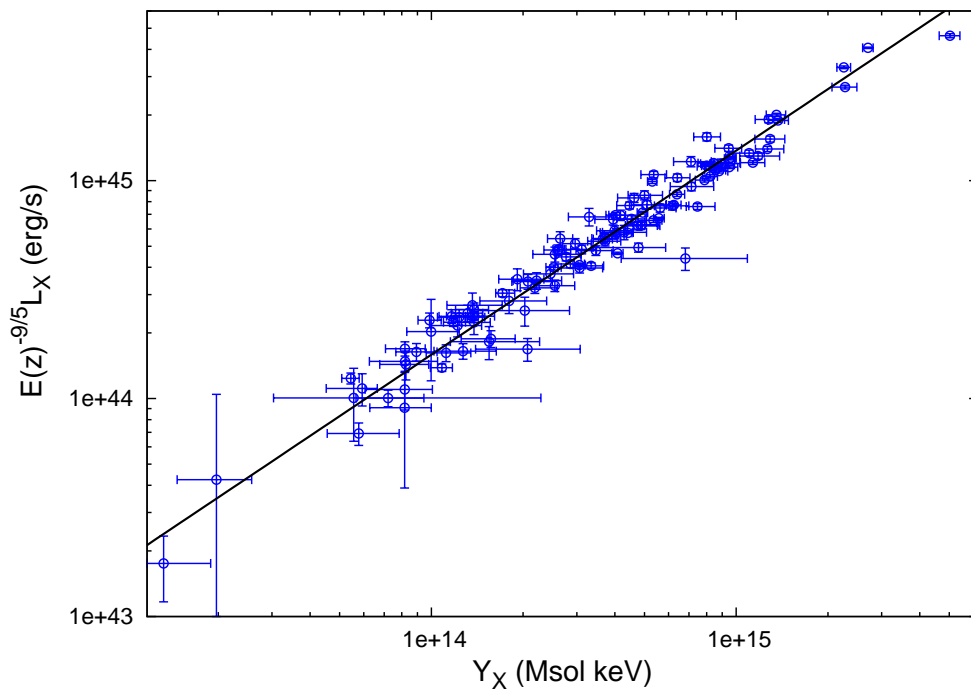


Figure 2.5: L-Y relation for bolometric luminosities measured in the ( $0.15 < r_{500} < 1$ ) aperture. Luminosities are scaled by the predicted self-similar evolution. Figure from Maughan (2007)

called SZ effect (for a full description of the SZ effect see Birkinshaw (1999); Narayan & Bartelmann (1996); Bartelmann (2010)). The SZ signal can be divided into a kinetic and a thermal effect, due to the cluster motion and the thermal motions of ICM electrons with respect to the microwave background, respectively. Since the kinetic SZ is a second-order effect, only the thermal one is considered in the follow.

To lowest order, the shape of the distorted spectrum depends on a single parameter proportional to the product of the probability that a photon passing through the cluster will suffer Compton scatter and the typical amount of energy gained by a scattered photon. Thus the so called Compton parameter can be read as:

$$y = \int \frac{k_B T}{m_e c^2} n_e \sigma_T dl , \quad (2.16)$$

where  $\sigma_T$  is the Thomson cross-section and the integral is over a line of sight through the cluster. Because the optical depth of the cluster is small, the change in microwave intensity at any frequency is linearly proportional to  $y \ll 1$ , with reduced intensity at long wavelengths and enhanced intensity at short wavelengths. The Compton parameter  $y$ , thus, measures the integral of the gas pressure along the line of sight and sets the amplitude of the SZ signal. This parameter does not suffer from cosmological surface brightness dimming, unlike the observation in the optical and X-ray bands.

Hence SZ surveys are expected to provide clean cluster samples over a wide range of redshifts, and can be considered in this sense close to an unbiased mass-limited selection sample. Currently the first SZ deep surveys covering hundreds of square degrees and capable of detecting many tens to hundreds of clusters, are performed by the South Pole Telescope (SPT; Carlstrom, 2006) and the Atacama Cosmology Telescope (ACT; Marriage & Atacama Cosmology Telescope Team, 2010). These surveys are accumulating data of first SZ selected new clusters and microwave observation of previously known clusters. Moreover, the Planck mission is now covering the entire sky, however, because clusters above  $z \sim 0.5$  have a typical angular size of  $1'$ , Planck's sensitivity to clusters will fall off at high redshift due to its larger beam ( $5'$  FWHM at 150 GHz versus  $1'$  for SPT and  $2'$  for ACT).

In Figure 2.6 it is shown a comparison between the limiting mass as a function of redshift, expected for an X-ray and for a SZ cluster survey. While the standard flux dimming with the luminosity distance,

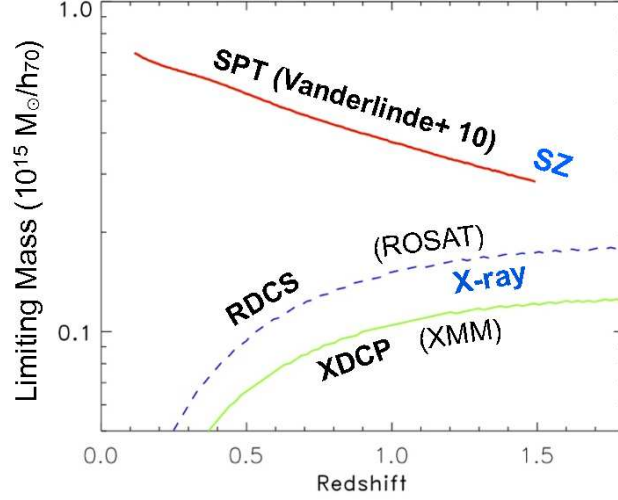


Figure 2.6: Minimum cluster virial mass detected in X-ray surveys (RDCS and XDCP) and in the SZ SPT survey.

$f_X \propto d_L^2(z)$ , causes the limiting mass to quickly increase with distance for the X-ray selection, this limiting mass has a much less sensitive dependence on redshift for the SZ selection. This is the reason why SZ surveys are generally considered as essentially providing mass-limited cluster samples.

### 2.3.1 SZ-Mass scaling relation

From the Compton parameter  $y$ , it is possible to define the integrated SZ signal parameter

$$Y_{SZ} = \int y dA \propto \int n_e T dV, \quad (2.17)$$

that describes the total thermal energy of the electrons, from which one can derive the total gas mass times its the electron temperature within a given region of space. Assuming that thermal energy results solely from gravitational collapse, it is possible to derive self-similar scaling between  $Y_{SZ}$  and cluster mass. Assuming virial and hydrostatic equilibrium, the cluster gas temperature can be related to the mass as explained in Section

2.2.3. Under assumptions of an isothermal ICM,

$$Y_{SZ} \propto d_A^{-2}(z) M T \propto d_A^{-2} M^{5/3} E(z)^{2/3}. \quad (2.18)$$

where  $d_A(z)$  is the angular diameter distance to the cluster.

Figure 2.7 shows  $Y_{200,m} d_A^2 E^{-2/3}$  against halo mass  $M_{200,m}$  (Hand et al., 2011). The expected  $Y_{SZ}$ -M relation as determined from numerical simulations is shown as a solid line and is given by

$$Y_{200,m} d_A^2 E^{-2/3} = 10^{-\gamma} \left( \frac{M_{200,m}}{10^{14} M_\odot} \right)^\alpha, \quad (2.19)$$

where the best-fit parameters are  $\alpha = 1.76$  and  $\gamma = 5.74$ . These parameters are obtained from the microwave sky simulations described in Sehgal et al. (2010), where halos of mass  $M_{200,m} > 2.82 \times 10^{13} M_\odot$  have been considered, and the redshift range of the clusters is  $0.15 < z < 0.50$ . The data are obtained from subset of the ACT 2009 equatorial data at the positions of luminous red galaxies (LRGs) measured by the Sloan Digital Sky Survey (SDSS) (Hand et al., 2011). The overall normalization of the Y-M relation appears lower than expected. As the SZ effect traces the thermalized cluster pressure, the possibility exists that there are significant non-thermal pressure components supporting the halo mass. Moreover, because the SZ signal is proportional to the total thermal energy of a cluster and is thus less affected by physical processes in the cluster core the scatter in the Y-M is of order 5 – 10% according to simulation provided by Sehgal et al. (2010).

The power of the SZ effect for finding distant clusters suffer from an important drawback, the contamination of the signal from foreground/background structures. Along any line of sight through the entire observable universe, the probability of passing within the virial radius of a cluster or group of galaxies is of order unity (e.g. Voit et al., 2001). In particular, small halos are not resolved in current SZ observations and their integrated contribution may provide a significant contamination. Using cosmological hydro-dynamical simulations, it has been shown that the scatter in the Y-M relation is significantly increased in projection (White et al., 2002). Part of the scatter is due to the different redshifts at which clusters seen in projection are placed. This contribution to the scatter can be removed once redshifts of clusters are known. Unfortunately it is not possible to measure the redshift of a cluster from the SZ survey and a optical or X-ray follow-up observation are always necessary.

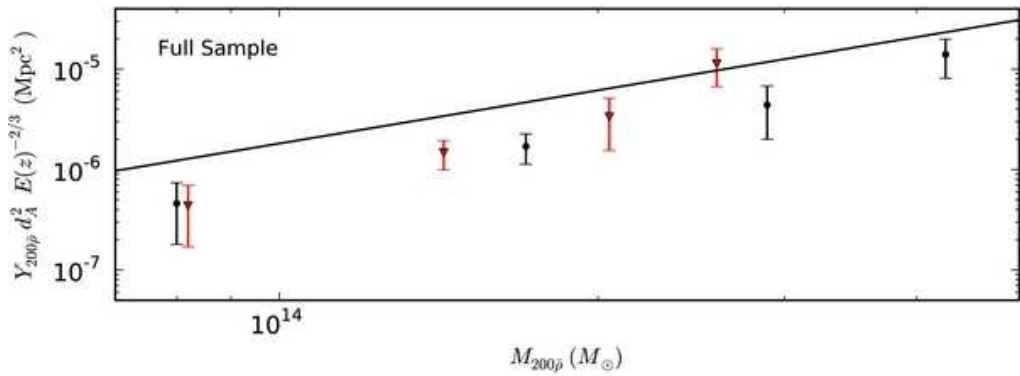


Figure 2.7:  $Y_{200,m}$  is plotted against cluster masses for each luminosity bin for stacking of a subset of the ACT 2009 equatorial data at the positions of luminous red galaxies (LRGs) measured by the Sloan Digital Sky Survey (SDSS). The two sets of points shown use separate mass estimates for the four LRG luminosity bins. The black circles correspond to mass estimates derived from analysis of halo bias. The red triangle correspond to mass estimates derived from weak gravitational lensing measurements (Reyes et al., 2008). The solid line shows the expected model for the Y-M relation as determined from the microwave sky simulations of Sehgal et al. (2010). Figure from Hand et al. (2011).

## Chapter 3

# Forecasting cosmological constraints from future cluster surveys

As discussed in Chapter 1, clusters of galaxies have long been recognized as potentially powerful probes of the nature of DE and cosmological models in general (e.g. Allen et al., 2011; Lombriser et al., 2010). In Section 1.10, we summarized constraints obtained from clusters on cosmological parameters over the last decade. Within the non-Gaussian scenario for the initial perturbation density field, at present, analyses of the CMB data provide the tightest upper limits on deviation from Gaussianity. Such analyses based on the WMAP experiment converge to indicate consistency with the Gaussian assumption (e.g., Komatsu et al. (2011) and references therein; see also Yadav & Wandelt (2008)). In the context of galaxy clusters, Jimenez & Verde (2009) have analysed the effect of non-Gaussianity on the population of massive high-redshift clusters, like the one discovered by Jee et al. (2009) at  $z \simeq 1.4$ .

While the first Sunyaev-Zeldovich (SZ) surveys have now started producing cluster samples, (e.g., Marriage & the ACT Team, 2011; Williamson & the SPT Team, 2011; Planck Collaboration, 2011), the next generation of X-ray and optical surveys like the forthcoming eROSITA<sup>1</sup>, DES<sup>2</sup>, and EUCLID<sup>3</sup> satellites will increase by orders of magnitude the statistics of detected clusters further extending the redshift range over which they trace the growth of

---

<sup>1</sup><http://www.mpe.mpg.de/heg/www/Projects/erosita/index.php>

<sup>2</sup><http://www.darkenergysurvey.org/>

<sup>3</sup><http://sci.esa.int/science-e/www/area/index.cfm?fareaid=102>

cosmic structures. Future higher sensitivity X-ray telescopes, such as the proposed Wide Field X-ray Telescope (WFXT)<sup>4</sup> will have the capability of measuring mass proxies for such clusters out to  $z \sim 2$ . Such large cluster surveys have the potential of placing very tight constraints on different classes of DE models, and possibly finding signatures of departures from the Gaussian prescription for the initial density fluctuation field.

In view of these future large surveys to be carried out with the next generation of telescopes, it is crucial to quantify the constraining power of such surveys, and to understand the optimal survey design to best constraint specific classes of cosmological models.

### 3.1 Forecasts on DE models

Several studies have dealt with constraints of DE models from future cluster surveys focusing on the impact of uncertainties in cluster mass estimates (e.g. Battye & Weller, 2003; Majumdar & Mohr, 2004; Lima & Hu, 2005, 2007; Cunha, 2009; Cunha & Evrard, 2010; Basilakos et al., 2010). All these analyses generally assume that, when a cluster is identified and included in a survey, the observable (i.e., X-ray flux, optical richness) on which the detection is based can be related to the actual cluster mass through a suitable relation, whose functional form is assumed to be known and depends on a set of additional parameters.

A more conservative approach would instead require that for all the clusters included in a survey detailed follow-up observations are carried out to calibrate suitable and robust mass proxies. As for X-ray surveys, such proxies can be computed when a relatively large number of photons is available. For instance, while measuring flux for an X-ray extended source requires only  $\sim 50$  photons, or less for missions with low background, the measurement of robust mass proxies require  $\sim 10^3$  photons. The possibility to define a flux-limit down to which measuring accurate mass proxies for all clusters allows one to set robust priors on the scaling relations between cluster mass and observables, which is one of the main source of uncertainty in the cosmological application of galaxy clusters (e.g., Albrecht et al., 2009).

In this Chapter, we will derive forecasts for constraints on cosmological parameters focusing on the EoS of DE ones, as obtained from future X-ray and optical surveys. The X-ray surveys are the ones to be carried

---

<sup>4</sup><http://www.wfxt.eu/>

out with a telescope (WFXT), see Section 3.4) with high-enough sensitivity to readily provide robust measurements of mass proxies for  $\gtrsim 10^4$  clusters. The great advantage of having a similar survey is that there is no need to assume any external follow-up observation to measure mass proxies and cluster redshift for a large subset of identified clusters.

Adopting the specifications of the WFXT surveys, we compute cosmological forecasts using the well-established Fisher Matrix approach (e.g., Dodelson, 2003), to combine information from cluster number counts and large-scale clustering. We will quantify the constraints expected on DE models and their dependence on the knowledge of the relation between X-ray observables and cluster mass, for a range of survey strategies (i.e. depth vs. sky coverage).

In the course of this study, we will discuss how number counts and the power spectrum of the large-scale distribution of clusters convey cosmological information. We will show how the detection of Baryonic Acoustic Oscillations (BAOs) and redshift space distortions (RSDs) on cluster scales can significantly contribute to constrain cosmological parameters, similarly to a number of previous studies based on the large scale distribution of galaxies (e.g., Guzzo et al., 2008; Rassat et al., 2008; Stril et al., 2010; Wang et al., 2010).

We will compare the results obtained with WFXT surveys with cosmological constraints provided by EUCLID mission (Laureijs et al., 2011) based on unprecedented optical/near infrared imaging and spectroscopic survey (see Section 3.5). The imaging channel of this experiment will measure the shapes over a billion galaxies, while a slitless spectroscopic survey will yield accurate redshifts of tens of millions of galaxies. Photometric redshifts will also be available with combination of NIR EUCLID photometry and ground-based optical photometry, and will be calibrated with  $10^7$  spectroscopic redshifts. This data set will also be very effective in finding clusters at  $z \approx 0.5 - 2$ , whose masses will be calibrated with a combination of EUCLID-based weak gravitational lensing measurements and dedicated follow-up programs.

### 3.1.1 DE models.

As for the DE EoS, the reference analysis will be carried out for the standard parametrization, originally proposed by Linder (2003),

$$w(a) = w_0 + w_a(1 - a), \quad (3.1)$$

where  $a$  is the cosmic expansion factor. This parametrization has been used in the Dark Energy Task Force reports (DETF; Albrecht et al., 2006, 2009) to assess the constraining power of different cosmological experiments. We will refer to this hereafter as *standard DE model*.

Albrecht et al. (2006) presented forecasts on the constraints on the  $w_0$  and  $w_a$  parameters from redshift number counts of cluster surveys. Mantz et al. (2010a) derived constraints on these parameters from the observed evolution of the cluster X-ray luminosity function, using a combination of nearby clusters selected from the RASS (Truemper, 1993; Ebeling et al., 1998; Böhringer et al., 2004) and medium-distant clusters selected from the (RASS based) MACS survey (e.g. Ebeling et al., 2010). An update on the constraints available at present on these parameters has been presented by Komatsu et al. (2011) using a combination of the 7-year WMAP CMB data, SN-Ia, Big-Bang Nucleosynthesis results and BAOs traced by the large-scale galaxy distribution.

Furthermore, we will also assess the constraining power of X-ray cluster surveys for the class of quintessence models, called Early Dark Energy (EDE) (Wetterich, 2004). In these models, DE drives not only the accelerated expansion of the Universe at relatively low redshift, but also provides a non-negligible contribution at early times, i.e. before the last scattering surface (Doran & Wetterich, 2003). A parametrization of a class of EDE models has been proposed by Wetterich (2004) as a function of the amount of DE at  $z = 0$ , the present equation of state parameter,  $w_0$ , and an average value of the energy density parameter at early times,  $\Omega_{DE}$ . The EoS parametrization that we choose is the one studied by Grossi & Springel (2009):

$$w(z) = \frac{w_0}{(1 + C \ln(1 + z))^2}. \quad (3.2)$$

In the above relation the quantity  $C$  is given by

$$C = \frac{3w_0}{\ln\left(\frac{1-\Omega_{e,de}}{\Omega_{e,de}}\right) + \ln\left(\frac{1-\Omega_{m,0}}{\Omega_{m,0}}\right)}, \quad (3.3)$$

and characterizes the redshift at which a constant EoS turns into a different behaviour according to the presence of DE at early times. Since both EDE and  $\Lambda$ CDM models have to reproduce the observed cluster abundance at low redshift, in EDE models we expect structures to form earlier and to have slower evolution of the halo population that in the  $\Lambda$ CDM one.

Alam et al. (2011) used the EDE parametrization by Corasaniti & Copeland (2003) to forecast constraints on these models from the abundance of X-ray clusters expected in the eROSITA survey (e.g. Predehl et al., 2007) and from the SZ power spectrum from the South Pole Telescope (SPT, Staniszewski et al., 2009). In our analysis, we use a different parametrization of EDE models, derive forecasts for high-sensitivity X-ray surveys, and particularly include the constraints from the redshift-space power spectrum of the large-scale distribution of clusters.

### 3.2 Forecast on Non-Gaussian primordial density fluctuations

Future surveys should cover a large enough volume at high redshift to test non-Gaussianity in the regimes where its effects are clearer, namely the high-mass tail of the mass function and the large-scale power spectrum of the cluster distribution. Oguri (2009) followed the self-calibration approach by Lima & Hu (2005) (see also Majumdar & Mohr, 2004) to forecast the capability of future optical cluster surveys to constrain non-Gaussian models. This study showed that combining number counts and clustering of galaxy clusters can potentially provide quite strong constraints on deviations from Gaussianity. Fedeli et al. (2009) and Roncarelli et al. (2010) presented predictions from the eROSITA X-ray survey and from the Sunyaev-Zeldovich SPT survey. While their analyses confirmed the potential of these surveys to provide interesting constraints on non-Gaussian models, they did not include detailed forecasts on the constraints on non-Gaussian models and a detailed assessment of the effect of uncertainties in the scaling relations between cluster masses and observables. A further study from Pillepich et al. (2011) used Fisher-Matrix analysis to forecast constraining power of eROSITA on the cosmological parameters together with the X-ray mass-observable scaling relations.

We derive forecasts, based on the Fisher-Matrix approach, on the capability of future cluster surveys to constrain deviations from Gaussian perturbations. Our analysis differs from that by Oguri (2009) for the method to include information from large-scale clustering. Oguri (2009) adopted the approach by Lima & Hu (2005) where clustering is included by accounting for fluctuations of cluster counts within cells having a fixed

angular size. This implies that, at each redshift, clustering information is restricted to one physical scale. In our analysis, we follow the approach originally presented by Tegmark (1997) (see also Feldman et al. 1994; Majumdar & Mohr 2003), in which the clustering Fisher-Matrix is computed for the allowed range of wavenumbers, by weighting them according to the effective volume covered by the surveys.

In principle, the method used in our analysis can be applied to any cluster surveys, including SZ ones. Our method only requires a well defined selection function and calibrated mass proxies. The results presented in this Chapter have been published in two papers on the “Monthly Notices of the Royal Astronomical Society”: Sartoris et al. (2010) and Sartoris et al. (2011). Moreover, the analysis carried out for the EUCLID mission has been included in the Mission Definition Document and will be part of a paper in preparation.

### 3.3 The analysis method

We use the Fisher Matrix (FM hereafter) formalism to understand how accurately we can estimate the values of a vector of parameters  $\theta$  for a given model from one or more data sets, under the assumption that all parameters follow a Gaussian distribution (e.g., Cash, 1979) (see Appendix A).

The information FM is defined (e.g. Heavens, 2009; Dodelson, 2003) as

$$F_{\alpha\beta} \equiv - \left\langle \frac{\partial^2 \ln \mathcal{L}}{\partial \theta_\alpha \partial \theta_\beta} \right\rangle, \quad (3.4)$$

where  $\mathcal{L}$  is the likelihood of an observable, in our case the number of galaxy clusters in a given redshift and mass range or the averaged power spectrum of the cluster distribution.

#### 3.3.1 Number counts

Following the approach of Holder et al. (2001) and Majumdar & Mohr (2003), the FM for the number density of clusters,  $N_{l,m}$ , within the  $l$ -th redshift bin and  $m$ -th bin in observed mass  $M^{ob}$ , can be written as

$$F_{\alpha\beta}^N = \sum_{l,m} \frac{\partial N_{l,m}}{\partial p_\alpha} \frac{\partial N_{l,m}}{\partial p_\beta} \frac{1}{N_{l,m}}, \quad (3.5)$$

where the sums over  $l$  and  $m$  run over redshift and mass intervals, respectively. With this notation, it is  $M_{l,m=0}^{ob} = M_{\text{thr}}(z)$ , where  $M_{\text{thr}}(z)$  is defined as the threshold value of the observed mass for a cluster to be included in the survey. According to the specific selection function of each specific survey, the value of  $M_{\text{thr}}(z)$  generally depends on redshift (see Figures 3.2 and 3.5). In this case, the number of mass bins can change with redshift accordingly.

We write the number of clusters expected in a survey having a sky coverage  $\Delta\Omega$  with observed mass between  $M_{l,m}^{ob}$  and  $M_{l,m+1}^{ob}$  and redshift between  $z_l$  and  $z_{l+1}$  as

$$N_{l,m} = \Delta\Omega \int_{z_l}^{z_{l+1}} dz \frac{dV}{dz d\Omega} \int_{M_{l,m}^{ob}}^{M_{l,m+1}^{ob}} \frac{dM^{ob}}{M^{ob}} \int_0^\infty dM n(M, z) p(M^{ob} \| M). \quad (3.6)$$

In the above equation  $dV/(dz d\Omega)$  is the cosmology-dependent comoving volume element per unity redshift interval and solid angle,  $n(M, z)$  the mass function, i.e. the number density of clusters with true mass  $M$  at redshift  $z$  (see Section 1.5).

We assume in the following the expression by Tinker et al. (2008) for the halo mass function in the case of Gaussian perturbations. We stress that while using the best-calibrated mass function is in fact important when deriving cosmological constraints from real data (e.g., Wu et al., 2009), it has only a minor impact when deriving forecasts on cosmological constraints. Indeed, what matters for the latter is the total number of clusters expected in a given cosmological model, which is far more sensitive to the choice of reference cosmological and observable-mass relation parameters than to the details of the fitting function.

As for the case of non-Gaussian perturbations, Grossi et al. (2009) have shown that analytic expressions of the cluster mass function provided by Matarrese et al. (2000) and LoVerde et al. (2008) are in agreement with N-body cosmological simulations, when the linear threshold for collapse is corrected for ellipsoidal density perturbations, according to  $\Delta_c \rightarrow \Delta_c \sqrt{q}$ , with  $q = 0.75$ . We adopted this correction when we calculate forecasts for constraints on deviations from Gaussianity.

Following Lima & Hu (2005), we assign to each cluster with true mass  $M$  a probability  $p(M^{ob} \| M)$  of having an observed mass  $M^{ob}$ , as inferred from a given mass proxy. Under the assumption of a log-normal distribution for the intrinsic scatter in the relation between true and observed

mass, with variance  $\sigma_{\ln M}^2$ , the expression for this probability is

$$p(M^{ob}||M) = \frac{\exp[-x^2(M^{ob})]}{\sqrt{(2\pi\sigma_{\ln M}^2)}}, \quad (3.7)$$

where

$$x(M^{ob}) = \frac{\ln M^{ob} - B_M - \ln M}{\sqrt{(2\sigma_{\ln M}^2)}}. \quad (3.8)$$

We characterize the relation between true and observed mass not only with an intrinsic scatter, but also with a systematic bias in the mass estimate, whose fractional value is given by  $B_M$ . By inserting Eq.(3.7) into Eq.(3.6) for the cluster counts in a given mass and redshift interval, we obtain

$$N_{l,m} = \frac{\Delta\Omega}{2} \int_{z_l}^{z_{l+1}} dz \frac{dV}{dzd\Omega} \int_0^\infty dM n(M, z) \times [\text{erfc}(x_m) - \text{erfc}(x_{m+1})] \quad (3.9)$$

with  $x_m = x(M_{l,m}^{ob})$  and  $\text{erfc}(x)$  the complementary error function.

We note that the possibility of factorising the sky-coverage outside the integration in Eq. 3.9 relies on the assumption that clusters are detected over the same area of the sky down to the survey completeness limit. The above expression can be easily generalized to include the possibility of a flux dependent sky coverage.

We remark that we neglect clustering contribution to the noise (i.e. cosmic variance) for all the surveys considered in our analysis.

Finally, we assume that errors on the cluster redshift measurements can be ignored (see Lima & Hu 2007 for a presentation of a method to include the effect of redshift errors in the computation of the FM for cluster number counts).

### 3.3.2 Power spectrum

In order to include in our analysis the information from the clustering of galaxy clusters, we follow the approach by Majumdar & Mohr (2004). We define the Fisher Matrix for the power spectrum of galaxy clusters as

$$F_{\alpha\beta} = \frac{1}{(2\pi)^2} \sum_{i,l,m} \frac{\partial \ln \bar{P}_{cl}(k_m, z_l, \mu_i)}{\partial p_\alpha} \frac{\partial \ln \bar{P}_{cl}(k_m, z_l, \mu_i)}{\partial p_\beta} V_{l,m}^{eff} k_m^2 \Delta k \Delta \mu, \quad (3.10)$$

where the sums in  $l$  and  $m$  run over redshift and wavenumber  $k$  bins, respectively, and the sum in  $i$  run over the angle  $\mu$  (Tegmark, 1997; Feldman et al., 1994). The quantity  $\mu$  is the cosine of the angle that  $\mathbf{k}$  makes with the line of sight. As we explained in Section 1.7, the power spectrum gains this an angular dependence when we take into accounts the effect of the Redshift Space Distortions. In the above equations  $\bar{P}_{cl}$  is the average cluster power spectrum calculated within the given redshift interval,

$$\bar{P}^{cl}(k_m, z_l, \mu_i) = \frac{\int_{z_l}^{z_{l+1}} dz \frac{dV}{dz} \tilde{N}^2(z) P^{cl}(k, z, \mu)}{\int_{z_l}^{z_{l+1}} dz \frac{dV}{dz} \tilde{N}^2(z)}. \quad (3.11)$$

where  $\tilde{N} = \int_0^\infty dM n(M, z) [\text{erfc}(x_m) - \text{erfc}(x_{m+1})]$ . This amounts to weight the cluster power spectrum,  $P^{cl}(k, z, \mu)$ , according to the square of the number density of clusters,  $N(z)$ , that are included in the survey at redshift  $z$ . This linear bias in Eq. 1.49 is weighted here by the mass function and defines the effective bias

$$b_{eff}(z, k) = \frac{\int_0^\infty dM n(M, z) \text{erfc}[x(M_{thr})] b(M, z, k)}{\int_0^\infty dM n(M, z) \text{erfc}[x(M_{thr})]}. \quad (3.12)$$

For the linear bias, we assume in the analysis the prescription from Tinker et al. (2010). The bias  $b(M, z, k)$  acquires the dependence on the wavenumber  $k$  in case of non-Gaussian models (see Section 1.9). In order to obtain agreement with the results of numerical simulations it is necessary to correct the linear overdensity for collapse, this time according to  $\Delta_c \rightarrow \Delta_c q$  with  $q = 0.75$  (Grossi et al., 2009). Semi-analytic results, with this correction, are also in agreement with the numerical results by Pillepich et al. (2010) (see also Desjacques et al. 2009). We adopted this correction in the non-Gaussian forecasts calculation.

Finally, the quantity  $V^{eff}(k, z)$  in Eq.(3.10) is the effective volume accessible by the survey at redshift  $z$  at wavenumber  $k$ . This effective volume is weighted by the shot noise level  $1/N(z)$ , so that

$$V^{eff}(k, z) = V_0(z) \left[ \frac{\tilde{N}(z) \bar{P}_{cl}(k, z, \mu)}{1 + \tilde{N}(z) \bar{P}_{cl}(k, z, \mu)} \right]^2, \quad (3.13)$$

with  $V_0(z)$  the total comoving volume covered by the redshift bin centred on  $z$ . In this way, constraints at redshift  $z$  are mostly contributed by wave modes  $k$ , which maximize  $\tilde{N}(z) \bar{P}_{cl}(k, z)$  and make  $V^{eff}$  approach  $V_0$ .

An alternative approach to include clustering information in deriving FM survey forecasts has been proposed by Lima & Hu (2005) and applied also by Oguri (2009) for constraints on non-Gaussian models from cluster surveys. In this approach, one makes a partition of the sky area covered by a survey into regular cells of a fixed angular size and then computes the fluctuations in the cluster counts within such cells. Since this method does not explicitly include the covariance between counts within different cells, it only samples clustering at a fixed angular scale (i.e. at a single physical scale for a fixed redshift). On the other hand, extracting the full information content in the scale dependence of the power spectrum is quite important when constraining non-Gaussian models, whose unique signature is given by the scale-dependent bias. Cunha & Evrard (2010) used the count-in-cell approach by also including the information from the covariance. Therefore, the information on the large-scale power spectrum, in the count-in-cell approach, is conveyed by the covariance terms. In our approach the different scales are weighted by the effective volume, defined by Eq.(3.13).

As for the power spectrum transfer function, we adopt the expression for Cold Dark Matter provided by Eisenstein & Hu (1998), which includes the effect of baryonic acoustic oscillations (BAOs). In order to quantify the information carried by the BAO detection, we use also, where specified, the power spectrum shape from Eisenstein & Hu (1998), which smoothly interpolates through the oscillations. Moreover, we study the geometric information carried by the shape of the power spectrum by describing it with a general free parameter  $\Gamma$ , and thus ignoring its CDM specific relation  $\Gamma = \Omega_m h$ .

### 3.3.3 Reference values for the cosmological parameters

We assume the following reference values for the cosmological parameters, consistent with the WMAP-7 best-fitting model (Komatsu et al., 2011):  $\Omega_m = 0.28$  for the present-day matter density parameter,  $\sigma_8 = 0.81$  for the normalization of the power spectrum,  $\Omega_k = 0$  for the contribution from the curvature,  $\Omega_b = 0.046$  for the contribution of baryons to the density parameter,  $h = 0.70$  for the Hubble parameter,  $n = 0.96$  for the primordial spectral index and  $f_{\text{NL}} = 0$  for the non-Gaussianity parameter. For the DE EoS parametrization of Eq. 3.1, we take  $w_0 = -0.99$  and  $w_a = 0$  as reference values, while for the EDE model of Eq. 3.2

we assumed the reference values of  $w_0 = -0.93$  and  $\Omega_{e,de} = 2 \cdot 10^{-4}$  (Grossi et al., 2009). We point out that for the reference EDE model, we adopt the same values of the non-DE parameters, including  $\sigma_8$ . This implies that both models are chosen to have the same low-redshift normalization as to provide the same cluster number counts (see also Figure 3.8), instead of being normalized to CMB. Therefore, we have in total nine cosmological parameters, which are left free to vary in the computation of the number counts and power spectrum Fisher Matrices defined in Eqs. (3.5) and (3.10).

### 3.3.4 Planck CMB experiment

Where stated, the results presented in the following are based on adding the Fisher Matrix for the Planck CMB experiment to those from the cluster surveys. This prior probability has been computed for each the two reference DE models based on Eqs. (3.1) and (3.2). We derive the cosmological constraints from Planck following the description laid out by the DETF Albrecht et al. (2009) and use the method described in Rassat et al. (2008). We conservatively assume that we will only use the 143 GHz channel as science channel. This channel has a beam of  $\theta_{\text{fwhm}} = 7.1'$  and sensitivities of  $\sigma_T = 2.2 \mu\text{K}/\text{K}$  and  $\sigma_P = 4.2 \mu\text{K}/\text{K}$ . We take  $f_{\text{sky}} = 0.80$  as the sky fraction in order to account for galactic foregrounds. We use as a minimum  $\ell$ -mode,  $\ell_{\text{min}} = 30$  in order to avoid problems with polarization foregrounds. As described in the DETF report (Albrecht et al., 2009), we choose as fiducial parameter set  $\vec{\theta} = (\omega_m, \theta_S, \ln A_S, \omega_b, n_S, \tau)$ , where  $\theta_S$  is the angular size of the sound horizon at last scattering,  $\ln A_S$  is the logarithm of the primordial amplitude of scalar perturbations and  $\tau$  is the optical depth due to reionization. After marginalization over the optical depth, we then calculate the Planck CMB Fisher matrix in the parameters  $(\Omega_m, \Omega_{de}, h, \sigma_8, \Omega_b, \mathbf{w}, n_S)$  by using the appropriate Jacobian of the involved parameter transformation (Rassat et al., 2008). Here  $\mathbf{w}$  is a two-component vector which includes the parameters of the two DE models considered:  $\mathbf{w} = (w_0, w_a)$  for the model of Eq. 3.1 and  $\mathbf{w} = (w_0, \Omega_{e,de})$  for the model of Eq. 3.2.

We point out that the Planck FM is computed for Gaussian perturbations. Therefore, while it adds quite strong constraints on the other cosmological parameters, especially on the curvature, it does not add any constraints on  $f_{\text{NL}}$ .

### 3.4 Characteristics of the WFXT surveys

We derive here forecasts for different X-ray surveys inspired to the strategy devised for the Wide Field X-ray Telescope (WFXT<sup>5</sup>), proposed to the Astro-2010 Decadal Survey panel (e.g. Murray & WFXT Team, 2010; Giacconi et al., 2009; Rosati et al., 2011; Borgani et al., 2011). The WFXT mission is designed to be 2-orders-of-magnitude more sensitive than any previous or planned X-ray mission for large area surveys and to match in sensitivity the next generation of wide-area optical, IR and radio surveys.

Using an innovative wide-field X-ray optics design (Burrows et al., 1992), WFXT provides a Field of View (FoV) of  $1 \text{ deg}^2$  (more than ten times *Chandra's* one), with an angular resolution of  $5''$  (Half Energy Width, HEW) nearly constant over the FoV, and a large collecting area (up to  $1 \text{ m}^2$  at 1 keV, nearly ten times the collecting area of *Chandra*) over the  $0.1 - 7 \text{ keV}$  band.

A HEW  $\approx 5''$  allows AGN/cluster discernment at any redshift, and enables confusion-free deep imaging. Moreover with such HEW it is possible to resolve cool cores of  $z > 1$  clusters (Santos et al., 2011), and to detect sharp features like shocks, cold fronts, and cavities in the ICM.

Combined with the large collecting area, WFXT sensitivity enables physical characterization of large samples of sources via their spectral analysis and allows to trace the mass function of clusters and AGN over a large range of masses and redshifts. Thus, WFXT would address many outstanding cosmological and astrophysical objectives: formation and evolution of clusters of galaxies and associated implications for cosmology and fundamental physics (e.g. the nature of Dark Matter, Dark Energy and gravity); black-hole formation and evolution; AGN interaction with the ICM and the Intrastellar Medium (ISM) in clusters and galaxies; and the high-energy stellar component and hot-phase ISM of galaxies, including the Milky Way.

In five years of operation, according to Giacconi et al. (2009), WFXT will carry out three extragalactic surveys: a Wide Survey, which will cover all the extragalactic sky ( $20000 \text{ deg}^2$ ) with a sensitivity  $\sim 500$  times better than the ROSAT All Sky Survey (RASS, e.g. Voges et al., 1999); a Medium Survey, which will reach over  $3000 \text{ deg}^2$  flux limits comparable to those of the deep *Chandra* and *XMM-Newton* deep COSMOS fields (Cappelluti et al., 2009); a Deep Survey that will reach over  $100 \text{ deg}^2$  a

---

<sup>5</sup><http://www.wfxt.eu/home/Overview.html>, <http://wfxt.pha.jhu.edu/>

sensitivity similar to those of the deepest *Chandra* pointings.

Based on the results presented by Giacconi et al. (2009), the left columns of Table 3.1 contains the limiting fluxes (in the 0.5-2 keV energy band) at which WFXT will detect a cluster as an extended source in the three surveys. We will refer to the cluster samples built from these limiting fluxes as *Detection Sample*.

At flux limits listed in the right column of Table 3.1 clusters are detected with at least 1500 photons. These high quality data enable a direct measurement of the mass proxies, and allow cluster redshifts to be measured from the Fe-K 6.7 keV line in the X-ray spectra (see Section 2.2) with a precision of  $\Delta z \lesssim 0.01$  (Yu et al., 2011), without resorting to demanding optical spectroscopic follow-up campaigns. Such higher flux limits define what we call in the following the *Bright Sample*.

### 3.4.1 Surveys mass thresholds.

In principle, a unique flux limit is not sufficient to define a completeness criterion in an X-ray survey. In fact, due to vignetting and PSF variation with off-axis angle, the flux limit for the detection of a source at a given signal-to-noise varies across the field of view. For this reason, rather than a flux limit, one should calibrate a flux-dependent sky coverage. Owing to the approximate uniformity of the WFXT PSF, we expect such a sky coverage to be steep around the flux limits reported in Table 3.1, so that we ignore its flux-dependence in the following analysis. In order to convert the flux limits into mass limits, we use the relation between X-ray luminosity and  $M_{500,c}$  calibrated by Maughan (2007), where masses are recovered from  $Y_X$ , using *Chandra* data for 115 clusters in the redshift range  $0.1 < z < 1.3$ . Among the fitting expressions reported in Table 1 of that paper, we choose the relation between  $L_X$  and  $M_{500,c}$ , obtained without excising the core region within  $0.15 R_{500,c}$ :

$$L_X = C E(z) \left( \frac{M_{500,c}}{4 \times 10^{14} M_\odot} \right)^B, \quad (3.14)$$

with  $C = 5.6$ ,  $B = 1.96$ . The reason for this choice is that we did not attempt to model the core contribution in computing the flux limits reported in Table 3.1.

We show in Figure 3.2 the redshift dependence of the limiting mass  $M_{500,c}$  associated to the survey flux limits for both the *Detection Sample*

and the *Bright Sample*. The prescriptions for the mass function that we use in the analysis are provided for different definitions of the mass. The values of the mass have been converted, following Hu & Kravtsov (2003), by adopting the NFW halo density profile (Navarro et al., 1997) for the reference cosmological model. In this analysis we assume that the concentration parameter is equal to 5 (see also Shang et al., 2009). Extrapolating the  $M-L_X$  relation by Maughan (2007) at faint fluxes of our surveys would imply unrealistically small mass limits at low redshift. For this reason, we decided to use a lower limit of  $M_{500,c} = 5 \times 10^{13} M_\odot$  in the definition of the selection function (shown with the horizontal dotted line in Figure 3.2). In fact, this is comparable to the lowest mass down to which mass proxies have been calibrated so far (e.g., Vikhlinin et al., 2009a). We also point out that we do not include the cosmology dependence of the selection function in our analysis.

We show in Figure 3.3 the cumulative redshift distributions for the clusters belonging to the *Detection Sample* (left panel) and to the *Bright Sample* (right panel). Overall, the three WFXT surveys would yield about  $3 \times 10^6$  detected clusters, out of which  $\sim 7.5 \times 10^4$  clusters should be found at  $z > 1$ . This will provide an improvement by about four orders or magnitude with respect to the  $\sim 10$   $z > 1$  clusters currently confirmed. At the same time, we expect to have about  $2 \times 10^4$  clusters with robustly measured mass proxies, of which  $\sim 4000$  would lie at  $z > 0.5$ . This would increase by more than two orders of magnitude the number of clusters for which mass proxies have been measured above this redshift, after intensive follow-up *Chandra* observations of clusters identified in ROSAT-based surveys (e.g., Vikhlinin et al., 2009a; Mantz et al., 2009; Ettori et al., 2009). We stress that, despite the small area covered, the Deep survey provides the dominant contribution to the *Bright Sample* at  $z > 1$ . This highlights the important role that the Deep survey has in providing mass proxies at high redshift. Although predicting the number of extremely distant clusters is highly uncertain, owing to the unknown evolution of the mass luminosity relation above  $z \simeq 1$ , we foresee that  $\sim 10^3$  clusters would be detected at  $z \gtrsim 2$ , with mass measurements available for few tens of them.

In Figure 3.4, we show the cumulative redshift distributions of clusters to be observed in the Wide, the Medium and the Deep surveys of the *Bright Sample* according to the EDE model. In the lower panel it is shown the ratio between the cumulative redshift distributions obtained for the

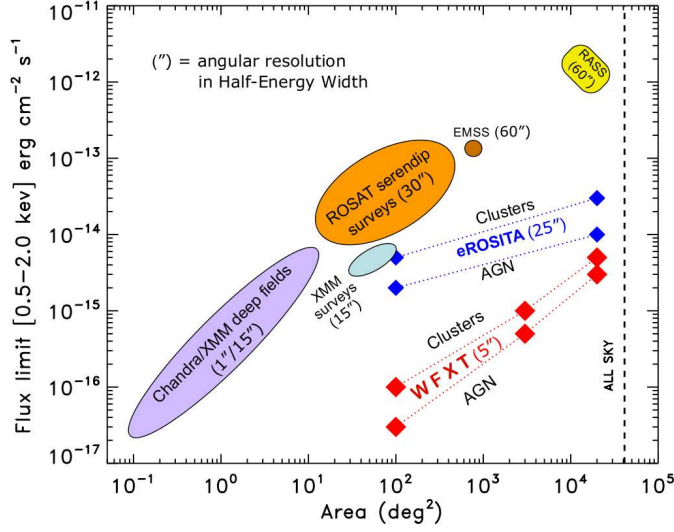


Figure 3.1: Effective flux limits and sky coverage for past and planned X-ray surveys.

Table 3.1: Characteristics of the X-ray surveys (Giacconi et al., 2009). Column 2: sky coverage  $\Omega$  (in sq.deg.); Column 3: flux limits for detection of extended sources (*Detection Sample*) in the [0.5-2] keV energy band (units of  $10^{-14} \text{ erg s}^{-1} \text{ cm}^{-2}$ ); Column 4: flux limits defining the *Bright Sample*.

	$\Omega$	$F_{\text{det}}$	$F_{\text{br}}$
Wide	20000	0.5	15.0
Medium	3000	0.1	3.0
Deep	100	0.01	0.3

DE and the EDE reference models by combining the three surveys. In order to reproduce the observed abundance of clusters at low redshift, in EDE models structures start to form earlier and the halo population follows a slower evolution than in the  $\Lambda\text{CDM}$  prescription.

### 3.4.2 Mass parameters

Besides the cosmological parameters, that describe the models that we use in our analysis, we consider also the parameters which specify the redshift dependence of the fraction mass bias  $B_M$  and the intrinsic scatter  $\sigma_{\ln M}$ , introduced in Eq.3.8, (in our analysis we do not consider the

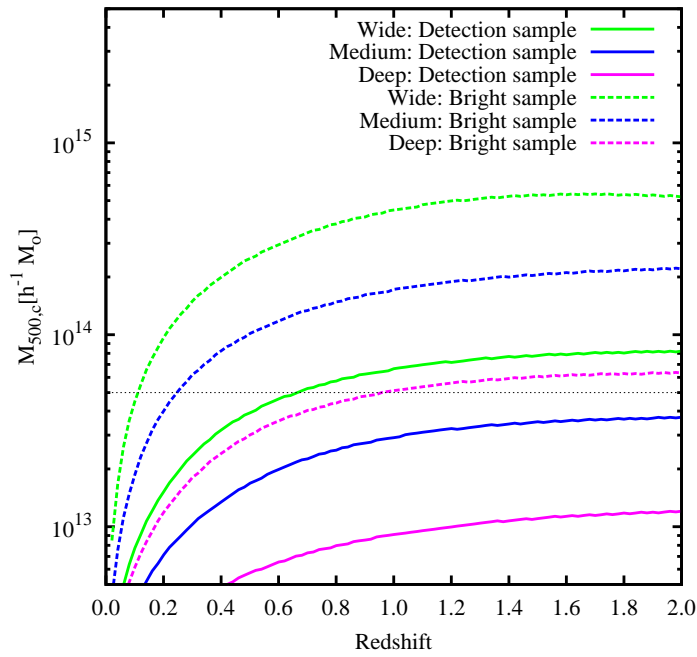


Figure 3.2: The redshift dependence of the  $M_{500,c}$  mass thresholds, corresponding to the flux limits for cluster detection for the three surveys, as reported in Table 3.1: the Wide, Medium and Deep surveys are shown with the green, the blue and magenta curves, respectively. The solid curves correspond to the *Detection Sample* and the dotted curves to the *Bright Sample*. The horizontal dotted line marks the mass limit of  $M_{500,c} = 5 \times 10^{13} h^{-1} M_{\odot}$  below which we discard clusters in our analysis.

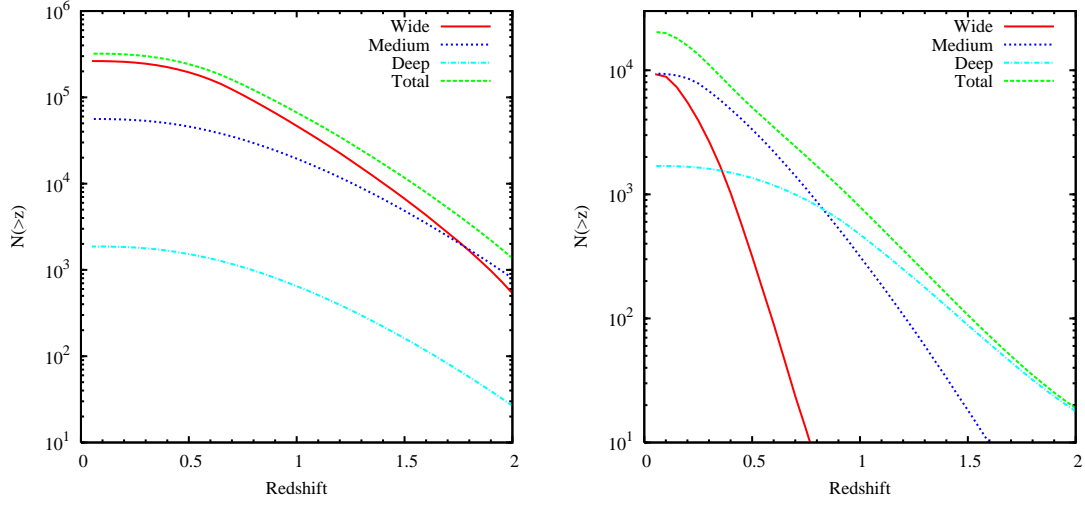


Figure 3.3: The cumulative redshift distribution for the three surveys, as predicted by the reference DE model of Eq. 3.1. The left panel is for the *Detection Sample*, while the right panel is for the *Bright Sample*. In both panels solid (red), dotted (blue) and dot-dashed (cyan) curves represent the Wide, Medium and Deep surveys, respectively, while the short-dashed (green) curve represents the sum of the three.

case of a possible mass dependence of these parameters). We assume the following parametrization for such redshift dependencies:

$$\begin{aligned} B_M(z) &= B_{M,0}(1+z)^\alpha \\ \sigma_{\ln M}(z) &= \sigma_{\ln M,0}(1+z)^\beta. \end{aligned} \quad (3.15)$$

We end up having four parameters,  $B_{M,0}$ ,  $\sigma_{\ln M,0}$ ,  $\alpha$  and  $\beta$ , which account for the uncertain knowledge in the relation between observables and mass (we refer them hereafter as *mass-parameters*). A negative value for  $B_M$  corresponds to a mass underestimate and, therefore, to a smaller number of clusters included in a survey, for a fixed selection function. The presence of the mass bias accounts for the possibility of a violation of hydrostatic equilibrium in the estimate of X-ray masses, on which the observable-mass scaling relation is calibrated. A number of independent analyses of a variety of cosmological hydrodynamic simulations of galaxy clusters converge to indicate that hydrostatic mass estimators provide underestimates of true mass within  $R_{500,c}$  by about 10-15 per cent (e.g., Borgani & Kravtsov, 2009; Ameglio et al., 2009; Piffaretti & Valdarnini, 2008; Nagai et al., 2007; Rasia et al., 2005). Such results are also in line with

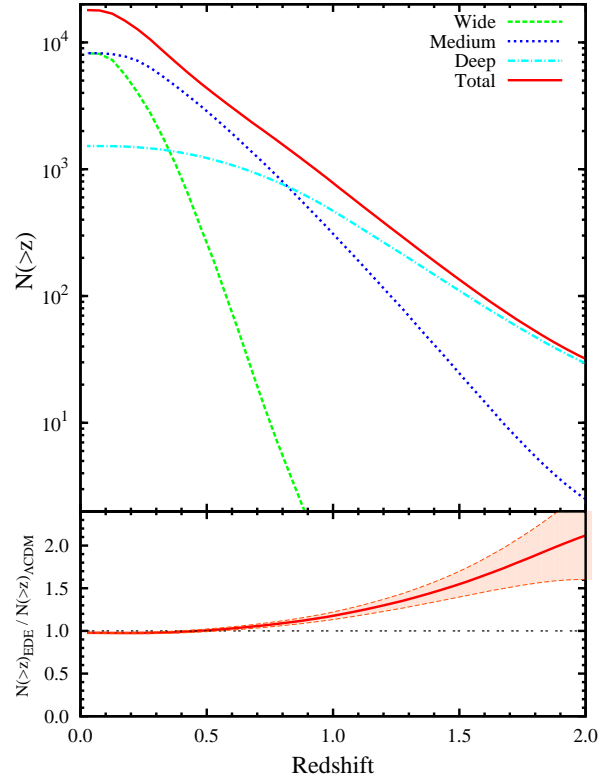


Figure 3.4: The cumulative cluster redshift distribution for the three surveys, as predicted by the reference EDE model of Eq. 3.2. Dashed (green), dotted (blue) and dot-dashed (cyan) curves are for the Wide, Medium and Deep WFXT *Bright Sample* surveys, respectively, while the solid (red) curve represents the sum of the three. In the bottom panel we show the ratio between the cumulative redshifts distributions for the combined survey, as predicted by the reference EDE model and the reference DE model shown in the right panel of Figure 3.3. The shaded region represents the Poissonian error on this ratio.

the observational results on the comparison between cluster masses estimated with weak lensing and with X-ray data (e.g., Mahdavi et al., 2008). In the following, we assume  $B_{M,0} = -0.15$  as a reference value for the mass bias and regarding its evolution, we take  $\alpha = 0$  as a reference value. As for the intrinsic scatter, it has the effect of increasing the number of clusters included in the survey. In fact, the number of low-mass clusters that are up-scattered above the survey mass limit is always larger than the number of rarer high-mass clusters which are down-scattered below the same mass limit (e.g., Cunha, 2009, and references therein). As a reference value, we assume  $\sigma_{\ln M,0} = 0.25$ , consistent with the intrinsic scatter in the  $M_{500,c}-L_X$  relation measured by Maughan (2007), with  $\beta = 0$  for its evolution. We stress here that, following Lima & Hu (2005), we use the variance  $\sigma_{\ln M}^2$  and not the scatter as the parameter to be varied in our Fisher matrix analysis. In fact, this quantity controls the excess of up-scattered and down-scattered clusters with respect the total number.

In summary, we have four mass-parameters that add up to the eight cosmological parameters for which we compute the Fisher Matrix. In order to quantify the effect of the uncertain knowledge of the mass parameters, we will set in the following four different levels of prior. In order of constraining strength, they can be described as follows.

1. *No prior*: all the four mass-parameters are left free to vary by assuming no prior knowledge on their range of variation.
2. *Weak prior*: we assume  $\Delta B_{M,0} = 0.05$ ,  $\Delta\alpha = 1$ ,  $\Delta\sigma_{\ln M,0}^2 = 0.2$  and  $\Delta\beta = 1$  for the  $1\sigma$  uncertainty with which the four mass-parameters are assumed to be known. The above value of  $\Delta B_{M,0}$  reflects the current uncertainty between different calibrations of violation of hydrostatic equilibrium from simulations and from the comparison of weak-lensing and X-ray masses. For instance, Vikhlinin et al. (2009a) compared weak lensing and Chandra X-ray mass measurements for a rather small sample of low- $z$  clusters and concluded that the mass scale can already be calibrated with a statistical uncertainty of about 10 per cent. A similar result has been obtained by Zhang et al. (2010) from the comparison of XMM-Newton X-ray masses and weak lensing masses for a set of 12 nearby clusters. Owing to these results, we also consider the case of the mass bias parameter to be known with a precision  $\Delta B_{M,0} = 0.05$ . An improvement by only a factor of two with respect to the present in the calibration of the cluster mass scale is probably over conservative,

owing to the orders-of-magnitude increase in the number of clusters with precise X-ray mass measurements to be provided by the three surveys and precise lensing mass measurements from both ground-based and space telescopes. As for the evolution, we assume  $\Delta\alpha = 1$  as a prior, which would correspond to an uncertainty in the mass bias calibration at  $z = 1$  comparable to that calibrated at present for nearby clusters. Regarding the prior on the intrinsic scatter, we assume  $\Delta\sigma_{\ln M,0} = 0.1$  and  $\Delta\beta = 1$ . We expect these to be rather conservative choices, in view of the large number of clusters that should be made available by future X-ray and optical/near-IR surveys at both low and high redshift.

3. *Evolution strong prior*: in order to emphasize the role played by the uncertain redshift evolution of the mass parameters, we assume in this case the uncertainty in  $B_{M,0}$  and  $\sigma_{\ln M,0}^2$  to be the same as in the *weak prior* case, while we assume their evolution to be known to good precision, so that  $\Delta\alpha = 0$  and  $\Delta\beta = 0$ .
4. *Strong prior*: in this case we consider the uncertainties in the calibration of the mass-observable relation are so small to be neglected. While this assumption is expected to be unrealistic for the *Detection Sample*, it may be rather plausible in case we restrict the analysis to the *Bright Sample*.

### 3.5 Characteristics of the EUCLID surveys

EUCLID mission, recently approved by the European Space Agency (ESA), will be launched in 2019. It has been designed in order to map large-scale structure over a cosmic time covering the last 10 billion years, more than 75 per cent the age of the Universe. The mission is optimised for two independent primary cosmological probes: Weak gravitational Lensing (WL) and Baryonic Acoustic Oscillations (BAOs). In addition, the EUCLID surveys yield data of several important complementary cosmological probes such as galaxy clusters, and the integrated Sachs Wolfe effect.

WL requires a high image quality on sub-arcsec scales for the galaxy shape measurements, and photometry visible and infrared wavelengths to measure the photometric distances of each lensed galaxy out to  $z \sim 2$ . BAOs analysis requires near-infrared spectroscopic capabilities to measure accurate redshifts of galaxies out to  $z \sim 0.7$ . Both probes require a

very high degree of system stability to minimise systematic effects, and the ability to survey a major fraction of the extra-galactic sky.

EUCLID produces images and photometry of more than a billion galaxies and several million spectra, out to redshift  $z \sim 2$ . Gravitational lensing together with near infrared photometry of lensing sources explores the relationship between light, baryons and dark matter between galaxy and super cluster scales as function of look-back time and environment.

For WL, EUCLID measures the shapes of 30 resolved galaxies per arcmin in one broad visible R+I+Z band (550-920 nm) down to AB mag 24.5 ( $10\sigma$ ). The photometric redshifts for these galaxies reaches a precision of  $\sigma_z/(1+z) < 0.05$ . They are derived from three additional EUCLID NIR bands (Y, J, H in the range 0.92-2.0 micron) reaching AB mag 24 ( $5\sigma$ ) in each, complemented by ground based photometry in visible bands derived from public data or through engaged collaborations with projects such as DES, KiDS, and Pan-STARRS.

The BAOs are determined from a spectroscopic survey with a redshift accuracy  $\sigma_z/(1+z) \leq 0.001$ . The slitless spectrometer, with  $\lambda/\Delta\lambda \sim 250$ , predominantly detects H $\alpha$  emission line galaxies. The limiting line flux is  $3 \times 10^{-16} \text{ erg s}^{-1} \text{ cm}^{-2}$  (1 arcsec extended source, 3.5 sigma at 1.6 micron), yielding over 50 million galaxy redshifts with a completeness higher than 45 per cent.

The Wide survey covers 15,000 deg<sup>2</sup> of the extragalactic sky and is complemented by two 20 deg<sup>2</sup> deep fields observed on a monthly basis. The latter survey is needed for the calibration of the slitless spectroscopy and will be the primary target for follow-up observations. As a self-standing survey, Deep data contain thousands of objects at  $z > 6$  and several tens of  $z > 8$  galaxy or quasar candidates.

Clusters will be detected with EUCLID by analysing the photometric data, an approach that has been used by the SDSS at low redshifts (e.g., Koester et al., 2007a). EUCLID will be able to push towards much higher redshifts over a large area, thanks to its unique capabilities in the infrared.

EUCLID is able to calibrate the important mass-observable relations and their scatter through lensing measurements. The high image quality and number density of sources will enable EUCLID to measure masses of clusters much more accurately and out to higher redshifts than is possible from the ground. The combination of Euclid data with other surveys, such as eROSITA, WFT or Planck, enables the cross-calibration of non-lensing mass-observable relations, which are currently limited to low

redshifts and small samples.

In the EUCLID Near-Infrared Imaging Photometer (NIP) wide-survey, we expect to be able to detect  $\sim 30,000$  clusters of galaxies more massive than  $\log(M) \sim 14.6$  at  $z > 0.2$ , of which  $\sim 4,000$  at  $z > 0.5$ ,  $\sim 600$  at  $z > 1$  and  $\sim 200$  at  $z > 1.4$  (see Figure 3.6). These predictions are for detections of  $5\text{-}\sigma$  over-densities in the galaxy counts at the scale corresponding to cluster virial radii,  $r_{200}$ , and are obtained by evaluating the expected cluster richnesses and the variance of the field galaxy counts within the cluster areas, at the depth of the EUCLID-NIP survey for different redshifts. In such estimates, cluster overdensities are expected to be enhanced by selecting galaxies in bins of photometric redshifts,  $z_p$ , adopting the EUCLID requirement for a  $z_p$  accuracy better than  $0.05 \times (1 + z_p)$  for all galaxies out to  $z \approx 2$ . Using mock catalogues of galaxy clusters based on the COSMOS data set, the resulting sample of clusters is expected to be almost 100 per cent complete, and with negligible contamination from spurious detections for  $z < 1$ . At  $z > 1$  contamination is estimated to be significant (up to 50 per cent) but it can be reduced by looking for concordant redshifts of galaxies in the candidate clusters, since for every  $z > 1$  cluster candidate a few redshifts will be available from the EUCLID Near-Infrared Imaging Spectrometer (NIS) survey. The resulting photometric section function is displayed in Figure 3.5 and it is expected to be nearly independent of  $z$ .

### 3.6 Results

Before proceeding with the derivation of forecasts for constraints on cosmological parameters, we verify that our fiducial cosmological models, with the reference choice for the mass-parameters, matches available observational data on X-ray cluster surveys. To this purpose, we show in Figure 3.7 the comparison between the cluster flux number counts observed in the [0.5-2] keV energy band from the ROSAT Deep Cluster Survey to an X-ray flux limit of  $3 \times 10^{-14} \text{ erg s}^{-1} \text{ cm}^{-2}$  (RDCS-3, Rosati et al. 1998, 2002) and the prediction of our reference model. The good agreement with the data is not surprising, owing to the fact that the reference cosmological parameters agree with constraints based on the evolution of the cluster mass function (e.g., Borgani et al., 2001; Vikhlinin et al., 2009b; Mantz et al., 2010a).

Moreover we show in Figure 3.8 a comparison between the predicted

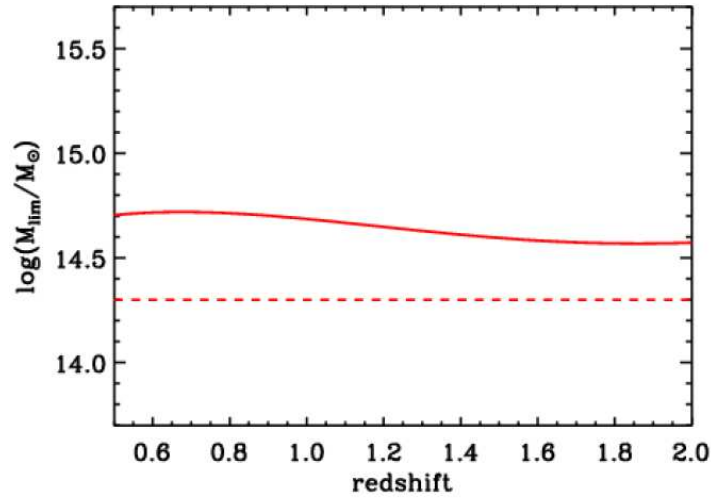


Figure 3.5: Selection function for the photometric survey. Solid and dashed lines are for  $5\sigma$  and  $3\sigma$  detection, respectively. Courtesy of A. Biviano.

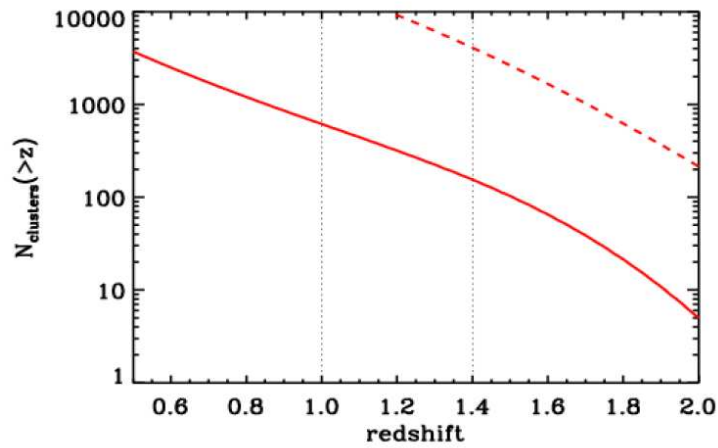


Figure 3.6: Number of clusters above a given redshift expected to be detected as  $5\sigma$  and  $3\sigma$  overdensities in the EUCLID photometric survey (solid and dashed lines, respectively). Courtesy of A. Biviano

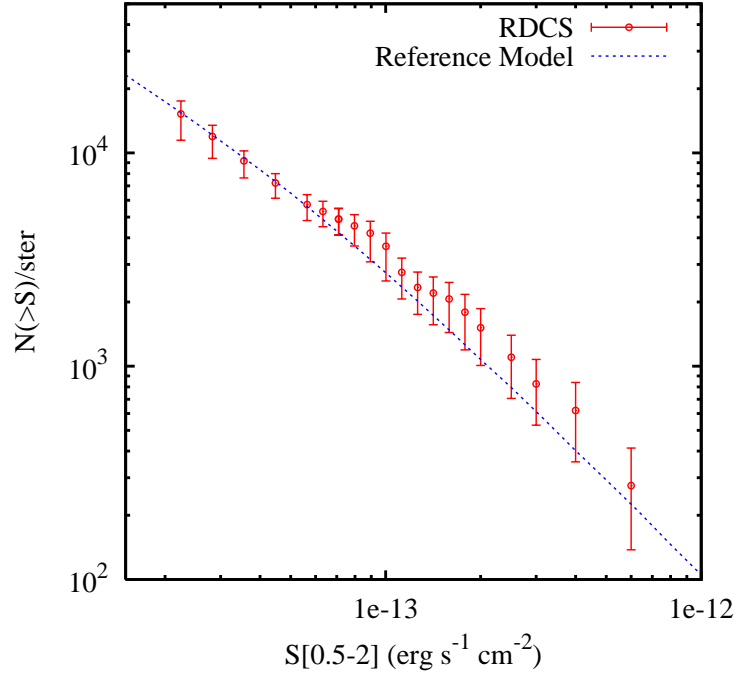


Figure 3.7: The comparison between observed cumulative cluster flux number counts (symbols with errorbars) and predictions from the reference  $\Lambda$ CDM model (dotted curve). Observational results refer to counts in the [0.5-2] keV band from the ROSAT Deep Cluster Survey (Rosati et al., 2002), with errorbars corresponding to  $1\sigma$  Poissonian uncertainties (Gehrels, 1986).

and the observed redshift distribution for the RDCS-3 according to both the standard DE and EDE models. We stress that this is not meant to be a fit to an observational measurement of the cluster abundance to  $z \sim 1$ , but rather a test that our reference model is consistent with current observations. The redshift distribution for the two reference DE models have been obtained by convolving the predicted redshift distributions with the flux-dependent RDCS sky coverage, which provides complete information on the survey selection function (Rosati et al., 2002).

The good agreement between available observational data and predictions of our reference model indicates that the latter can be used to provide a realistic extrapolation of the evolution of the cluster mass function over redshift and mass ranges which are not probed by currently available data.

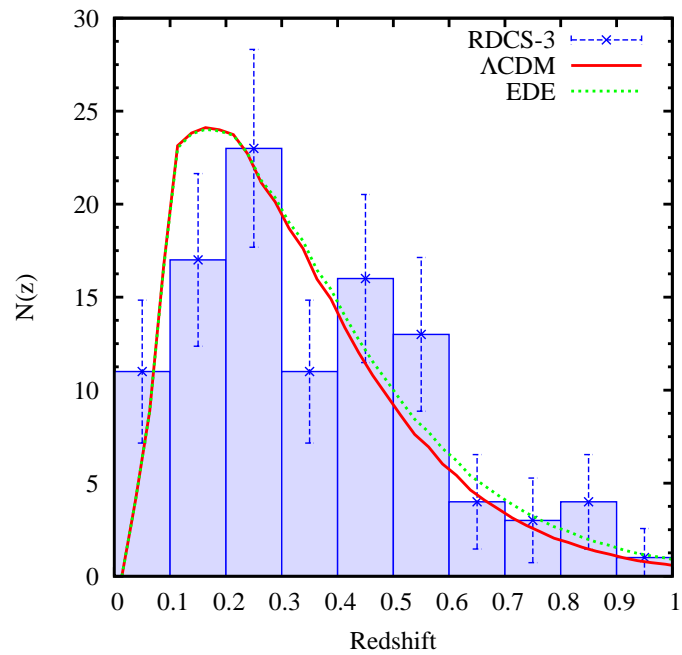


Figure 3.8: Comparison between the observed redshift distribution of X-ray selected galaxy clusters (histogram with symbols with errorbars) from the ROSAT Deep Cluster Survey -3 (Rosati et al., 2002) and predictions from the reference DE models based on Eq. 3.1 (red solid curve) and Eq. 3.2 (green dotted curve). Errorbars on observational data points correspond to  $1\sigma$  Poissonian uncertainties (Gehrels, 1986).

### 3.6.1 Cosmological constraints

Having defined the reference cosmological model and the characteristics of the X-ray cluster surveys, we present forecasts on constraints of cosmological parameters. We show first our results on DE EoS and  $(\Omega_m, \sigma_8)$  parameters based on the assumption of Gaussian initial density field perturbations for the WFXT surveys of the *Bright Sample*. In the Section 3.6.2 we show constraints from non-Gaussian model.

We will present our results in terms of constraints on the  $(\Omega_m, \sigma_8)$  and the  $(w_0, w_a)$  plane at the 68 per cent confidence level, after marginalizing over the other cosmological and mass-parameters, and in terms of Figure of Merit (FoM). The concept of FoM for DE constraints was introduced in the Dark Energy Task Force (DETF) report (e.g., Albrecht et al., 2009) in order to quantify the knowledge on DE EoS parameters that future cosmological experiments can reach. In general, the FoM for the capability of an experiment to constrain a pair of cosmological parameters  $(\theta_\alpha, \theta_\beta)$  can be defined as

$$\text{FoM} = (\det [\text{Cov}(\theta_\alpha, \theta_\beta)])^{-1/2}, \quad (3.16)$$

where  $\text{Cov}(\theta_\alpha, \theta_\beta)$  is the covariance matrix between the two interesting parameters. With this definition, the FoM is proportional to the area encompassed by the ellipse representing the 68 per cent confidence level for model exclusion.

In the computation of the cluster number counts Fisher Matrix, Eq. 3.5,  $N_{l,n}$  is calculated within intervals of observed redshift, having width  $\Delta z = 0.05$  out to  $z_{max} = 2$ . As for the observed mass, we use bins of width  $\Delta \log M = 0.01$ , extending from the lowest mass limit determined by the survey selection function at a given redshift, up to  $10^{16} h^{-1} M_\odot$ . We have verified that with this tight binning in mass we saturate information provided by cluster number counts to constrain cosmological and mass-parameters.

In the computation of the power spectrum Fisher Matrix, given by Eq. 3.10, the average cluster power spectrum defined by Eq. 3.11 is calculated by integrating over redshift intervals having constant width  $\Delta z = 0.2$ . This binning is coarser than that adopted for the analysis of number counts. It represents a compromise between the need of extracting the maximum amount of information from clustering evolution and the request of limiting the covariance between  $z$ -intervals (e.g., Striel et al.,

2010). Indeed, the contribution from different  $z$ -bins can be added in Fisher Matrix defined by Eq. 3.10 only if they carry statistically independent information. As for the wavenumber, we consider a minimum value of  $k = 0.001 \text{ Mpc}^{-1}$ ; the choice of this minimum value does not change the final results, because extremely large wave modes are not sampled by the surveys used and, therefore, do not provide any contribution to the Fisher Matrix. The maximum value chosen is  $k_{max} = 0.3 \text{ Mpc}^{-1}$ . This choice derives from the need to maximize the information extracted from the surveys, while avoiding at the same time the contribution from small-scale modes where the validity of the linear bias model is compromised by the onset non-linearity (e.g. Percival & White, 2009). Wavenumber bins have been chosen to have log-uniform width  $\Delta \log k = 0.1$ . Lastly, introducing redshift space distortions information, the power spectrum acquires a dependence on  $\mu$ , which is defined as the cosine of the angle that  $\mathbf{k}$  makes with the line of sight (Eq. 1.49). This implies that the Fisher Matrix also involves a sum on  $\mu$  that runs from  $\mu = -1$  to  $\mu = 1$ . After analysing how to maximize the information from the RSDs, we choose to divide the interval of  $\mu$  into 9 bins, while no significant information is added by using a finer binning.

The results of our analysis on cosmological parameters in the standard DE model from the WFXT surveys of the *Bright Sample* are presented in Figure 3.9 where we plot the 68 per cent confidence levels on the  $(\Omega_m, \sigma_8)$  and  $(w_0, w_a)$  plane, in the left and right panels, respectively. In each panel, we show the contours obtained for each of the three surveys and for their combination. Contours are all obtained by combining information from number counts and power spectrum, also including the prior information from Planck. A *strong prior* is also assumed for the knowledge of the mass-parameters (see Sect. 3.2).

The results in Figure 3.9 show the trade-off between surveys area and depth in constraining different cosmological parameters. As for the results on  $(\Omega_m, \sigma_8)$ , there is no continuous trend in the constraining power of the three surveys as we reduce the covered area and increase sensitivity. The Medium Survey is in fact the one with most constraining power, especially for  $\sigma_8$ , while the Deep and the Wide Surveys are somewhat less constraining. Furthermore, the three surveys provide comparable constraints on  $\Omega_m$ . This is consistent with the expectation that constraints on this parameter are mainly provided by information on the CMB anisotropies, carried by the Planck prior. As for  $\sigma_8$ , we remind that this parameter de-

Table 3.2: Figure of Merit and r.m.s. uncertainty in the DE EoS parameters, for the three WFXT surveys of the *Bright Sample*, and for their combination. The analysis is carried out by including the Planck prior and assuming *strong prior* for the mass-parameters.

Surveys	Deep	Medium	Wide	Total
FoM	20	60	17	106
$\sigma_{w_0}$	0.20	0.097	0.14	0.064
$\sigma_{w_a}$	0.94	0.54	0.70	0.41

termines the timing of structure formation. Therefore, constraints on its value are sensitive to both the statistics of massive clusters included in a survey, and on the effective redshift range covered by the survey itself. In this respect, the Medium Survey provides the best compromise between number of massive clusters detected within its area and depth.

As for the constraints on  $(w_0, w_a)$ , we note that their dependence on the survey area/depth is different from the case of the  $(\Omega_m, \sigma_8)$  parameters. While the Medium survey is still the most constraining one, we note that the Deep Survey predicts a tighter degeneracy between  $w_0$  and  $w_a$  than the Wide survey. This translates into tighter constraints on the redshift evolution of the DE EoS, if a prior knowledge on  $w_0$  is available, consistent with the fact that the Deep Survey covers a larger redshift interval. This example illustrates that the choice of the survey strategy depends in principle on the cosmological parameters that one is mostly interested in. In Table 3.2 we report the values of the FoM and the r.m.s. uncertainty in the DE EoS parameters for each survey and for their combination, after marginalizing over the other parameters. The values of the FoM in this table confirm that Medium Survey alone carries most of the contribution to the FoM obtained by combining the three surveys.

### Effect of mass-parameter priors

As a first test, we present the effect that using progressively stronger priors on the mass-parameters has on the cosmological constraints. The results of this analysis are shown in Figure 3.10, where we plot the constraints on cosmological parameters obtained by combining information from cluster number counts and power spectrum, from the three surveys together. The Fisher Matrix from the cluster experiment is also combined

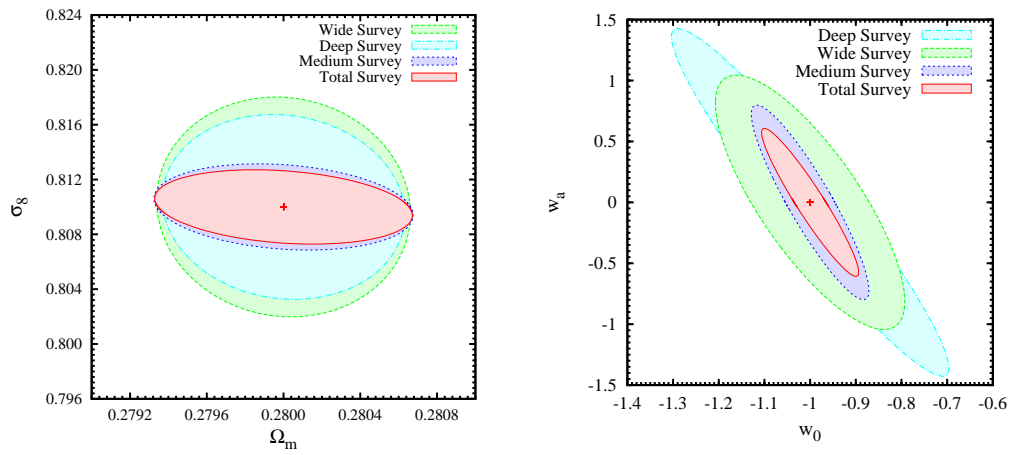


Figure 3.9: Constraints at the 68 per cent confidence level on the  $(\Omega_m, \sigma_8)$  parameters (left panel) and on the  $(w_0, w_a)$  DE parameters (right panel). In each panel, forecasts for the Deep, Medium and Wide cluster WFXT surveys of the *Bright Sample* are shown with the cyan, blue and green ellipses, respectively, by combining number counts and power spectrum information. Also shown with the red ellipse are the constraints obtained from the combination of the three surveys. All constraints are obtained by assuming a *strong prior* on the knowledge of the mass-parameters and combining the Fisher Matrices for cluster number counts, cluster power spectrum and CMB Planck experiment.

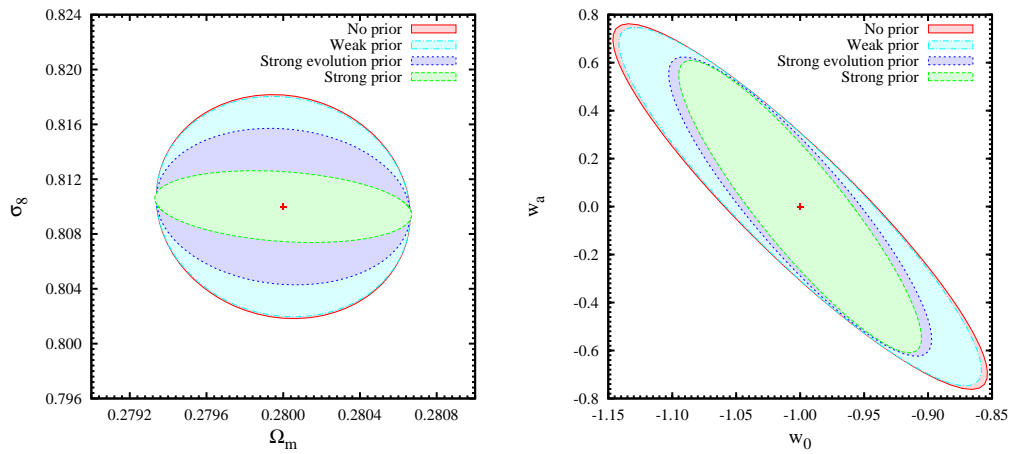


Figure 3.10: Constraints at the 68% confidence level on the  $(\Omega_m, \sigma_8)$  plane (left panel) and on the  $(w_0, w_a)$  parameters (right panel). Different ellipses correspond to different assumptions on the prior for the mass-parameters (see text): *no prior* case (red), *weak prior* case (cyan), *evolution strong prior* case (blue), and *strong prior* (green). All constraints are obtained by combining cluster number counts and power spectrum information for the combination of the three surveys. The Fisher Matrix from Planck CMB experiment.

with the Planck Fisher Matrix.

In the left panel of Figure 3.10 we show the constraints in the  $(\Omega_m, \sigma_8)$  plane. Assuming a progressively better knowledge of the relation between X-ray observable and cluster mass turns into progressively tighter constraints on the  $\sigma_8$  parameter, while leaving the results on  $\Omega_m$  basically unchanged. The reason for this behaviour is that constraints on  $\Omega_m$  are mainly determined by the measurement of the CMB anisotropies and by the shape of power spectrum, which however only provide rather loose constraints on  $\sigma_8$ . On the other hand, the power spectrum normalization is determined by the growth of cosmic structures, which is traced by the evolution of the halo mass function. Since a precise measurement of the mass function can only be obtained through a detailed knowledge of the mass-parameters, it is of little surprise that such parameters determine the accuracy with which  $\sigma_8$  can be measured.

As for the constraints on the DE EoS parameters, (see right panel of Figure 3.10), we note that improving the knowledge of the mass parameters from the *no prior* (red ellipse) to the *weak prior* (cyan ellipse) case only brings a modest enhancement of the constraining power of the surveys. The main reason for this is that constraints on DE parameters are here mainly contributed by the evolution of linear perturbation growth. On the other hand, constraints on the growth are rather degenerate with the uncertainty in the redshift evolution of the mass-parameters, which is assumed to be rather generous also in the *weak prior* case. Indeed, a more significant improvement in the constraints on the DE parameters is obtained for the *evolution strong prior* case (blue ellipse), which assumes a precise knowledge of the parameters determining the evolution of the mass-observable relation. The slight improvement in the constraints obtained for the *strong prior* case (green ellipse) confirms the importance of accurately calibrating the evolution of the scatter and bias parameters by measuring different mass proxies in high redshift clusters selected in the Deep survey. This result, which is confirmed by the FoM values reported in Table 3.3, also highlights the importance of the Deep Survey. Indeed covering at a high sensitivity an even small sky area allows one to obtain a robust calibration of the scaling relations between the cluster mass and X-ray mass proxies over a large redshift baseline. As shown in the right panel of Figure 3.3, this survey will provide about 400 clusters at  $z > 1$  for which measurements of redshift,  $M_{gas}$  and  $Y_X$  will be possible, out of which about 100 are expected to lie at  $z > 1.5$ .

Table 3.3: Prior on mass parameters assumed in the four cases under study (see text) and relative Figure of Merit (FoM) [see Eq. 3.16] from the combination of three WFXT surveys of the *Bright Sample*. The analysis is carried out by including the Planck prior.

Reference values:	$B_{M,0} = -0.15$	$\alpha = 0$	$\sigma_{\ln M,0}^2 = (0.25)^2$	$\beta = 0$
Cases:	<i>Strong</i>	<i>Evolution</i>	<i>Weak</i>	<i>No Prior</i>
$\Delta B_{M,0}$	0	0.05	0.05	/
$\Delta\alpha$	0	0	1	/
$\Delta\sigma_{\ln M,0}^2$	0	0.2	0.2	/
$\Delta\beta$	0	0	1	/
FoM	106	91	64	61

### Combining cluster number counts and power spectrum

We discuss now how the combination of number counts and power spectrum information enhances cosmological constraints. To this aim, we show the improvement on constraints obtained by adding progressively information from the cluster number counts, the mean cluster power spectrum analysis and the CMB prior from Planck. The results are presented in Figure 3.11 in the  $(\Omega_m, \sigma_8)$  (left panel) and  $(w_0, w_a)$  planes. Constraints are obtained by combining information from the three WFXT surveys of the *Bright Sample* together and assuming *strong prior* on mass-parameters. The redshift evolution of the cluster number counts set the direction of degeneracy for the constraints on  $\Omega_m$  and  $\sigma_8$ . Such constraints are mainly placed on the linear growth factor of density perturbations through the mass function. Furthermore, since the density parameters contributed by matter and DE also affect the expansion history of the universe, we expect their values to be constrained by the cluster number counts, through the redshift evolution of the comoving volume element. As for the power spectrum analysis, it provides information on the growth rate of cosmic structure through the bias factor, and the RSDs effect. Moreover BAO features, that depend on the expansion history of the universe (see sec. 3.6.1), and the power spectrum shape (see sec. 3.6.1) are also sensitive to the underlying DM distribution.

In Figure 3.11 we show that adding the power spectrum information to the number counts substantially shrinks the contours. Including the infor-

mation from the Planck prior (red contour) further contribute to tighten the contours in the  $(\Omega_m, \sigma_8)$  plane. In order to verify whether CMB add information only by constraining the curvature of the Universe, we also show with the green contour the effect of assuming instead a flat Universe on the cluster constraints. In this case, results on  $(\Omega_m, \sigma_8)$  are not drastically improved with respect to the case in which curvature is a free parameter, while they are significantly worse than with the Planck prior. The reason for this result is that CMB anisotropies provide constraints not only on the curvature, but also on the Hubble parameter  $h$ , on  $\Omega_b$  and on the primordial spectral index  $n_s$ . All these parameters enter in defining the shape of the power spectrum, along with  $\Omega_m$ . Therefore, precisely determining them from the CMB turns into a significant improvement of the constraints on the density parameter from the shape of the power spectrum.

As for the constraints on  $(w_0, w_a)$ , their direction of degeneracy changes as a specific geometry is assumed. Imposing the flat prior corresponds to fix the redshift at which DE component,  $\Omega_{de}$ , starts dominating over  $\Omega_m$  and, therefore, breaks the degeneracy between  $w_0$  and  $w_a$ . By including the Planck prior, instead of assuming flatness, has a smaller impact than for the  $(\Omega_m, \sigma_8)$  constraints. Therefore, even though CMB alone does not provide in itself stringent constraints on the DE EoS (Komatsu et al., 2011), it is quite effective in improving the corresponding constraints from cluster number counts and power spectrum, through the constraints placed on the geometry of the Universe. The Deep and Medium surveys dominate the cluster counts at  $z \gtrsim 0.4$  (see right panel of Figure 3.3), thus improving the constraints on the growth rate of perturbations in a redshift range where it is sensitive to the DE EoS.

### Information from Baryonic Acoustic Oscillations

We quantify the geometrical information brought by the presence of BAOs features in the matter power spectrum. BAOs appear as wiggles superposed on the power spectrum of the dominant dark matter component (e.g. Eisenstein & Hu, 1998). As we showed in Section 1.4, the position and the amplitude of the wiggles are related to the amount of dark matter and baryons. In this analysis, we study the constraints on the  $(w_0, w_a)$  DE EoS parameters as obtained by using the transfer function by Eisenstein & Hu (1998), which includes BAOs, and by using instead the transfer function that smoothly interpolates through the oscillations (see

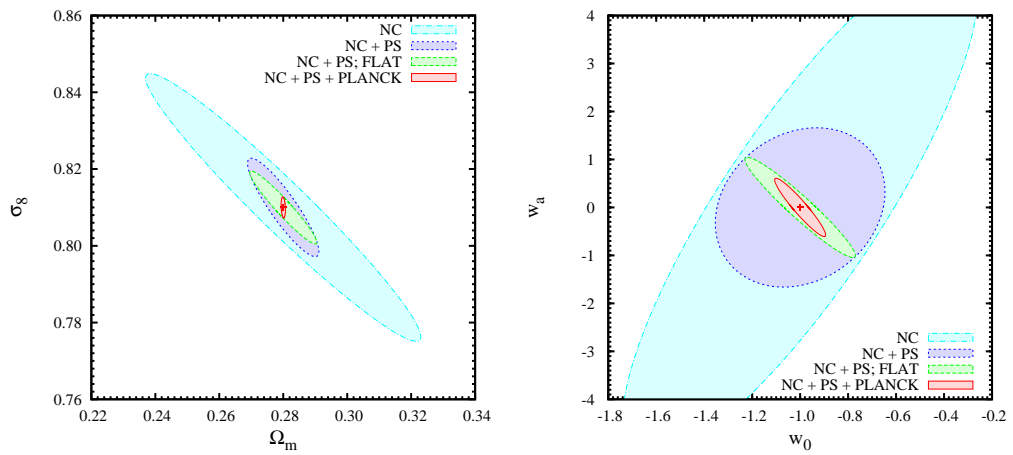


Figure 3.11: Constraints at the 68 per cent confidence level on the  $(\Omega_m, \sigma_8)$  parameters (left panel) and on the  $(w_0, w_a)$  DE EoS parameters (right panel). Contours, from the wider to the narrower ones, are obtained by including the Fisher Matrix from cluster number counts only (cyan ellipse), adding cluster power spectrum information (blue ellipse), further assuming a flat Universe (green ellipse) and adding priors from the Planck experiment while leaving geometry free (red ellipse). All constraints are obtained by combining information from the three surveys and assuming the *strong prior* on the mass parameters.

Eq. 30 of Eisenstein & Hu 1998). In the latter case the presence of baryons manifests itself only by modifying the overall shape of the transfer function.

We carried out the analysis including and excluding BAOs in the shape of the matter power spectrum used to compute cluster number counts and bias. In order to better appreciate the information carried by BAOs, in both cases we do not assume any prior on cosmological parameters, while we use strong prior on the mass-parameters. As expected, constraints from Wide survey are those that benefit most from the presence of the BAOs. This is mainly due to the fact that this survey provides the best sampling of the long wavelength modes corresponding to the most prominent first oscillation harmonics. The inclusion of the BAOs analysis increases the FoM by a factor of 2.1 in this case. On the other hand, no significant information on BAOs is provided by the Medium and the Deep surveys. As for the Medium survey, FoM does not increase, while the FoM provided by Deep survey increases by a factor of 1.2. In fact, the Deep survey seems to convey slightly more information on the BAOs. This is mainly due to higher number density of clusters in this survey, that allows to decrease the noise in the sampling of the BAOs.

### Information from the power spectrum shape

To quantify the geometrical information encoded in the matter power spectrum shape, we fit the shape parameter  $\Gamma$  in our analysis, regardless of its dependence on  $\Omega_m$ ,  $h$  and  $\Omega_b$  which is specific to the type of Dark Matter. We compare the results obtained by assuming Dark Matter to be Cold with those obtained for a general form of Dark Matter. In the latter case  $\Gamma$  is treated as a free parameter. In the former case, under the CDM assumption, the shape of the transfer function is determined by  $\Omega_m h$ , that specify the size of horizon at the matter-radiation equality epoch, and by the baryon density parameter. For this reason, the power spectrum shape carries information on the cosmic expansion history. Relaxing the CDM assumption, other characteristic scales could enter in determining the shape of the power spectrum. For instance, if massive neutrinos provide a contribution to the DM budget, the power spectrum is expected to be suppressed with respect to the pure CDM scale on scales smaller than the characteristic neutrino free streaming scale (e.g., Hannestad, 2010; Marulli et al., 2011), and already available data on the evolution of the cluster mass function have been used to set

interesting constraints on neutrino mass (Mantz et al., 2010b).

In Figure 3.12 we show the expected 68 per cent confidence ellipse on the  $(\Omega_m, \sigma_8)$  plane, by combining cluster number counts and power spectrum information for the three surveys together, when leaving the shape  $\Gamma$  as a free parameter (blue dotted ellipse) and when using instead its CDM expression (red solid ellipse). In order to make more clear the effect of assuming a CDM power spectrum on these constraints, we fix to their reference values the parameters that, along with  $\Omega_m$ , determine the power spectrum shape, namely  $\Omega_b$ , the Hubble parameter  $h$  and the primordial spectral index  $n_s$ . Relaxing the assumption of a CDM spectrum relaxes the constraints; since the effect is more pronounced for the matter density parameter, the direction of degeneracy also changes in the sense of a milder dependence of  $\sigma_8$  on  $\Omega_m$ .

As for the constraints on the DE parameters, since the largest survey area provides the best sampling of the power spectrum shape, we find that if we relax the assumption of CDM, the FoM of the Wide survey decreases by 7 per cent. This decrement is less pronounced in the Medium and Deep surveys, whose FoM decreases respectively by 4 and 5 per cent, owing to their weaker sensitivity to the spectrum shape.

### Information from redshift-space distortions

In this section we discuss the effect of including information from RSDs in the power spectrum analysis. We remind here that we restrict our analysis to the linear regime, while we do not attempt to include the non-linear distortions taking place on small scales. In this case the dependence of the power spectrum on the angle between line of sight and wavenumber directions is expressed by Eq. 1.49. Including information on the RSDs provides additional information on the linear growth rate of perturbations.

In Figure 3.13 we show the constraints on the  $(w_0, w_a)$  DE EoS parameters obtained by either including (blue dotted ellipse) or excluding (dot-dashed cyan ellipse) RSDs information in the analysis of the cluster power spectrum. Both contours represent constraints derived by combining the power spectrum Fisher Matrix from the combination of the three surveys, also including Planck prior on cosmological parameters and *strong prior* on mass-parameters. Including information from RSDs turns into a significant tightening of the DE constraints, thanks to the additional constraints provided on the linear perturbation growth rate.

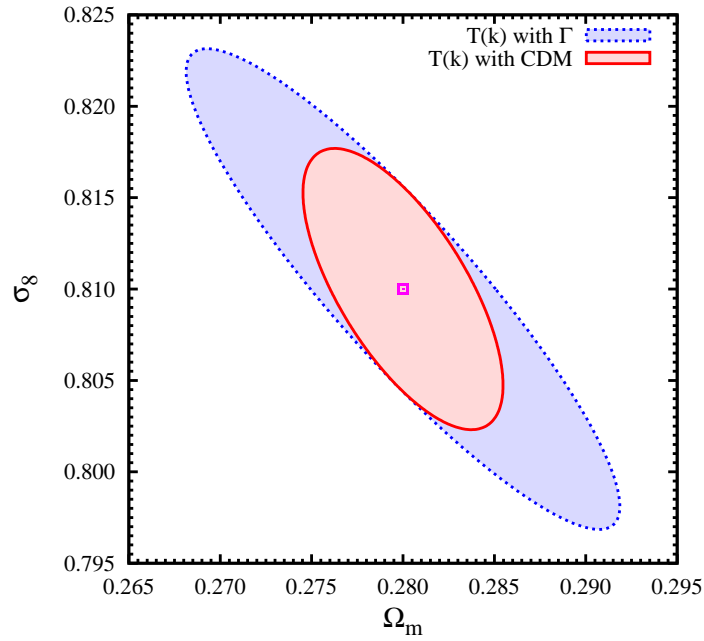


Figure 3.12: Constraints at the 68 per cent confidence level on the  $(\Omega_m, \sigma_8)$  parameters by leaving the shape parameter  $\Gamma$  as a free fitting parameter (dotted blue ellipse) or assuming its CDM dependence on  $\Omega_m$ ,  $h$  and  $\Omega_b$ , (solid red ellipse). All constraints are obtained by combining information from the three surveys together, including number counts and power spectrum information. In both cases, we assume here the values of the parameters  $h$ ,  $\Omega_b$  and  $n_s$  to be fixed at their reference values (see text). No Planck prior are assumed in this case, while *strong priors* are assumed on the mass-parameters.

Such an extra constraint turns into an increase of the FoM by a factor of 2.2. By analysing the three surveys separately, if we do not add Planck prior, we find that including RSDs information enhance the value of the FoM by a factor of about 35, 7.75 and 6.8 for the Wide, Medium and Deep surveys, respectively. The increasing contribution of RSDs with survey depth is due to the fact that tighter constraints are obtained by extending the redshift baseline over which the evolution of perturbation growth is followed.

We emphasize once again that large surveys of galaxy clusters do have the potential of conveying cosmological information from RSDs. This in turn highlights the importance for such surveys of providing precise measurements of redshifts for all clusters included.

### Constraints on Early DE models

As a final analysis, we derive forecasts for the constraints on the parameters defining the EoS of Early Dark Energy (EDE) model of Eq. 3.2, which assumes the parametrization by Grossi et al. (2009) from WFXT *Bright Sample*. In Figure 3.14, we show constraints obtained on the  $(\Omega_{DE}, w_0)$  parameters. Cluster number counts and bias are computed by using the standard mass function by Jenkins et al. (2001). In fact, as discussed by Grossi et al. (2009), the expression of the mass function calibrated on N-body simulation according to  $\Lambda$ CDM model is a reliable description also of the one provided by simulations of EDE models, at least as long as DE is homogeneous on small scales (see also Francis et al., 2009).

Left panel of Figure 3.14 presents the constraints obtained for each of the three surveys and for their combination. They are obtained by combining cluster number counts and power spectrum information. We include constraints from the Planck prior and assume *strong prior* on mass-parameters. The results shown in this figure confirm that the Medium survey is the one carrying most of the information on the DE EoS, thus extending to EDE models what shown in the right panel of Figure 3.9.

In order to analyse the origin of the constraints on EDE parameters, we show in the right panel of Figure 3.14 how such constraints progressively tighten as we add information from cluster power spectrum and Planck experiment to the cluster number counts. They are expected to provide rather degenerate constraints on  $(w_0, \Omega_{e,de})$ , which is basically associated to the freedom of choosing a generic geometry of the Universe. Including the power spectrum analysis brings both information on geometry

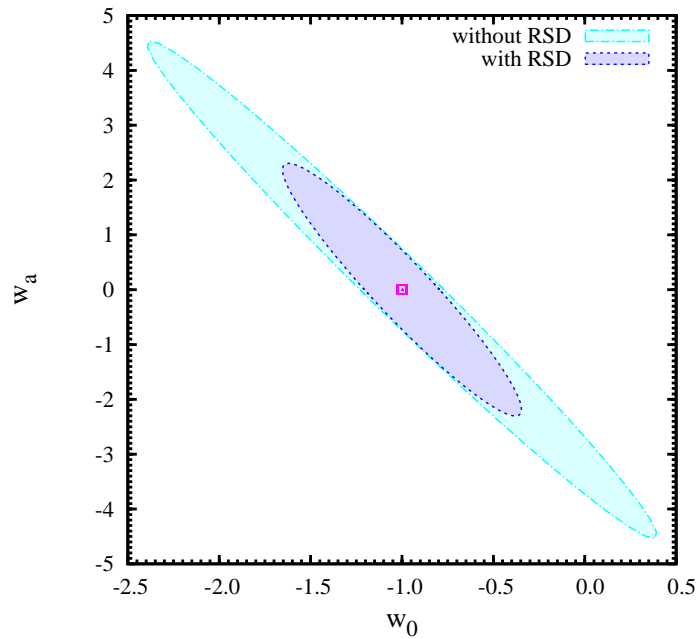


Figure 3.13: Constraints at the 68 per cent confidence level on the  $(w_0, w_a)$  DE EoS parameters, after including (dotted blue curve) or excluding (dot-dashed cyan curve) information from redshift-space distortions in the cluster power spectrum analysis. Constraints shown here are obtained by combining information for the three surveys together, including the prior information from the CMB Planck experiment, and assuming *strong prior* on the mass-parameters.

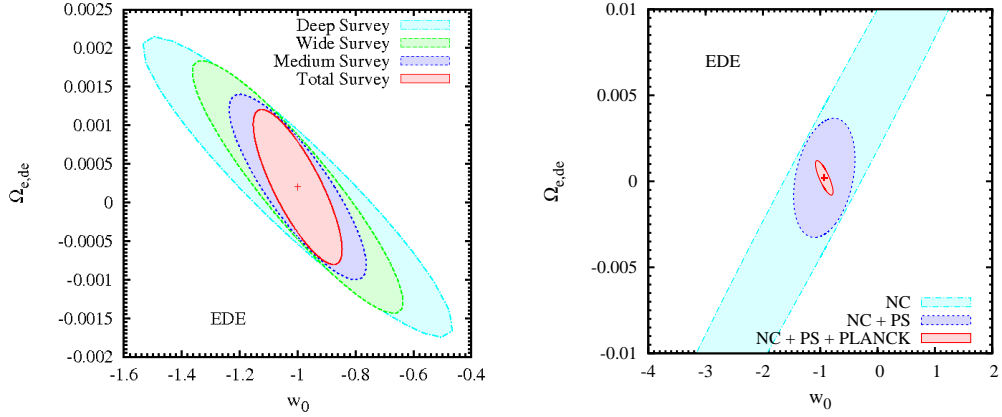


Figure 3.14: Constraints at the 68 per cent confidence level on EDE EoS parameters assuming *strong prior* on mass parameters from the Deep, Medium and Wide WFXT surveys for the *Bright Sample* (dot-dash cyan, dotted blue and dashed green curves, respectively). *Left panel*: Constraints obtained by combining number counts and power spectrum information. Also shown with the solid red curve are the constraints obtained from the combination of the three surveys. The FM from Planck experiment included in the calculation of all constraints. *Right panel* Constraints obtained by including the FM from number counts of cluster (dot-dashed cyan curve), adding power spectrum (dotted blue curve) and adding prior from Planck experiment (solid red curve). Such constraints are obtained by combining information for the three surveys together.

through the shape of the transfer function and additional information on perturbation growth through RSDs. Furthermore, adding also constraints expected from the Planck experiment causes constraints to be much improved, while changing the degeneracy direction. The reason for this is that in the EDE scenario, the purely geometrical constraints from CMB anisotropies become critical due to a non-negligible DE contribution to the total energy density of the Universe at  $z \sim 10^3$ . In general, this further highlights that tracing cosmic growth over the widest possible range of redshift is required in order to tightly constrain the values of DE EoS parameters.

### Comparison of constraints from WFXT and other cosmological experiments

In order to compare the constraints from the WFXT cluster surveys to those expected from other cosmological experiments, we also compare in Figure 3.15 the FoM expected from WFXT to those presented by Albrecht et al. (2006) for different large-scale structure probes. In the DETF report, they showed that Stage II cluster projects (ongoing surveys) provide FoM  $\sim 2$  (Figure 3.15) when combined with Planck priors. This analysis was carried out for a generic cluster count survey covering  $200 \text{ deg}^2$  up to  $z_{max} = 2$ , with the simple assumption of a constant mass selection function. According to Stage IV future experiments, by extending the survey area to  $20000 \text{ deg}^2$ , the FoM rises in the optimistic configuration <sup>6</sup> up to  $\sim 40$  with the contribution of the CMB Planck priors. We point out that the DETF analysis did not include the constraints expected from the power spectrum analysis. A similar value of the FoM was also obtained from an optimistic version of Stage IV project for BAO analysis based on galaxy redshift surveys, again including Planck priors. The constraining power of these optimistic <sup>7</sup> Stage IV experiments is somewhat weaker than that of the WFXT surveys, with the latter having a FoM larger by a factor of  $\gtrsim 2$ . In Figure 3.15, we also show for reference the FoM expected for an optimistic <sup>8</sup> Stage IV Weak Lensing experiment, which should reach a value of about 300.

We stress that the above forecasts from the WFXT surveys are obtained by considering a subsample of clusters with at least 1500 net photon counts. With this restriction robust mass and redshift measurements can be readily available from the same survey data, without resorting to external follow-up calibrations or observations. As such, the derived

---

<sup>6</sup> As for the clusters analysis, according to the optimistic configuration, the mean of the mass-observable relation and its variance per redshift interval of  $\Delta z = 0.1$  is assumed in the DETF report to be determined up to a level of 1.6 per cent.

<sup>7</sup> As for the BAOs analysis, the DETF report introduces the  $\sigma_F$  parameter, which describes the scatter in the relation between the true and the photometric redshifts,  $\sigma_F^2 = \text{Var}(z - z_{phot}) / (1 + z)^2$ . In the optimistic configuration  $\sigma_F = 0.01$ .

<sup>8</sup> As for the WL analysis in the DETF report, the r.m.s. bias  $\sigma_{\ln(1+z)}$  between the mean  $z$  and photometric redshift for galaxies in  $\ln(1 + z)$  for each bin of width 0.15 is assumed to be determined with a precision of 0.001. Moreover, the shear measurement is assumed to be miscalibrated by a factor  $(1 + f_{cal})$  that varies independently for each redshift bin. It is assumed that the calibration factor of each redshift bin has a Gaussian prior of width  $\sigma(f_{cal})$ . In the optimistic scenario this parameter was fixed to  $\sigma(f_{cal}) = 0.001$ .

constraints should be considered as rather conservative since they do not include possible information carried by clusters detected with a smaller number of photons or any other information to constrain mass from external observations (e.g., Sunyaev-Zeldvich fluxes, weak lensing masses and optical richness from future surveys). Lowering the flux limits of the WFXT surveys by a factor of 30 would still guarantee detection of clusters as extended sources, without however allowing a measurement of redshifts and robust mass proxies. Figure 3.15 shows that by including all the detectable clusters, the FoM increases by about one order of magnitude, even by assuming no prior on the mass parameters to compensate for the lack of robust mass measurements. We note that the Wide survey provides the largest constraining power for the DE parameters when we include all clusters down to the detection limit. In fact, in this case the Wide survey dominates the statistics of clusters counts out to redshift 1.5 (see Figure 3.3). Clearly, the results obtained from all the detected clusters must be considered as optimistic, since they rely on the possibility of confirming all these extended sources and measuring their redshifts with the aid of large follow-up observations.

### Constraints from EUCLID mission

We performed our analysis for the optical near-infrared EUCLID mission in order to obtain forecast on the DE Standard EoS parameters (Eq. 3.1). The photometrical EUCLID survey will cover an area of 20000 sq. deg. and will detect clusters down to the limiting mass  $M_{200,c} = 2 \times 10^{14} M_{\odot}$ , constant over the entire redshift range ( $0.2 < z < 2$ ) (Figure 3.5). This mass limit is calculated at  $3\sigma$  level of detection (i.e. the number of EUCLID-detected galaxies within  $r_{200,c}$  is 3 times the r.m.s. of the field counts in the cluster area). EUCLID will detect  $\sim 1.6 \times 10^5$  clusters,  $3.8 \times 10^4$  of them at  $z \geq 1$ . It will estimate the redshifts and calibrate the observable-mass relation using the WL EUCLID analysis and large follow up campaign.

In Figure 3.16 we show constraints on the DE EoS parameters from EUCLID. The combination of the FM analysis of the cluster number density and power spectrum from the EUCLID sample alone can constrain  $w_0$  and  $w_a$  at the level of  $\sigma_{w_0} = 0.09$  and  $\sigma_{w_a} = 0.88$  and by assuming *strong prior* on the mass parameters the constraining power i.e. the FoM increase from 16 to 37. As in the analysis performed for WFXT we found that clusters analysis alone cannot determinate the direction of degener-

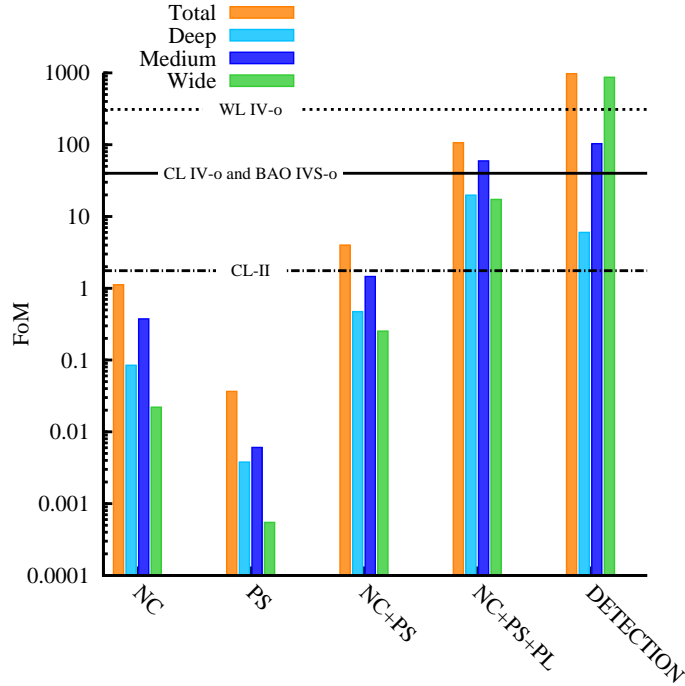


Figure 3.15: The histograms represent the Figures-of-Merit for the  $(w_0, w_a)$  parameters, as derived in the following configurations: by including the Fisher Matrix for the cluster number counts only (NC), for the cluster mean power spectrum only (PS), for the sum of the two (NC+PS), and by adding the prior from the Planck experiment (NC+PS+PL). All these FoM are obtained by assuming *strong prior* on mass-parameters for the *Bright Sample*. The last group of histograms shows FoM as obtained in the configuration NC+PS+PL by considering clusters in the *Detection Sample* and by assuming *no prior* on mass-parameters. The FoM for the Deep the Medium and the Wide cluster survey are shown with the cyan, blue, green histograms. The yellow histogram represent the FoM obtained from the combination of the three surveys. The horizontal lines show the FoM as reported in the DETF (Albrecht et al., 2006) for Stage II Cluster projects (CL-II; dot-dashed), for optimistic Stage IV BAO and Cluster projects (BAO IVS-o and CL IVS-o, respectively; solid line) and for optimistic Stage IV Weak Lensing project (WL IV-o; dotted line), by combining each probe with CMB Planck priors.

acy of the constraints in the  $(w_0, w_a)$  plane. By adding priors from Planck experiments, the geometry of the universe is in fact fixed and we obtain FoM=785 (176 if we consider *no prior* on mass parameters) and constraints on  $w_0$  and  $w_a$  of  $\sigma_{w_0} = 0.02$  and  $\sigma_{w_a} = 0.13$ . Constraints from WFXT, also represented in Figure 3.16, are weaker than those provided by EUCLID because at high redshifts the X-ray mass limit is much higher than the optical one because of the dimming of the surface brightness as  $(1+z)^4$ . More over we stress that we constraints shown for WFXT are obtained from the *Bright Sample*, within all the clusters are detected with at least 1500 photons, so the mass and the redshift of each cluster can be calculate directly in survey mode without any further follow-up observation.

In figure 3.17 we show constraints on the DE parameters  $w_0$  and  $\Omega_{DE}$  in the standard  $\Lambda$ CDM scenario for current data sets and future WFXT and EUCLID missions. Constraints from current clusters data have been provided by using the 400d sample based on ROSAT X-ray survey observation Vikhlinin et al. (2009b) that contains less than 90 clusters. With future experiments this number will increase of many order of magnitudes, and the constraining power of clusters will consequently increase.

### 3.6.2 Constraints on non-Gaussianity

We present results on non-Gaussian models from WFXT *Detection Sample*. These results are shown in terms of constraints on the  $(\sigma_8, f_{NL})$  plane after marginalizing over the other cosmological and mass parameters. Unless differently specified, all constraints are provided by adding Planck priors and assuming *no prior* on mass parameters. The reason for this choice is that, for a fixed Friedmann background,  $\sigma_8$  and  $f_{NL}$  are the two parameters which determine the timing of structure formation and, therefore, the evolution of number density and large-scale clustering of galaxy clusters. In the following, we will always show constraints on the  $(\sigma_8, f_{NL})$  plane at the 68 per cent confidence level.

In analogy with the Figure-of-Merit introduced to quantify the constraining power of an experiment for the Dark Energy EoS (e.g., Albrecht et al., 2006, 2009; Wang, 2008), we introduce a Figure-of-Merit for the timing of structure formation in non-Gaussian models:

$$\text{FoM}_{\text{SFT}} = (\det[\text{Cov}(\sigma_8, f_{NL})])^{-1/2}, \quad (3.17)$$

where  $\text{Cov}(\sigma_8, f_{NL})$  is the covariance matrix between  $\sigma_8$  and  $f_{NL}$ , which

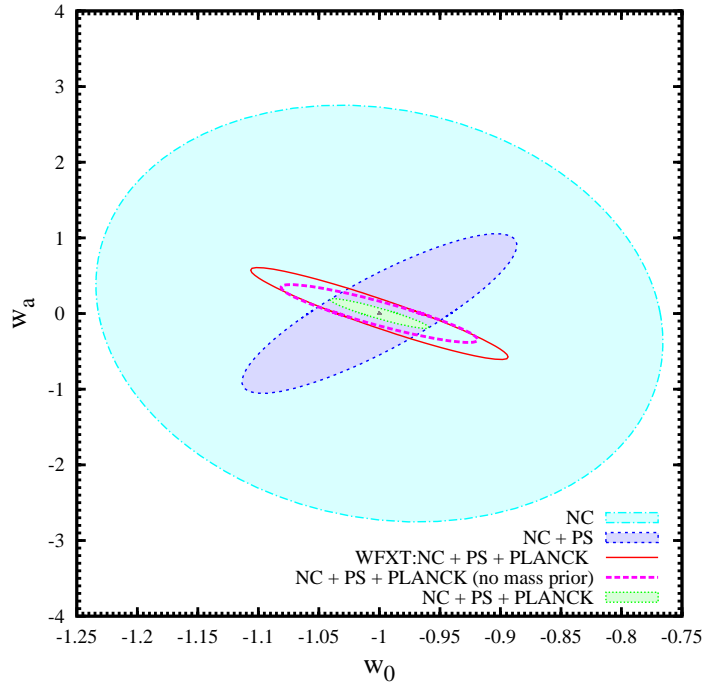


Figure 3.16: Constraints at the 68 per cent confidence level on the  $(w_0, w_a)$  DE EoS parameters. Contours are obtained by including the Fisher Matrix from cluster number counts only (NC; cyan ellipse), adding cluster power spectrum information (NC+PS; blue ellipse), and adding priors from the Planck experiment (NC+PS+PLANCK; red ellipse). All these constraints are obtained by combining information from the EUCLID survey and assuming the *strong prior* on the mass parameters. For comparison we also show the NC+PS+PLANCK results (magenta-dashed curve) assuming *no prior* on mass parameters. The solid-red curve represent constraints obtained from the combination of the three WFXT survey of the *Bright Sample* including the Fisher Matrix from NC+PS+PLANCK and assuming *strong prior* on the mass parameters.

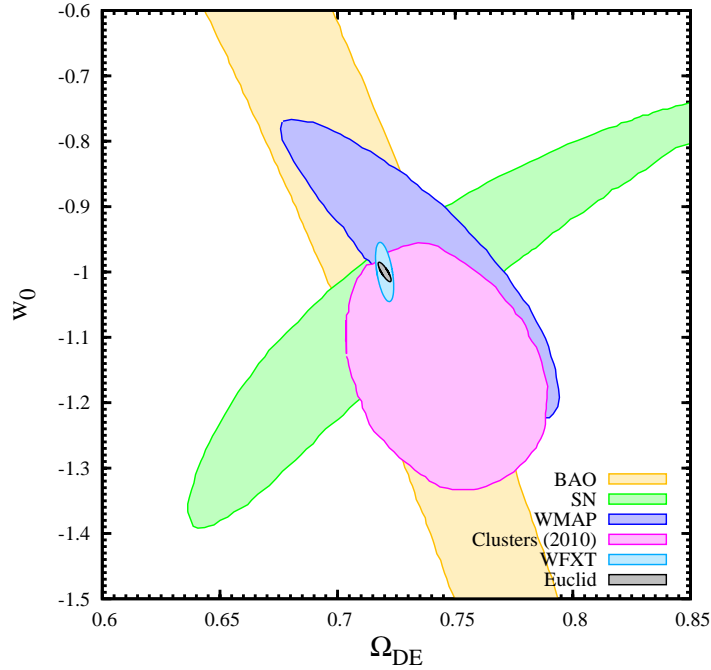


Figure 3.17: Constraints on  $(w_0, \Omega_{DE})$  parameters from current data sets: Baryonic Acoustic Oscillations (yellow region), type-Ia SNe (green region), WMAP (blue region) and current constraints from cluster samples 400d (Vikhlinin et al., 2009b). The ellipses represent constraints from future experiments, based on both the evolution of the cluster abundance and the power spectrum information and assuming *strong prior* on the mass parameters. Cyan ellipse show constraints from the combination of the three WFXT surveys of the *Bright Sample*, and grey ellipse constraints from EUCLID sample. All constraints corresponds to  $\chi^2 = 1$  (i.e. 68 per cent confidence level for one significant parameter) and are obtained under the assumptions of flat Universe, constant DE EoS, prior on Hubble parameter ( $h = 0.08$ ).  $\Omega_b$  parameter is fixed to its reference value.

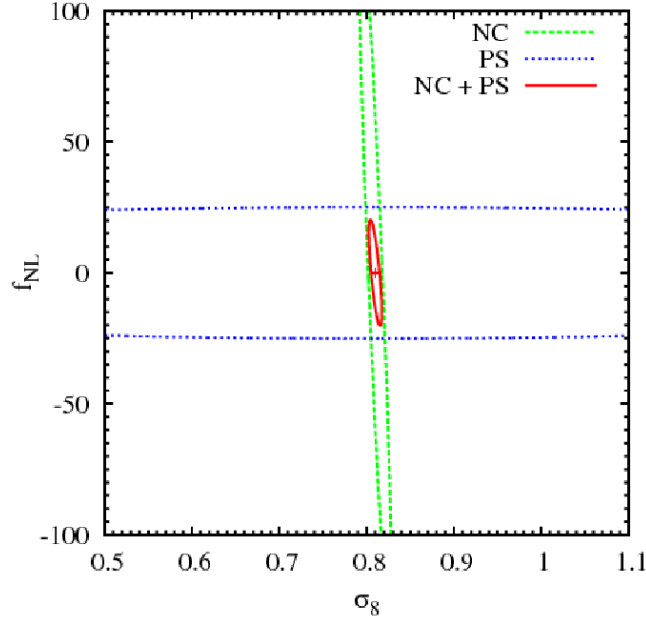


Figure 3.18: Constraints at the 68 per cent confidence level on non-Gaussian parameter  $f_{\text{NL}}$  and power spectrum normalization  $\sigma_8$  coming from number counts alone (short-dashed green curve), power spectrum alone (dotted blue curve) and from the combination of the two (solid red curve). The analysis refer to the in the Wide Survey of the WFXT *Detection Sample*. *No prior* is assumed for the values of the mass parameters. The Fisher Matrix from Planck experiment is included in the calculation of all constraints.

is obtained by inverting the FM and marginalizing over all the other parameters.

We show in Figure 3.18 the constraints on the  $f_{\text{NL}}$  and  $\sigma_8$  parameters computed from the number counts and from the power spectrum within the Wide survey, by assuming *no prior* on the values of the mass parameters. This plot clearly demonstrates the strong complementarity that number counts and large-scale clustering have to constrain  $\sigma_8$  and  $f_{\text{NL}}$ : while number counts are highly sensitive to the value of  $\sigma_8$ , the weak sensitivity of the high-end of the mass function to non-Gaussianity (e.g., Fedeli et al., 2009, and references therein) provides only very weak constraints on  $f_{\text{NL}}$ ; conversely, the scale-dependence of bias makes the power spectrum a powerful diagnostic for non-Gaussianity, while providing only loose constraints on  $\sigma_8$ .

Table 3.4: Figure-of-merit of structure formation timing,  $\text{FoM}_{\text{SFT}}$  [see Eq. 3.17], and r.m.s. uncertainty in the non-Gaussian parameter,  $\sigma_{f_{\text{NL}}}$ , for the three surveys, and for their combination, assuming different priors for the mass parameters. Columns 3-6 show the results for the Wide, Medium and Deep Surveys, and for the combination of the three.

Sample - mass prior		Wide	Medium	Deep	Total
Detection - no pr.	$\text{FoM}_{\text{SFT}}$	33.1	8.5	0.4	39.2
	$\sigma_{f_{\text{NL}}}$	11.3	18.5	84.2	10.4
Detection - weak pr.	$\text{FoM}_{\text{SFT}}$	33.3	8.8	0.6	39.4
	$\sigma_{f_{\text{NL}}}$	11.3	18.4	84.3	10.4
Detection - strong pr.	$\text{FoM}_{\text{SFT}}$	157.2	49.3	3.0	183.2
	$\sigma_{f_{\text{NL}}}$	11.2	18.0	80.9	10.3
Bright - strong pr.	$\text{FoM}_{\text{SFT}}$	7.3	14.3	3.0	22.3
	$\sigma_{f_{\text{NL}}}$	55.9	45.9	85.7	33.8

If we combine all the information obtainable from the three WFXT surveys of the *Detection Sample*, we obtain the constraints shown in Figure 3.19. Most of the constraining power is provided by the Wide survey, with only little information on structure formation timing carried by the Medium and Deep ones. There are two main reasons for this. First, the Wide survey provides the largest statistical baseline out to  $z \simeq 1.5$ , when including all clusters down to the mass limit corresponding to detection (see left panel of Figure 3.3). This implies a better determined mass function and, therefore, stronger constraints on  $\sigma_8$ . Second, the larger area coverage of the Wide survey allows it to better sample long-wavelength modes, where the scale-dependence of the bias induced by non-Gaussianity can be better assessed, thus turning into stronger constraints on  $f_{\text{NL}}$ . As shown in Table 3.4 the value of  $\text{FoM}_{\text{SFT}}$  for the combination of the three surveys is in fact dominated by the Wide Survey.

The contribution of information to the Fisher Matrix carried by the power spectrum at different redshifts and wavenumbers can be understood by looking at the dependence of the effective volume,  $V_{\text{eff}}$ , on the power spectrum, which is set by the bias parameter, and on the level of Poisson noise, which is set by the number density of clusters. Following Eq.(3.13), we define the quantity

$$W_v(k, z) = \left[ \frac{\tilde{N}(z)\bar{P}_{cl}(k, z)}{1 + \tilde{N}(z)\bar{P}_{cl}(k, z)} \right]^2, \quad (3.18)$$

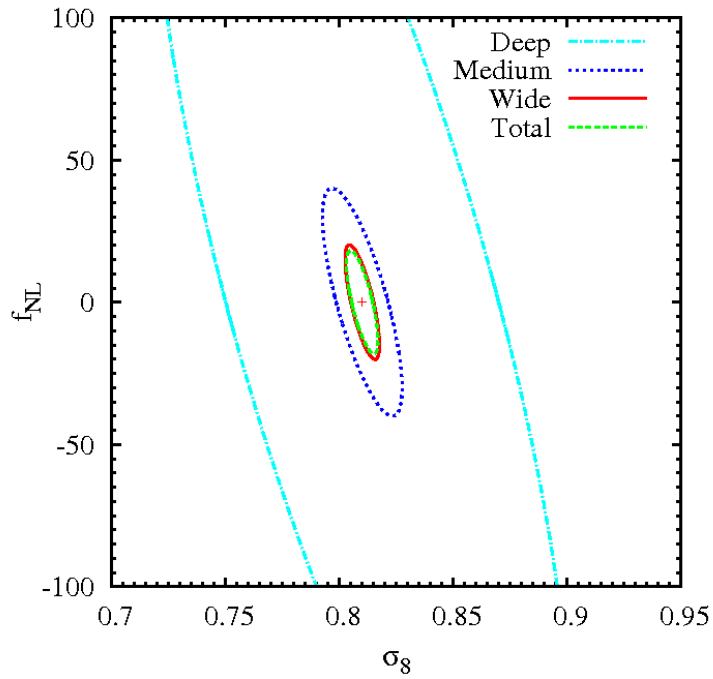


Figure 3.19: Constraints at the 68 per cent confidence level on  $(f_{\text{NL}}, \sigma_8)$  parameters from the Deep, Medium and Wide surveys of *Detection Sample* (dot-dashed cyan, dotted blue and solid red curves, respectively), by combining number counts and power spectrum information, by using no priors on the mass parameters. Also shown with the short-dashed green curve are the constraints obtained from the combination of the three surveys. *No prior* is assumed for the values of the mass parameters. The Fisher Matrix from Planck experiment is included in the calculation of all constraints.

which gives the weight carried by the wavenumber  $k$  to the computation of the clustering Fisher Matrix at redshift  $z$ . In the left panel of Figure 3.20 we show the redshift dependence of the effective volume computed within redshift intervals of constant width  $\Delta z = 0.2$ , for different values of  $k$ , and compare them to the total comoving volume computed within the same redshift intervals. The effective volume lies always well below the total comoving volume: this is the consequence of the relatively low value of the cluster number density, which makes Poisson noise always dominating. While the total comoving volume  $V_0$  increases with redshift, the effective volume  $V_{eff}$  starts declining after reaching a maximum, at  $z \simeq 0.5$ , for all wavenumbers. As for the dependence on  $k$ , at a fixed redshift, the value of  $V_{eff}$  decreases for both very high and very low values of  $k$ . As shown in the right panel of Figure 3.20, the value of the weight function  $W_v(k, z)$  is maximized at  $k \simeq 0.01 \text{ Mpc}^{-1}$ . In fact, for  $W_V \ll 1$  (i.e.  $\tilde{N}(z)\bar{P}_{cl}(k, z) \ll 1$ ), the  $k$ -dependence of  $W_V$  reflects that of  $\bar{P}_{cl}$ . Poisson noise is, again, responsible for the low values of  $W_V$ , well below unity. Decreasing of the level of this noise would require increasing the number density of objects to be included in the survey. This could be accomplished in principle by decreasing the mass threshold. However, this would require bringing into the surveys low-mass clusters and groups, for which our parametrization of the mass-observable relation may not still be valid.

So far, we presented results by assuming prior on cosmological parameters from Planck experiment and *no prior* knowledge on the mass parameters. We want to stress that, as already discussed in Sect. 3.4.2, this is probably too much a conservative approach, in view of the calibration of the relation between robust mass proxies (e.g.,  $Y_X$  and  $M_{gas}$ ) and X-ray luminosity for a large number of clusters within the planned surveys. In Figure 3.21 we show the effect of assuming a prior knowledge of the mass parameters. If we assume the *weak priors* for these parameters (see Sect. 3.4.2), constraints are only slightly improved. Quite interestingly, even assuming the *strong prior* (i.e. mass parameters fixed) improves the constraints on  $\sigma_8$ , while having a smaller impact on those for  $f_{NL}$ . Indeed, we find that the error on non-Gaussianity only decrease from  $\sigma_{f_{NL}} \simeq 10.4$  to 10.3 when passing from the *no prior* to the *strong prior* assumption, while the Figure-of-Merit increases from  $\text{FoM}_{\text{SFT}} \simeq 39.2$  to  $\simeq 183.2$  (table: 3.4).

To better understand the reason for the weak dependence of the  $f_{NL}$  constraints on the uncertain knowledge of the mass parameters, we show

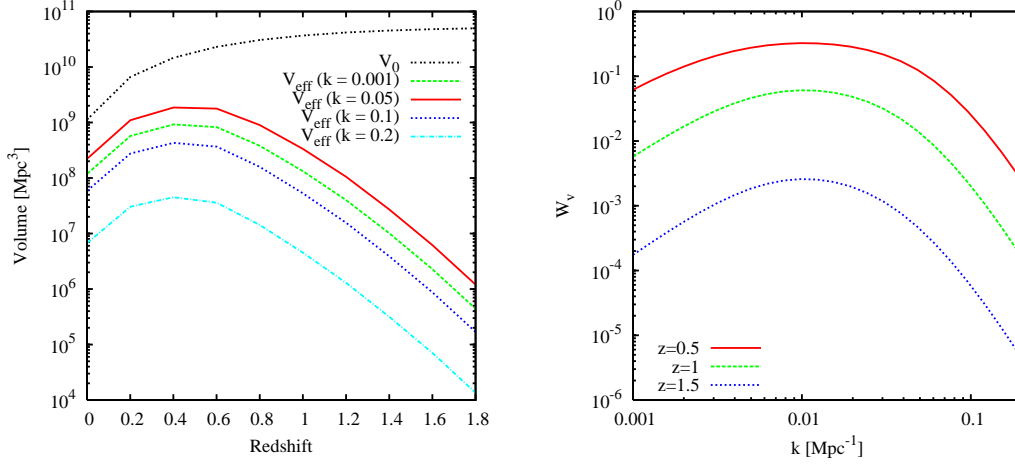


Figure 3.20: *Left panel*: the redshift dependence of the effective volume, defined as in Eq.(3.13), within redshift intervals of constant width  $\Delta z = 0.2$ , for four values of the wavenumber  $k$ . Short-dashed (green), solid (red), dotted (blue) and dot-dashed (cyan) curves correspond to  $k = 0.001, 0.05, 0.1$  and  $0.2 \text{ Mpc}^{-1}$ , respectively. *Right panel*: the dependence on the wavenumber of the weight  $W_v(k, z)$ , defined as in Eq.(3.18), at three different redshifts. Solid (red), dashed (green) and dotted (blue) curves are for  $z = 0.5, 1$  and  $1.5$ , respectively.

in Figure 3.22 by how much number counts and effective bias change with respect to the value that they take in the Gaussian case, as we vary the mass bias parameter  $B_M$  (left panels) and the intrinsic mass-scatter  $\sigma_{\ln M}$  (right panels). As a reference value for the non-Gaussianity, we take here  $f_{\text{NL}} = 10$ , which is comparable to the forecasted precision with which non-Gaussianity can be constrained from our analysis. At  $z = 0.5$  the deviation of the number counts from the non-Gaussianity (upper panels) varies only by about one part over thousand when a generous range of variation is allowed for both  $B_M$  and  $\sigma_{\ln M}$ , with only a slightly higher sensitivity to these parameters at  $z = 1$ . In the bottom panels of Figure 3.22 we show the sensitivity of the effective bias on mass parameters for different values of the wavenumber  $k$ . Results are shown at  $z = 0.5$  which is close to the redshift where the effective volume  $V_{\text{eff}}$  reaches its maximum value (see left panel of Figure 3.20). For the level of non-Gaussianity assumed here, the deviation from the Gaussian effective bias is negligible at the wavenumbers,  $k \simeq 0.01 \text{ Mpc}^{-1}$ , which are mostly weighted in the computation of the Fisher Matrix (see right panel of Figure 3.20). However, as expected, the effect of non-Gaussianity on  $b_{\text{eff}}$  shows up at very

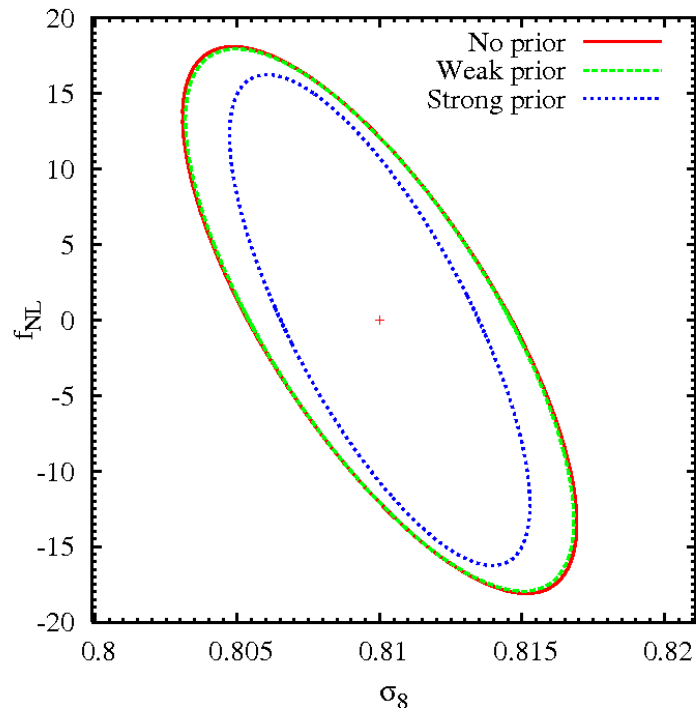


Figure 3.21: Constraints at the 68 per cent confidence level on  $(f_{NL}, \sigma_8)$  parameters by assuming *no prior* (solid red curve), *weak prior* (dashed green) and *strong prior* (dotted blue) on the mass parameters. All constraints are obtained by combining cluster number counts and power spectrum information for the three surveys together. The Fisher Matrix from Planck experiment is included in the calculation of all constraints.

large scales, with a deviation with respect to the Gaussian result by  $\gtrsim 40$  per cent for  $k \simeq 10^{-3} \text{ Mpc}^{-1}$ . This highlights the importance for future surveys to have a highly uniform calibration of the selection function over large area of the sky, for them to be able to appreciate any subtle scale dependence of the bias parameter. Also in this case, any variation with the value of the mass parameters is far smaller than the deviation from Gaussianity. This justifies the weak dependence of the  $f_{\text{NL}}$  constraints on the uncertain knowledge of the cluster mass calibration.

### 3.7 Conclusions

In this Chapter, have been presented forecasts on the capability of future surveys of galaxy clusters to yield constraints on the parameters defining Dark Energy (DE) equation of states (EoS), and in the deviation from Gaussianity primordial perturbations. As for the DE EoS we consider standard parametrization provided by equation (3.1) and the class of Early DE models of equation (3.2). Our analysis was carried out for both optical and X-ray future surveys. As for the X-ray, we consider an experiment which covers wide area and have, at the same time, enough sensibility to provide accurate measurements of X-ray mass proxies for a large subsample of clusters. The proposed WFXT answer such requirements so we use this experiments as a reference mission concept along with the Wide (20000 sq.deg.), Medium (3000 sq.deg.) and Deep (100 sq.deg.) survey configurations. As for the optical band, we consider the optical near infrared EUCLID mission with a survey area of 20000 sq. deg., and a mass limit approximately constant ( $M_{200,c} \simeq 2 \times 10^{14} M_{\odot}$ ) over the entire redshift range ( $0.2 < z < 2$ ).

In order to conduct our analysis we develop a code that calculate the Fisher Matrix by combining information on the cluster number density and power spectrum.

As for forecast on the standard DE, we carry out our reference analysis for the WFXT *Bright Sample* (see Table 3.1). The main results of this study can be summarized as follows.

- (a) When constraining the parameters of the DE EoS of equation (3.1), we further demonstrate the fundamental importance of having a well calibrated X-ray observable-mass relation and, most importantly, its redshift evolution.

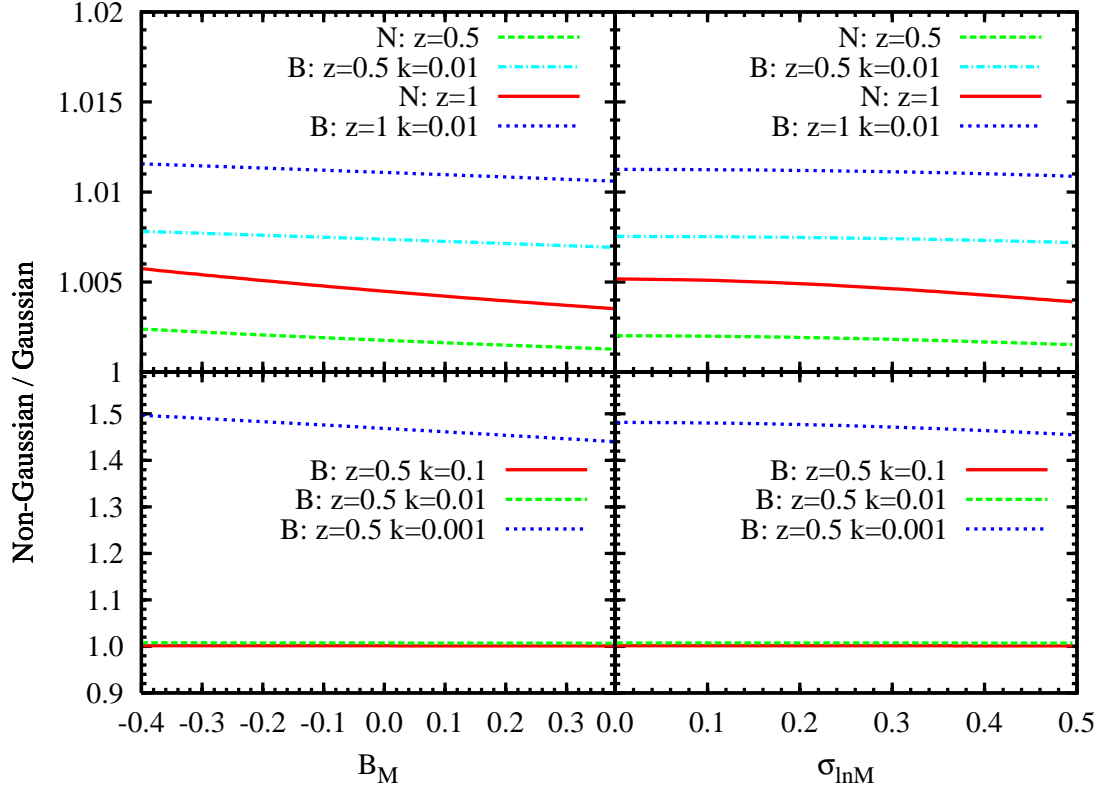


Figure 3.22: Effect of changing the values of the mass parameters of mass bias  $B_M$  (left panels) and intrinsic mass scatter  $\sigma_{\ln M}$  on the deviations of number counts and effective bias from the Gaussian case. The results shown here are obtained by assuming a mass-limit of  $10^{14}M_{\odot}$ . The reference value of non-Gaussianity assumed here is  $f_{\text{NL}} = 10$ .  $N$  is the ratio between the redshift distributions in the Gaussian and non-Gaussian cases, while  $B$  is the ratio between the effective bias, as defined in Eq. 3.12, in the Gaussian and non-Gaussian cases. Upper panels show the results for number counts and effective bias at two different redshifts,  $z = 0.5$  and  $z = 1$ . Lower panels show results for the effective bias at  $z = 0.5$  for different wavenumbers,  $k = 0.1, 0.01$  and  $0.001 \text{ Mpc}^{-1}$ .

We verified that the Figure of Merit (FoM) of the DE EoS increases up to 106 when we assume a strong prior on the mass parameters, as resulting from a precise and robust calibration of the mass-observable relation, with respect to the case in which no such prior is available (FoM = 61) (see Table 3.3). Such an internal calibration can be achieved only by having at least  $\sim 10^3$  net photon counts for each cluster included in the survey.

- (b) We find that the Medium survey is the one carrying most of the constraining power (Table (3.2)), since this survey is expected to yield the largest number of cluster out to redshift  $z \sim 1$ . As such, it shows the tightest constraints on the evolution of the DE EoS ( $\sigma_{w_0} = 0.097$  and  $\sigma_{w_a} = 0.54$ ) and the corresponding highest Figure of Merit (FoM = 60). The Deep survey, although covering a much smaller area than the Wide survey, adds an important contribution to constrain DE parameters (FoM = 20).
- (c) We quantified the increase of the constraining power from the three surveys separately and from their combination, by adding progressively information from the cluster number counts, the mean cluster power spectrum analysis and the CMB prior from Planck experiment. We summarize in Figure 3.15 the resulting improvements on FoM. The slightly different directions of degeneracy of the constraints in the  $(w_0, w_a)$  parameters space from cluster number counts and power spectrum explains why the constraints substantially improve when we consider the two contribution together rather than separately. We verified that adding the CMB information improve the corresponding constraints on the DE EoS, mostly as a consequence of the constraint provided by CMB data on the geometry of the Universe (right panel of Figure 3.11).
- (d) We find that RSDs carries important cosmological information through the linear growth of perturbations, also in the case of cluster surveys. Indeed, the DE FoM from the power spectrum analysis of the Wide survey increases by a factor 35 when including RSDs, while increasing by a factor 7.7 and 6.8 for the Medium and the Deep surveys, respectively.
- (e) As for the information carried by the shape of the power spectrum, a smaller increase in the FoM is instead measured when includ-

ing BAOs. In this case the FoM from the power spectrum analysis of the Wide survey increases by a factor of 2, while no significant information on BAOs is provided by the Medium and the Deep surveys. Furthermore, relaxing the assumption of CDM and treating the shape of the power spectrum as a free parameter reduces the FoM by a factor of 1.7 in the analysis of the Wide survey.

We extend the analysis carried out for the standard DE EoS to the Early-DE one. Such analysis confirm that the Medium survey is the one carrying most of the information on the DE EoS, and emphasize once more the importance of tracing cosmic growth over the widest possible range of redshift. By extending the redshift range of the sample and with the ability to internally calibrate the observable-mass relation, we expect to measure the EDE EoS parameter ( $\Omega_{DE}$ ) with an uncertainty of  $\sigma_{\Omega_{e,de}} = 6.6 \times 10^{-4}$ .

We extend our analysis for standard DE model to optical based EUCLID mission. and we find constraints the  $w_0$  and  $w_a$  at the level of  $\sigma_{w_0} = 0.02$  and  $\sigma_{w_a} = 0.13$  and a FoM=785, by combining results from EUCLID survey and Planck experiment.

Further analysis carried out in order to forecast constraints on non-Gaussian initial perturbations scenario indicates that the optimization of the survey strategy depends on the class of cosmological models that one wants to constrain. We used for this analysis the *Detection Sample* of WFXT (see Table 3.1). We showed forecasts for the two parameters that, for a fixed expansion history, define the timing of cosmic structure formation, namely  $\sigma_8$  and  $f_{NL}$ , while marginalizing over all the remaining parameters. Informations on such constraints are quantified by introducing the figure-of-merit for structure formation timing of Eq.(3.16).

The main results obtained from non-Gaussian analysis can be summarized as follows.

- (a) Power spectrum and number counts of galaxy clusters are highly complementary in providing constraints: while the former is sensitive to deviations from Gaussianity, through the scale dependence of the bias, the latter is mostly sensitive to  $\sigma_8$ .
- (b) Most of the constraining power for these two parameters lies in the *Wide Survey*, while the *Medium* and the *Deep Surveys* play an important role for the estimate of X-ray mass proxies for  $\simeq 2 \times 10^4$  clusters out to  $z \sim 1.5$ .

- (c) Combining number counts and power spectrum information for the three surveys turns into  $\Delta f_{\text{NL}} \simeq 10$  for the  $1\sigma$  uncertainty with which a deviation from Gaussianity associated to a “local shape” model can be constrained. Correspondingly, we find  $\text{FoM}_{\text{SFT}} \simeq 39$  for the figure-of-merit of structure formation timing.
- (d) The value of  $\text{FoM}_{\text{SFT}}$  significantly worsens when assuming more conservative priors on the nuisance parameters, the above constraint on  $f_{\text{NL}}$  is weakly sensitive on such priors.



## Chapter 4

# Cosmological constraints from current X-ray cluster surveys

As we showed in the previous Chapter, the evolution in the number density and the power spectrum of massive galaxy clusters can be used to constraints Dark Energy (DE) parameters from future X-ray and optical surveys. However, theoretical predictions always provide the number density and power spectrum bias of clusters as a function of mass, which is not a directly observed quantity. Consequently, we rely on observable quantities such as X-ray temperature, weak lensing shear, or other such signals, to estimate cluster masses. This link between the observable mass tracer (or proxy) and the theoretical cluster mass is the dominant source of systematics uncertainty in the analysis (e.g. Henry et al., 2009). Moreover, a cluster sample is needed which spans a large  $z$  range. In fact, we showed that constraints on DE Equation of State (EoS) parameters can be substantially improved by extending the redshift range over which the evolution of perturbation growth is studied.

In Section 1.10, we summarized the current state of constraints on cosmological parameters provided by the last X-ray (e.g. Vikhlinin et al., 2009b; Mantz et al., 2010a) and optical (e.g. Rozo et al., 2010) analyses. According to the  $\Lambda$ CDM model, the  $w$  parameter, describing the DE EoS, is constant and equal to  $-1$ ; observational signatures of possible deviations of  $w$  from such value are very small, and hence a great effort is necessary to the treatment of the systematic errors. In this sense, it is crucial that DE constraints at this level of accuracy are obtained from combination of several independent cosmological tests. Such combined analysis reduces systematics and improves statistical accuracy on

the models parameters in general, by breaking degeneracies among them. In fact, while constraints obtained on DE EoS parameters from 400d X-ray cluster survey alone are  $w = -1.14 \pm 0.21$  in a spatial flat Universe (Vikhlinin et al., 2009b), by combining results from CMB (Dunkley et al., 2009), SN Ia (Miknaitis et al., 2007), and BAO in the SDSS survey (Eisenstein et al., 2005), and from 400d cluster survey (Vikhlinin et al., 2009b), one obtains  $w = -0.991 \pm 0.045$ .

In this scenario, our analysis has been thought to explore the constraining power of cluster mass function at high redshift. To this aim, we use a sample of nine galaxy clusters at redshift  $z \geq 0.8$ , selected in the X-ray RDCS catalogue (Rosati et al., 1995, 1998). Despite the fact that in the last few years the number of clusters detected at high- $z$  increased from a handful to a few tens (e.g. Williamson & the SPT Team, 2011; Fassbender et al., 2011), high redshifts RDCS sample has the advantages that all the clusters are spectroscopically confirmed and the majority of them have very good mass determinations from extensive *Chandra*, HST and VLT follow-up programs carried out in the last ten years. The detection of high redshift massive clusters with XMM and SZ surveys have been used recently to quantify possible deviations from the  $\Lambda$ CDM model (e.g. Mortonson et al., 2011; Jee et al., 2011; Hoyle et al., 2011). In this prospect, having a well defined survey selection function and accurate mass measurements of the majority of clusters in our sample, we have studied how results obtained on cosmological parameters from clusters surveys at redshift  $z \simeq 0.5$  (Vikhlinin et al., 2009b) can be extended to redshifts higher than 0.8, by combine the high- $z$  RDCS sample with the Vikhlinin et al.'s sample. In this way, we strengthen cosmological constraints by computing for the first time the mass function at redshift  $z \geq 0.8$ .

## 4.1 The ROSAT Deep Cluster Survey

### 4.1.1 The sample selection

The RDCS sample was constructed from a serendipitous search for extended sources in deep pointed observation from the ROSAT PSPC archive with exposure time longer than 15 ks. We refer to Rosati et al. (1995) for a full discussion of the analysis of the X-ray data and the selection technique for the RDCS sample.

A wavelet detection algorithm (WDA) was used to identify and measure the angular extent of X-ray sources. The multi-scale analysis performed by the WDA reduces biases against low surface brightness source and is particularly efficient in minimizing the confusion effect, the main limiting factor in deep X-ray images and in separating extended from point-like emission. Over 160 cluster candidates were selected in 180 PSPC fields scattered across the two galactic caps ( $|b| > 20^\circ$ ) as sources with an extent exceeding the local PSF with a 90% confidence level, which was statistically determined by a control sample of several thousands sources (Rosati et al., 1995, 1998).

The completeness flux limit of the survey is determined by the flux level at which extended and point like emission can be reliably distinguished. In addition, the completeness depends critically on the off-axis angle  $\theta$  within which the candidates are selected; because of the PSF degradation, the selection function was modelled by using a combination of simulation and control sample of known distant clusters and by studying number counts as a function of the limiting X-ray flux,  $f_x$ , and  $\theta$ . The final sky coverage as calculated in Rosati et al. (1995) is plotted in Figure 4.1. For comparison, we show in Figure 4.2 the overview of the reference flux limits and areas of all major cluster surveys carried out after the completion of the ROSAT all-sky survey. In particular dark circles in this figure represent the ROSAT serendipitous surveys, like RDCS, that were constructed from thousands of pointed observations by selecting cluster candidates from a serendipitous search for extended X-ray sources above a given flux limit.

The final RDCS sample contains 103 spectroscopically confirmed clusters at  $z \leq 0.85$  identified over an area of approximately  $50 \text{ deg}^2$  down to the flux limit  $F_{\text{lim}} = 3 \times 10^{-14} \text{ erg s}^{-1} \text{ cm}^{-2}$  (RDCS-3). In Figure 4.4 we show the differential redshift distributions of the sample. RDCS-3 has overall a median redshift  $z_{\text{med}} = 0.29$ , with  $z_{\text{max}} = 0.85$ ; 26 clusters lie at  $z > 0.5$ , and 4 clusters at  $z > 0.8$ . One more cluster, XMMU-J0236.1-5254, which remained spectroscopically unidentified in RDCS-3, has recently been rediscovered in the XDCP survey (Fassbender et al., 2011) and its redshift measured at 0.865 (this cluster is included in Figure 4.4). We stress also that the cluster RDCS-J0152.7-1357 has been considered as a single system although both the optical galaxy distribution and the *Chandra* X-ray observation show two distinct clumps (see Figure 4.5). Moreover the dynamical analysis conducted by Demarco et al. (2007) shows that the velocity distribution of the cluster is consistent with two groups

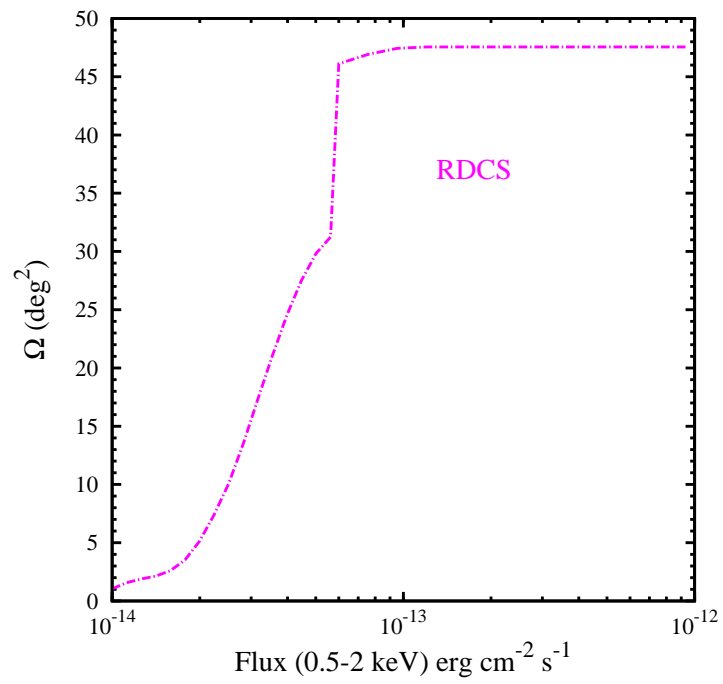


Figure 4.1: Sky coverage as a function of X-ray flux of RDCS sample (Rosati et al., 1998).

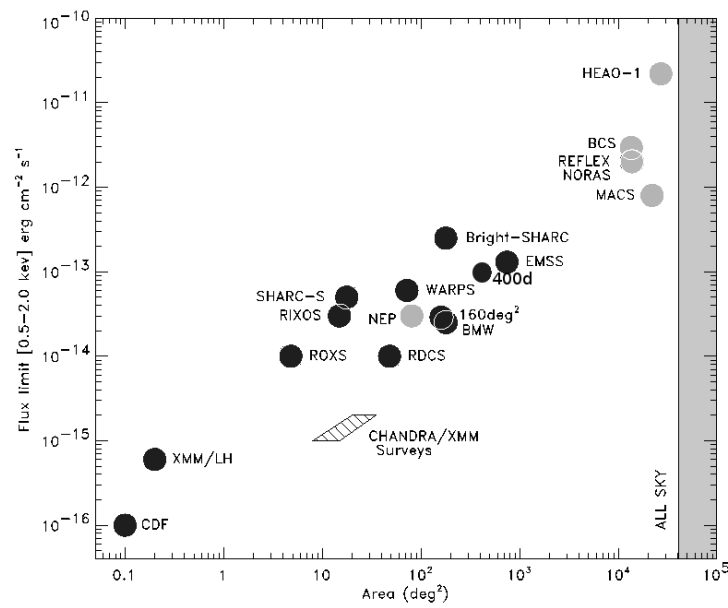


Figure 4.2: Areas and flux limits of X-ray cluster surveys carried out from the ROSAT all-sky observations. The light circles represent surveys covering contiguous areas, while the dark circles represent serendipitous surveys constructed from ROSAT-PSPC pointed observations. Figure adapted from Rosati et al. (2002).

that are also responsible for the projected elongation of the cluster. However, since the two clumps of RDCS0152.7-1357 lie within 1 Mpc (the two cores are 0.7 Mpc apart), we consider it as a unique massive object in a merging phase.

Several other clusters with  $z < 0.9$  have been identified in the RDCS at  $F_X < 3 \times 10^{-14} \text{ erg s}^{-1} \text{ cm}^{-2}$ . A deeper sub-sample of four clusters identified down to  $F_{lim} = 1 \times 10^{-14} \text{ erg s}^{-1} \text{ cm}^{-2}$  in the redshift range  $0.90 \leq z \leq 1.26$  (RDCS-1) is defined, whose redshift distribution is also shown in Figure 4.4. As discussed in Rosati et al. (1998), the sample is well characterized and complete at fluxes  $\gtrsim 3 \times 10^{-14} \text{ erg s}^{-1} \text{ cm}^{-2}$ . Below such value, the completeness of the sample becomes not as solid because with  $\lesssim 50$  counts, which roughly corresponds to the above flux for the typical exposure time of the selected PSPC fields, the detection and characterization of extended sources becomes increasingly uncertain. Despite such uncertainties of the sky coverage at fluxes  $\lesssim 3 \times 10^{-14} \text{ erg s}^{-1} \text{ cm}^{-2}$ , several follow-up analyses have suggested a substantial completeness of the sample and the correct characterization of the sky coverage down to  $f_x \simeq 1 \times 10^{-14} \text{ erg s}^{-1} \text{ cm}^{-2}$ . Borgani et al. (2001) showed that the XLF evolution traced by brighter clusters at  $z \lesssim 0.85$  also extends at fainter fluxes out to the highest redshift reached by RDCS. In Figure 4.3, we show the cumulative surface density of clusters above a given flux limit versus the flux value (the cluster LogN-LogS relation) as obtained for different cluster survey. In order to take into account the difference between the total and the observed fluxes, the LogN-LogS relation is computed by assigning to each cluster a weight equal to the inverse value of the area for its observed flux. Results from Finoguenov et al. (2007) from the XMM COSMOS survey found a good agreement with LogN-LogS relations of the RDCS sample (Rosati et al., 2002) for fluxes  $f_x > 10^{-14} \text{ erg s}^{-1} \text{ cm}^{-2}$ .

We define and use in this work a high- $z$  low flux cluster sub sample of nine clusters from the RDCS catalogue (zRDCS-1 hereafter). This new sample is shown in Figure 4.4 with magenta boxes. In Figures 4.5 and 4.6 we show the optical/nearIR colour images on the nine clusters with overlaid X-ray contours. In Table 4.1 are presented the details of the zRDCS-1 sample, whose redshift range starts at  $z = 0.805$  and extends to  $z = 1.273$ , with the median redshift  $\tilde{z} = 0.865$ . Extensive follow-up observations over the last decade have been performed in order to measure the mass of these clusters with different methods, minimizing the possibility of systematics errors. These include WL masses from HST observations, hydrostatic masses from *Chandra* data and spectroscopical analysis from

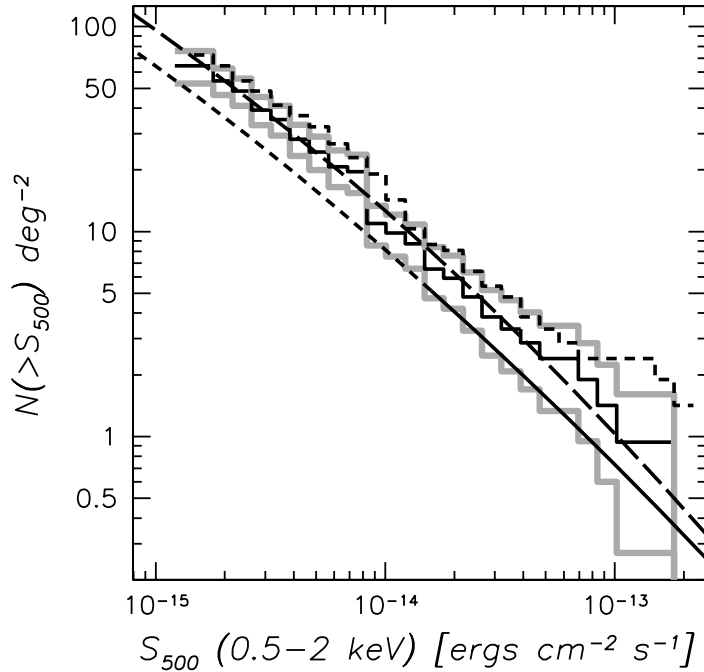


Figure 4.3: Cumulative cluster number counts. The black solid histogram shows the data for the XMM COSMOS survey, and grey histograms denote the 68% confidence interval (Finoguenov et al., 2007). The black solid/short-dashed curve shows the results from modelling the evolution of the RDCS sample (Rosati et al., 2002), with the solid part corresponding to fluxes sampled by RDCS, while the short-dashed curve denotes the prediction for evolution in the luminosity function. The long-dashed curve shows the prediction for no evolution in the luminosity function (Rosati et al., 2002).

VLT.

For two clusters, RDCS-J0337-34 and RDCS-J0236-52 (Figure 4.5), no follow up *Chandra* HST observations are available at present. The XMM serendipitous pointing on 0236-52 (Fassbender et al., 2011) is too shallow to provide useful temperature. For the two clusters, we resort to mass estimates from the well established  $L_X - M$  relation at relatively high redshift (Maughan, 2007)

#### 4.1.2 Mass measurements

**Weak-lensing masses.** In order to derive the lensing mass from the tangential shear, Jee et al. (2011) used the parametrized halo model fitting

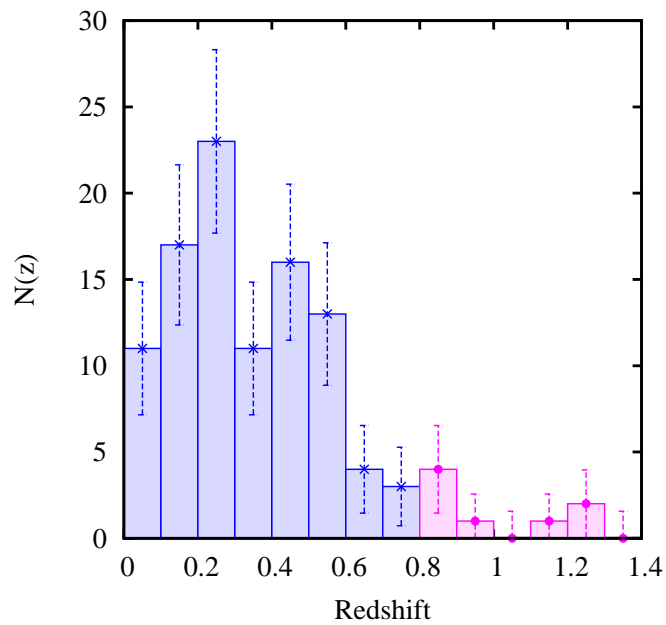


Figure 4.4: Redshift distribution of X-ray selected galaxy clusters from the RDCS (Rosati et al., 2002) (blue histogram) and its extension at the high- $z$  and low fluxes denoted as zRDCS-1 sample (magenta histogram). Error bars on data points correspond to  $1\sigma$  Poissonian uncertainties (Gehrels, 1986).

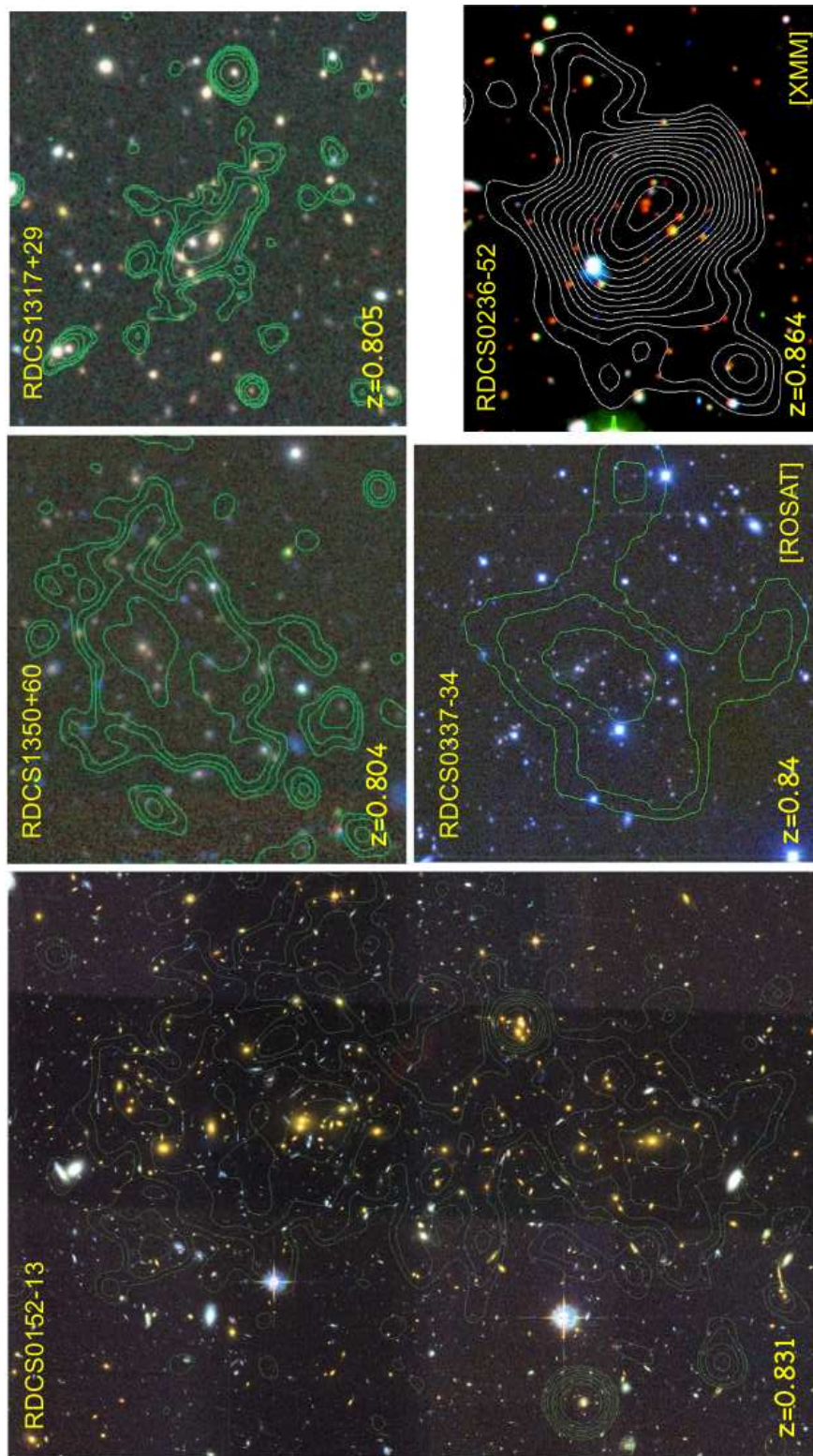


Figure 4.5: Optical/nearIR colour images with overlaid X-ray contours from *Chandra*, unless otherwise noted, for the five clusters of *z*RDCS-1 sample at  $0.8 < z < 0.9$ . Figures adapted from Holden et al. (2002) (RDCS 1350+60, RDCS 1317+29), Blakeslee et al. (2006) (RDCS 0152-13), Fassbender et al. (2011) (RDCS 0236-52).

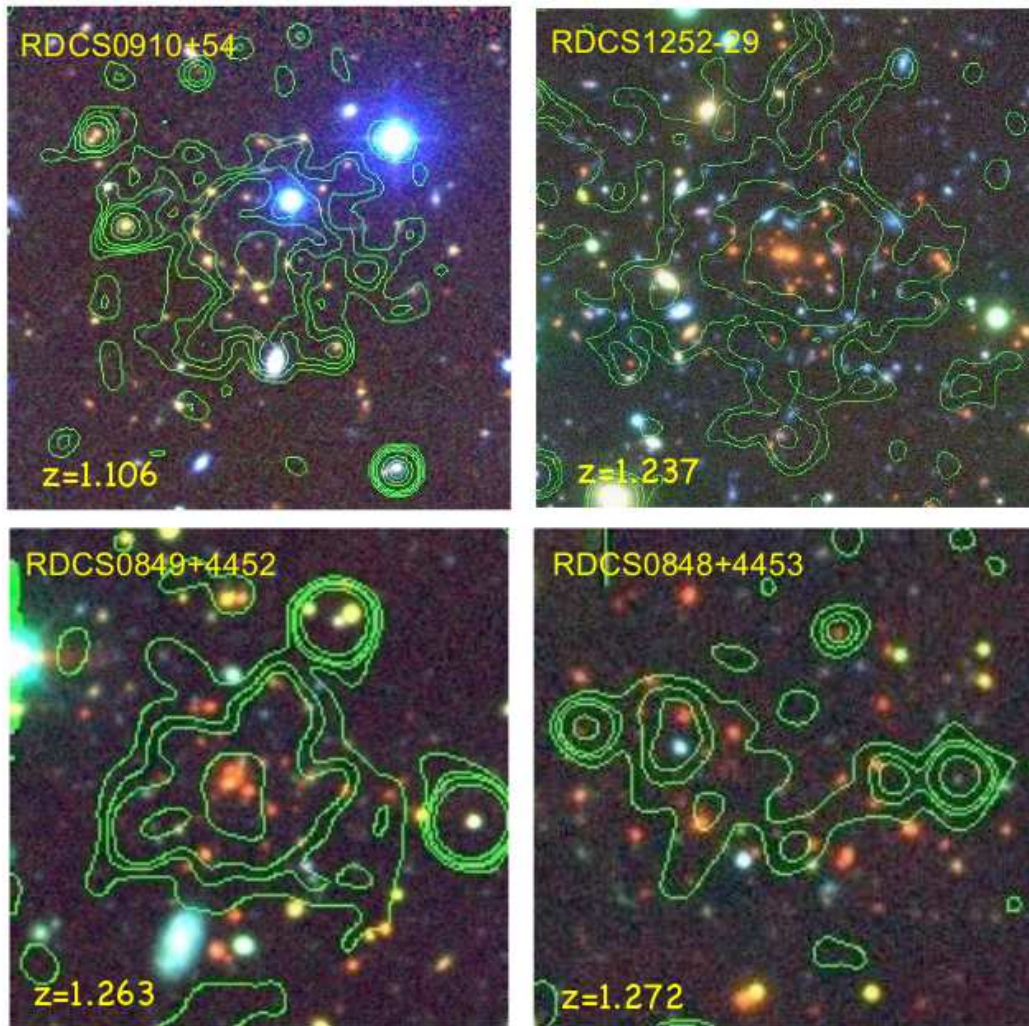


Figure 4.6: Optical/nearIR colour images with overlaid X-ray contours from *Chandra*, for the four clusters of  $z$ RDCS-1 sample at  $1 < z < 1.3$ . Figures from Stanford et al. (2002) (RDCS 0910+54), Rosati et al. (2004) (RDCS 1252-29), and Stanford et al. (2001) (RDCS 0849+4452, RDCS 0848+4453).

Table 4.1: Properties of the zRDCS-1 clusters. Column 2: redshifts. Column 3: effective exposure time after removal of high background intervals from *Chandra* observations (Balestra et al., 2007). Column 4: X-ray gas temperature. Column 5:  $R_{200}$  radius encompassing the density contrast  $\Delta_c = 200$  with respect to the critical density  $\rho_c(z)$ . Column 6: total mass at the radius inside  $R_{200,c}$  as obtained from the hydrostatic method. Column 7: cluster mass within  $R_{200,c}$  as obtained from weak lensing analysis (Jee et al., 2011).

Cluster	$z$	$t_{exp}$ [ks]	$T_X$ [keV]	$R_{200,c}$ [kpc]	$M_{X,200c}$ [ $10^{14} M_\odot$ ]	$M_{WL,200c}$ [ $10^{14} M_\odot$ ]
J1350.0+6007	0.804	58	$5.6 \pm 1.0$	$1151 \pm 103$	$4.3 \pm 1.1$	-
J1317.4+2911	0.805	110.5	$5.1 \pm 1.8$	$1100 \pm 199$	$3.7 \pm 2.0$	-
J0152.7-1357	0.831	36	$7.6 \pm 1.1$	$1324 \pm 100$	$6.7 \pm 1.5$	$4.4^{+0.7}_{-0.5}$
J0337.4-3457	0.840	-	-	-	-	-
J0236.1-5254	0.865	-	-	-	-	-
J0910+5422	1.106	170	$5.9 \pm 1.4$	$991 \pm 116$	$3.9 \pm 1.4$	$5.0^{+1.2}_{-1.0}$
J1252-29176	1.237	188.4	$7.0 \pm 1.3$	$1008 \pm 97$	$4.7 \pm 1.4$	$6.8^{+1.2}_{-1.0}$
J0849+4452	1.261	184.5	$4.0 \pm 0.8$	$749 \pm 75$	$2.0 \pm 0.6$	$4.4^{+1.1}_{-0.9}$
J0848+4453	1.273	-	$1.8 \pm 0.4$	$458 \pm 63$	$0.5 \pm 0.2$	$3.1^{+1.0}_{-0.8}$

The values of the involved cosmological parameters are  $\Omega_m = 0.3$  and  $h = 0.7$  in the  $\Lambda$ CDM model.

method (see also Section 2.1.2). By assuming a projected mass density profile (e.g. NFW Navarro et al. (1997), Singular Isothermal Sphere), the tangential shear (see Figure 4.7) is computed and compared with the measured values, whose errors are strictly related to the mean ellipticities measurements of the background galaxies. In particular, such errors are determined by the surface density of background galaxies and the signal-to-noise of each measurement (associated to the depth and angular resolution of the observations). As a results they became very large towards the cluster centre.

In the calculation of the masses of the clusters belonging to the zRDCS-1 sample, the assumed halo model is the NFW profile. When NFW profiles (Eq. 2.7) are calculated, it is assumed that the cluster virial mass  $M_{200,c}$  is tied to the concentration  $c$  via the relation from Duffy et al. (2008):

$$c = 5.71 \left( \frac{M_{200,c}}{2 \times 10^{12} [h^{-1} M_{\odot}]} \right)^{-0.084} (1+z)^{-0.47}. \quad (4.1)$$

Then the two-dimensional projected mass distribution  $\kappa$  is calculated (see central and right panels in Figure 4.7). In principle,  $\kappa$  can be obtained by convolving the shear  $\gamma$  as follows (Kaiser & Squires, 1993):

$$\kappa(\mathbf{x}) = \frac{1}{\pi} D * (\mathbf{x} - \mathbf{x}') \gamma(x) d^2 \mathbf{x}, \quad (4.2)$$

where  $D(x) = -1/(x_1 - ix_2)^2$  is the convolution kernel. However, a more robust two-dimensional mass reconstruction algorithm is required in practical applications and in particular the masses reported in Table 4.1 are calculated in Jee et al. (2011) by reconstructing the two-dimensional mass maps with the entropy-regularized, maximum likelihood code of (Jee et al., 2007). We refer to these two papers for details in the calculation of clusters mass with weak lensing analysis.

As part of the systematic error budget, we stress that for clusters at such a high redshift the uncertain knowledge of the mean redshift of the background galaxies has a non negligible effect on the final mass estimate (as mentioned in Section 2.1.2). The masses obtained from weak lensing analysis for five out of nine clusters are reported in Table 4.1.

**Hydrostatic masses.** The X-ray masses in the same Table have been calculated assuming the hydrostatic equilibrium using Eq. 2.12, as detailed in Ettori et al. (2004), for those clusters with *Chandra* observations.

These measurements have been computed using the latest *Chandra* calibration files. Despite the large *Chandra* exposure times (see Table 4.1), these clusters are so faint that only a few thousand counts are available and hence a single temperature measurement is possible. Thus, the hydrostatic masses are computed in the isothermal case using the deprojected gas density profile which is well determined thanks to *Chandra* high angular resolution. However, it remains generally difficult to trace the X-ray surface brightness profile beyond  $r_{500,c}$ , therefore mass density profiles are extrapolated to  $r_{200}$  assuming a NFW profile (Eq. 2.7). For the isothermal case, the mass errors depend essentially on the accuracy of the temperature and the parameters of  $\beta$  profile which describes the gas density. The masses of seven out of nine clusters of our sample are reported in Table 4.1.

Finally, for two clusters of our high- $z$  sample, RDCS-J0337.4-3457 which has only ROSAT observations from the original RDCS detection, and XMMU-J0236.1-5254 which is serendipitously present in a XMM shallow pointing, the masses have been estimated from their X-ray luminosities using the  $L_X$ - $M_{500,c}$  relation by Maughan (2007) (Eq. 3.14).

In the following analysis, we use the WL masses when available and the X-ray masses for the other clusters. preliminary investigation shows that results do not change significantly by using X-ray masses for all the clusters of our sample.

## 4.2 The analysis method

In this Section, we present the method to obtain the constraints of the cosmological parameters from our zRDCS-1 sample. We develop a fitting algorithm based on the MonteCarlo Markov Chain (MCMC) and the maximum likelihood (ML) criteria to compare the cluster distribution in the mass-redshift plane with predictions from different cosmological models for a sample characterized by the zRDCS-1 sky-coverage.

We divide the plane of redshifts and measured masses ( $M_{ob}, z$ ) into narrow elements of size  $dM dz$ . If the bin size is small enough, we will have at most one cluster of the sample per bin, and, according to Cash (1979), we can compute the logarithm of the likelihood function as:

$$\ln L = \sum_i \ln (P(M_{ob_i}, z_i) \Delta M_i) - \int_{z_{min}}^{z_{max}} P(M_{ob}, z) dM'_{ob} dz'. \quad (4.3)$$

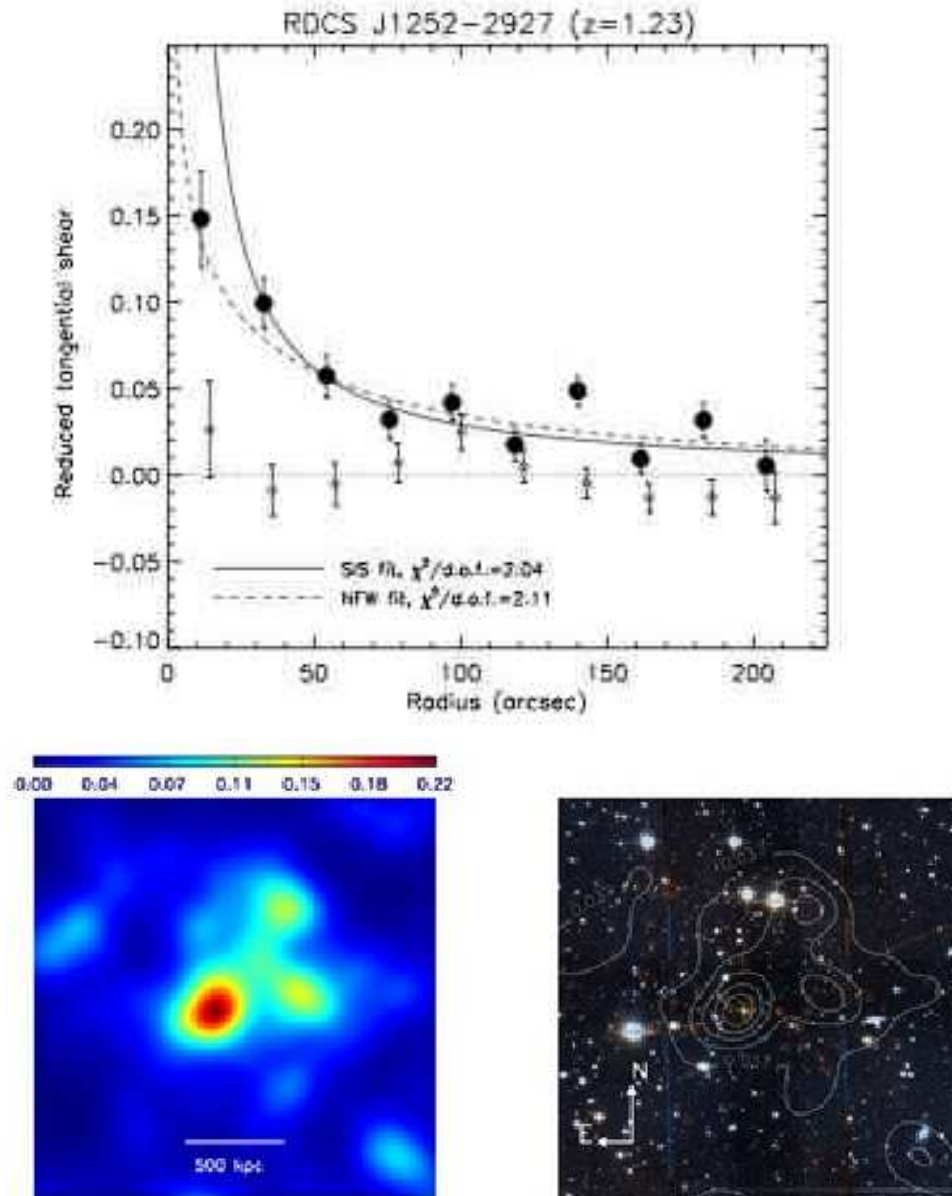


Figure 4.7: Mass reconstruction of RDCS-J1252-2927 cluster (see also Figure 4.6, top right panel). *Top panel*: filled circles represent the reduced tangential shears and the dashed line represents the NFW model fit. *Bottom left panel*: the mass reconstruction, whose colour represents the mass density. *Bottom right panel*: mass contours overlay on the pseudo-colour composite created by combining the *i*775 and *z*850 HST images. The green "X" symbol marks the location of the X-ray peak in the *Chandra* image. Spectroscopically confirmed members are encircled in red. Figures from Jee et al. (2011).

where  $P(M_{ob,i}, z_i)$  is the cluster number density in the  $z_i$  and  $M_{ob,i}$  bin. In the above equation the sum runs over the bins which contain one cluster and  $z_{max}$  represents the highest redshift at which the cluster RDCS identification algorithm can detect extended sources. We point out that, in principle,  $z_{max}$  does not coincide with the highest redshift cluster identified in the survey because of the redshift cut-off due to the surface brightness dimming. We choose in our analysis  $z_{max} = 1.5$ .

The probability density distribution of clusters is given in principle by the product of the theoretical mass function and survey comoving volume at redshift  $z$  and mass  $M$ . In order to take into account the difference between the observed mass ( $M_{ob}$ ) and the true mass ( $M_{tr}$ ) of clusters, we use the same approach presented in Section 3.3.1. The probability  $P(M_{ob,i}, z_i)$  is then

$$P(M_{ob,i}, z) = \int_0^\infty \frac{dn}{dM_{tr}} \frac{dV(M_{tr}, z)}{dz} [\text{erfc}(x_{i-1/2}) - \text{erfc}(x_{i+1/2})] dM_{tr} \quad (4.4)$$

where  $dn/dM$  is the mass function. In this analysis, we use the calibration of the halo mass function by Tinker et al. (2008), which is formally accurate to better than 5% for the cosmologies close to the concordance  $\Lambda$ CDM cosmology and for the mass and redshift range of interest in our study; at this level, the theoretical uncertainties in the mass function do not contribute significantly to the systematic error budget.

In Eq. 4.4  $\text{erfc}(x)$  is the complementary error function and  $x_i = x(M_{ob,i})$  is

$$x(M_{ob}) = \frac{\ln M_{ob} - B_M - \ln M}{\sqrt{(2\sigma_{\ln M}^2)}}. \quad (4.5)$$

In this equation the scatter in the relation between true and observed mass  $\sigma_{\ln M}$  is the total uncertainties of the mass estimates. The scatter includes the intrinsic scatter and the measurement errors

$$\sigma_{\ln M} = \left( \sigma_{\text{intr}}^2(z) + \sigma_{\text{meas},i}^2 \right)^{1/2}. \quad (4.6)$$

where the intrinsic scatter evolves with redshift as

$$\sigma_{\text{intr}}(z) = \sigma_{\text{intr},0}(1+z)^\beta \quad (4.7)$$

and  $\sigma_{\text{meas},i}$  varies from cluster to cluster. The mass bias  $B_M$  evolves with redshift as

$$B_M(z) = B_{M,0}(1+z)^\alpha. \quad (4.8)$$

Once the cluster likelihood function is computed we define the quantity  $-2 \ln L$ , whose statistical properties are equivalent to the  $\chi^2$  distribution (Cash, 1979), to find the best fit parameters. We derive constraints on cosmological parameters by searching for the absolute minimum of the  $\chi^2$  distribution in the N-dimensional parameter space. We explore the parameters space by using the MCMC approach.

We carry out our analysis for the zRDCS-1 sample for the  $\Lambda$ CDM model assuming no prior on the considered cosmological parameters. A second analysis is performed by using the constraints from 400d sample (Vikhlinin et al., 2009b, <sup>1</sup>) as a prior. In this case the  $\chi^2$  is defined as  $\chi^2 = -2 \ln P$  where  $P$  is posterior probability (see Appendix A) calculated by combining the likelihood from the zRDCS-1 and the 400d samples for each step in the parameters space explored with the MCMC. Moreover, we study constraints on the DE EoS  $w(a) = w_0 + w_a(1 - a)$  as obtained from the zRDCS-1 data alone and from the combination of the zRDCS-1 and the 400d samples; both analyses have been carried out in the case of a flat Universe.

### 4.2.1 Survey Volume

As we empathized in Chapter 2, a critical component in the analysis of cluster survey is the determination of the effective survey volume. In order to fit mass function models to the data, we need to know the survey volume as a function of mass. The zRDCS-1 sample is derived from a purely X-ray flux limited survey, thus we can compute the survey volume per unit redshift interval as

$$\frac{dV(M, z)}{dz} = \Omega(f_X) \frac{dV(z)}{dz d\Omega} \quad (4.9)$$

where  $\Omega(f_X)$  is the flux-dependent sky coverage (see Figure 4.1) and  $dV/dz/d\Omega$  is the comoving volume element per unit solid angle.

The X-ray flux is related to the luminosity  $L_X$  as

$$f = \frac{L_X}{4\pi d_L(z)^2} K(z), \quad (4.10)$$

this relation depends on the cosmological background through the luminosity distance  $d_L(z)$  and the  $K$ -correction factor that converts the flux

---

<sup>1</sup>The likelihood calculated in each point of the parameters space for the  $\Lambda$ CDM and the standard DE models are available on <http://hea.iki.rssi.ru/400d/cosm/chi2grids>

measured in a given band (0.5-2 keV as we use here) from an object at redshift  $z$  to an equivalent measurement in the rest frame of the object.

A dominant source of uncertainty in the measurements of the volume  $dV(M, z)/dz$  is the details of the  $L_X - M$  relation. To take such uncertainties into account in our analysis, we calculate the survey volume at redshift  $z$  as

$$\frac{dV(M, z)}{dz} = \int_L \frac{dV(z)}{dzd\Omega} P(L_X|M, z) \Omega(L, z) dL, \quad (4.11)$$

where  $P(L_X|M, z)$  is the probability for a cluster with true mass  $M$  to have a luminosity  $L_X$  at redshift  $z$ .

The simplest model that describes the observed  $L_X - M$  relation (see Section 2.2.3) is a power law with log-normal intrinsic scatter,  $\sigma_{\ln M}$  around the mean which is assumed to be independent from mass and redshift

$$P(\ln L|M) \propto \exp\left(-\frac{(\ln L - \ln L_0)^2}{2\sigma_{\ln L}^2}\right), \quad (4.12)$$

where

$$L_0 = A E(z)^\gamma M^\eta \quad (4.13)$$

In such equation we assume that the redshift evolution changes the normalization but keeps constant the slope of the power law, thus, the  $L_X - M$  relation is characterized by four parameters,  $A$ ,  $\eta$ ,  $\gamma$  and the scatter  $\sigma_{\ln L}$ .

Observational determinations of the  $L_X - M$  relation can be significantly affected by the Malmquist bias (MB). According to this effect in a flux limited sample, the intrinsically most luminous objects can be observed up to a higher distance, giving the impression that the average luminosity of the population increases with redshift. The MB effect becomes strong if the scatter in  $L_X$  for fixed  $M$  is large (e.g. Stanek et al., 2006; Nord et al., 2008).

We note that in addition to the Poisson cluster counting uncertainties, there is sample variance in the number of clusters in a survey of limited volume due to large-scale clustering. Depending on the mass scale, the sample variance can be comparable to, or larger than, the Poisson errors (Hu & Kravtsov, 2003). Assuming that the individual pointings are uncorrelated (a good assumption for the widely separated pointings of the RDCS survey), we can neglect the contribution of the sample variance in our analysis. We should note however that each RDCS pointing covers at

$z \sim 1$  approximately 7 Mpc (or 15 Mpc comoving), therefore to some level clustering effect on the mass function determination are not completely negligible.

### 4.3 Results

We present results on constraints parameters for two cosmological models,  $\Lambda$ CDM one and the standard DE one (i.e. with the DE EoS parametrized as in Eq. 3.1).

The first model is characterized by five parameters: the present day matter density parameter  $\Omega_m$ , the normalization of the power spectrum  $\sigma_8$ , the Hubble parameter  $h$ , the constant DE EoS parameter  $w_0$ , the baryon critical density  $\Omega_b$ , and the primordial spectral index  $n_s$ . In order to describe the standard DE model, we need a further parameter  $w_a$  that accounts for the evolution with redshift of the DE EoS according to Eq. 3.1. In both models, the geometry of the Universe is assumed to be flat,  $\Omega_b$  is fixed at the best value found by the combined analysis of WMAP-7, BAO and SNIa data provided by Komatsu et al. (2011),  $\Omega_b = 0.046$ . The spectral index is assumed to be  $n_s = 0.95$  in agreement with the results from the WMAP-7 analysis. Following Vikhlinin et al. (2009a), we keep fixed this parameter although it has a quite strong influence on the timing of structure formation and is thus significantly degenerate with  $\sigma_8$ .

Together with cosmological parameters, we include in our analysis the so called *mass parameters* which describe the relation between the observable and the mass of clusters. We applied in this analysis the same approach used in the previous Chapter and explained in Section 3.4.2. Thus we consider four mass parameters: the fractional mass bias  $B_M$ , the intrinsic scatter  $\sigma_{\ln M}$  and their evolution with redshift as parametrized in Eqs. 4.8 and 4.7. In addition, we include in our fitting procedure the four parameters that describe the  $L_X - M$  relation, according to Eqs. 4.12 and 4.13 (we call them hereafter *L-M parameters*).

In summary, we carry out our analysis by constraining at once the parameters that describe the constant DE EoS model ( $\Omega_m, \sigma_8, w, h$ ) or the DE standard model ( $\Omega_m, \sigma_8, w_0, w_a, h$ ), the four parameters that account for the uncertainties in the estimation of the cluster mass ( $B_m, \sigma_{\ln M}, \alpha, \beta$ ), and the four parameters that treat the effect of the Malmquist Bias on a flux limited sample ( $A, \eta, \gamma, \sigma_{\ln L}$ ). The values obtained in the  $\Lambda$ CDM and DE standard models from the analysis of the zRDCS-1 sample alone, for

Table 4.2: Best fit values for the mass and L-M parameters defined by Eqs. 4.7, 4.8 and 4.13 with their respective errors, for both the  $\Lambda$ CDM and standard DE model analysis carried out with the zRDCS-1 sample.

zRDCS-1		
	$\Lambda$ CDM	DE
$B_M(z=0)$	$-0.052 \pm 0.024$	$-0.043 \pm 0.027$
$\sigma_{\ln M}(z=0)$	$0.28 \pm 0.13$	$0.24 \pm 0.11$
$\alpha$	$0.034 \pm 0.012$	$0.030 \pm 0.015$
$\beta$	$0.15 \pm 0.09$	$0.13 \pm 0.08$
A	$3.859 \pm 0.054$	$3.853 \pm 0.067$
$\gamma$	$2.1 \pm 0.31$	$1.9 \pm 0.29$
$\eta$	$1.54 \pm 0.25$	$1.52 \pm 0.23$
$\sigma_{\ln L}$	$0.422 \pm 0.075$	$0.407 \pm 0.069$

the mass and the L-M parameters are presented in Table 4.2. The errors at 68% have been obtained for each parameter after marginalizing over all the others.

The best fit values for the L-M parameters are in agreement with those obtained by Vikhlinin et al. (2009a) (their Eq. 22) from a sample with median redshift  $\bar{z} = 0.5$  and also with the luminosity-mass relation provided by Maughan (2007) for clusters at redshift up to 1.3 (see their Table 1).

The calibration of the  $L_X - M$  relation is the most important source of uncertainty in the calculation of the effective survey volume (Eq. 4.11). The effect is stronger for the high- $z$  data because the  $L_X - M$  relation is derived using a small number of clusters, with larger measurement uncertainties. In particular, the observed high value of the scatter  $\sigma_{\ln L}$  in the  $L_X - M$  confirms that the Malmquist bias effects are significant, as expected for the zRDCS-1 sample which lies near the detection limit of the RDCS survey. The effect of the  $\sigma_{\ln L}$  scatter is also important when the X-ray luminosity is used to compute the total mass of a cluster as we do only for the RDCS-J0337.4-3457 and XMMU-J0236.1-5254.

As for the mass parameters, we present in the Table 4.2 the best fit values derived from the analysis of the  $\Lambda$ CDM and standard DE models for the zRDCS-1 sample. We see that a mild evolution with redshift for the mass bias  $B_M$  and especially for the scatter  $\sigma_{\ln M}$  parameters is suggested. As of today there are no strong constraints on the evolution of such parameters that, as showed in Section 3.6.1, affect the accuracy of

constraints on cosmological parameters in a significant fashion.

In the following, we show constraints on cosmological parameters focusing on those that describe the DE component of the Universe. The analysis is performed using the zRDCS-1 sample for both the  $\Lambda$ CDM and the standard DE model, keeping the mass and the luminosity parameters fixed at the reference values reported in Table 4.2. The results from Vikhlinin et al. (2009b) are used as priors information in our analysis.

Vikhlinin et al. selected two cluster samples, originally compiled from ROSAT X-ray surveys (Vikhlinin et al., 2009a). The low redshift sample includes the 49 highest-flux clusters detected in the All-Sky Survey in the redshift range  $0.025 < z < 0.15$  ( $\bar{z} = 0.05$ ). The second sample includes 37 objects detected in the 400d survey, at redshift  $0.35 < z < 0.9$  ( $\bar{z} = 0.5$ ). All the clusters have been observed with *Chandra*. Thus, different proxies ( $T_X, M_{gas}, Y_X$ ) have been computed to estimate the mass of each system. As we do in our analysis, Vikhlinin et al. take into account the errors in the calibration of the mass scaling relations and measurement errors in the computation of the likelihood function on the model parameters, and the evolving  $L_X - M$  relation was internally calibrated in the computation of the survey volume. The cosmological parameters considered in Vikhlinin et al. (2009b) are  $(\Omega_m, \sigma_8, w, h)$  for the  $\Lambda$ CDM model and  $(\Omega_m, \sigma_8, w_0, w_a, h)$  for the DE standard model.

We present our results by computing 68% and 95% confidence level for each pair of interesting parameters, obtained marginalizing over all the other parameters.

### 4.3.1 High redshift cluster mass function

We run the MCMC algorithm and calculate the likelihood for the  $(\Omega_m, \sigma_8, w, h)$  parameters according to the  $\Lambda$ CDM model from the zRDCS-1 and 400d sample. We fixed the L-M parameters to the best values in Table 4.2 and we assume the Universe to be spatially flat. By using the best fit set of cosmological parameters obtained from this analysis, we compute the survey volume following Eq. 4.11, and we compute the cumulative mass function as

$$N(> M) = \sum_{M_i > M} \left( \frac{dV(M_i, z)}{dz} \right)^{-1}. \quad (4.14)$$

In this equation  $V(M_i)$  is the sample volume element integrated over the redshift range of the zRDCS-1 sample. Figure 4.8 shows the cumulative mass function that we obtain for  $0.8 < z < 1.3$  compared with results from Vikhlinin et al. (2009a) at redshifts  $z \simeq 0$  and  $\bar{z} \simeq 0.5$ . We point out that this is the first robust measurement of the cluster mass function at  $z > 0.8$ .

A significant decrease in the comoving cluster number density at a fixed mass is observed among different redshift intervals, by a factor of 5 at  $M_{500} = 2.5 \times 10^{14} h^{-1} M_{\odot}$  between  $z = 0$  and  $\bar{z} = 0.5$ , and by a factor of 7 between  $\bar{z} = 0.5$  and  $\bar{z} = 0.865$ . This reflects the growth of cosmic structure between these redshifts. The observed evolution of the cluster mass function is in good agreement with prediction from the  $\Lambda$ CDM cosmological model (solid line in Figure 4.8). In order to calculate the predicted mass function we use the prescription from Tinker et al. (2008); the theoretical mass functions shown in Figure 4.8 were calculated respectively at redshift  $z = 0$ ,  $z = 0.5$  and  $z = 0.865$ . In fact,  $z = 0.5$  is close to the median value of the high- $z$  sample from Vikhlinin et al. (2009a) and  $z = 0.865$  is the median redshift for the zRDCS-1 sample. Following Vikhlinin et al. (2009a), when showing the mass function at varying redshifts we use the  $\Lambda$ CDM parameters, with  $\Omega_m = 0.3$ , for the measurements and the theoretical mass function curves (Figure 4.8).

### 4.3.2 Constraints on $\sigma_8$ and $\Omega_m$

The normalization of the cluster mass function is exponentially sensitive to  $\sigma_8$ . On the other hand, determination of  $\sigma_8$  is highly sensitive to systematics effects in the calibration of the observable-mass scaling relations as we showed in the forecast analysis from WFXT surveys (see Section 3.6.1). In fact, Huterer & White (2002) show that if  $M_{tot}$  for a fixed value of  $T_X$  is varied by a factor of 1.5, the value of  $\sigma_8$  derived from the local cluster temperature function changes by  $\Delta\sigma_8 \approx 0.13$ .

It is well known that constraints on  $\sigma_8$  from the cluster abundance data show a strong degeneracy with  $\Omega_m$ . The mass function determines the r.m.s. amplitude of fluctuations at the given mass scale. The corresponding length scale is a function of  $\Omega_m$  ( $M \sim \Omega_m l^3$ ) and, thus, the derived  $\sigma_8$  depends also on  $\Omega_m$  and more weakly on the local slope of the linear power spectrum (White et al., 1993).

Final results obtained on  $\sigma_8$  and  $\Omega_m$  parameters in the  $\Lambda$ CDM scenario from the combined analysis of the zRDCS-1 and 400d sample are

presented in the Figure 4.9 (right panel). For comparison, we also show the results obtained from 400d data alone (Vikhlinin et al., 2009b) in the left panel of Figure 4.9. The best fit values obtained from the analysis of the zRDCS-1 sample using the 400d sample as a prior are:

$$\sigma_8 = 0.81 \pm 0.07 \quad \Omega_m = 0.24 \pm 0.06 .$$

Measurements based on different cosmological probes such as lensing shear surveys and WMAP-7, are all consistent at 68% CL with our best fit value for  $\sigma_8$ .

### 4.3.3 Constraints on Dark Energy parameters

First we show constraints on DE in a spatially flat Universe as obtained from the combination of the zRDCS-1 and the 400d sample. We run the MCMC and compute the posterior probability for the cluster mass function with Eq. 4.4 on the parameters  $(\Omega_m, \sigma_8, h, w)$  for the  $\Lambda$ CDM model. Constraints on the parameters  $\Omega_{DE} = 1 - \Omega_m$  and  $w$  are presented in Figure 4.10. This figure shows results from our analysis superimposed to constraints obtained from Vikhlinin et al. (2009b).

In the  $\Lambda$ CDM scenario, we measure

$$w_0 = -1.25 \pm 0.19 \quad \Omega_{DE} = 0.77 \pm 0.06$$

combining zRDCS-1 and 400d data.

The cosmological information relevant for DE constraints lies in changes of the comoving cluster number density. Such changes constrain the perturbations growth factor combined with the relative distances between 400d and zRDCS-1 samples. Errors on the  $\Omega_{DE}$  and especially  $w$  measurements are dominated by uncertainties on the evolution of the observable-mass relations, as we learned when we carried out forecast on DE EoS parameters in the previous Chapter (see Section 3.6.1).

Using high- $z$  clusters also slightly improves equation of state constraints for evolving  $w$ . We obtain parameter constraints on DE EoS parameters  $w_0$  and  $w_a$  using the likelihood function computed on  $(\Omega_m, \sigma_8, h, w_0, w_a)$  that describe the standard DE model, by combining the zRDCS-1 and 400d sample. Constraints are weak by themselves, and adding the zRDCS-1 information does not significantly improve the  $w_a$  constraints. With current data, clusters can be used in combinations with other cosmological datasets, like CMB and SNIa, and help in breaking the degen-

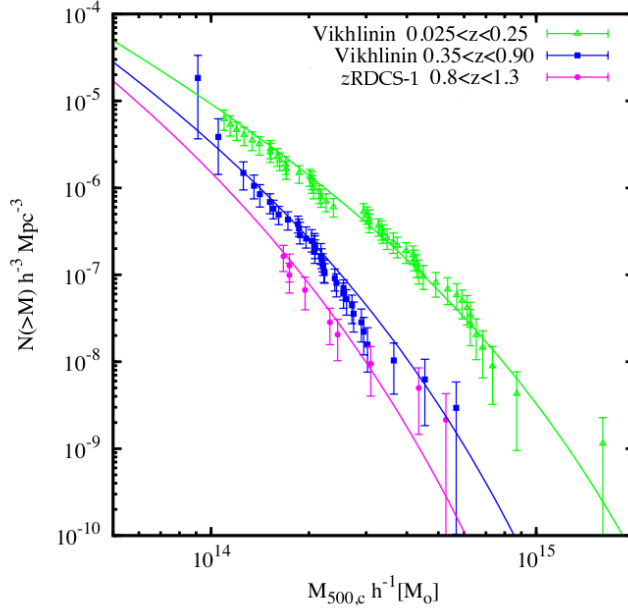


Figure 4.8: Cluster mass functions for 3 redshift bins from the low and high redshift samples from Vikhlinin et al. (2009a) and from the zRDCS-1 sample. The errorbars show the Poisson uncertainties. Solid lines show the model predictions for the  $\Lambda$ CDM model, with  $\Omega_m = 0.3$ .

eracy between the two DE EoS parameters (e.g. Vikhlinin et al., 2009b; Mantz et al., 2010a).

## 4.4 High redshift massive cluster test

The analysis presented in the previous Section confirms the potential of high redshift samples of galaxy clusters in constraining cosmological parameters. As explained in Section 1.5 we emphasize how important is the contribution that even a single high redshift massive galaxy cluster can provide in constraining the cosmological parameters and in falsifying models.

Mullis et al. (2005) reported the discovery of a massive cluster at  $z \simeq 1.4$ , XMMU-J2235.3, identified as part of the initial 11 sq.deg. of the XMM Distant Cluster Project survey (XDCP; Fassbender et al., 2011), which reaches a flux limit of  $1 \times 10^{-14} \text{ erg s}^{-1} \text{ cm}^{-2}$ . Based on weak lensing (Jee et al., 2009) and X-ray (Rosati et al., 2009) analyses, a robust  $1\sigma$  lower

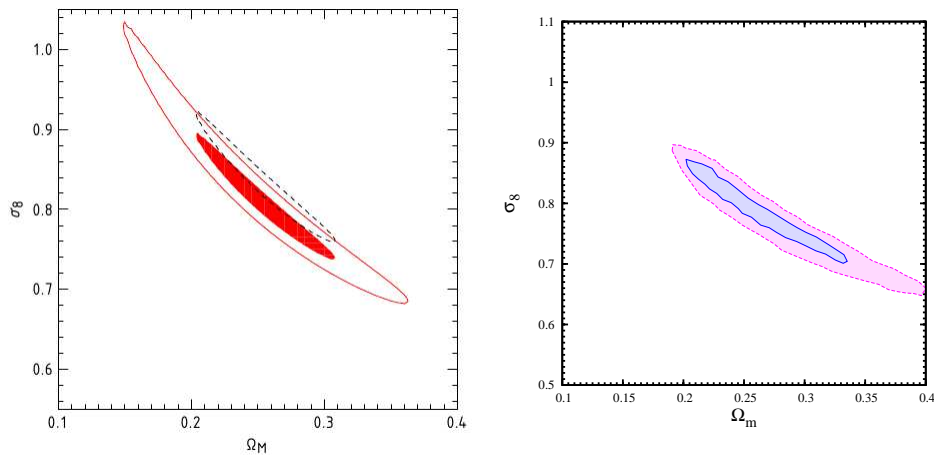


Figure 4.9: *Left panel:* Constraints on the  $(\Omega_m, \sigma_8)$  parameters in a flat  $\Lambda$ CDM cosmology as obtained from the 400d sample (Vikhlinin et al., 2009b). The inner solid region corresponds to the 68% CL intervals for one interesting parameter, and the solid contour shows the one-parameter 95% CL region. The dashed black contour shows how the inner solid confidence region is modified if the normalization of the absolute cluster observable-mass relations is changed by +9% (an estimate of the systematic errors). Figure from Vikhlinin et al. (2009b). *Right panel:* Constraints at the 68 % (blue curve) and 95 % (magenta curve) confidence level on the  $(\Omega_m, \sigma_8)$  parameters for the  $\Lambda$ CDM model as obtained by combining information from the zRDCS-1 and the 400d sample from Vikhlinin et al. (2009b).

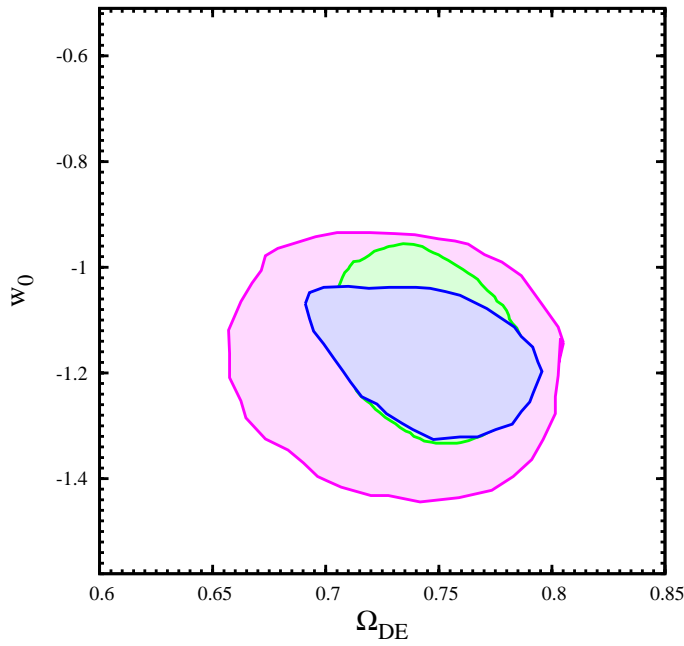


Figure 4.10: Constraints on the present day DE density parameter  $\Omega_{DE}$  and constant equation of state parameter  $w$ , derived from cluster number density in a spatially flat  $\Lambda$ CDM Universe. *Left panel:* Constraints at the 68% confidence level provided the analysis of the 400d sample (Vikhlinin et al., 2009b). *Right panel:* Constraints at the 68 (blue curve) and 95 (magenta curve) % confidence level as obtained by combining information from the zRDCS-1 and the 400d samples. For comparison constraints at the 68% confidence level provided the analysis of the 400d sample (Vikhlinin et al., 2009b) (green curve) are shown.

limit of  $5 \times 10^{14}$  is obtained for the cluster virial mass.

This results triggered a number of studies on whether such a single cluster is consistent with the expected  $\Lambda$ CDM cluster mass function. By assuming a WMAP-5 cosmology, with  $\sigma_8 = 0.81$  and  $\Omega_m = 0.28$ , and using the mass function by Jenkins et al. (2001), Jee et al. (2009) found that only  $\simeq 5 \times 10^{-3}$  of such massive clusters should be expected within the survey area. Thus, they concluded that XMMU-J2235.3 is a rather unlikely event in a standard cosmological scenario. Jimenez & Verde (2009) argued that, for a fixed value of  $\sigma_8$  ( $= 0.77$  in their analysis) the expected number of such massive clusters can in fact be significantly enhanced in the case of a positively skewed non-Gaussian distribution of primordial perturbations.

Assuming a “local shape” for the non-Gaussian scenario, in Figure 4.11 we show the curves in the  $(\sigma_8, f_{\text{NL}})$  plane corresponding to different numbers of clusters expected at  $z > 1.4$  within 11 sq.deg. and having mass of at least  $5 \times 10^{14} M_\odot$ . Results are given for the reference non-Gaussian mass function from LoVerde et al. (2008) (dot-dashed curves), that we used for our forecasts (see Section 3.3.1), and for the mass function by Matarrese et al. (2000) (solid curves). For both mass functions, we applied the correction to  $\Delta_c$  suggested by Grossi et al. (2009) (see Section 3.3.1). These two mass functions come from different approaches to approximate the exact result for small values of  $f_{\text{NL}}$  as we discuss in Section 1.9. As expected, the difference between the two mass functions becomes non negligible for  $f_{\text{NL}} > 100$  for the rare event of such a massive cluster at  $z \simeq 1.4$ . For each model, the four curves, from right to left, are for 0.05, 0.02, 0.01 and 0.005 such massive clusters found within the 11 sq.deg of survey area, respectively. For homogeneity with the analysis carried out by Jee et al. (2009), we used here the Gaussian mass function by Jenkins et al. (2001). While  $f_{\text{NL}}$  and  $\sigma_8$  are left free to vary, all the other cosmological parameters are kept fixed at the fiducial values reported in Section 3.3.3. The results shown in this plot confirm that a positive skewness helps increasing the expected number of clusters. The effect of non-Gaussianity is strongly degenerate with that of changing  $\sigma_8$ . For instance, increasing the expected number of clusters by about a factor of ten for  $\sigma_8 = 0.8$  requires  $f_{\text{NL}}$  values in excess of the range allowed already at present by CMB (e.g., Komatsu et al., 2011, and references therein) and Large Scale Structure (LSS) (Slosar et al., 2008) data. On the other hand, the same boost in the cluster number can be achieved by requiring  $f_{\text{NL}} \simeq 100$  and increasing  $\sigma_8$  to  $\simeq 0.87$ , again in tension

with current CMB and LSS constraints. The conclusion of this analysis is that for XMMU-J2235.3 not to be a very unlikely event, a degree of non-Gaussianity in excess of the currently allowed CMB bounds is required, unless one wants to violate current constraints on  $\sigma_8$ . Clearly, this conclusion is based on assuming that errors in mass measurement are so small not to affect the analysis. Also, more than a single detection of such massive distant clusters are needed to draw firm conclusions. However, this example further confirms the strong constraining power of even few massive clusters at  $z > 1$ . In addition, since galaxy clusters probe much smaller scales than the CMB, they offer a complementary approach to test a possible scale-dependence of non-Gaussianity.

Having such precise measurement of the mass of the XMMU-J2235.3, based on consistent values from both X-ray and WL analysis we also computed the probability of finding a cluster like XMMU-J2235.3 according to the  $\Lambda$ CDM model. We calculated the probability by using Eq. 4.4, and by considering errors in the calibration of the mass scaling relations, and corrections due to the Malmquist Bias effect. As for the mass and L-M parameters we use the reference values reported in Table 4.2, while as for cosmological parameters we use the reference values for the  $\Lambda$ CDM model reported in Section 3.3.3. We obtain a probability of finding at least one such cluster at redshift  $z \geq 1.4$  with mass  $M_{200,c} \geq 7.3 \times 10^{14} M_{\odot}$  of 6.7 % within the survey area of 50 sq. deg. (the updated area of the XDCP survey according to Fassbender et al., 2011). In Figure 4.12 we show the probability of finding at least one cluster as a function of mass and redshift within a survey area of 50 sq. deg. with flux  $f_X \geq 1 \times 10^{-14} \text{ erg s}^{-1} \text{ cm}^{-2}$ . Even a single cluster found in the “tension region” could falsify the reference model chosen for the analysis. However, as we stressed in Section 1.5, in order to use massive clusters to test the validity of cosmological models, we need to carefully calibrate the mass observable scaling relations especially at such high redshift. Also a detailed understanding of the survey sky coverage and of the effect of the Malmquist bias in the calculation of the survey is needed. For example, if we do not include the treatment of the Malmquist bias in the calculation of the survey volume, the probability of XMMU-J2235.3 decreases to 4.8 %. Moreover, a very good understanding of the high mass end of mass function is needed. As we showed in Figure 1.6 for masses higher than  $5 \times 10^{14} M_{\odot}$  in particular at high redshift, different mass function prescriptions can predict quite different number of clusters because the existing limited-volume simulations do not constrain this regime with

sufficient accuracy.

The sensitivity of cluster mass function to the value of cosmological parameters is also shown in Figure 4.12, where we plot the probability of finding one or more clusters as a function of mass and redshift for a different value of the constant DE EoS  $w$ . The green, blue and magenta curves in Figure 4.12 are calculated for  $w = -1$  while the cyan curve, which represents the probability of 11%, corresponds to  $w = -0.8$ .

## 4.5 Conclusions

In this Chapter, we derived constraints on cosmological parameters from current X-ray selected cluster samples. We analysed the evolution of the cluster number density as defined by the the ROSAT Deep Cluster Survey at redshift  $z > 0.8$  (zRDCS-1), thus extending the analysis of Vikhlinin et al. (2009b) who measured the cluster abundance in two cluster samples at median redshifts  $\bar{z} = 0.05$  and  $\bar{z} = 0.5$ , containing 49 and 37 clusters, respectively. The zRDCS-1 sample contains nine clusters, selected in the RDCS catalogue, with flux  $f_X \geq 1 \times 10^{14} \text{ erg s}^{-1} \text{ cm}^{-2}$  in the  $[0.5 - 2] \text{ keV}$  energy band and with redshift range from  $z = 0.805$  to  $z = 1.273$ , with median redshift  $\bar{z} = 0.865$  (Rosati et al., 1995, 1998).

All the clusters belonging to the zRDCS-1 sample are spectroscopically confirmed and the majority of them have a precise mass determination. Specifically, extensive follow-up campaign have been carried out over the last decade in order to measure the mass of these clusters with weak lensing using HST/ACS observations and deep, high-quality X-ray pointings with *Chandra*. Ass these clusters have a large number of spectroscopic members observed with the VLT and Keck telescopes.

Both the analyses from our zRDCS-1 sample and of the 400d samples have been carried out including the errors on the measurements of the weak lensing and X-ray masses and the uncertainties in the calibration of the observable-mass relation. Moreover in the calculation of the volume sample the effect of the Malmquist bias that affect flux limited samples has been included.

Our analysis was aimed at understanding whether results obtained on cosmological parameters from clusters surveys at redshifts  $\bar{z} = 0.05$  and  $\bar{z} = 0.5$  (Vikhlinin et al., 2009a) can be extended, and positively strengthen, to redshifts higher then 0.8 by combining the zRDCS-1 and 400d samples. Thus we used the high- $z$  tail of the RDCS sample to compute

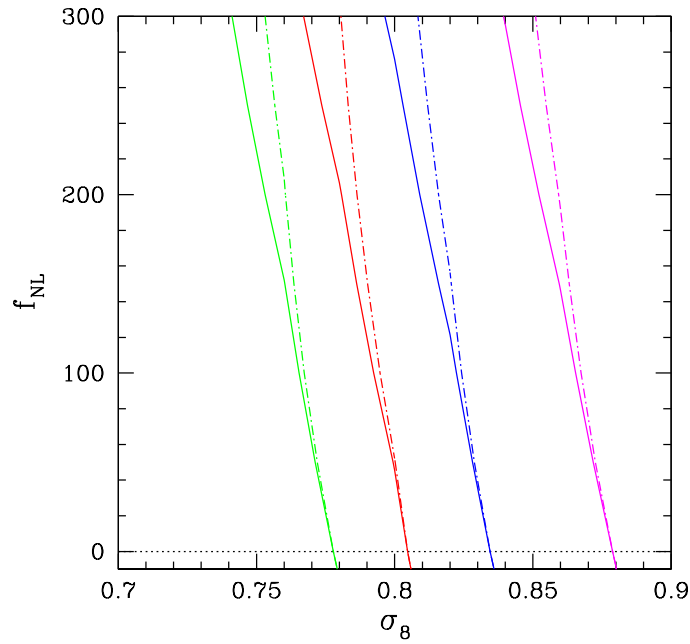


Figure 4.11: The number of clusters with mass larger than  $5 \times 10^{14} M_{\odot}$ , found in the redshift range  $1.4 < z < 2$  within the same survey area of 11 sq.deg. where the XMMU-J2235.3 cluster has been originally detected (Mullis et al., 2005). non-Gaussian mass function by LoVerde et al. (2008) (dot-dashed curves) and by Matarrese et al. (2000) (solid curves) are shown. From right to left, magenta, blue, red and green curves show the models on the  $\sigma_8$ - $f_{\text{NL}}$  plane predicting 0.05, 0.02, 0.01 and 0.005 clusters within the survey area, respectively. All other cosmological parameters have been kept fixed to reference values indicate in Section 3.3.3.

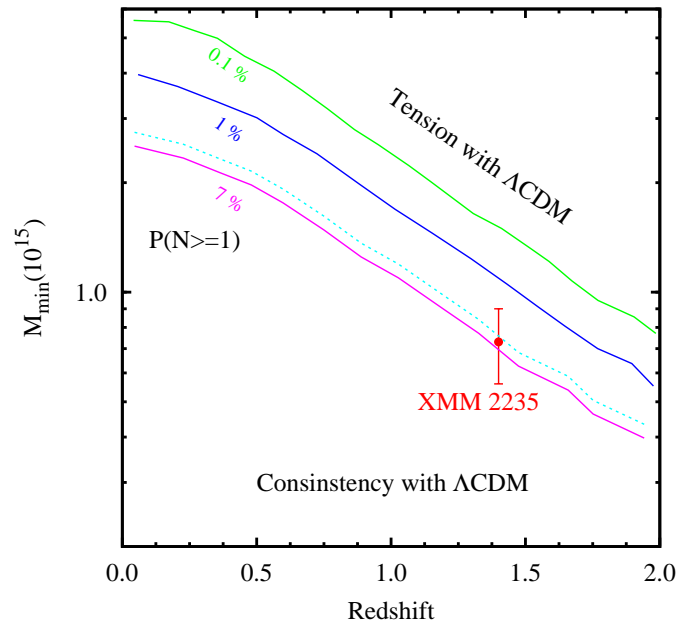


Figure 4.12: Probability of finding at least one cluster in a survey area of 50 sq. deg. with flux  $f_X \geq 1 \times 10^{-14} \text{ erg s}^{-1} \text{ cm}^{-2}$  as a function of mass and redshift. The curves correspond to the Poissonian probability of 0.1% (green curve), 1% (blue curve), and 7% (magenta curve). All cosmological parameters have been kept fixed to reference values indicated in Section 3.3.3. The value of mass and L-M parameters are reported in Table 4.2. The cyan curve corresponds to the  $P(N \geq 1) = 11\%$  for  $w = -0.8$  instead of  $w = -1$ .

for the first time the mass function at  $z > 0.8$ .

Using the MCMC approach, we calculated constraints for the  $\Lambda$ CDM and standard DE models. In the first case, we computed the likelihood on 4 four cosmological parameters ( $\Omega_m, \sigma_8, w_0, h$ ) while, for the standard DE model, we add a further parameter,  $w_a$ , that takes into account a possible evolution of the DE EoS with redshift, according to Eq.3.1.

The main results of the study can be summarized as follows.

- (1) Based on the RDCS sample alone, we determined the best fit values of the parameters that describe the uncertainties in observable-mass relation (see Eqs. 4.8 and 4.7). We see that a mild evolution with redshift of both the bias and especially the scatter is preferred, as expected for such high redshift clusters (see Table 4.2). In fact, as for the X-ray analysis the assumption of the hydrostatic equilibrium is not always fulfilled because clusters at such high redshift can be still not completely relaxed. In case of WL analysis, projection effects and uncertainties in the determination of the redshift of background galaxies become more important at high redshift.
- (2) Using the zRDCS-1 sample, we calculated the values of the parameters that define the relation between the X-ray luminosity and mass (Eqs. 4.13 and 4.11), that represents the most important source of uncertainty in the calculation of the effective survey volume (Eq. 4.11). Our results are in agreement with those obtained by Vikhlinin et al. (2009a). Based on these results, we conclude that the L-M relation calibrated with clusters at relatively lower redshift is still valid for clusters at  $z > 0.8$ . However, the scatter in the  $L_X - M$  relation in the zRDCS-1 sample is stronger because the relation is derived using a small number of clusters. Moreover, the Malmquist bias effects become significant, as expected for the zRDCS-1 sample which lies near the detection limit of the RDCS survey.
- (3) Finally we computed the cluster mass function at median redshift  $\bar{z} = 0.865$ . The observed evolution of the mass function as calculated from zRDCS-1 sample is in agreement with prediction of  $\Lambda$ CDM at high redshift.
- (4) Calculating the likelihood from the zRDCS-1 sample and using constraints of cluster space density from the 400d sample as prior, we derive constraints on  $\Omega_{DE}, w_0$  and  $w_a$ . Our results are consistent

with the results obtained with cluster surveys at lower redshifts (e.g. Rozo et al., 2010; Vikhlinin et al., 2009b; Mantz et al., 2010a). The best fit value obtained for the  $\Lambda$ CDM models are:  $w_0 = 1.25 \pm 0.19$   $\Omega_{DE} = 0.77 \pm 0.06$ . These results slightly improve the constraints from Vikhlinin et al. (2009b). In the case of the standard DE model, the extension to  $z \sim 1$  with zRDCS-1 does not improve constraints based on the larger sample at lower redshift. However, as shown by Vikhlinin et al. (2009b), clusters can be important in breaking the degeneracy between DE EoS parameters and their contribution becomes important when we combine cluster with other cosmological probes.

Therefore, our analysis of the zRDCS-1 sample does not show any evidence for population of massive clusters at  $z > 1$ , possibly in tension with  $\Lambda$ CDM and standard quintessence models.

In order to further investigate this last points, we also performed a test with a high redshift massive cluster. In fact, the detection of such high objects have been used recently to quantify possible deviations from the  $\Lambda$ CDM model (e.g. Mortonson et al., 2011). We calculated the probability of finding at least one cluster with a given redshift and mass. In principle, even a single cluster found in the “tension region” (see Figure 4.7) could falsify a given cosmological model. A robust assessment of the likelihood requires a detailed understanding of the survey sky coverage, including the Malmquist bias, and a precise estimation of the cluster mass. We used for our study the XMMU-J2235.3 cluster at  $z = 1.4$  which has a robust measurement of the mass from both the weak lensing (Jee et al., 2009) and X-ray (Rosati et al., 2009) data. We obtained a probability of finding at least one cluster at redshift  $z \geq 1.4$  with mass  $M_{200,c} \geq 7.3 \times 10^{14} M_{\odot}$  of 6.7 % within the survey area of 50 sq. deg. (Fassbender et al., 2011), according to the  $\Lambda$ CDM model. We showed how much such probability sensitive to the values of the cosmological parameters. by changing the DE EoS from  $w = -1$  to  $w = -0.8$ , the value of the likelihood rise from 6.7 up to 11 %.

Our analysis further stresses the importance of having a well defined measure of the clusters mass obtained with different methods in order to minimize systematic effects. Moreover our study confirms the validity of the  $\Lambda$ CDM model at redshift  $0.8 < z < 1.3$ , within the limited statistic provided by current data.

# Conclusions

This Ph.D. Thesis is devoted to the study of galaxy clusters as probes to derive cosmological constraints from future and current surveys.

Providing information on both the growth structure history and the geometry of the Universe, galaxy clusters have been recognized as important in establishing the standard model of cosmology, with a Universe dominated by Dark Matter (DM) and Dark Energy (DE).

Clusters are the most massive bound structures that emerge in the cosmic web of Large-Scale Structure, and they arise from the collapse of initial perturbations having a typical comoving scale of about  $10 h^{-1}$  Mpc. On scales larger than that, according to the standard model of cosmic structure formation, gravitational dynamics dominated the Universe and density perturbations can be treated in the linear approximation regime (see Chapter 1). However, in order for clusters to be used as cosmological tools, one needs to understand in detail the astrophysical processes which determine cluster observational properties across the electromagnetic spectrum, as we explain in Chapter 2.

Current cosmological constraints obtained from clusters have been mainly derived from ROSAT-based samples, containing  $\sim 100$  objects at  $z < 1$  with detailed follow-up observations to infer cluster masses proxies. However, current and forthcoming experiments in the optical band (EUCLID), in the X-ray band (eROSITA), and based on the SZ effect (SPT, ACT, Planck), will increase by orders of magnitude the statistics of detected clusters at high redshifts. Moreover, future high-sensitivity wide-area telescopes, such as the proposed Wide Field X-ray Telescope (WFXT), will measure mass proxies for a large amount of clusters ( $\sim 10^4$ ) out to  $z \sim 1.5$ .

In this respect, it is worthy to study the cosmological constraining power of such future cluster surveys. In the first part of our work (see Chapter 3), we derived cosmological constraints from future cluster surveys, dissecting the information provided by geometrical and growth

tests, as they are included in the analysis of the number density and the power spectrum of clusters. Moreover, we studied how much uncertainties in the calibration of the mass-observable relation can affect the constraints provided by clusters, and we explored how the optimization of the survey strategy depends on the specific cosmological models that we want to analyse.

To this aim, we developed an algorithm that derived forecast for constraints on cosmological parameters by using the Fisher Matrix approach given the sky coverage of a specific cluster survey. Thanks to the large number of detected clusters, future surveys, such as WFXT or EUCLID, will contain so much information to allow one to constrain at the same time cosmological parameters and those parameters related to the physical properties of clusters, by using the so-called self-calibration approach.

Exploring the DE component of the Universe is one of the most important challenge of cosmology nowadays. The goal is to unveil the nature of the energy component which dominates the overall dynamics of the Universe at the present time. In this respect, we forecasted constraints on parameters that define the standard parametrization of DE equation of state (EoS, Eq. 3.1), as obtained from WFXT samples. Given the high signal to noise of the data and the well defined selection function, it will be possible to provide a complete characterization of mass and redshift of objects detected with such telescope with X-ray data alone, without resorting to time-consuming follow-up observations. The mission survey strategy plans three survey configurations (see Table 3.1): the Wide (20000 sq.deg.), the Medium (3000 sq.deg.) and the Deep (100 sq.deg.) one.

We showed constraints on the DE EoS parameters in terms of the Figure of Merit. Such quantity has been defined by DETF to provide a simple tool to compare the performance of a given cosmological experiment with respect to another, according to the standard DE model prescription.

We quantified the increase of the constraining power of WFXT surveys by adding progressively information from the cluster number counts, the mean cluster power spectrum analysis and the CMB prior from Planck experiment. The number density of nearby galaxy clusters provides constraints on the amplitude of the power spectrum and its evolution is directly related to the growth rate of density perturbations and, thus, to the amount of DE at a given redshift. The power spectrum provides direct information on the shape and amplitude of the underlying DM model and the evolution of clustering properties is again sensitive to the growth rate of perturbations. The slightly different directions of degeneracy of the

constraints in the  $(w_0, w_a)$  parameters space from cluster number density and power spectrum explains why the constraints substantially improve when we consider the two contribution together rather than separately. We verified that adding the CMB information improve the corresponding constraints on the DE EoS, mostly as a consequence of the constraint provided by CMB data on the geometry of the Universe. In particular for the first time we see that with a sufficient large survey area and a high statistics of clusters, Redshift Space Distortions carries important cosmological information through the linear growth of perturbations, also in the case of cluster surveys. Indeed, the DE FoM from the power spectrum analysis of a large survey area increases by a factor 35 when including RSDs.

We extend the previous analysis computing forecasts for constraints on deviations from Gaussian distribution of primordial density perturbations, from the WFXT experiment. We expect that a positively skewed distribution provides an enhanced probability of forming large collapsed structures at high redshift, thereby changing the timing of structure formation and the shape and evolution of the cluster mass function. A peculiar feature of such models is that the halo bias acquires an extra scale dependence due to primordial non-Gaussianity, thus we find that the power spectrum provides strong constraints on the non-Gaussian  $f_{\text{NL}}$  parameter, which complement the stringent constraints on the power spectrum normalization,  $\sigma_8$ , from the number counts.

Therefore, we demonstrated that the combination of information from the evolution of the cluster population and its clustering can significantly enhance the constraining power of cluster surveys. However, a large statistics of objects on a large redshift range is needed in order to carry out the the power spectrum analysis.

A crucial aspect concerning the possibility of using clusters as cosmological tools regards the measurement of their mass and how this mass can be related to observational quantities (i.e., X-ray temperature, velocity dispersion of member galaxies, strong and weak lensing effects). In fact, we showed that uncertainties on the calibration of the mass-observable relation and its evolution with redshift can strongly affect the constraining power of clusters. We compared cosmological constraints obtained by assuming different levels of prior knowledge of the parameters which define the relation between cluster mass and X-ray observables. The FoM of the DE EoS parameters increases by an order of magnitude when we assume a precise and robust calibration of the mass-observable relation, with respect to the case in which no such information is available. Pa-

rameters whose constraints are entirely derived from growth tests such as  $\sigma_8$  are the most strongly affected by the uncertainties on the mass-observable relation. Interestingly, instead, the level of uncertainties on the scaling relation does not affect directly constraints on the  $f_{\text{NL}}$  parameter. However, due to the strong degeneracy between  $\sigma_8$  and  $f_{\text{NL}}$ , in order to detect deviation from the Gaussian paradigm a well defined calibration of the scaling relation is necessary.

This analysis emphasizes that a full exploitation of the cosmological information carried by future cluster surveys require not only large statistics but also a robust measurement of mass proxies for a significant fraction of the cluster sample, which ought to be derived from the same X-ray survey data. This will be possible with future X-ray surveys only with an adequate combination of survey area, sensitivity and angular resolution that provide at least  $\sim 10^3$  net photon counts for the majority of cluster included in the survey.

We demonstrated that the optimization of the survey strategy depends on the class of cosmological models that one wants to constrain. As for the DE EoS analysis we found that the Medium survey is the one carrying most of the constraining power (Table (3.2)). Since this survey is expected to yield the largest number of cluster out to  $z \sim 1$ , it is the best suited to trace the growth history of perturbation over a large redshift baseline, as required to follow the redshift dependence of the DE EoS. On the contrary, our results showed that the Wide survey is the best suited to constrain deviations from non-Gaussian initial conditions, because, sampling the long wavelength modes, it is possible to detect a scale-dependence of the bias. With the Fisher Matrix algorithm, we also provided forecasts for constraints on the DE EoS parameters for the cluster survey to be carried out with the optical near-infrared EUCLID satellite, which has been recently approved by the European Space Agency (ESA).

The techniques developed to forecast constraints from future survey, presented in this Thesis, can be used to optimize the design of future surveys of galaxy clusters in order to explore the nature of the “Dark Sector” of the Universe. Moreover, models of modified gravity and of clustered DE represent other broad classes of models for which clusters can provide important constraints. This studies will require a multiwavelength approach, combining the strengths of the available techniques for finding clusters, calibrating their masses and obtaining low-scatter mass proxies, by minimizing sistematic effects of each method. The power of our method and the robustness of the predictions on constraints on cos-

mological parameters is inextricably linked to the possibility of accurately modelling the relations between mass and observables, and detailed hydrodynamical simulations, where both cluster mass and observable quantities can be exactly computed, have to be further used to this aim (e.g. Borgani & Kravtsov, 2009). Thus, simulations can be used to verify in detail the validity of assumptions on which the mass estimators, applied to observations, are based, like the assumption of hydrostatic equilibrium, for which a violation in simulations at the 10 – 20% level has been found.

Given the importance of having an extended redshift range over which the evolution of perturbation growth is studied, and an accurate determination of masses for the clusters included in a survey, in the second part of this Thesis (see Chapter 4), we analysed the evolution of the cluster number density as defined by the the ROSAT Deep Cluster Survey at redshift  $z > 0.8$  (zRDCS-1). The zRDCS-1 sample contains nine clusters, within the redshift range  $0.8 < z < 1.3$ , all of them are spectroscopically confirmed and the majority have a precise mass determination both from WL and X-ray analysis. In our analysis, as prior information we used constraints obtained by Vikhlinin et al. (2009b) from two cluster samples with 49 and 37 clusters with median redshifts  $\bar{z} = 0.01$  and  $\bar{z} = 0.5$  respectively.

In order to perform our analysis, we developed a fitting algorithm based on the Montecarlo Markov-Chain (MCMC) and the maximum likelihood criterion, to calculate constraints on cosmological parameters from sample of clusters with a well defined sky coverage and a precise measure of cluster masses. We computed for the first time the mass function of clusters with median redshift  $\bar{z} = 0.865$ . Our analysis showed that number density of clusters as observed in the high- $z$  RDCS sample, is in agreement with predictions of the  $\Lambda$ CDM model based on cluster observation at lower redshift. Moreover, combining the likelihood obtained from the analysis of the zRDCS-1 with the prior probability provided by the analysis performed by Vikhlinin et al. (2009b), we slightly improves constraints on cosmological parameters that describe the  $\Lambda$ CDM model as calculated by Vikhlinin et al. (2009b).

All the analyses that we performed in this Thesis stress that a precise estimation of the cluster mass, is required. In particular with future high-sensitive surveys of clusters, we will be able to calculate masses with different method in order to minimize the systematics errors, and consequently obtain important constraints on cosmological parameters. A second important point is that we need to sample the growth of struc-

ture history in a large redshift range in order to discriminate between the  $\Lambda$ CDM and the quintessence cosmological models.

Moreover, it is necessary to further investigate the high mass end of mass function as provided with simulations. The commonly used fitting functions are simply extrapolated results in extremely massive clusters regime, because the existing limited-volume simulations do not constrain the number density of such clusters accurately. Another potentially important contribution from numerical simulation is the predicted mass function specific for a given survey, which takes into account the various aspects of selection limits and projection effects. The projection effect is always a concern in the cosmological interpretation of extremely massive clusters. Moreover, the theoretical calibration of the mass function for precision cosmology should include careful examination of subtle dependencies of mass function on cosmological parameters (especially on the DE EoS), effects of neutrinos with non-zero mass, effects of non-Gaussianity. Finally, we need to understand the effects of baryonic physics on the mass distribution of halos and related effects on the mass function, which can be quite significant (Cui et al., 2011).

# Appendix A

## The Fisher Matrix statistical technique

In order to define what the Fisher Matix information is, we have to give some bases on the Bayesian statistics.

According to the Bayesian approach, we measure the mean (or the variance) value of a given parameter by asking, which is the probability that the mean (or the variance) takes a specific value, given a set of observations and a set of assumptions (the prior). Commonly, the prior is subdivided into assumptions that one asserts are true, and a model equipped with parameters whose values one wishes to estimate.

Suppose that a data set consists of  $N$  real numbers  $x_1, x_2, \dots, x_N$ , which is arranged in an  $N$ -dimensional vector  $\mathbf{x}$ . Before collecting the data, we think of  $\mathbf{x}$  as a random variable with some probability distribution  $L(\mathbf{x}|\boldsymbol{\theta})$ , which depends in some known way on a vector of  $M$  model parameters  $\boldsymbol{\theta} = (\theta_1, \theta_2, \dots, \theta_M)$ .

We will let  $\tilde{\boldsymbol{\theta}}$  denote the true parameter values and let  $\boldsymbol{\theta}$  refer to our estimate of  $\boldsymbol{\theta}$ . Since  $\boldsymbol{\theta}$  is some function of the data vector  $\mathbf{x}$ , it too is a random variable. For it to be a good estimate, it has to be unbiased,  $\langle \boldsymbol{\theta} \rangle = \tilde{\boldsymbol{\theta}}$  and minimize the standard deviations

$$\Delta\theta_\alpha \equiv \left( \langle \theta_\alpha^2 \rangle - \langle \theta_\alpha \rangle^2 \right)^{1/2}. \quad (\text{A.1})$$

The foundation of Bayesian statistics is Bayes' theorem.

The Bayes' Theorem states that the posterior probability  $P(\boldsymbol{\theta}|\mathbf{x}, y)$  that the parameters  $\boldsymbol{\theta}$  take on certain values, given the observational data  $\mathbf{x}$  and prior assumptions  $y$ , is proportional to the likelihood function, the probability  $P(\mathbf{x}|\boldsymbol{\theta}, y) \equiv L(\mathbf{x}|\boldsymbol{\theta}, y)$  of the observations  $\mathbf{x}$  given parameters

$\theta$  and prior assumptions  $y$ , multiplied by the prior probability  $P(\theta|y)$  of the parameters  $\theta$  given the prior assumptions  $y$ :

$$P(\theta|\mathbf{x}, y) = \frac{P(\mathbf{x}|\theta, y) P(\theta|y)}{P(\mathbf{x}|y)}. \quad (\text{A.2})$$

The probability  $P(\mathbf{x}|y)$  is the evidence. For parameter estimation, the evidence simply acts to normalise the probabilities,

$$P(\mathbf{x}|y) = \int d\theta P(\mathbf{x}|\theta y) P(\theta|y) \quad (\text{A.3})$$

and the relative probabilities of the parameters do not depend on it, so it is often ignored and not even calculated.

However, the evidence does play an important role in *model selection*, when more than one theoretical model is being considered, and one wants to choose which model is most likely, whatever the parameters are.

The prior  $y$  may be the result of previous experiments, or may be a theoretical prior, in the absence of any data. In such cases, it is common to adopt the principle of indifference and assume that all values of the parameter(s) is (are) equally likely, and take  $p(\theta|y) = \text{constant}$ . This is referred to as a *flat prior*.

If we have some more information, from another experiment, then we can use Bayes' theorem to update our estimate of the probabilities associated with each parameter. It is possible to show that adding the results of a new experiment,  $\mathbf{x}'$ , to the probability of the parameters is the same as doing the two experiments first, and then seeing how they both affect the probability of the parameters:

$$P(\theta|\mathbf{x}'\mathbf{x}y) = \frac{P(\theta|\mathbf{x}y) P(\mathbf{x}'|\theta\mathbf{x}y)}{P(\mathbf{x}'|\mathbf{x}y)} = \frac{P(\theta|y) P(\mathbf{x}'\mathbf{x}|\theta y)}{P(\mathbf{x}'\mathbf{x}|y)}. \quad (\text{A.4})$$

Let us assume to have a posterior probability distribution, which is single-peaked and that the prior is flat, so the posterior is proportional to the likelihood. In this case, close to the peak, a Taylor expansion of the log likelihood implies that locally  $\ln L$  is a multivariate Gaussian in parameter space:

$$\ln L(\mathbf{x}|\theta) = \ln L(\mathbf{x}|\tilde{\theta}) + \frac{1}{2}(\theta_\alpha - \tilde{\theta}_\alpha) \frac{\partial^2 \ln L}{\partial \theta_\alpha \partial \theta_\beta} (\theta_\beta - \tilde{\theta}_\beta) + \dots \quad (\text{A.5})$$

or

$$L(\mathbf{x}|\theta) = L(\mathbf{x}|\tilde{\theta}) \exp \left[ -\frac{1}{2}(\theta_\alpha - \tilde{\theta}_\alpha) H_{\alpha\beta} (\theta_\beta - \tilde{\theta}_\beta) \right]. \quad (\text{A.6})$$

The Hessian matrix  $H_{\alpha\beta} \equiv -\frac{\partial^2 \ln L}{\partial \theta_\alpha \partial \theta_\beta}$  controls whether the estimates of  $\theta_\alpha$  and  $\theta_\beta$  are correlated or not. If it is diagonal, the estimates are uncorrelated. Note that this is a statement about estimates of the quantities, not the quantities themselves, which may be entirely independent, but if they have a similar effect on the data, their estimates may be correlated.

We can now define the Fisher information matrix  $F_{\alpha\beta}$  of a set of parameters  $\theta$  to be minus the expectation value of the second derivative of the log-likelihood function with respect to the parameters:

$$F_{\alpha\beta} \equiv - \left\langle \frac{\partial^2 \ln L}{\partial \theta_\alpha \partial \theta_\beta} \right\rangle. \quad (\text{A.7})$$

Expectation value here means averaged over an ensemble of observational data  $\mathbf{x}$  predicted by the likelihood function

$$\langle t \rangle \equiv \int t L(\mathbf{x}|\theta) d\mathbf{x}. \quad (\text{A.8})$$

Since the likelihood  $L$  is multiplicative over statistically independent sets of observations, it follows that the Fisher matrix is additive over statistically independent observations.

**Marginalising over a gaussian likelihood** The marginal distribution of  $\theta_1$  is obtained by integrating over the other parameters:

$$P(\theta_1) = \int d\theta_2 \dots d\theta_N P(\theta). \quad (\text{A.9})$$

Often one sees marginal distributions of all parameters in pairs, in this case two variables are left out of the integration and the error on these two parameters is represent by an ellipse where one has to specify what contour confidence level to plot. In case of a multivariate Gaussian likelihood the marginal error on parameter  $\theta_\alpha$  is

$$\sigma_\alpha = \sqrt{(H^{-1})_{\alpha\alpha}} = \sqrt{(F^{-1})_{\alpha\alpha}}. \quad (\text{A.10})$$



# Bibliography

- Abell, G. O., Corwin, Jr., H. G., & Olowin, R. P. (1989). A catalog of rich clusters of galaxies. *ApJS*, **70**, 1–138.
- Alam, U., Lukić, Z., & Bhattacharya, S. (2011). Galaxy Clusters as a Probe of Early Dark Energy. *ApJ*, **727**, 87–+.
- Albrecht, A., Bernstein, G., Cahn, R., Freedman, W. L., Hewitt, J., Hu, W., Huth, J., Kamionkowski, M., Kolb, E. W., Knox, L., Mather, J. C., Staggs, S., & Suntzeff, N. B. (2006). Report of the Dark Energy Task Force. *ArXiv e-prints*, 0609591.
- Albrecht, A., Amendola, L., Bernstein, G., Clowe, D., Eisenstein, D., Guzzo, L., Hirata, C., Huterer, D., Kirshner, R., Kolb, E., & Nichol, R. (2009). Findings of the Joint Dark Energy Mission Figure of Merit Science Working Group. *ArXiv e-prints*, 0901.0721.
- Allen, S. W., Schmidt, R. W., Fabian, A. C., & Ebeling, H. (2003). Cosmological constraints from the local X-ray luminosity function of the most X-ray-luminous galaxy clusters. *MNRAS*, **342**, 287–298.
- Allen, S. W., Schmidt, R. W., Ebeling, H., Fabian, A. C., & van Speybroeck, L. (2004). Constraints on dark energy from Chandra observations of the largest relaxed galaxy clusters. *MNRAS*, **353**, 457–467.
- Allen, S. W., Rapetti, D. A., Schmidt, R. W., Ebeling, H., Morris, R. G., & Fabian, A. C. (2008). Improved constraints on dark energy from Chandra X-ray observations of the largest relaxed galaxy clusters. *MNRAS*, **383**, 879–896.
- Allen, S. W., Evrard, A. E., & Mantz, A. B. (2011). Cosmological Parameters from Observations of Galaxy Clusters. *ArXiv e-prints*, 1103.4829.

- Ameglio, S., Borgani, S., Pierpaoli, E., Dolag, K., Ettori, S., & Morandi, A. (2009). Reconstructing mass profiles of simulated galaxy clusters by combining Sunyaev-Zeldovich and X-ray images. *MNRAS*, **394**, 479–490.
- Armendariz-Picon, C., Mukhanov, V., & Steinhardt, P. J. (2000). Dynamical Solution to the Problem of a Small Cosmological Constant and Late-Time Cosmic Acceleration. *Physical Review Letters*, **85**, 4438–4441.
- Astier, P., Guy, J., Regnault, N., Pain, R., & et al. (2006). The Supernova Legacy Survey: measurement of  $\Omega_M$ ,  $\Omega_\Lambda$  and  $w$  from the first year data set. *A&A*, **447**, 31–48.
- Bahcall, N. A. & Bode, P. (2003). The Amplitude of Mass Fluctuations. *ApJ*, **588**, L1–L4.
- Bahcall, N. A. & Soneira, R. M. (1983). The spatial correlation function of rich clusters of galaxies. *ApJ*, **270**, 20–38.
- Bahcall, N. A., Dong, F., Bode, P., Kim, R., Annis, J., McKay, T. A., Hansen, S., Schroeder, J., Gunn, J., Ostriker, J. P., Postman, M., Nichol, R. C., Miller, C., Goto, T., Brinkmann, J., Knapp, G. R., Lamb, D. O., Schneider, D. P., Vogeley, M. S., & York, D. G. (2003). The Cluster Mass Function from Early Sloan Digital Sky Survey Data: Cosmological Implications. *ApJ*, **585**, 182–190.
- Balestra, I., Tozzi, P., Ettori, S., Rosati, P., Borgani, S., Mainieri, V., Norman, C., & Viola, M. (2007). Tracing the evolution in the iron content of the intra-cluster medium. *A&A*, **462**, 429–442.
- Barkhouse, W. A., Green, P. J., Vikhlinin, A., Kim, D.-W., Perley, D., Cameron, R., Silverman, J., Mossman, A., Burenin, R., Jannuzi, B. T., Kim, M., Smith, M. G., Smith, R. C., Tananbaum, H., & Wilkes, B. J. (2006). ChaMP Serendipitous Galaxy Cluster Survey. *ApJ*, **645**, 955–976.
- Bartelmann, M. (2010). TOPICAL REVIEW Gravitational lensing. *Classical and Quantum Gravity*, **27**(23), 233001.
- Bartolo, N., Komatsu, E., Matarrese, S., & Riotto, A. (2004). Non-Gaussianity from inflation: theory and observations. *Phys. Rept.*, **402**, 103–266.

- Basilakos, S., Plionis, M., & Lima, J. A. S. (2010). Confronting dark energy models using galaxy cluster number counts. *Phys. Rev. D*, **82**(8), 083517–+.
- Battye, R. A. & Weller, J. (2003). Constraining cosmological parameters using Sunyaev-Zel’dovich cluster surveys. *Phys. Rev. D*, **68**(8), 083506–+.
- Becker, M. R. & Kravtsov, A. V. (2011). On the Accuracy of Weak-lensing Cluster Mass Reconstructions. *ApJ*, **740**, 25.
- Bertacca, D., Matarrese, S., & Pietroni, M. (2007). Unified Dark Matter in Scalar Field Cosmologies. *Modern Physics Letters A*, **22**, 2893–2907.
- Bertacca, D., Bartolo, N., Diaferio, A., & Matarrese, S. (2008). How the scalar field of unified dark matter models can cluster. *JCAP*, **10**, 23–+.
- Bignamini, A. (2010). The Swift-XRT Survey of Groups and Clusters of Galaxies. *ArXiv e-prints*, 1007.1804.
- Birkinshaw, M. (1999). The Sunyaev-Zel’dovich effect. *Phys. Rept.*, **310**, 97–195.
- Biviano, A. & Girardi, M. (2003). The Mass Profile of Galaxy Clusters out to  $\sim 2r_{200}$ . *ApJ*, **585**, 205–214.
- Biviano, A., Murante, G., Borgani, S., Diaferio, A., Dolag, K., & Girardi, M. (2006). On the efficiency and reliability of cluster mass estimates based on member galaxies. *A&A*, **456**, 23–36.
- Blakeslee, J. P., Holden, B. P., Franx, M., Rosati, P., Bouwens, R. J., Demarco, R., Ford, H. C., Homeier, N. L., Illingworth, G. D., Jee, M. J., Mei, S., Menanteau, F., Meurer, G. R., Postman, M., & Tran, K.-V. H. (2006). Clusters at Half Hubble Time: Galaxy Structure and Colors in RX J0152.7-1357 and MS 1054-03. *ApJ*, **644**, 30–53.
- Böhringer, H., Schuecker, P., Guzzo, L., Collins, C. A., Voges, W., Cradace, R. G., Ortiz-Gil, A., Chincarini, G., De Grandi, S., Edge, A. C., MacGillivray, H. T., Neumann, D. M., Schindler, S., & Shaver, P. (2004). The ROSAT-ESO Flux Limited X-ray (REFLEX) Galaxy cluster survey. V. The cluster catalogue. *A&A*, **425**, 367–383.

- Bond, J. R., Cole, S., Efstathiou, G., & Kaiser, N. (1991). Excursion set mass functions for hierarchical Gaussian fluctuations. *ApJ*, **379**, 440–460.
- Borgani, S. & Kravtsov, A. (2009). Cosmological simulations of galaxy clusters. *ArXiv e-prints*, 0906.4370.
- Borgani, S., Moscardini, L., Plionis, M., Gorski, K. M., Holtzman, J., Klypin, A., Primack, J., Smith, C., & Stompor, R. (1997). Constraining the power spectrum using clusters. *New Astronomy*, **1**, 321–347.
- Borgani, S., Girardi, M., Carlberg, R. G., Yee, H. K. C., & Ellingson, E. (1999). Velocity Dispersions of CNOG Clusters and the Evolution of the Cluster Abundance. *ApJ*, **527**, 561–572.
- Borgani, S., Rosati, P., Tozzi, P., Stanford, S. A., Eisenhardt, P. R., Lidman, C., Holden, B., Della Ceca, R., Norman, C., & Squires, G. (2001). Measuring  $\Omega_m$  with the ROSAT Deep Cluster Survey. *ApJ*, **561**, 13–21.
- Borgani, S., Rosati, P., Sartoris, B., Tozzi, P., Giacconi, R., & WFXT Team (2011). Astrophysics and cosmology with galaxy clusters: the WFXT perspective. *Memorie della Societa Astronomica Italiana Supplementi*, **17**, 36.
- Boschin, W. (2002). A deep cluster survey in Chandra archival data. First results. *A&A*, **396**, 397–409.
- Brodwin, M., Ruel, J., & SPT Team (2010). SPT-CL J0546-5345: A Massive  $z > 1$  Galaxy Cluster Selected Via the Sunyaev-Zel'dovich Effect with the South Pole Telescope. *ApJ*, **721**, 90–97.
- Brookfield, A. W., van de Bruck, C., & Hall, L. M. H. (2008). New interactions in the dark sector mediated by dark energy. *Phys. Rev. D*, **77**(4), 043006–+.
- Burenin, R. A., Vikhlinin, A., Hornstrup, A., Ebeling, H., Quintana, H., & Mescheryakov, A. (2007). The 400 Square Degree ROSAT PSPC Galaxy Cluster Survey: Catalog and Statistical Calibration. *ApJS*, **172**, 561–582.
- Burrows, C. J., Burg, R., & Giacconi, R. (1992). Optimal grazing incidence optics and its application to wide-field X-ray imaging. *ApJ*, **392**, 760–765.

- Caldwell, R. R., Dave, R., & Steinhardt, P. J. (1998). Cosmological Imprint of an Energy Component with General Equation of State. *Physical Review Letters*, **80**, 1582–1585.
- Camera, S., Diaferio, A., & Cardone, V. F. (2011). Testing a phenomenologically extended DGP model with upcoming weak lensing surveys. *JCAP*, **1**, 29–+.
- Cappelluti, N., Brusa, M., Hasinger, G., Comastri, A., Zamorani, G., & et al. (2009). The XMM-Newton wide-field survey in the COSMOS field. The point-like X-ray source catalogue. *A&A*, **497**, 635–648.
- Carlstrom, J. E. (2006). The Sunyaev-Zel'dovich Array and the 10-m South Pole Telescope. In D. C. Backer, J. M. Moran, & J. L. Turner, editor, *Revealing the Molecular Universe: One Antenna is Never Enough*, volume 356 of *Astronomical Society of the Pacific Conference Series*, page 35.
- Cash, W. (1979). Parameter estimation in astronomy through application of the likelihood ratio. *ApJ*, **228**, 939–947.
- Cavaliere, A. & Fusco-Femiano, R. (1976). X-rays from hot plasma in clusters of galaxies. *A&A*, **49**, 137–144.
- Cohn, J. D. & White, M. (2008). Dark matter halo abundances, clustering and assembly histories at high redshift. *MNRAS*, **385**, 2025–2033.
- Cohn, J. D., Evrard, A. E., White, M., Croton, D., & Ellingson, E. (2007). Red-sequence cluster finding in the Millennium Simulation. *MNRAS*, **382**, 1738–1750.
- Cole, S. & Kaiser, N. (1989). Biased clustering in the cold dark matter cosmogony. *MNRAS*, **237**, 1127–1146.
- Coles, P. & Lucchin, F. (2002). *Cosmology: The Origin and Evolution of Cosmic Structure, Second Edition*.
- Corasaniti, P. S. & Copeland, E. J. (2003). Model independent approach to the dark energy equation of state. *Phys. Rev. D*, **67**(6), 063521–+.
- Corless, V. L. & King, L. J. (2007). A statistical study of weak lensing by triaxial dark matter haloes: consequences for parameter estimation. *MNRAS*, **380**, 149–161.

- Creminelli, P., Senatore, L., Zaldarriaga, M., & Tegmark, M. (2007). Limits on  $f_{NL}$  parameters from Wilkinson Microwave Anisotropy Probe three-year data. *Journal of Cosmology and Astro-Particle Physics*, **3**, 5–+.
- Crociani, D., Moscardini, L., Viel, M., & Matarrese, S. (2009). The effects of primordial non-Gaussianity on the cosmological reionization. *MNRAS*, **394**, 133–141.
- Cui, W., Borgani, S., Dolag, K., Murante, G., & Tornatore, L. (2011). The effects of baryons on the halo mass function. *ArXiv e-prints*, 1111.3066.
- Cunha, C. (2009). Cross-calibration of cluster mass observables. *Phys. Rev. D*, **79**(6), 063009–+.
- Cunha, C. E. & Evrard, A. E. (2010). Sensitivity of galaxy cluster dark energy constraints to halo modeling uncertainties. *Phys. Rev. D*, **81**(8), 083509–+.
- Dalal, N., Doré, O., Huterer, D., & Shirokov, A. (2008). Imprints of primordial non-Gaussianities on large-scale structure: Scale-dependent bias and abundance of virialized objects. *Phys. Rev. D*, **77**(12), 123514–+.
- Davis, M. & Peebles, P. J. E. (1983). A survey of galaxy redshifts. V - The two-point position and velocity correlations. *ApJ*, **267**, 465–482.
- Demarco, R., Rosati, P., Lidman, C., Girardi, M., Nonino, M., Rettura, A., Strazzullo, V., van der Wel, A., Ford, H. C., Mainieri, V., Holden, B. P., Stanford, S. A., Blakeslee, J. P., Gobat, R., Postman, M., Tozzi, P., Overzier, R. A., Zirm, A. W., Benítez, N., Homeier, N. L., Illingworth, G. D., Infante, L., Jee, M. J., Mei, S., Menanteau, F., Motta, V., Zheng, W., Clampin, M., & Hartig, G. (2007). VLT and ACS Observations of RDCS J1252.9-2927: Dynamical Structure and Galaxy Populations in a Massive Cluster at  $z = 1.237$ . *ApJ*, **663**, 164–182.
- Desjacques, V., Seljak, U., & Iliev, I. T. (2009). Scale-dependent bias induced by local non-Gaussianity: a comparison to N-body simulations. *MNRAS*, **396**, 85–96.
- Dodelson, S. (2003). *Modern cosmology*.
- Doran, M. & Wetterich, C. (2003). Quintessence and the cosmological constant. *Nuclear Physics B Proceedings Supplements*, **124**, 57–62.

- Duffy, A. R., Schaye, J., Kay, S. T., & Dalla Vecchia, C. (2008). Dark matter halo concentrations in the Wilkinson Microwave Anisotropy Probe year 5 cosmology. *MNRAS*, **390**, L64–L68.
- Dunkley, J., Komatsu, E., Nolta, M. R., Spergel, D. N., Larson, D., Hinshaw, G., Page, L., Bennett, C. L., Gold, B., Jarosik, N., Weiland, J. L., Halpern, M., Hill, R. S., Kogut, A., Limon, M., Meyer, S. S., Tucker, G. S., Wollack, E., & Wright, E. L. (2009). Five-Year Wilkinson Microwave Anisotropy Probe (WMAP) Observations: Likelihoods and Parameters from the WMAP data. *ApJS*, **180**, 306–376.
- Dvali, G., Gabadadze, G., & Porrati, M. (2000). 4D gravity on a brane in 5D Minkowski space. *Physics Letters B*, **485**, 208–214.
- Ebeling, H., Edge, A. C., Bohringer, H., Allen, S. W., Crawford, C. S., Fabian, A. C., Voges, W., & Huchra, J. P. (1998). The ROSAT Brightest Cluster Sample - I. The compilation of the sample and the cluster log N-log S distribution. *MNRAS*, **301**, 881–914.
- Ebeling, H., Edge, A. C., Mantz, A., Barrett, E., Henry, J. P., Ma, C. J., & van Speybroeck, L. (2010). The X-ray brightest clusters of galaxies from the Massive Cluster Survey. *MNRAS*, **407**, 83–93.
- Eisenstein, D. J. & Hu, W. (1998). Baryonic Features in the Matter Transfer Function. *ApJ*, **496**, 605–+.
- Eisenstein, D. J. & Hu, W. (1999). Power Spectra for Cold Dark Matter and Its Variants. *ApJ*, **511**, 5–15.
- Eisenstein, D. J., Zehavi, I., Hogg, D. W., Scoccimarro, R., Blanton, M. R., Nichol, R. C., Scranton, R., Seo, H.-J., Tegmark, M., Zheng, Z., & et al. (2005). Detection of the Baryon Acoustic Peak in the Large-Scale Correlation Function of SDSS Luminous Red Galaxies. *ApJ*, **633**, 560–574.
- Eke, V. R., Cole, S., & Frenk, C. S. (1996). Cluster evolution as a diagnostic for Omega. *MNRAS*, **282**, 263–280.
- Ettori, S., Tozzi, P., Borgani, S., & Rosati, P. (2004). Scaling laws in X-ray galaxy clusters at redshift between 0.4 and 1.3. *A&A*, **417**, 13–27.

- Ettori, S., Morandi, A., Tozzi, P., Balestra, I., Borgani, S., Rosati, P., Lovisari, L., & Terenziani, F. (2009). The cluster gas mass fraction as a cosmological probe: a revised study. *A&A*, **501**, 61–73.
- Evrard, A. E., MacFarland, T. J., Couchman, H. M. P., Colberg, J. M., Yoshida, N., White, S. D. M., Jenkins, A., Frenk, C. S., Pearce, F. R., Peacock, J. A., & Thomas, P. A. (2002). Galaxy Clusters in Hubble Volume Simulations: Cosmological Constraints from Sky Survey Populations. *ApJ*, **573**, 7–36.
- Fabjan, D., Borgani, S., Rasia, E., Bonafede, A., Dolag, K., Murante, G., & Tornatore, L. (2011). X-ray mass proxies from hydrodynamic simulations of galaxy clusters - I. *MNRAS*, **416**, 801–816.
- Fahlman, G., Kaiser, N., Squires, G., & Woods, D. (1994). Dark matter in MS 1224 from distortion of background galaxies. *ApJ*, **437**, 56–62.
- Fassbender, R., Boehringer, H., Nastasi, A., Suhada, R., Muehleger, M., de Hoon, A., Kohnert, J., Lamer, G., Mohr, J. J., Pierini, D., Pratt, G. W., Quintana, H., Rosati, P., Santos, J. S., & Schwobe, A. D. (2011). The X-ray luminous galaxy cluster population at  $0.9L_X-T \leq L_X-T \sim 1.6$  as revealed by the XMM-Newton Distant Cluster Project. *ArXiv e-prints*.
- Fedeli, C., Moscardini, L., & Matarrese, S. (2009). The clustering of galaxy clusters in cosmological models with non-Gaussian initial conditions: predictions for future surveys. *MNRAS*, **397**, 1125–1137.
- Feldman, H. A., Kaiser, N., & Peacock, J. A. (1994). Power-spectrum analysis of three-dimensional redshift surveys. *ApJ*, **426**, 23–37.
- Felten, J. E., Gould, R. J., Stein, W. A., & Woolf, N. J. (1966). X-Rays from the Coma Cluster of Galaxies. *ApJ*, **146**, 955–958.
- Finoguenov, A., Guzzo, L., Hasinger, G., Scoville, N. Z., Aussel, H., Böhringer, H., Brusa, M., Capak, P., Cappelluti, N., Comastri, A., Gioldini, S., Griffiths, R. E., Impey, C., Koekemoer, A. M., Kneib, J.-P., Leauthaud, A., Le Fèvre, O., Lilly, S., Mainieri, V., Massey, R., McCracken, H. J., Mobasher, B., Murayama, T., Peacock, J. A., Sakelliou, I., Schinnerer, E., Silverman, J. D., Smolčić, V., Taniguchi, Y., Tasca, L., Taylor, J. E., Trump, J. R., & Zamorani, G. (2007). The XMM-Newton Wide-Field Survey in the COSMOS Field: Statistical Properties of Clusters of Galaxies. *ApJS*, **172**, 182–195.

- Francis, M. J., Lewis, G. F., & Linder, E. V. (2009). Halo mass functions in early dark energy cosmologies. *MNRAS*, **393**, L31–L35.
- Frenk, C. S., Evrard, A. E., White, S. D. M., & Summers, F. J. (1996). Galaxy Dynamics in Clusters. *ApJ*, **472**, 460.
- Gehrels, N. (1986). Confidence limits for small numbers of events in astrophysical data. *ApJ*, **303**, 336–346.
- Giacconi, R., Borgani, S., Rosati, P., Tozzi, P., Gilli, R., & et al. (2009). Galaxy clusters and the cosmic cycle of baryons across cosmic times. In *AGB Stars and Related Phenomena 2010: The Astronomy and Astrophysics Decadal Survey*, volume 2010 of *Astronomy*, pages 90–+.
- Giannantonio, T. & Porciani, C. (2010). Structure formation from non-Gaussian initial conditions: Multivariate biasing, statistics, and comparison with N-body simulations. *Phys. Rev. D*, **81**(6), 063530.
- Girardi, M. & Mezzetti, M. (2001). Evolution of the Internal Dynamics of Galaxy Clusters. *ApJ*, **548**, 79–96.
- Girardi, M., Demarco, R., Rosati, P., & Borgani, S. (2005). Internal dynamics of the  $z \sim 0.8$  cluster RX J0152.7-1357. *A&A*, **442**, 29–41.
- Gladders, M. D. & Yee, H. K. C. (2000). A New Method For Galaxy Cluster Detection. I. The Algorithm. *AJ*, **120**, 2148–2162.
- Gladders, M. D., Yee, H. K. C., Majumdar, S., Barrientos, L. F., Hoekstra, H., Hall, P. B., & Infante, L. (2007). Cosmological Constraints from the Red-Sequence Cluster Survey. *ApJ*, **655**, 128–134.
- Grossi, M. & Springel, V. (2009). The impact of early dark energy on non-linear structure formation. *MNRAS*, **394**, 1559–1574.
- Grossi, M., Dolag, K., Branchini, E., Matarrese, S., & Moscardini, L. (2007). Evolution of massive haloes in non-Gaussian scenarios. *MNRAS*, **382**, 1261–1267.
- Grossi, M., Verde, L., Carbone, C., Dolag, K., Branchini, E., Iannuzzi, F., Matarrese, S., & Moscardini, L. (2009). Large-scale non-Gaussian mass function and halo bias: tests on N-body simulations. *MNRAS*, **398**, 321–332.

- Guth, A. H. (1981). Inflationary universe: A possible solution to the horizon and flatness problems. *Phys. Rev. D*, **23**, 347–356.
- Guzzo, L., Pierleoni, M., Meneux, B., Branchini, E., Le Fèvre, O., & et al. (2008). A test of the nature of cosmic acceleration using galaxy redshift distortions. *Nature*, **451**, 541–544.
- Hamuy, M., Phillips, M. M., Maza, J., Suntzeff, N. B., Schommer, R. A., & Aviles, R. (1995). A Hubble diagram of distant type IA supernovae. *AJ*, **109**, 1–13.
- Hand, N., Appel, J. W., Battaglia, N., Bond, J. R., Das, S., Devlin, M. J., & et al. (2011). The Atacama Cosmology Telescope: Detection of Sunyaev-Zel'Dovich Decrement in Groups and Clusters Associated with Luminous Red Galaxies. *ApJ*, **736**, 39.
- Hannestad, S. (2010). Neutrino physics from precision cosmology. *Progress in Particle and Nuclear Physics*, **65**, 185–208.
- Hao, J., McKay, T. A., Koester, B. P., Rykoff, E. S., Rozo, E., Annis, J., Wechsler, R. H., Evrard, A., Siegel, S. R., Becker, M., Busha, M., Gerdes, D., Johnston, D. E., & Sheldon, E. (2010). A GMBCG Galaxy Cluster Catalog of 55,424 Rich Clusters from SDSS DR7. *ApJS*, **191**, 254–274.
- Heavens, A. (2009). Statistical techniques in cosmology. *ArXiv e-prints*, 0906.0664.
- Henry, J. P. (2000). Measuring Cosmological Parameters from the Evolution of Cluster X-Ray Temperatures. *ApJ*, **534**, 565–580.
- Henry, J. P. (2004). X-Ray Temperatures for the Extended Medium-Sensitivity Survey High-Redshift Cluster Sample: Constraints on Cosmology and the Dark Energy Equation of State. *ApJ*, **609**, 603–616.
- Henry, J. P. & Arnaud, K. A. (1991). A measurement of the mass fluctuation spectrum from the cluster X-ray temperature function. *ApJ*, **372**, 410–418.
- Henry, J. P., Evrard, A. E., Hoekstra, H., Babul, A., & Mahdavi, A. (2009). The X-Ray Cluster Normalization of the Matter Power Spectrum. *ApJ*, **691**, 1307–1321.

- Hoekstra, H. (2001). The effect of distant large scale structure on weak lensing mass estimates. *A&A*, **370**, 743–753.
- Hoekstra, H. (2007). A comparison of weak-lensing masses and X-ray properties of galaxy clusters. *MNRAS*, **379**, 317–330.
- Holden, B. P., Stanford, S. A., Squires, G. K., Rosati, P., Tozzi, P., Eisenhardt, P., & Spinrad, H. (2002). Moderate-Temperature Clusters of Galaxies from the RDCS and the High-Redshift Luminosity-Temperature Relation. *AJ*, **124**, 33–45.
- Holder, G., Haiman, Z., & Mohr, J. J. (2001). Constraints on  $\Omega_m$ ,  $\Omega_\Lambda$ , and  $\sigma_8$  from Galaxy Cluster Redshift Distributions. *ApJ*, **560**, L111–L114.
- Holman, R. & Tolley, A. J. (2008). Enhanced non-Gaussianity from excited initial states. *Journal of Cosmology and Astro-Particle Physics*, **5**, 1–+.
- Holz, D. E. & Perlmutter, S. (2010). The most massive objects in the Universe. *ArXiv e-prints*, 1004.5349.
- Hoyle, B., Jimenez, R., & Verde, L. (2011). Implications of multiple high-redshift galaxy clusters. *Phys. Rev. D*, **83**(10), 103502.
- Hu, W. & Kravtsov, A. V. (2003). Sample Variance Considerations for Cluster Surveys. *ApJ*, **584**, 702–715.
- Huterer, D. & White, M. (2002). Weak Lensing as a Calibrator of the Cluster Mass-Temperature Relation. *ApJ*, **578**, L95–L98.
- Jee, M. J., White, R. L., Benítez, N., Ford, H. C., Blakeslee, J. P., Rosati, P., Demarco, R., & Illingworth, G. D. (2005). Weak-Lensing Analysis of the  $z \sim 0.8$  Cluster CL 0152-1357 with the Advanced Camera for Surveys. *ApJ*, **618**, 46–67.
- Jee, M. J., Ford, H. C., Illingworth, G. D., White, R. L., Broadhurst, T. J., Coe, D. A., Meurer, G. R., van der Wel, A., Benítez, N., Blakeslee, J. P., Bouwens, R. J., Bradley, L. D., Demarco, R., Homeier, N. L., Martel, A. R., & Mei, S. (2007). Discovery of a Ringlike Dark Matter Structure in the Core of the Galaxy Cluster Cl 0024+17. *ApJ*, **661**, 728–749.
- Jee, M. J., Rosati, P., Ford, H. C., Dawson, K. S., Lidman, C., Perlmutter, S., Demarco, R., Strazzullo, V., Mullis, C., Böhringer, H., & Fassbender, R. (2009). Hubble Space Telescope Weak-lensing Study of the Galaxy

- Cluster XMMU J2235.3 - 2557 at  $z \sim 1.4$ : A Surprisingly Massive Galaxy Cluster When the Universe is One-third of its Current Age. *ApJ*, **704**, 672–686.
- Jee, M. J., Dawson, K. S., Hoekstra, H., Perlmutter, S., Rosati, P., Brodwin, M., Suzuki, N., Koester, B., Postman, M., Lubin, L., Meyers, J., Stanford, S. A., Barbary, K., Barrientos, F., Eisenhardt, P., Ford, H. C., Gilbank, D. G., Gladders, M. D., Gonzalez, A., Harris, D. W., Huang, X., Lidman, C., Rykoff, E. S., Rubin, D., & Spadafora, A. L. (2011). Scaling Relations and Overabundance of Massive Clusters at  $z > \sim 1$  from Weak-lensing Studies with the Hubble Space Telescope. *ApJ*, **737**, 59.
- Jenkins, A., Frenk, C. S., White, S. D. M., Colberg, J. M., Cole, S., Evrard, A. E., Couchman, H. M. P., & Yoshida, N. (2001). The mass function of dark matter haloes. *MNRAS*, **321**, 372–384.
- Jimenez, R. & Verde, L. (2009). Implications for primordial non-Gaussianity ( $f_{NL}$ ) from weak lensing masses of high- $z$  galaxy clusters. *Phys. Rev. D*, **80**(12), 127302–+.
- Jing, Y. P. (1998). Accurate Fitting Formula for the Two-Point Correlation Function of Dark Matter Halos. *ApJ*, **503**, L9.
- Jing, Y. P. (1999). Accurate Determination of the Lagrangian Bias for the Dark Matter Halos. *ApJ*, **515**, L45–L48.
- Johnston, D. E., Sheldon, E. S., Wechsler, R. H., Rozo, E., Koester, B. P., Frieman, J. A., McKay, T. A., Evrard, A. E., Becker, M. R., & Annis, J. (2007). Cross-correlation Weak Lensing of SDSS galaxy Clusters II: Cluster Density Profiles and the Mass–Richness Relation. *ArXiv e-prints*.
- Kaiser, N. (1987). Clustering in real space and in redshift space. *MNRAS*, **227**, 1–21.
- Kaiser, N. & Squires, G. (1993). Mapping the dark matter with weak gravitational lensing. *ApJ*, **404**, 441–450.
- King, I. R. (1966). The structure of star clusters. IV. Photoelectric surface photometry in nine globular clusters. *AJ*, **71**, 276–+.
- Klypin, A. A. & Kopylov, A. I. (1983). The Spatial Covariance Function for Rich Clusters of Galaxies. *Soviet Astronomy Letters*, **9**, 41–+.

- Koester, B. P., McKay, T. A., Annis, J., Wechsler, R. H., Evrard, A., Bleem, L., Becker, M., Johnston, D., Sheldon, E., Nichol, R., Miller, C., Scranton, R., Bahcall, N., Barentine, J., Brewington, H., Brinkmann, J., Harvanek, M., Kleinman, S., Krzesinski, J., Long, D., Nitta, A., Schneider, D. P., Sneddin, S., Voges, W., & York, D. (2007a). A MaxBCG Catalog of 13,823 Galaxy Clusters from the Sloan Digital Sky Survey. *ApJ*, **660**, 239–255.
- Koester, B. P., McKay, T. A., Annis, J., Wechsler, R. H., Evrard, A. E., Rozo, E., Bleem, L., Sheldon, E. S., & Johnston, D. (2007b). MaxBCG: A Red-Sequence Galaxy Cluster Finder. *ApJ*, **660**, 221–238.
- Komatsu, E. & Spergel, D. N. (2001). Acoustic signatures in the primary microwave background bispectrum. *Phys. Rev. D*, **63**(6), 063002–+.
- Komatsu, E., Dunkley, J., Nolta, M. R., Bennett, C. L., Gold, B., Hinshaw, G., Jarosik, N., Larson, D., Limon, M., Page, L., Spergel, D. N., Halpern, M., Hill, R. S., Kogut, A., Meyer, S. S., Tucker, G. S., Weiland, J. L., Wollack, E., & Wright, E. L. (2009). Five-Year Wilkinson Microwave Anisotropy Probe Observations: Cosmological Interpretation. *ApJS*, **180**, 330–376.
- Komatsu, E., Smith, K. M., Dunkley, J., Bennett, C. L., Gold, B., Hinshaw, G., Jarosik, N., Larson, D., Nolta, M. R., Page, L., & et al. (2011). Seven-year Wilkinson Microwave Anisotropy Probe (WMAP) Observations: Cosmological Interpretation. *ApJS*, **192**, 18–+.
- Kowalski, M., Rubin, D., Aldering, G., Agostinho, R. J., Amadon, A., & et al. (2008). Improved Cosmological Constraints from New, Old, and Combined Supernova Data Sets. *ApJ*, **686**, 749–778.
- Kravtsov, A. V., Vikhlinin, A., & Nagai, D. (2006). A New Robust Low-Scatter X-Ray Mass Indicator for Clusters of Galaxies. *ApJ*, **650**, 128–136.
- Lamer, G., Hoeft, M., Kohnert, J., Schwöpe, A., & Storm, J. (2008). 2XMM J083026+524133: the most X-ray luminous cluster at redshift 1. *A&A*, **487**, L33–L36.
- Laureijs, R., Amiaux, J., Arduini, S., Auguères, J. ., Brinchmann, J., Cole, R., Cropper, M., Dabin, C., Duvet, L., Ealet, A., & et al. (2011). Euclid Definition Study Report. *ArXiv e-prints*, 1110.3193.

- Lazkoz, R. & Majerotto, E. (2007). Cosmological constraints combining  $H(z)$ , CMB shift and SNIa observational data. *JCAP*, **7**, 15–+.
- Lima, M. & Hu, W. (2005). Self-calibration of cluster dark energy studies: Observable-mass distribution. *Phys. Rev. D*, **72**(4), 043006–+.
- Lima, M. & Hu, W. (2007). Photometric redshift requirements for self-calibration of cluster dark energy studies. *Phys. Rev. D*, **76**(12), 123013–+.
- Linde, A. D. (1983). Chaotic inflation. *Physics Letters B*, **129**, 177–181.
- Linder, E. V. (2003). Exploring the Expansion History of the Universe. *Physical Review Letters*, **90**(9), 091301–+.
- Lombardi, M. & Bertin, G. (1998). Improving the accuracy of mass reconstructions from weak lensing: from the shear map to the mass distribution. *A&A*, **335**, 1–11.
- Lombardi, M., Rosati, P., Blakeslee, J. P., Ettori, S., Demarco, R., Ford, H. C., Illingworth, G. D., Clampin, M., Hartig, G. F., Benítez, N., Broadhurst, T. J., Franx, M., Jee, M. J., Postman, M., & White, R. L. (2005). Hubble Space Telescope ACS Weak-Lensing Analysis of the Galaxy Cluster RDCS 1252.9-2927 at  $z = 1.24$ . *ApJ*, **623**, 42–56.
- Lombriser, L., Slosar, A., Seljak, U., & Hu, W. (2010). Constraints on  $f(R)$  gravity from probing the large-scale structure. *ArXiv e-prints*.
- LoVerde, M., Miller, A., Shandera, S., & Verde, L. (2008). Effects of scale-dependent non-Gaussianity on cosmological structures. *Journal of Cosmology and Astro-Particle Physics*, **4**, 14–+.
- Lukić, Z., Heitmann, K., Habib, S., Bashinsky, S., & Ricker, P. M. (2007). The Halo Mass Function: High-Redshift Evolution and Universality. *ApJ*, **671**, 1160–1181.
- Mahdavi, A., Hoekstra, H., Babul, A., & Henry, J. P. (2008). Evidence for non-hydrostatic gas from the cluster X-ray to lensing mass ratio. *MNRAS*, **384**, 1567–1574.
- Majumdar, S. & Mohr, J. J. (2003). Importance of Cluster Structural Evolution in Using X-Ray and Sunyaev-Zeldovich Effect Galaxy Cluster Surveys to Study Dark Energy. *ApJ*, **585**, 603–610.

- Majumdar, S. & Mohr, J. J. (2004). Self-Calibration in Cluster Studies of Dark Energy: Combining the Cluster Redshift Distribution, the Power Spectrum, and Mass Measurements. *ApJ*, **613**, 41–50.
- Mantz, A., Allen, S. W., Ebeling, H., & Rapetti, D. (2008). New constraints on dark energy from the observed growth of the most X-ray luminous galaxy clusters. *MNRAS*, **387**, 1179–1192.
- Mantz, A., Allen, S. W., Ebeling, H., Rapetti, D., & Drlica-Wagner, A. (2009). The Observed Growth of Massive Galaxy Clusters II: X-ray Scaling Relations. *ArXiv e-prints*, 0909.3099.
- Mantz, A., Allen, S. W., Rapetti, D., & Ebeling, H. (2010a). The observed growth of massive galaxy clusters - I. Statistical methods and cosmological constraints. *MNRAS*, **406**, 1759–1772.
- Mantz, A., Allen, S. W., & Rapetti, D. (2010b). The observed growth of massive galaxy clusters - IV. Robust constraints on neutrino properties. *MNRAS*, **406**, 1805–1814.
- Marriage, T. & Atacama Cosmology Telescope Team (2010). The Atacama Cosmology Telescope: High Significance SZ Clusters and Extragalactic Sources. In *American Astronomical Society Meeting Abstracts #215*, volume 42 of *Bulletin of the American Astronomical Society*, page 384.03.
- Marriage, T. A. & the ACT Team (2011). The Atacama Cosmology Telescope: Sunyaev-Zel'dovich-Selected Galaxy Clusters at 148 GHz in the 2008 Survey. *ApJ*, **737**, 61–+.
- Marulli, F., Carbone, C., Viel, M., Moscardini, L., & Cimatti, A. (2011). Effects of Massive Neutrinos on the Large-Scale Structure of the Universe. *ArXiv e-prints*, 1103.0278.
- Matarrese, S. & Verde, L. (2008). The Effect of Primordial Non-Gaussianity on Halo Bias. *ApJ*, **677**, L77–L80.
- Matarrese, S., Verde, L., & Jimenez, R. (2000). The Abundance of High-Redshift Objects as a Probe of Non-Gaussian Initial Conditions. *ApJ*, **541**, 10–24.
- Mather, J. C., Cheng, E. S., Eplee, Jr., R. E., Isaacman, R. B., Meyer, S. S., Shafer, R. A., Weiss, R., Wright, E. L., & et al. (1990). A preliminary

- measurement of the cosmic microwave background spectrum by the Cosmic Background Explorer (COBE) satellite. *ApJ*, **354**, L37–L40.
- Maughan, B. J. (2007). The  $L_X - Y_X$  Relation: Using Galaxy Cluster X-Ray Luminosity as a Robust, Low-Scatter Mass Proxy. *ApJ*, **668**, 772–780.
- Maughan, B. J., Jones, L. R., Ebeling, H., & Scharf, C. (2006). The evolution of the cluster X-ray scaling relations in the Wide Angle ROSAT Pointed Survey sample at  $0.6 < z < 1.0$ . *MNRAS*, **365**, 509–529.
- Meerburg, P. D., van der Schaar, J. P., & Stefano Corasaniti, P. (2009). Signatures of initial state modifications on bispectrum statistics. *Journal of Cosmology and Astro-Particle Physics*, **5**, 18–+.
- Meneghetti, M., Rasia, E., Merten, J., Bellagamba, F., Ettori, S., Mazzotta, P., Dolag, K., & Marri, S. (2010). Weighing simulated galaxy clusters using lensing and X-ray. *A&A*, **514**, A93.
- Metzler, C. A., White, M., & Loken, C. (2001). The Effect of the Cosmic Web on Cluster Weak Lensing Mass Estimates. *ApJ*, **547**, 560–573.
- Miknaitis, G., Pignata, G., Rest, A., Wood-Vasey, W. M., Blondin, S., Chailis, P., Smith, R. C., Stubbs, C. W., Suntzeff, N. B., Foley, R. J., Matheson, T., Tonry, J. L., & et al. (2007). The ESSENCE Supernova Survey: Survey Optimization, Observations, and Supernova Photometry. *ApJ*, **666**, 674–693.
- Mo, H. J. & White, S. D. M. (1996). An analytic model for the spatial clustering of dark matter haloes. *MNRAS*, **282**, 347–361.
- Mortonson, M. J., Hu, W., & Huterer, D. (2011). Simultaneous falsification of  $\Lambda$ CDM and quintessence with massive, distant clusters. *Phys. Rev. D*, **83**(2), 023015–+.
- Mullis, C. R., Rosati, P., Lamer, G., Böhringer, H., Schwobe, A., Schuecker, P., & Fassbender, R. (2005). Discovery of an X-Ray-luminous Galaxy Cluster at  $z=1.4$ . *ApJ*, **623**, L85–L88.
- Murray, S. S. & WFXT Team (2010). The Wide Field X-ray Telescope Mission. In *Bulletin of the American Astronomical Society*, volume 41 of *Bulletin of the American Astronomical Society*, pages 520–+.

- Nagai, D., Vikhlinin, A., & Kravtsov, A. V. (2007). Testing X-Ray Measurements of Galaxy Clusters with Cosmological Simulations. *ApJ*, **655**, 98–108.
- Narayan, R. & Bartelmann, M. (1996). Lectures on Gravitational Lensing. *ArXiv Astrophysics e-prints*.
- Navarro, J. F., Frenk, C. S., & White, S. D. M. (1997). A Universal Density Profile from Hierarchical Clustering. *ApJ*, **490**, 493–+.
- Nord, B., Stanek, R., Rasia, E., & Evrard, A. E. (2008). Effects of selection and covariance on X-ray scaling relations of galaxy clusters. *MNRAS*, **383**, L10–L14.
- Oguri, M. (2009). Self-Calibrated Cluster Counts as a Probe of Primordial Non-Gaussianity. *Physical Review Letters*, **102**(21), 211301–+.
- Peacock, J. & Schneider, P. (2006). The ESO-ESA Working Group on Fundamental Cosmology. *The Messenger*, **125**, 48–+.
- Peacock, J. A. (1999). *Cosmological Physics*.
- Peebles, P. J. E. (1980). *The large-scale structure of the universe*. Research supported by the National Science Foundation. Princeton, N.J., Princeton University Press, 1980. 435 p.
- Peebles, P. J. E. (1993). *Principles of Physical Cosmology*.
- Percival, W. J. & White, M. (2009). Testing cosmological structure formation using redshift-space distortions. *MNRAS*, **393**, 297–308.
- Percival, W. J., Cole, S., Eisenstein, D. J., Nichol, R. C., Peacock, J. A., Pope, A. C., & Szalay, A. S. (2007). Measuring the Baryon Acoustic Oscillation scale using the Sloan Digital Sky Survey and 2dF Galaxy Redshift Survey. *MNRAS*, **381**, 1053–1066.
- Perlmutter, S. (2003). Supernovae, Dark Energy, and the Accelerating Universe. *Physics Today*, **56**(4), 040000–62.
- Perlmutter, S., Aldering, G., Goldhaber, G., Knop, R. A., Nugent, P., Castro, P. G., Deustua, S., Fabbro, S., & The Supernova Cosmology Project (1999). Measurements of Omega and Lambda from 42 High-Redshift Supernovae. *ApJ*, **517**, 565–586.

- Pierpaoli, E., Scott, D., & White, M. (2001). Power-spectrum normalization from the local abundance of rich clusters of galaxies. *MNRAS*, **325**, 77–88.
- Pierre, M., Pacaud, F., Juin, J. B., Melin, J. B., Valageas, P., Clerc, N., & Corasaniti, P. S. (2011). Precision cosmology with a wide area XMM cluster survey. *MNRAS*, **414**, 1732–1746.
- Piffaretti, R. & Valdarnini, R. (2008). Total mass biases in X-ray galaxy clusters. *A&A*, **491**, 71–87.
- Pillepich, A., Porciani, C., & Hahn, O. (2010). Halo mass function and scale-dependent bias from N-body simulations with non-Gaussian initial conditions. *MNRAS*, **402**, 191–206.
- Pillepich, A., Porciani, C., & Reiprich, T. H. (2011). The X-ray cluster survey with eROSITA: forecasts for cosmology, cluster physics, and primordial non-Gaussianity. *ArXiv e-prints*.
- Planck Collaboration (2011). Planck Early Results: The all-sky Early Sunyaev-Zeldovich cluster sample. *ArXiv e-prints*, 1101.2024.
- Pogosian, L. & Silvestri, A. (2008). Pattern of growth in viable  $f(R)$  cosmologies. *Phys. Rev. D*, **77**(2), 023503.
- Popesso, P., Biviano, A., Böhringer, H., Romaniello, M., & Voges, W. (2005). RASS-SDSS galaxy cluster survey. III. Scaling relations of galaxy clusters. *A&A*, **433**, 431–445.
- Predehl, P., Andritschke, R., Bornemann, W., Bräuninger, H., Briel, U., & et al. (2007). eROSITA. In *Society of Photo-Optical Instrumentation Engineers (SPIE) Conference Series*, volume 6686 of *Society of Photo-Optical Instrumentation Engineers (SPIE) Conference Series*.
- Press, W. H. & Schechter, P. (1974). Formation of Galaxies and Clusters of Galaxies by Self-Similar Gravitational Condensation. *ApJ*, **187**, 425–438.
- Rasia, E., Mazzotta, P., Borgani, S., Moscardini, L., Dolag, K., Tormen, G., Diaferio, A., & Murante, G. (2005). Mismatch between X-Ray and Emission-weighted Temperatures in Galaxy Clusters: Cosmological Implications. *ApJ*, **618**, L1–L4.

- Rasia, E., Ettori, S., Moscardini, L., Mazzotta, P., Borgani, S., Dolag, K., Tormen, G., Cheng, L. M., & Diaferio, A. (2006). Systematics in the X-ray cluster mass estimators. *MNRAS*, **369**, 2013–2024.
- Rasia, E., Meneghetti, M., Martino, R., Borgani, S., Bonafede, A., Dolag, K., Ettori, S., Fabjan, D., Giocoli, C., Mazzotta, P., Merten, J., Radovich, M., & Tornatore, L. (2012). Lensing and X-ray mass estimates of clusters (SIMULATION). *ArXiv e-prints*.
- Rassat, A., Amara, A., Amendola, L., Castander, F. J., Kitching, T., Kunz, M., Refregier, A., Wang, Y., & Weller, J. (2008). Deconstructing Baryon Acoustic Oscillations: A Comparison of Methods. *ArXiv e-prints*, 0810.0003.
- Raymond, J. C. & Smith, B. W. (1977). Soft X-ray spectrum of a hot plasma. *ApJS*, **35**, 419–439.
- Reed, D., Gardner, J., Quinn, T., Stadel, J., Fardal, M., Lake, G., & Governato, F. (2003). Evolution of the mass function of dark matter haloes. *MNRAS*, **346**, 565–572.
- Reed, D. S., Bower, R., Frenk, C. S., Jenkins, A., & Theuns, T. (2007). The halo mass function from the dark ages through the present day. *MNRAS*, **374**, 2–15.
- Reyes, R., Mandelbaum, R., Hirata, C., Bahcall, N., & Seljak, U. (2008). Improved optical mass tracer for galaxy clusters calibrated using weak lensing measurements. *MNRAS*, **390**, 1157–1169.
- Riess, A. G., Filippenko, A. V., Challis, P., Clocchiatti, A., Diercks, A., & et al. (1998). Observational Evidence from Supernovae for an Accelerating Universe and a Cosmological Constant. *AJ*, **116**, 1009–1038.
- Rines, K., Geller, M. J., Kurtz, M. J., & Diaferio, A. (2003). CAIRNS: The Cluster and Infall Region Nearby Survey. I. Redshifts and Mass Profiles. *AJ*, **126**, 2152–2170.
- Rines, K., Diaferio, A., & Natarajan, P. (2007). The Virial Mass Function of Nearby SDSS Galaxy Clusters. *ApJ*, **657**, 183–196.
- Robertson, B. E., Kravtsov, A. V., Tinker, J., & Zentner, A. R. (2009). Collapse Barriers and Halo Abundance: Testing the Excursion Set Ansatz. *ApJ*, **696**, 636–652.

- Roncarelli, M., Moscardini, L., Branchini, E., Dolag, K., Grossi, M., Iannuzzi, F., & Matarrese, S. (2010). Imprints of primordial non-Gaussianities in X-ray and SZ signals from galaxy clusters. *MNRAS*, **402**, 923–933.
- Rosati, P., Della Ceca, R., Burg, R., Norman, C., & Giacconi, R. (1995). A first determination of the surface density of galaxy clusters at very low x-ray fluxes. *ApJ*, **445**, L11–L14.
- Rosati, P., della Ceca, R., Norman, C., & Giacconi, R. (1998). The ROSAT Deep Cluster Survey: The X-Ray Luminosity Function Out to  $z=0.8$ . *ApJ*, **492**, L21+.
- Rosati, P., Borgani, S., & Norman, C. (2002). The Evolution of X-ray Clusters of Galaxies. *ARAA*, **40**, 539–577.
- Rosati, P., Tozzi, P., Ettori, S., Mainieri, V., Demarco, R., Stanford, S. A., Lidman, C., Nonino, M., Borgani, S., Della Ceca, R., Eisenhardt, P., Holden, B. P., & Norman, C. (2004). Chandra and XMM-Newton Observations of RDCS 1252.9-2927, A Massive Cluster at  $z=1.24$ . *AJ*, **127**, 230–238.
- Rosati, P., Tozzi, P., Gobat, R., Santos, J. S., Nonino, M., Demarco, R., Lidman, C., Mullis, C. R., Strazzullo, V., Böhringer, H., Fassbender, R., Dawson, K., Tanaka, M., Jee, J., Ford, H., Lamer, G., & Schwobe, A. (2009). Multi-wavelength study of XMMU J2235.3-2557: the most massive galaxy cluster at  $z > 1$ . *A&A*, **508**, 583–591.
- Rosati, P., Borgani, S., Gilli, R., Paolillo, M., Tozzi, P., Murray, S., Giacconi, R., Ptak, A., Weisskopf, M., Forman, W., Jones, C., & WFXT Team (2011). Wide Field X-ray Telescope: Mission Overview. *Memorie della Societa Astronomica Italiana Supplementi*, **17**, 8+.
- Rozo, E., Wechsler, R. H., Koester, B. P., McKay, T. A., Evrard, A. E., Johnston, D., Sheldon, E. S., Annis, J., & Frieman, J. A. (2007). Cosmological Constraints from SDSS maxBCG Cluster Abundances. *ArXiv Astrophysics e-prints*.
- Rozo, E., Wechsler, R. H., Rykoff, E. S., Annis, J. T., Becker, M. R., Evrard, A. E., Frieman, J. A., Hansen, S. M., Hao, J., Johnston, D. E., Koester,

- B. P., McKay, T. A., Sheldon, E. S., & Weinberg, D. H. (2010). Cosmological Constraints from the Sloan Digital Sky Survey maxBCG Cluster Catalog. *ApJ*, **708**, 645–660.
- Rozo, E., Rykoff, E., Koester, B., Nord, B., Wu, H.-Y., Evrard, A., & Wechsler, R. (2011). Extrinsic Sources of Scatter in the Richness-mass Relation of Galaxy Clusters. *ApJ*, **740**, 53.
- Rudd, D. H., Zentner, A. R., & Kravtsov, A. V. (2008). Effects of Baryons and Dissipation on the Matter Power Spectrum. *ApJ*, **672**, 19–32.
- Saito, S., Takada, M., & Taruya, A. (2011). Neutrino mass constraint from the Sloan Digital Sky Survey power spectrum of luminous red galaxies and perturbation theory. *Phys. Rev. D*, **83**(4), 043529–+.
- Salopek, D. S. & Bond, J. R. (1990). Nonlinear evolution of long-wavelength metric fluctuations in inflationary models. *Phys. Rev. D*, **42**, 3936–3962.
- Santos, J. S., Tozzi, P., Rosati, P., Nonino, M., & Giovannini, G. (2011). Deep Chandra observation of the galaxy cluster WARPJ1415.1+3612 at  $z=1$ : an evolved cool-core cluster at high-redshift. *ArXiv e-prints*, 1111.3642.
- Sartoris, B., Borgani, S., Fedeli, C., Matarrese, S., Moscardini, L., Rosati, P., & Weller, J. (2010). The potential of X-ray cluster surveys to constrain primordial non-Gaussianity. *ArXiv e-prints*.
- Sartoris, B., Borgani, S., Rosati, P., & Weller, J. (2011). Probing dark energy with the next generation X-ray surveys of galaxy clusters. *ArXiv e-prints*, 1112.0327.
- Schmidt, F., Lima, M., Oyaizu, H., & Hu, W. (2009). Nonlinear evolution of  $f(R)$  cosmologies. III. Halo statistics. *Phys. Rev. D*, **79**(8), 083518–+.
- Schneider, P. (2006). Part 3: Weak gravitational lensing. In G. Meylan, P. Jetzer, P. North, P. Schneider, C. S. Kochanek, & J. Wambsganss, editor, *Saas-Fee Advanced Course 33: Gravitational Lensing: Strong, Weak and Micro*, pages 269–451.
- Schuecker, P., Böhringer, H., Collins, C. A., & Guzzo, L. (2003). The REFLEX galaxy cluster survey. VII.  $\Omega_m$  and  $\sigma_8$  from cluster abundance and large-scale clustering. *A&A*, **398**, 867–877.

- Sehgal, N., Bode, P., Das, S., Hernandez-Monteagudo, C., Huffenberger, K., Lin, Y.-T., Ostriker, J. P., & Trac, H. (2010). Simulations of the Microwave Sky. *ApJ*, **709**, 920–936.
- Seljak, U. (2002). Cluster number density normalization from the observed mass-temperature relation. *MNRAS*, **337**, 769–773.
- Shang, C., Haiman, Z., & Verde, L. (2009). Probing cosmology and galaxy cluster structure with the Sunyaev-Zel’dovich decrement versus X-ray temperature scaling relation. *MNRAS*, **400**, 1085–1104.
- Sheth, R. K. & Tormen, G. (1999). Large-scale bias and the peak background split. *MNRAS*, **308**, 119–126.
- Sheth, R. K., Mo, H. J., & Tormen, G. (2001). Ellipsoidal collapse and an improved model for the number and spatial distribution of dark matter haloes. *MNRAS*, **323**, 1–12.
- Silk, J. (1976). Accretion by galaxy clusters and the relationship between X-ray luminosity and velocity dispersion. *ApJ*, **208**, 646–649.
- Silvestri, A. & Trodden, M. (2009). Approaches to understanding cosmic acceleration. *Reports on Progress in Physics*, **72**(9), 096901–+.
- Slosar, A., Hirata, C., Seljak, U., Ho, S., & Padmanabhan, N. (2008). Constraints on local primordial non-Gaussianity from large scale structure. *Journal of Cosmology and Astro-Particle Physics*, **8**, 31–+.
- Sotiriou, T. P. & Faraoni, V. (2010).  $f(R)$  theories of gravity. *Reviews of Modern Physics*, **82**, 451–497.
- Spiegel, D. N., Bean, R., Doré, O., Nolta, M. R., Bennett, C. L., & et al. (2007). Three-Year Wilkinson Microwave Anisotropy Probe (WMAP) Observations: Implications for Cosmology. *ApJS*, **170**, 377–408.
- Stanek, R., Evrard, A. E., Böhringer, H., Schuecker, P., & Nord, B. (2006). The X-Ray Luminosity-Mass Relation for Local Clusters of Galaxies. *ApJ*, **648**, 956–968.
- Stanek, R., Rudd, D., & Evrard, A. E. (2009). The effect of gas physics on the halo mass function. *MNRAS*, **394**, L11–L15.

- Stanek, R., Rasia, E., Evrard, A. E., Pearce, F., & Gazzola, L. (2010). Massive Halos in Millennium Gas Simulations: Multivariate Scaling Relations. *ApJ*, **715**, 1508–1523.
- Stanford, S. A., Holden, B., Rosati, P., Tozzi, P., Borgani, S., Eisenhardt, P. R., & Spinrad, H. (2001). The Intracluster Medium in  $z>1$  Galaxy Clusters. *ApJ*, **552**, 504–507.
- Stanford, S. A., Holden, B., Rosati, P., Eisenhardt, P. R., Stern, D., Squires, G., & Spinrad, H. (2002). An X-Ray-Selected Galaxy Cluster at  $z=1.11$  in the ROSAT Deep Cluster Survey. *AJ*, **123**, 619–626.
- Staniszewski, Z., Ade, P. A. R., Aird, K. A., Benson, B. A., Bleem, L. E., & et al. (2009). Galaxy Clusters Discovered with a Sunyaev-Zel'dovich Effect Survey. *ApJ*, **701**, 32–41.
- Stril, A., Cahn, R. N., & Linder, E. V. (2010). Testing standard cosmology with large-scale structure. *MNRAS*, **404**, 239–246.
- Sunyaev, R. A. & Zeldovich, Y. B. (1970). Small-Scale Fluctuations of Relic Radiation. *Astroph. Sp. Sci.*, **7**, 3–19.
- Sunyaev, R. A. & Zeldovich, Y. B. (1972). The Observations of Relic Radiation as a Test of the Nature of X-Ray Radiation from the Clusters of Galaxies. *Comments on Astrophysics and Space Physics*, **4**, 173–+.
- Taruya, A., Koyama, K., & Matsubara, T. (2008). Signature of primordial non-Gaussianity on the matter power spectrum. *Phys. Rev. D*, **78**(12), 123534–+.
- Tegmark, M. (1997). Measuring Cosmological Parameters with Galaxy Surveys. *Physical Review Letters*, **79**, 3806–3809.
- Tinker, J., Kravtsov, A. V., Klypin, A., Abazajian, K., Warren, M., Yepes, G., Gottlöber, S., & Holz, D. E. (2008). Toward a Halo Mass Function for Precision Cosmology: The Limits of Universality. *ApJ*, **688**, 709–728.
- Tinker, J. L., Robertson, B. E., Kravtsov, A. V., Klypin, A., Warren, M. S., Yepes, G., & Gottlöber, S. (2010). The Large-scale Bias of Dark Matter Halos: Numerical Calibration and Model Tests. *ApJ*, **724**, 878–886.
- Truemper, J. (1993). ROSAT - A new look at the X-ray sky. *Science*, **260**, 1769–1771.

- Tsujikawa, S. (2010). Dark energy: investigation and modeling. *ArXiv e-prints*, 1004.1493.
- Umetsu, K., Broadhurst, T., Zitrin, A., Medezinski, E., Coe, D., & Postman, M. (2011). A Precise Cluster Mass Profile Averaged from the Highest-quality Lensing Data. *ApJ*, **738**, 41.
- Verde, L. & Matarrese, S. (2009). Detectability of the Effect of Inflationary Non-Gaussianity on Halo Bias. *ApJ*, **706**, L91–L95.
- Viana, P. T. P. & Liddle, A. R. (1996). The cluster abundance in flat and open cosmologies. *MNRAS*, **281**, 323.
- Viana, P. T. P. & Liddle, A. R. (1999). Galaxy clusters at  $0.3 < z < 0.4$  and the value of  $\Omega_0$ . *MNRAS*, **303**, 535–545.
- Viana, P. T. P., Nichol, R. C., & Liddle, A. R. (2002). Constraining the Matter Power Spectrum Normalization Using the Sloan Digital Sky Survey/ROSAT All-Sky Survey and REFLEX Cluster Surveys. *ApJ*, **569**, L75–L78.
- Vikhlinin, A., Kravtsov, A., Forman, W., Jones, C., Markevitch, M., Murray, S. S., & Van Speybroeck, L. (2006). Chandra Sample of Nearby Relaxed Galaxy Clusters: Mass, Gas Fraction, and Mass-Temperature Relation. *ApJ*, **640**, 691–709.
- Vikhlinin, A., Burenin, R. A., Ebeling, H., Forman, W. R., Hornstrup, A., Jones, C., Kravtsov, A. V., Murray, S. S., Nagai, D., Quintana, H., & Voevodkin, A. (2009a). Chandra Cluster Cosmology Project. II. Samples and X-Ray Data Reduction. *ApJ*, **692**, 1033–1059.
- Vikhlinin, A., Kravtsov, A. V., Burenin, R. A., Ebeling, H., Forman, W. R., Hornstrup, A., Jones, C., Murray, S. S., Nagai, D., Quintana, H., & Voevodkin, A. (2009b). Chandra Cluster Cosmology Project III: Cosmological Parameter Constraints. *ApJ*, **692**, 1060–1074.
- Voevodkin, A. & Vikhlinin, A. (2004). Constraining Amplitude and Slope of the Mass Fluctuation Spectrum Using a Cluster Baryon Mass Function. *ApJ*, **601**, 610–620.
- Voges, W., Aschenbach, B., Boller, T., Bräuninger, H., Briel, U., & et al. (1999). The ROSAT all-sky survey bright source catalogue. *A&A*, **349**, 389–405.

- Voit, G. M. (2005). Tracing cosmic evolution with clusters of galaxies. *Reviews of Modern Physics*, **77**, 207–258.
- Voit, G. M., Evrard, A. E., & Bryan, G. L. (2001). Confusion of Diffuse Objects in the X-Ray Sky. *ApJ*, **548**, L123–L126.
- Wang, Y. (2008). Figure of merit for dark energy constraints from current observational data. *Phys. Rev. D*, **77**(12), 123525.
- Wang, Y., Percival, W., Cimatti, A., Mukherjee, P., Guzzo, L., Baugh, C. M., Carbone, C., Franzetti, P., Garilli, B., Geach, J. E., Lacey, C. G., Majerotto, E., Orsi, A., Rosati, P., Samushia, L., & Zamorani, G. (2010). Designing a space-based galaxy redshift survey to probe dark energy. *MNRAS*, **409**, 737–749.
- Weinberg, S. (1972). *Gravitation and Cosmology: Principles and Applications of the General Theory of Relativity*.
- Weinberg, S. (1989). The cosmological constant problem. *Reviews of Modern Physics*, **61**, 1–23.
- Wen, Z. L., Han, J. L., & Liu, F. S. (2009). Galaxy Clusters Identified from the SDSS DR6 and Their Properties. *ApJS*, **183**, 197–213.
- Wetterich, C. (2004). Phenomenological parameterization of quintessence. *Physics Letters B*, **594**, 17–22.
- Weymann, R. (1966). The Energy Spectrum of Radiation in the Expanding Universe. *ApJ*, **145**, 560.
- White, M., Hernquist, L., & Springel, V. (2002). Simulating the Sunyaev-Zeldovich Effect(s): Including Radiative Cooling and Energy Injection by Galactic Winds. *ApJ*, **579**, 16–22.
- White, S. D. M., Efstathiou, G., & Frenk, C. S. (1993). The amplitude of mass fluctuations in the universe. *MNRAS*, **262**, 1023–1028.
- Williamson, R. & the SPT Team (2011). A Sunyaev-Zel'dovich-selected Sample of the Most Massive Galaxy Clusters in the 2500 deg<sup>2</sup> South Pole Telescope Survey. *ApJ*, **738**, 139–+.
- Wu, H., Zentner, A. R., & Wechsler, R. H. (2009). The Impact of Theoretical Uncertainties in the Halo Mass Function and Halo Bias on Precision Cosmology. *ArXiv e-prints*, 0910.3668.

- Yadav, A. P. S. & Wandelt, B. D. (2008). Evidence of Primordial Non-Gaussianity ( $f_{NL}$ ) in the Wilkinson Microwave Anisotropy Probe 3-Year Data at  $2.8\sigma$ . *Physical Review Letters*, **100**(18), 181301–+.
- York, D. G., Adelman, J., Anderson, Jr., J. E., Anderson, S. F., Annis, J., Bahcall, N. A., Bakken, J. A., Barkhouser, R., & et al. (2000). The Sloan Digital Sky Survey: Technical Summary. *AJ*, **120**, 1579–1587.
- Yu, H., Tozzi, P., Borgani, S., Rosati, P., & Zhu, Z.-H. (2011). Measuring redshifts using X-ray spectroscopy of galaxy clusters: results from Chandra data and future prospects. *A&A*, **529**, A65+.
- Zhang, Y.-Y., Okabe, N., Finoguenov, A., Smith, G. P., Piffaretti, R., Valdarnini, R., Babul, A., Evrard, A. E., Mazzotta, P., Sanderson, A. J. R., & Marrone, D. P. (2010). LoCuSS: A Comparison of Cluster Mass Measurements from XMM-Newton and Subaru—Testing Deviation from Hydrostatic Equilibrium and Non-thermal Pressure Support. *ApJ*, **711**, 1033–1043.
- Zlatev, I., Wang, L., & Steinhardt, P. J. (1999). Quintessence, Cosmic Coincidence, and the Cosmological Constant. *Physical Review Letters*, **82**, 896–899.